

The Microphysical and Radiative Interactions of Arctic Multilayer Clouds

Zur Erlangung des akademischen Grades eines
DOKTORS DER NATURWISSENSCHAFTEN
(Dr. rer. nat.)

von der KIT-Fakultät für Physik des
Karlsruher Instituts für Technologie (KIT)

genehmigte

DISSERTATION

von

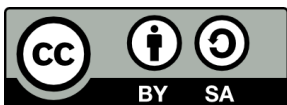
Master of Chemical Physics
Gabriella Linnea Wallentin
aus Östersund, Schweden

Tag der mündlichen Prüfung: 06.12.2024

Referentin: Prof. Dr. Corinna Hoose

Korreferentin: Prof. Dr. Luisa Ickes





This document is licensed under a Creative Commons Attribution-Share Alike 4.0 International License (CC BY-SA 4.0):

<https://creativecommons.org/licenses/by-sa/4.0/deed.en>

ABSTRACT

Multilayer clouds (MLCs) are common in the Arctic, yet they are hitherto underrepresented in the existing literature. MLCs are defined as clouds that are vertically stacked. The Arctic is, in general, a cloudy region that has been significantly affected by the phenomenon of Arctic Amplification, which refers to the accelerated warming of the Arctic region due to climate change over recent decades. This mechanism is not yet fully understood. The role of clouds is of critical importance in understanding these changes and their future impacts in the region. Consequently, there is a need for further research to enhance our understanding of how we can more accurately represent Arctic clouds in climate and weather models and to what extent multilayer clouds play a role in the climate system.

To gain further insight into these cloud systems, we study multilayer clouds during the high-Arctic Multidisciplinary drifting Observatory for the Study of Arctic Climate (MOSAiC) campaign during 2019/2020. This was the largest year-long campaign in the high-Arctic and has provided us with ground-breaking new measurements and long-term statistics of the Arctic system. To this effect, it serves as a long-term evaluation site for model development. We set up the ICOSahedral Non-hydrostatic (ICON) model, using case studies, to evaluate the representation of MLCs, deepen our understanding of how they interact, microphysically and radiatively, and improve the general modelling of Arctic clouds.

We find a 67% occurrence frequency of MLCs across the Arctic during the early Autumn of 2020, indicating that they govern the observational signals in the region. However, MLCs remain a challenge to model. In particular, accurate thermodynamic profiles are required for vertical layering and an improved representation of Arctic aerosols must be included. The relative abundance of aerosols governs cloud liquid and ice mass (and number) concentrations. The model consistently underestimates ice mass concentrations compared to observations. We find that representing the primary ice production is vital but secondary ice production, whereby cloud hydrometeors interact and produce ice splinters, is required to reach observed values.

Multilayer clouds interact through radiation and microphysics. Radiatively, a suppression in cloud-top longwave radiative cooling is found in lower cloud layers when overlaying clouds are present. The reduction amounts to 24 K day^{-1} for mixed-phase cloud tops. Microphysically, they interact through the seeder-feeder mechanism, whereby frozen hydrometeors such as ice, snow, and graupel fall from an upper seeder cloud into a lower feeder cloud. The hydrometeors act as seeds for ice formation and efficiently promote ice growth and further precipitation. We find a 48% occurrence of seeding in our modelled multilayer clouds, stressing this process as a major influence on Arctic MLCs.

This work highlights the importance of studying multilayer clouds in the Arctic due to their abundance in the region. Microphysical and radiative impacts on other cloud layers as well as the surface are quantified and we have acquired a deeper understanding of how the clouds interact with each other and the surface. With this study, we provide improved modelling methods and a solid foundation for further modelling studies on multilayer clouds.

KURZFASSUNG

Mehrschichtige Wolken ("Multilayer Clouds", MLCs) treten in der Arktis häufig auf, sind aber in der vorhandenen Literatur bisher unterrepräsentiert. MLCs sind definiert als mehrere Wolkenschichten, welche vertikal überlagert sind. Die Arktis ist im Allgemeinen eine wolkenreiche Region, die durch das Phänomen der polaren Amplifikation (Arctic Amplification), d. h. die beschleunigte Erwärmung der arktischen Region aufgrund des Klimawandels in den letzten Jahrzehnten, erheblich beeinträchtigt wurde. Dieser Mechanismus ist noch nicht vollständig geklärt. Die Rolle der Wolken ist für das Verständnis dieser Veränderungen und ihrer künftigen Auswirkungen in der Region von entscheidender Bedeutung. Folglich besteht weiterer Forschungsbedarf, um unser Verständnis dafür zu verbessern, wie wir arktische Wolken in Wetter- und Klimamodellen genauer darstellen können und inwieweit mehrschichtige Wolken eine Rolle spielen.

Um weitere Einblicke in diese Wolkensysteme zu gewinnen, untersuchen wir MLCs während der Multidisciplinary drifting Observatory for the Study of Arctic Climate (MOSAIC) Kampagne in der Arktis, welche in den Jahren 2019/2020 statt fand. Dies war die größte einjährige Kampagne in der Hocharktis und hat bahnbrechende neue Messungen und Langzeitstatistiken geliefert. Daher dient sie als Standort für die Evaluierung für die Modellentwicklung. Wir verwenden das nicht-hydrostatische ICOsahedral-Modell (ICON), um die Darstellung dieser Wolken in Modellsimulationen zu bewerten, unser Verständnis ihrer mikrophysikalischen und strahlungsbezogenen Wechselwirkungen zu vertiefen und die allgemeine Modellierung arktischer Wolken zu verbessern.

Wir stellen fest, dass die Häufigkeit von MLCs in der Arktis 67% beträgt, was darauf hindeutet, dass sie die Messungen und Wolkenbeobachtungen in der Region dominieren. Allerdings sind MLCs nach wie vor schwer zu modellieren, da eine korrekte Darstellung der thermodynamischen Profile für die vertikale Schichtung sowie der arktischen Aerosole erforderlich ist. Die relative Häufigkeit von Aerosolen bestimmt die Massen- und Anzahlkonzentrationen von Wolkenwasser und Wolkeneis. Das Modell unterschätzt durchweg die Eismassenkonzentration im Vergleich zu den Beobachtungen. Wir stellen fest, dass die Darstellung der primären Eisproduktion von entscheidender Bedeutung ist, dass aber die sekundäre Eisproduktion, bei welcher Wolkenhydrometeore

interagieren und Eissplitter bilden, erforderlich ist, um die beobachteten Werte zu erreichen.

Mehrschichtige Wolken interagieren durch Strahlung und Mikrophysik. In Bezug auf die Strahlung wird eine Unterdrückung der langwelligen Strahlungskühlung der Wolkenoberkante in den unteren Wolkenschichten festgestellt, wenn überlagernde Wolken vorhanden sind. Die Reduktion beträgt 24 K pro Tag an der Wolkenoberseite von Mischphasenwolken. Mikrophysikalisch interagieren sie durch den Seeder-Feeder-Mechanismus, bei dem gefrorene Hydrometeore wie Eis, Schnee und Graupel von einer oberen "Seeder"-Wolke in eine untere "Feeder"-Wolke fallen. Die Hydrometeore wirken als Nukleationskeim für die Eisbildung und fördern effizient das Eiswachstum und dadurch die Niederschlagsbildung. Wir stellen fest, dass "Seeding" (Impfen) in 48% unserer modellierten MLCs vorkommt, was diesen Prozess als einen wichtigen Einfluss auf die Struktur arktischer MLCs hervorhebt.

Diese Arbeit unterstreicht die Bedeutung der Untersuchung MLCs in der Arktis aufgrund ihrer Häufigkeit in dieser Region. Die mikrophysikalischen und strahlungsbedingten Interaktionen zwischen den Wolkenschichten und der Oberfläche werden quantifiziert, und wir liefern eine solide mikrophysikalische Grundlage für weitere Studien zu diesen Wolkensystemen.

PREFACE

The PhD candidate confirms that the research presented in this thesis contains significant scientific contributions produced by herself. This thesis reuses material from the following publication:

Wallentin, G., Oertel, A., Ickes, L., Achtert, P., Tesche, M., and Hoose, C.: Arctic Multilayer Clouds Require Accurate Thermodynamic Profiles and Efficient Primary and Secondary Ice Processes for a Realistic Structure and Composition, EGU sphere [preprint], Available at: <https://doi.org/10.5194/egusphere-2024-2988>, 2024.

The funding was supplied by the Federal Ministry of Education and Research under project number 03F0891B.

The observational MLC algorithm, used for model evaluation, was run by our project collaborator, Peggy Achtert, at the University of Leipzig. The code is available on GitHub (https://github.com/maikenv/Classification_algorithm_of_multilayer_clouds).

Grammarly, DeepL, and ChatGPT have been used for the improvement of post-processing scripts, plotting scripts, and stylistic improvements in the thesis. The virtual whiteboard Excalidraw has been used to generate sketches.

©2025, Karlsruhe Institute of Technology and Gabriella Wallentin

"The only true wisdom is in knowing you know nothing."
– Socrates

CONTENTS

Abstract	i
Kurzfassung	iii
Preface	v
Acronyms and symbols	xi
1 Introduction	1
2 Research Questions	5
3 Theoretical Background and its Representation in ICON	9
3.1 The ICON Model	9
3.1.1 Parameterisations	11
3.2 Cloud Microphysics	14
3.2.1 Warm Processes	17
3.2.2 Cold Processes	22
3.3 Cloud-Radiation Interaction	31
3.4 The Arctic System	34
4 Data and Methods	41
4.1 General Model Setup	41
4.1.1 COOKIE Implementation	45
4.1.2 Diagnostics	46
4.2 Observational Data	48
4.2.1 The MOSAiC Campaign	48
4.2.2 Additional Aerosol Measurements	52
4.2.3 Observational Multilayer Cloud Algorithm	53
4.3 Analysis Methods	54
4.3.1 Methods for Model Evaluation	54
4.3.2 Trajectories	54
4.3.3 Statistical Metrics	55

5 Case Study on the Microphysical Interactions of Arctic Multilayer Clouds	57
5.1 Aerosol Constraints	57
5.1.1 Case Description	60
5.2 Evaluating the Coarse Simulations of MLCs	62
5.3 Microphysical Sensitivity Simulations	64
5.3.1 1.6 km Simulations for 1st of September	64
5.3.2 1.6 km Simulations for 3rd of September	66
5.3.3 Can the Lack of Cloud Ice be Explained by SIP?	70
5.4 Summary & Discussion	73
6 Case Study on the Radiative Interactions of Multilayer Clouds	77
6.1 COOKIE Setup	77
6.2 Case Description	78
6.3 The Radiative Impact of Overlapping Layers	79
6.4 The Radiative Impact on the Splitting of a Cloud	83
6.5 Regional Signal in the Suppression of Cloud-top Longwave Radiative Cooling	86
6.6 Summary & Discussion	91
7 Long-term Model Evaluation at the MOSAiC Site	95
7.1 Aerosol Constraints	95
7.2 Long-term Comparison at the MOSAiC Site	97
7.3 Summary & Discussion	103
8 Regional Long-term Arctic Simulations of Multilayer Clouds	105
8.1 Multilayer Clouds at MOSAiC	106
8.2 Modelled Microphysical Differences between MLCs and SLC at the MOSAiC Site	110
8.3 Multilayer Clouds Across the Arctic	114
8.4 Summary & Discussion	116
9 Conclusions	123
10 Outlook	133
Appendices	137
A Appendix to Chapter 5	138
A.1 High resolution simulations	138
A.2 Additional Figures	142
B Appendix to Chapter 6	144

C Appendix to Chapter 8	148
C.1 MLC Algorithm Evaluation	148
C.2 Additional Figures	150
Acknowledgements	153
Bibliography	155

ACRONYMS

MLC Multilayer Clouds
SLC Single-Layer Clouds
CCN.....Cloud Condensation Nuclei
INP.....Ice Nucleating Particle
SLF Supercooled Liquid Fraction
SIP Secondary Ice Production
QV Specific Humidity
LWC.....Liquid Water Content
IWC.....Ice Water Content
SWC Snow Water Content
LWP.....Liquid Water Path
IWP.....Ice Water Path
SWP Snow Water Path
GWP Graupel Water Path
FWP Frozen Water Path (IWP+SWP+GWP)
CT Cloud Top
CB Cloud Base

LW Longwave Radiation
SW Shortwave Radiation
CRE.....Cloud Radiative Effect
CRH.....Cloud Radiative Heating

NWP Numerical Weather Prediction
ICON.....ICOsahedral Non-hydrostatic
LES Large Eddy Simulation
COOKIE Clouds On and Off Klimate Intercomparison Experiment
MOSAiC.....Multidisciplinary drifting Observatory for the Study of Arctic Climate

1 | INTRODUCTION

A multilayer cloud (MLC), is a cloud system of two or more vertically stacked cloud layers. With a global mean frequency of about 30%, determined from satellite studies (Wind et al., 2010; Liu et al., 2012; Wang et al., 2016; Subrahmanyam and Kumar, 2017; Matus and L’Ecuyer, 2017; L’Ecuyer et al., 2019; Marchant et al., 2020), they contribute to about 40% to the global mean net cloud radiative effect (CRE), which helps to cool the planet (Li et al., 2015; L’Ecuyer et al., 2019). Regional studies using in-situ measurements and modelling approaches have further elucidated the frequency of occurrence of multilayer clouds. A measurement campaign conducted in the Southern Ocean revealed a 34% multilayer cloud occurrence, comparable to the global mean. In contrast, a 50% occurrence was found for the Swiss Alps, using a weather model (Dedekind et al., 2024). At stations and during campaigns in the Arctic, MLCs are reported more frequently (Herman and Goody, 1976; Tsay and Jayaweera, 1984; Intrieri et al., 2002b; Liu et al., 2012; Vassel et al., 2019; Nomokonova et al., 2019; Vüllers et al., 2021; Silber and Shupe, 2022). Data obtained from the Multidisciplinary drifting Observatory for the Study of Arctic Climate (MOSAIC) expedition, conducted during 2019/2020, indicate that liquid-bearing MLCs occurred with a frequency of 51% (Silber and Shupe, 2022). During the 2018 Microbiology-Ocean-Cloud-Coupling in the High Arctic (MOCCHA) campaign, a 54% occurrence was identified (Vüllers et al., 2021). The first year-long Arctic campaign, Surface Heat Budget of the Arctic Ocean (SHEBA), indicated a prevalence of approximately 60% for MLCs (Intrieri et al., 2002a). At lower latitudes, during the aircraft campaign PS106 an occurrence of 36% of MLCs was reported (Barrientos-Velasco et al., 2022) and at the research station at Ny Ålesund, Svalbard, frequencies of 29% (Vassel et al., 2019) and 44% (Nomokonova et al., 2019) were found. In contrast, in their investigation of cloudy profiles in the Arctic (60°N - 82°N) using satellite products, Liu et al. (2012) found an MLC frequency of only 20%. Furthermore, they observed no clear spatial preference indicating that the high Arctic would have a higher MLC occurrence as been noted by the ship-based studies. Considering that low-level clouds are prevalent in the Arctic, a clear limitation to the satellite classification can be noted as requirements include the exclusion of the lowest 500 m of the troposphere due to ground clutter (Dietel et al., 2024). Satellites may also

struggle to capture thin cloud layers in general (L'Ecuyer et al., 2019). Thus, based on ship data, we hypothesise there is an increase of MLCs towards the pole, but this is yet to be determined from a large-scale perspective.

With a strong dependence on location, the presence of MLCs can lead to warming outside of the tropics (Li et al., 2011). Optically thin high clouds tend to warm the surface, whereas optically thick low clouds typically exert a cooling effect. In the Arctic region, clouds have an overall warming effect (Shupe and Intrieri, 2003; L'Ecuyer et al., 2019). This is due to the strong longwave signal during the polar night and the high albedo of the sea ice. MLCs in the Arctic region, up to 82°N , have been found to exert the largest heating at the surface from a satellite perspective (L'Ecuyer et al., 2019). The impact of MLCs in the high-Arctic has not been further studied due to the lack of vertically resolved satellites above 82°N .

Despite their relatively large global occurrence, we know very little about these cloud systems, with few studies investigating their formation, interaction, persistence, and dissipation mechanisms. Many classification studies exist (e.g. Liu et al., 2012; Wang et al., 2016; Subrahmanyam and Kumar, 2017; Matus and L'Ecuyer, 2017; Oreopoulos et al., 2017) but studies on large-scale persistence of MLCs have only recently emerged (Jian et al., 2022). Due to their large abundance in the Arctic region, observational studies (e.g. Tsay and Jayaweera, 1984; Turner et al., 2018; Lonardi et al., 2022), several idealised modelling approaches (e.g. Herman and Goody, 1976; McInnes and Curry, 1995; Harrington et al., 1999; Luo et al., 2008; Chen et al., 2020; Bulatovic et al., 2023), and real setups (e.g. Morrison et al., 2009; Fu et al., 2019) have been used to gain a process-understanding on how these clouds form, dissipate, and interact. Through these studies, a consensus is emerging that MLCs tend to form through advection (Tsay and Jayaweera, 1984; Luo et al., 2008; Morrison et al., 2009). However, this is a highly debated topic with each case study finding limits and prerequisites to this assumption.

In regards to the interplay between the cloud layers, they may interact through radiation. Clouds emit longwave radiation, which acts to cool the cloud while heating the atmosphere surrounding it. In the multilayer cloud system, a longwave radiative cooling suppression of an underlying cloud has been found to occur when an upper cloud layer is present. This phenomenon has been seen in observational case studies in the Arctic (Shupe et al., 2013; Turner et al., 2018; Lonardi et al., 2022), idealised modelling studies (Chen and Cotton, 1987; Luo et al., 2008; Chen et al., 2020) and satellite studies (Christensen et al., 2013; Adebisi et al., 2020; Jian et al., 2022). All these studies exhibit a large difference in the magnitude of reduction in cloud-top longwave radiative cooling and the limits of the occurrence. Turner et al. (2018), investigated the cloud top cooling for clouds on the northern slope of Alaska and found a 7-fold suppression of longwave radiative cooling for cloud layers with an overlaying liquid-bearing cloud. The suppression of longwave radiative cooling of clouds in the high-Arctic, though noted by observational studies (Shupe et al., 2013; Lonardi et al., 2022), is yet to be quantified.

Arctic clouds are commonly found in the mixed-phase temperature regime, $0^{\circ}\text{C} < T < -38^{\circ}\text{C}$, (Mossop, 1954; Korolev et al., 2017), where ice particles and supercooled liquid droplets may coexist. In the atmosphere, cloud droplets and ice particles do not form easily. The phase change from water vapour requires an abundance of aerosols capable of cloud formation; cloud condensation nuclei (CCN) and ice nucleating particles (INP). Commonly soluble, CCN particles allow for cloud droplet activation while INPs, insoluble larger particles, promote ice nucleation. Few studies exist on the response of multilayer clouds to microphysical perturbations. As with single-layer clouds, a linear correlation between the abundance of CCN and cloud liquid mass has been reported (Bulatovic et al., 2021). However, models struggle to capture the ice phase for both single-layer (Fridlind and Ackerman, 2017; Stevens et al., 2018) and multilayer clouds (Morrison et al., 2009; Fu et al., 2019). Furthermore, overlapping cloud layers may interact through the seeder-feeder mechanism. According to this process, frozen hydrometeors falling into a lower layer can lead to efficient glaciation and precipitation enhancement of a lower cloud through the Wegener-Bergeron-Findeisen (WBF) mechanism (Wegener, 1911; Bergeron, 1928; Findeisen, 1938) as evidenced by previous studies (Chen et al., 2020; Proske et al., 2021; Jian et al., 2022; Dedekind et al., 2024). The WBF mechanism describes the process where ice crystals grow at the expense of cloud droplets due to differences in saturation water vapour pressure (Korolev, 2007). This process may be further enhanced by secondary ice production (SIP) (Georgakaki et al., 2022), whereby ice fragments are generated from interactions between cloud hydrometeors. Several modelling studies have shown the importance of including SIP as a source of cloud ice in Arctic clouds (Sotiropoulou et al., 2020; Schäfer et al., 2024; Sotiropoulou et al., 2024) with a large occurrence of the breakup upon ice-ice collision mechanism. Droplet freezing followed by shattering into small ice fragments is another SIP which has been shown to have a large impact on the clouds at the northern slope of Alaska for both single-layer (Zhao et al., 2021) and multilayer (Fu et al., 2019) clouds. The frequency and limitations of these microphysical interactions are still largely unknown for Arctic MLCs.

Gaps in our understanding of multilayer clouds are studied in this thesis with the help of the German Weather Service (Deutsche Wetterdienst, DWD) operational forecast model ICosahedral Non-hydrostatic (ICON) model (Zängl et al., 2015). In Chapter 2 these gaps are further identified and contextualised into research questions and aims of this thesis; some of these are sketched in Fig. 1.1. Chapter 3 provides a solid background into the concepts of cloud physics and how we model these processes using ICON. The data and methods chapter, Chapter 4, gives a detailed model setup description together with an introduction to the observational data from the MOSAiC campaign and other datasets used for model constraint and evaluation. The results are divided into four chapters. The first result chapter, Chapter 5, is based on the submitted paper by Wallentin et al. (2024) and provides a case study during the MOSAiC campaign

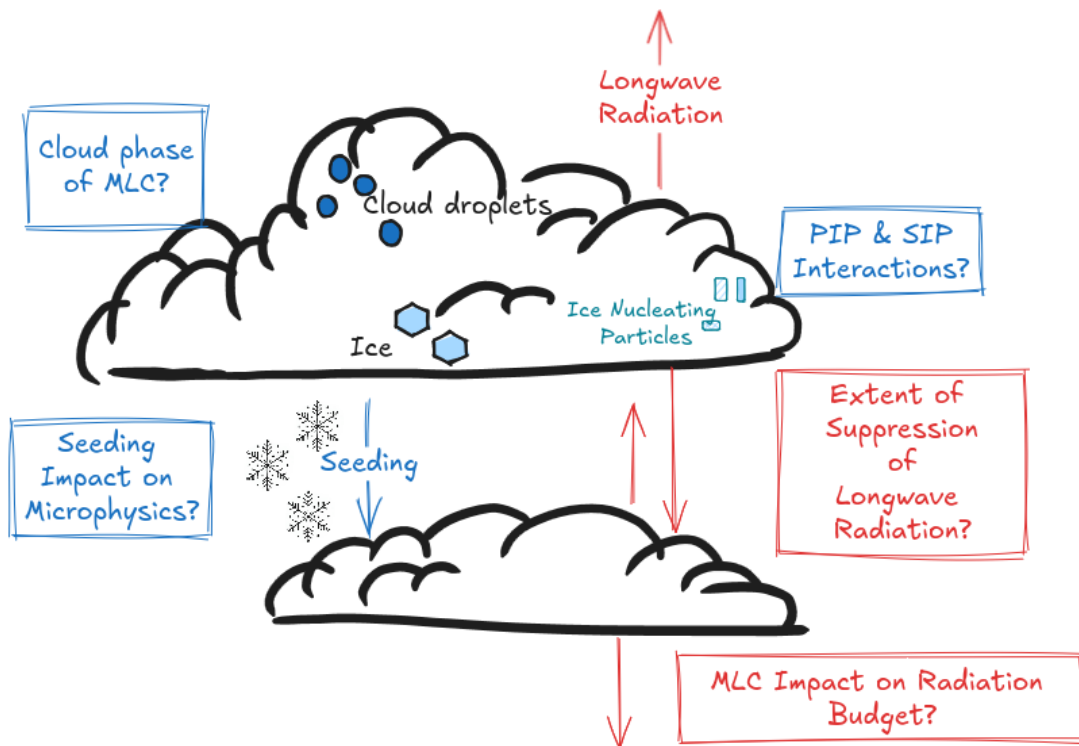


Figure 1.1: The multilayer cloud system with some of the questions posed in this thesis.

including a detailed evaluation of the most accurate ways of modelling multilayer clouds. Furthermore, a robust sensitivity study of droplet activation, primary ice (PIP) and secondary ice production is presented. Chapter 6, presents another aspect of the case study in Chapter 5 where the radiative impact on and of multilayer clouds is investigated. To further explore multilayer clouds in the Arctic region, in the final chapters, Chapter 7 and Chapter 8, we expand on the first chapter, exploring a long-term simulation across the Arctic region. The model is evaluated against the extensive dataset retrieved at the MOSAiC site in Chapter 7 while the focus of the last chapter, Chapter 8, is the observed and modelled multilayer clouds on a local and regional scale. The regional occurrence frequency of MLCs is determined and compared to observations at the MOSAiC site. Microphysical and radiative differences between MLCs and single-layer clouds (SLCs) are further explored within this chapter. To conclude, a general discussion is provided in Chapter 9, where the research questions are answered in detail followed by an outlook for future work in Chapter 10.

2 | RESEARCH QUESTIONS

As outlined in the introduction, we can identify certain gaps in our understanding of multilayer clouds:

- a) Microphysically, do MLCs differ from single-layer clouds due to their interactions?
- b) What is the preferred formation mechanism of MLCs?
- c) How do MLCs interact with radiation and what is the impact on other clouds and the surface in the high Arctic?
- d) Are MLCs more common in the Arctic region than globally?

We can further distinguish gaps in our understanding of modelling Arctic clouds that do not only pertain to the multilayer cloud systems:

- e) Which model biases, if any, can we highlight in the high-Arctic?
- f) How do we better represent Arctic clouds in the model, with a focus on the general misrepresentation of cloud ice?

To approach these knowledge gaps we use simulations. This allows us to control the environment, perform sensitivity studies, and study processes that may not be observed. With the ICON model, we set up a study region in the Arctic and model clouds through a limited-area setup. Most previous studies in the high-Arctic use idealised setups, providing thermodynamic profiles from observations to constrain the model. In this thesis, we would like to explore the way we currently represent the Arctic region with a weather model, using global model data to initialise the simulations and update the boundaries. This will further point to critical situations where model development is necessary.

With very few studies in the Arctic, and even fewer in the high Arctic, we aim to provide a thorough modelling study into the occurrence frequency of MLCs, their response to microphysical perturbations, and radiation impacts. The common question for all chapters will be the theory of the formation of the layers: **Can we capture**

a preferred formation mechanism in the model and what does this tell us about the Arctic system?

As introduced in Chapter 1, we know very little about the microphysical response of multilayer clouds. Regarding the question posed above, do multilayer clouds differ from single-layer clouds? If we assume a high MLC occurrence in the Arctic this is an important question to answer as these clouds would dominate the measurement signal in the region. To this effect, a detailed case study of these cloud systems on a microphysical level using highly resolved model simulations is presented in Chapter 5. We would like to understand the differences that pertain to modelling MLCs instead of single-layer clouds and we would like to further our understanding of how we can better represent Arctic clouds in general.

In Chapter 5 we aim to answer:

RQ1.1 Can we accurately model MLCs in the high Arctic? What are the limitations imposed by the modelling strategy and setup, i.e. grid spacing and initial and boundary conditions?

RQ1.2 How do MLCs respond to microphysical perturbations?

RQ1.2a Does constraining the microphysical parameterisations towards observations improve the representation of the clouds?

RQ1.2b How important are secondary ice processes and how do they interact with the primary ice?

RQ1.2c Do we simulate seeding between the layers? Which microphysical processes are involved and are we accurately representing them in the model?

The extent of the suppression of longwave radiative cooling by upper clouds has not been classified for the high-Arctic. Furthermore, we know very little about how radiative heating impacts cloud formation and the persistence of cloud layers. Chapter 6 provides a case study on the radiative impact of multilayer clouds, where we employ a radiative modelling strategy to isolate the radiative effects of the individual layers.

In Chapter 6, we specifically aim to answer:

RQ2.1 How does the cloud-radiation interaction impact the evolution and persistence of the MLC system?

RQ2.2 Can we capture the suppression in longwave radiative cooling seen by observations?

Multilayer clouds seem to be frequent in the Arctic. Due to the lack of vertically resolved satellites above 80°N, no spatial occurrence frequency across the Arctic is possible to deduce using observations. Thus, the evidence of frequently occurring clouds in the Arctic is based on observational campaigns during a few weeks to a year, covering only a small part of the Arctic region. We may thus pose the question: Are MLCs more common in the Arctic region than globally? To approach this, in Chapter 7 and Chapter 8, we set up a long-term, large-scale simulation strategy. With a lack of permanent research stations in the Arctic, due to the sea ice, we have limited options for model evaluation and we thus make use of the data from the MOSAiC campaign in 2019/2020 to evaluate the model close to the North Pole. While this site will serve as our comparison, the full region analysis will only be performed using the model. Following research question 1.2a, we further explore an improved primary ice nucleation parameterisation using measured INPs across the Arctic region.

In Chapter 7 we then aim to answer

RQ3.1 How does the model compare with the MOSAiC data?

RQ3.2 Does an improved representation of the Arctic INP population impact the clouds in the region?

To further benefit from this modelling approach, we explore differences in MLCs and SLCs on a process level where we try to answer the question of "Do multilayer clouds differ from single-layer clouds?" from a statistical approach, looking at differences, not in responses to perturbations but if they possess significant characteristics. We finally make use of the large-scale data set to answer the last part of the question: How do MLCs interact with radiation and what is the impact on other clouds and the surface in the Arctic? The focus here is on the large-scale surface impact of the MLCs.

The specific research questions we aim to answer in Chapter 8 are:

RQ4.1 What is the occurrence frequency of Arctic MLCs?

RQ4.2 Can we find microphysical differences between multilayer and single-layer clouds?

RQ4.3 What is the impact of MLCs on the Arctic surface radiative balance?

3 | THEORETICAL BACKGROUND AND ITS REPRESENTATION IN ICON

In this chapter, the background theory needed to understand the result chapters is introduced. The model used in this thesis is introduced in Chapter 3.1, this is followed by an overview of cloud physics and cloud-radiation interactions that are explained in terms of the actual processes and how we parameterise them in the model. Finally, in Chapter 3.4, the Arctic system is introduced together with an overview of Arctic single-layer and multilayer clouds.

3.1 The ICON Model

A numerical weather prediction (NWP) model is a tool for weather forecasting and has been used to predict the weather since the 1950s (Pu and Kalnay, 2018). An NWP model describes the atmospheric state using variables such as temperature, wind fields, water vapour, pressure, and clouds by numerically solving the primitive equations on a set of grid points. To obtain a future state, i.e., a forecast, accurate knowledge of the current state and a keen understanding of the dynamics of the atmospheric system must be known. This was termed the *initial value problem* already in the early 1900s by Bjerknes (1904). To solve this, he outlined the three basic components of every modern-day NWP; the current state, analysis (diagnostic), and prognostic components. The current state describes the current weather, while the analysis combines this state with short-range forecasts through data assimilation to obtain the best initial state. The prognostic component involves solving partial differential equations over time to obtain the next atmospheric state.

The ICosahedral Non-hydrostatic (ICON) model (Zängl et al., 2015) is the German Weather Service (Deutsche Wetterdienst, DWD) operational forecast model, developed jointly by DWD, Max-Planck Institute for Meteorology (MPI-M), Deutsche Klimarechenzentrum (DKRZ), and KIT, and has been active since 2015. The ICON model is non-hydrostatic. On the scales of operational forecasts (10 km), the hydrostatic approximation is valid (Wedi and Malardel, 2010). The hydrostatic approximation

(AMS Glossary) assumes that the vertical pressure gradient force is balanced by gravity. When considering smaller scales, on the order of 2 km, vertical and horizontal scales converge. By explicitly calculating the vertical motion, the non-hydrostatic dynamical core of ICON thus allows for high-resolution (particularly at scales finer than 3 km) modelling.

The grid structure of ICON is icosahedral, a triangular projection onto the globe. The number of triangles defines how many grid points the equations are solved on, the resolution, and how well the atmospheric processes are represented. The grid spacing, not to be confused with the spatial resolution, defines the spacing between grid points, i.e. how far apart they spatially occur. The grid in ICON is identified by $RnBk$, where n identifies the original icosahedron that has been divided into n parts with subsequent k bisections of the edges (Prill et al., 2020). This gives the number of cells in the grid

$$n_{cells} = 20n^24^k. \quad (3.1)$$

A larger number of cells normally indicates better resolution for a specified domain, a region where the simulations take place. The average triangle area of the grid, the grid spacing, $\overline{\Delta x}$, is defined as

$$\overline{\Delta x} \approx \frac{5050}{n2^k} \text{ [km]} \quad (3.2)$$

where the number 5050 is derived from the surface area of the Earth divided by the number of triangles (Prill et al., 2020). The effective resolution of the grid, the length scale of the resolved atmospheric processes, is on the order of 4-10 times $\overline{\Delta x}$ (DWD Intro Course). The grid is an icosahedral-triangular Arakawa C grid (Arakawa and Lamb, 1977), with staggered grid points such that variables can be represented by different locations within the same grid box. The wind components in ICON are, for example, solved at midpoints of the triangular edges instead of the cell centre (Prill et al., 2020). This improves the effective resolution of the model (Guichard and Couvreur, 2017).

Dynamical Core

The dynamical core of an NWP model is responsible for simulating atmospheric motion. In its simplest explanation, the model solves a set of equations at a certain point in space and time based on a previous time step. The equations are the coupled primitive equations; the mass continuity equation, equations of motion (conservation of momentum, Newton's second law), the ideal gas equation, conservation of energy (first law of thermodynamics) and conservation of water mass (Pu and Kalnay, 2018). No analytical solution exists to these equations and only a numerical solution may be obtained which is the basis for these models. The final numerical solution describes the

atmospheric state; the velocity, temperature, pressure, and density of a moving fluid. The set of equations for the ICON model is outlined in Gassmann and Herzog (2008) and Zängl et al. (2015).

3.1.1 Parameterisations

The grid spacing defines the resolution of the simulation. While atmospheric motion happens on a range of spatial scales, only processes happening on a larger or similar extent as the model resolution can be accurately captured. Many atmospheric processes occur on such small scales that to capture them, we need resolutions of a maximum of a few meters. This would require an enormous amount of computational power and thus we make use of parameterisations. These parameterisations implicitly represent processes we cannot explicitly resolve at the resolution of the model. They include microphysics, convection, radiation, and turbulence. The parameterisations important for this thesis are presented in this chapter. A general introduction to the microphysics parameterisation is provided below while detailed descriptions are provided within Chapter 3.2. A brief intro to the turbulence, sea ice, and cloud cover parameterisations is provided here while Chapter 3.3 describes how radiation is parameterised.

Microphysics

The microphysical parameterisations deal with the subgrid-scale of a cloud. How it forms, evolves and dissipates. First of all, let us define some basic definitions. The liquid water content (LWC), is the mass of condensed water in a unit volume of air, also known as the mass mixing ratio of water. Ice water content (IWC), is similarly defined as the mass of ice in a volume of air. The liquid water path (LWP) and similarly, the ice water path (IWP), are defined as the column integral of LWC and IWC respectively. We may here define the particle size distribution, $f(D)$, the number of particles with a diameter between D and $D+dD$, described as a continuous distribution of particle sizes. From this function, we may extract more information using the moments of the size distribution. This can be in general written as

$$M_n = \int_0^{\infty} D^n f(D) d(D) \quad (3.3)$$

where the moment, M_n , is the integral of the size distribution, $f(D)$. The number concentration of a species, how many particles exist in a cubic meter of air (number per m^{-3}), is the zeroth moment, M_0 , with D^0 ,

$$N = \int_{-\infty}^{\infty} f(D) d(D). \quad (3.4)$$

The first moment follows similarly and represents the mean particle diameter. The second and third moments are the surface area and volume respectively. The volume

is commonly used to further derive the mass concentration. With a spherical particle approximation, we may use the mass $m = \rho V$, with ρ as the density and V as the spherical particle volume, and write

$$M_3 = \rho \frac{4\pi}{3} \int_{\infty}^{\infty} D^3 f(D) d(D) \quad (3.5)$$

with the liquid water density ρ .

These moments are used to describe which tracers are tracked in time and space. For the 1-moment microphysics scheme, the third moment is used, the mass concentration of hydrometeors, whilst in the 2-moment scheme, the mass and the number concentration are traced. This can improve the representation of clouds, specifically mixed-phase clouds as they are more sensitive to the distribution of ice and water, and their relative number concentrations within the cloud (Seifert and Beheng, 2006). In ICON, we use a gamma distribution for describing the size distribution of cloud droplets on the form:

$$f(x) = Ax^{\nu} \exp\{-\lambda x^{\mu}\} \quad (3.6)$$

where ν is the shape parameter, and μ the dispersion parameter for particle mass, x (Barthlott et al., 2022). For the standard setup in ICON, we use $\nu = \mu = 1$. A and λ are calculated from the number and mass concentrations. Using $x = \frac{\pi}{6}\rho D^3$ the function with respect to the diameter can be written as

$$f(D) = N'_0 D^{\nu'} \exp\{-\lambda' D^{\mu'}\} \quad (3.7)$$

with $N'_0 = 3N_0(\frac{\pi}{6}\rho)^{\nu+1}$ where N_0 is an intercept parameter and ρ the bulk density, $\nu' = 3\nu + 2$, $\lambda' = \lambda(\frac{\pi}{6}\rho)^{\mu}$, and $\mu' = 3\mu$.

In the 2-moment microphysics scheme, subroutines are called one after the other. In general, the sources are called first, then the sinks followed by a saturation adjustment. The saturation adjustment is a call to ensure liquid saturation within clouds. If supersaturation is still present at the end of the microphysics call, condensation onto existing cloud droplets occurs. In the case of sub-saturation, evaporation of droplets is performed. The saturation adjustment is called twice, once before the microphysics and then again after microphysics to ensure that when the dynamics are called, it is done with an adjusted temperature and water vapour mixing ratio.

The call order of the 2-moment microphysics is as follows;

1. Cloud droplet activation
2. Heterogeneous nucleation routines

- a) Immersion freezing
- b) Deposition nucleation
3. Homogeneous nucleation
4. Homogeneous freezing ("cloud-freeze")
5. Depositional growth by vapour
6. Collisions and coalescence
7. Riming
8. Rain freezing
9. Melting of frozen hydrometeors
10. Evaporation of frozen hydrometeors
11. Rain formation and evaporation

These mechanisms are described in detail below (Chapter 3.1.1).

Cloud Cover

The cloud cover scheme in ICON combines information from microphysics, turbulence, and convection. It determines the distribution of water vapour, liquid water, and cloud ice from the subgrid variability of water. From this, a cloud fraction, how much of the grid box is covered with clouds, may be determined (Prill et al., 2020). This is further used in the call for radiation (Chapter 3.3).

Turbulence

Turbulence in the Earth's atmosphere is responsible for the vertical and horizontal mixing of air. In clouds, radiative cooling at the cloud-top induces turbulent eddies that cause entrainment (Mellado, 2017). The atmospheric boundary layer is by definition turbulent, due to a combination of shear and buoyancy production (Nieuwstadt and Duynkerke, 1996). Even at scales of hundreds of meters, turbulence can only be partially resolved and we make use of parameterisations to describe the rotational flow causing eddies in the atmosphere. The turbulence parameterisation derives tendencies (changes in variables with time) due to unresolved turbulent motions. To do this, the closure (achieving defined mathematical solutions) problem of Reynold's equations for the transport of momentum by turbulent fluctuations requires attention. The large-eddy simulation (LES) setup, at 100 m grid spacing, makes use of the Lilly-Smagorinsky scheme (Lilly, 1962; Smagorinsky, 1963). This scheme resolves large-scale turbulence while parameterising smaller scales using a sub-grid stress tensor. The limit between the resolved and the modelled scales is based on a method of filtering the length scales

defined by the resolution (filter width = $(\Delta x \Delta y \Delta z)^{1/3}$ (Prill et al., 2020)). At coarser grid spacings, the turbulence is represented by a 2^{nd} order closure scheme (Raschendorfer, 2001). The 2^{nd} order closure scheme is a higher order closure (HOC) scheme based on Mellor and Yamada (1982). This scheme achieves closure up to the second moment of turbulent fluxes ($\overline{u'_i u'_j}$) and applies closure approximations for higher moments such that further unknown variables are approximated. A prognostic equation for turbulent kinetic energy (turbulence intensity) is included, making this parameterisation (Raschendorfer, 2001) a 2.5-order according to the definition by Mellor and Yamada (1982).

Sea Ice

The sea ice in ICON is very basically parameterised where no rheology is considered (Mironov et al., 2012). The heat transfer is treated through a bulk approach with an assumed shape of the evolving temperature profile and is reduced to solving ordinary differential equations in time for the ice surface temperature and thickness only. The sea ice fraction is initialised by the data assimilation scheme, based on satellite data. If a grid box is initialised ice-free, no ice will form during the simulation (Prill et al., 2020). Sea ice thickness is computed with respect to the sea ice temperature but melting from below is disregarded as well as solar radiation penetrating the ice slab. To be added, snow on top of sea ice is not explicitly represented but is described through the increase in surface albedo through the prognostic sea ice albedo parameterisation.

3.2 Cloud Microphysics

Clouds are defined by the American Glossary of Meteorology (AMS Glossary) as

A visible aggregate of minute water droplets and/or ice particles in the atmosphere above the earth's surface.

and thus comprises our understanding of what a cloud may contain; ice and/or water droplets and its location; above the surface of the earth. A fog is technically not a cloud and some of the clouds investigated in this thesis will come under the formal definition of a fog (a cloud touching the surface) but will hereafter be interchanged with the word cloud as it is assumed it constitutes the same microphysical pathways. Following is an introduction to the microphysical processes within the clouds we are studying in this thesis. An overview of (some of) the processes occurring within the clouds is sketched in Fig. 3.1.

Some Basic Concepts

The differences in scales of cloud physics are substantial. An aerosol can range in size from nanometers to micrometres (Schmale et al., 2021), while a cloud droplet is typically in the size range around $10 \mu\text{m}$ (Lamb and Verlinde, 2011). Drizzle drops are

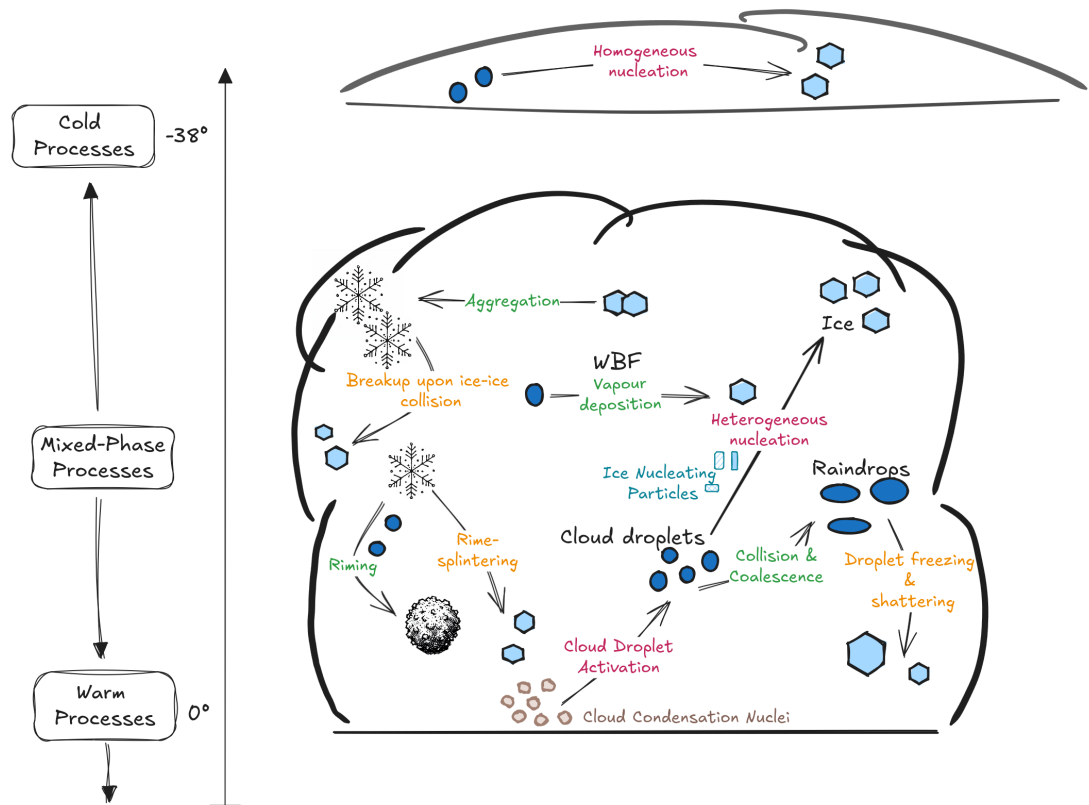


Figure 3.1: Sketch of microphysical processes within clouds. The processes are colour-coded by; phase changes, including droplet activation and ice nucleation, in pink, growth processes in green, and secondary ice production in orange.

≈ 0.1 mm and raindrops an order of magnitude larger. Ice crystals exist as small as tens of micrometres to hail on the centimetre scale. Then clouds themselves can span anything from 100 metres to several hundreds of kilometres.

The word hydrometeor will be often used in this thesis and refers to the partitioned types of liquid and frozen cloud particles; cloud droplets, rain, ice crystals, graupel, snow and hail particles. The frozen hydrometeors include the last four and are, realistically, different growth pathways of particles but in the model world they are partitioned in different size categories. For this thesis, hail will not be further discussed as it is a rare hydrometeor to find in the non-convective clouds in the Arctic.

Requirements for Cloud Formation

Only three ingredients are needed when it comes to cloud formation; moisture, aerosols, and cooling (Lamb and Verlinde, 2011). Moisture is the presence of water vapour available in a gaseous form in the atmosphere and drives cloud formation and growth. Cooling, here, means reaching supersaturation. At saturation, the vapour pressure of the environment, e , equals the equilibrium water vapour pressure, e_s , determined theoretically from the Clausius-Clapeyron equation (Clapeyron, 1834; Clausius, 1850; Pruppacher and Klett, 1979);

$$e_s(T) = e_0 \exp\left\{\frac{L_v}{R_v}\left(\frac{1}{T_0} - \frac{1}{T}\right)\right\} \quad (3.8)$$

where L_v is the latent heat of vaporisation (the amount of energy required to evaporate a substance), R_v is the gas constant for water vapour, T_0 (and the corresponding vapour pressure, $e_0(T_0)$) denotes the triple point in the phase diagram for water and T the temperature. Cooling, and supersaturation, can be achieved by three means; radiation, uplift or mixing. Radiation refers to the radiative cooling in the longwave spectrum by any object, proportional to T^4 following Boltzmann's law and efficiently allows for supersaturations to occur. Uplift, through adiabatic cooling, requires large-scale dynamics or topography whereby air is forced up to higher levels in the atmosphere where the air parcel is cooled. Finally, mixing corresponds to the combination of two air parcels of different origins such that the final temperature in the parcel is lower and reaches supersaturation.

Aerosols

An aerosol is a colloidal suspension of particles and can be of natural (dust, sea salt, biomass from natural fires, sulphate and soot from volcanos) or anthropogenic origin. The man-made sources of aerosols include biomass burning, emissions from vehicles as well as dust from agriculture (Arfin et al., 2023). The anthropogenic sources of aerosols mainly contribute to secondary aerosols, in comparison to natural sources that emit primary aerosols. Secondary aerosols go through chemical reactions before they are involved in cloud formation in the atmosphere.

Cloud condensation nuclei (CCN) act as catalysts for droplet formation, thus reducing the supersaturation required for the condensation of water vapour. These CCNs are hydrophilic and/or soluble aerosols and common CCNs are ammonium sulfate, ammonium nitrate and sea salt (Hande et al., 2016). In the Arctic, species such as locally emitted sea salt and sulfate from DMS (Schmale et al., 2021) as well as long-range transport of anthropogenic sulfates (Udisti et al., 2016) and aged black carbon (Zieger et al., 2023) are the main contributors to cloud droplet formation. In general, the concentration of these species in the Arctic is very low, in the range of 10-200 cm^{-3} (Mauritsen et al., 2011; Dada et al., 2022). Sometimes the low concentrations force the dissipation of clouds in this aerosol-limited environment (Mauritsen et al., 2011; Bulatovic et al., 2023; Sterzinger and Igel, 2024).

Ice nucleating particles (INP) are aerosols that are typically insoluble and are the reason ice is observed at temperatures above the freezing temperature of pure water droplets (at approximately -38°C (Mossop, 1954; Korolev et al., 2017)). Acting as a seed for ice formation, water vapour may deposit onto the INP to form ice through the deposition nucleation mechanism, while INPs immersed within liquid droplets may freeze through immersion freezing (Hoose and Möhler, 2012) (see Chapter 3.2.2). The INPs in

the Arctic region are commonly mineral dust, transported from the south, and biological (heat labile) or organic aerosols (Creamean et al., 2022) emitted through sea spray (DeMott et al., 2016). Previously, the CCN and INP concentrations in the Arctic have only been known from shorter expeditions, now thanks to the Multidisciplinary drifting Observatory for the Study of Arctic Climate (MOSAIC) expedition during 2019/2020 (Shupe et al., 2022) one-year-long surface-based concentrations of CCN (Koontz et al., 2020; Bergner et al., 2023; Dada et al., 2022) and INP (Creamean et al., 2022) are available.

Cloud Phase

Clouds can exist in three phases; as a stable pure liquid, ice only or in a meta-stable mixed phase state consisting of a mixture of supercooled liquid droplets (SLD) (liquid droplets existing below 0°C) and ice particles. In the mixed-phase temperature regime (0°C < T < -38°C, (Mossop, 1954; Korolev et al., 2017)), ice and SLD may coexist. The mixed-phase state is meta-stable as the saturation vapour pressure over water, $e_{s,w}$ (the point where condensation and evaporation fluxes are equal) is higher than the saturation vapour pressure over ice, $e_{s,i}$ (the point where deposition and sublimation fluxes are equal), for temperatures below 0°C. The saturation water vapour pressures are calculated by the Clausius-Clapeyron formula (Eq. 3.8) but may be approximated by the Tetens's formula (Tetens, 1930; Murray, 1967; Monteith and Unsworth, 2007)

$$e_{s,w} = 610.78 \exp \left\{ 17.269 \frac{T - 273.15}{T - 35.86} \right\} \quad (3.9)$$

$$e_{s,i} = 610.78 \exp \left\{ 21.875 \frac{T - 273.15}{T - 7.66} \right\} \quad (3.10)$$

for the saturation vapour pressure over water, $e_{s,w}$, and ice, $e_{s,i}$, where T is the atmospheric temperature. This difference, $e_{s,w} > e_{s,i}$ is due to the larger latent heat of sublimation than evaporation (vaporisation). Simply put, it requires more energy to change a solid to a gas than a liquid due to the chemical bonds between the molecules. The following impact on the cloud is a meta-stable state which during favourable conditions (vertical velocity, particle size, and number limited) will favour the growth of ice crystals, enabling vapour flux from cloud droplets to the ice particles. This process is known as the Wegener-Bergeron-Findeisen mechanism (WBF) (Wegener, 1911; Bergeron, 1928; Findeisen, 1938; Korolev, 2007) and is an efficient way of glaciating a supercooled liquid cloud. This process is sketched in Fig. 3.2.

3.2.1 Warm Processes

We now move into the processes of cloud formation and start with the warm processes, occurring at temperatures above 0°C.

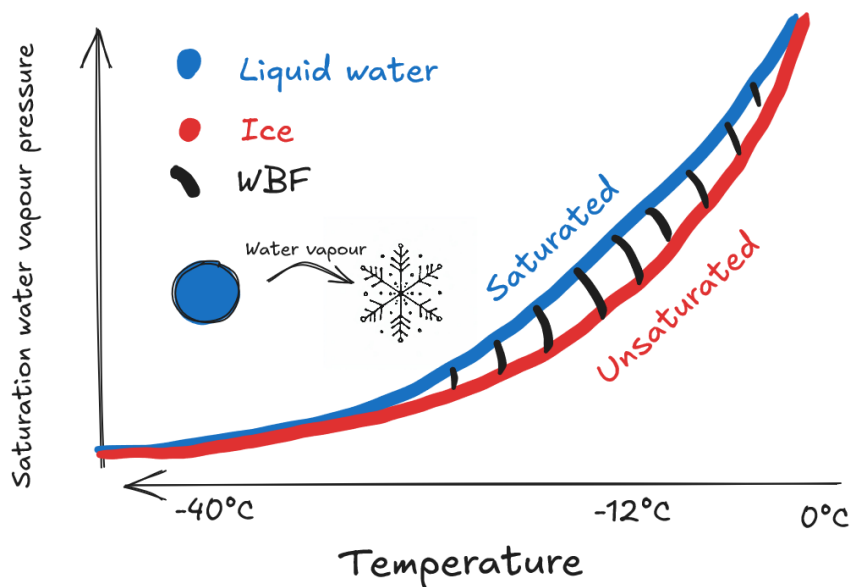


Figure 3.2: Saturation water vapour pressure over (a flat surface of) liquid water and ice with temperature. The WBF regime is identified in shaded black, where sub-saturation with respect to liquid water and super-saturation with respect to ice coincide.

Aerosol Activation

Hygroscopic (water-liking) aerosols will start absorbing moisture below water saturation. Saturation refers to a state where the rate of condensation is equal to the rate of evaporation leading to vapour flux towards the particle and growth by vapour deposition. Saturation with respect to substances other than water is, in general, lower than for over water, leading to vapour flux towards the aerosol (Lamb and Verlinde, 2011). Once the air reaches supersaturation with respect to the aerosol it will deliquesce, take up water and dissolve, into a solution droplet. Salt (NaCl), for example, starts to deliquesce already around 80% relative humidity (with respect to water at 298K) (Sato and Hattanji, 2018) but atmospheric particles often contain a myriad of different species making the deliquesce point hard to determine.

Cloud Droplet Activation

Cloud droplets exist in an unstable equilibrium. After the deliquesce of an aerosol, further increases in the ambient humidity will overcome an energy barrier for activation into a state of spontaneous growth and evaporation. This requires an activation from a solution droplet (aqueous aerosol droplet) which depends on the environmental conditions surrounding the droplet. As with most activation mechanisms, there is an energy barrier to activation. Two competing effects put together through Köhler theory (Köhler, 1936) describe this energy barrier. The environmental condition necessary for activation is a saturation ratio, $S = e/e_s > 1$ (or supersaturation $s = S - 1$ above 0).

This barrier is individual for each droplet and depends on the size of the droplet and the chemical composition of the aerosol it consists of (Lamb and Verlinde, 2011). Solutions, such as deliquesced aerosols, have different equilibrium points (different relative humidity threshold for activation) than pure water and the addition of a solvent to a pure droplet decreases the saturation vapour pressure. This is, in simple terms, due to the removal of surface sites for the water molecules to efficiently evaporate from, making evaporation less likely (Lamb and Verlinde, 2011). This effect is named the Raoult, or the solute effect, and a highly saturated solution droplet would be less likely to evaporate, thus efficiently reducing the saturation ratio. The competing effect for cloud droplet activation is the fact that the equilibrium between condensation and evaporation is not between the air and a flat surface but a curved one. This introduces the second term in the Köhler equation, the curvature term or the Kelvin term. When a droplet forms, the vapour pressure changes. If we consider the molecular structure of the water when a droplet forms it will have fewer molecular bonds compared to a flat, planar structure, due to the curved structure. Thus, the molecules may more easily evaporate. In pressure terms, the curvature of the droplet increases the equilibrium vapour pressure by increasing the internal pressure (Lamb and Verlinde, 2011).

The combined Köhler equation for the saturation vapour pressure, S , reads;

$$S \approx 1 + \frac{A}{r} - \frac{B}{r^3} \quad (3.11)$$

with the radius of the solution droplet (deliquesced CCN) activating into a cloud droplet, r , saturation ratio (equilibrium saturation water vapour pressure) S , the curvature term, A/r , with the A term weakly depending on temperature, and the solute term B/r^3 where B is determined from the chemical properties of the aerosol. At small radii, the solute term is dominating while the curvature term quickly diminishes as the radius of the particle grows. The critical supersaturation pressure, s_c , is found by setting $dS/dr = 0$, which predicts the requirement for activation of each droplet. A large, highly concentrated solution droplet would be the easiest to activate into a cloud droplet. Solution droplets that do not acquire a supersaturation large enough for activation are stuck as haze particles, where they grow by vapour condensation and evaporate depending on the supersaturation surrounding it.

The Köhler theory nicely explains the reason why we do not get homogeneous cloud droplet activation. The size constraint, $s_c \propto D_p^{-3/2}$, follows from the theory, that the critical supersaturation needed for activation is proportional to the particle diameter, D_p . With atmospheric supersaturations rarely exceeding 10% (Pruppacher and Klett, 1979; Lamb and Verlinde, 2011), particles must be larger than 0.01 μm and thus activation without a CCN particle present is close to impossible (in the atmospheric setting) (Lamb and Verlinde, 2011). We may thus clarify the term CCN as aerosols that have the potential of activating into a cloud droplet, meaning they are of certain

chemical composition and hygroscopicity to deliquesce into a size needed to overcome the curvature effect.

In the model, the microphysics routine starts with the CCN activation into cloud droplets. Köhler theory, where each droplet is considered explicitly and activated one by one, is a too expensive method for most of the scales we are looking at so a bulk parameterisation is used. Bulk parameterisations aim to explain the behaviour of all aerosols present and are parameterised with respect to atmospheric variables. We use the Hande parameterisation (Hande et al., 2016) in this thesis for cloud droplet activation. The parameterisation is based on previous work by Abdul-Razzak and Ghan (2000) and the number of cloud droplets activating is parameterised as;

$$CCN(w, P) = a(P) \cdot \arctan(b(P)(w) + c(P)) + d(P) \quad (3.12)$$

with the updraft velocity, w , and pressure, P . Letters a-d are extracted from a best fit of a modelled aerosol size distribution evaluated against observational data collected from the High Definition Clouds and Precipitation for advancing Climate Prediction (HD(CP)²) Observational Prototype Experiment (HOPE) in 2013. A predecessor to ICON, the Consortium for Small-scale Modelling (COSMO) meteorological model coupled to the Multi-Scale Chemistry Aerosol Transport (MUSCAT) was used to model the generation of aerosols and their atmospheric transport. The species traced in the model include sulfate (SO_4^{-2}), ammonium nitrate (NH_4NO_3), ammonium sulfate ($(NH_4)_2SO_4$), 5 sizes of dust, elemental and organic carbon, and 2 sizes of sea salt. Sea salt has the largest hygroscopicity, κ , while the carbon species followed by the dust samples have low values ($\kappa < 0.2$). The CCN activation is then performed using a parameterisation by Abdul-Razzak and Ghan (2000) who used Köhler theory to account for aerosol size distribution and composition. The spatial distribution of aerosols over Germany was evaluated and though differences in aerosol concentrations could be seen, only small variations in CCN concentration were observed. This makes the parameterisation more robust for usage also outside of the evaluated domain, with some modifications discussed in Chapter 4.1. This parameterisation requires positive updrafts (above 0 ms^{-1}) for new activation. The vertical profiles of CCNs at certain updraft velocities are plotted for the updrafts commonly seen in the Arctic in Chapter 4.1 together with the observational data used to constrain the parameterisation.

Growth of a Cloud Droplet

The supersaturation, $s = S - 1$, required for activating cloud droplets is impacted by the environment surrounding the droplet. It evolves in time by;

$$\frac{ds}{dt} = Q_1 w - Q_2 \frac{dq_l}{dt} \quad (3.13)$$

where the change in supersaturation with time is explained by a source term, $Q_1 w$, and the sink term, $Q_2 \frac{dq_l}{dt}$. In the source term, a higher supersaturation is achieved with higher vertical velocities. The sink term describes the condensation into cloud droplets which removes vapour from the air. Q_1 and Q_2 are slowly varying with time. Once supersaturation has been established, the cloud droplet may grow through condensational growth, vapour flux towards the droplet. This is achieved as long as there is a gradient in water vapour with a deficiency at the droplet surface and efficient means of removing latent heat upon the phase transition.

In the model, supersaturation is not technically a traceable quantity as the supersaturation is adjusted for in the so-called saturation adjustment calls. This scheme can be thought of as a condensation step to ensure saturation. Thus the updraft is used instead of the supersaturation in the CCN activation described above.

Rain Formation

The rate of change in radius due to condensation of vapour (while in supersaturated conditions) onto cloud droplets is inversely proportional to its radius

$$\frac{dr}{dt} \propto \frac{1}{r} \tag{3.14}$$

at a constant supersaturation and with fixed environmental conditions. This implies a radius increasing with \sqrt{time} . Considered a slow process, the condensational growth plateaus at around 20 μm , while a raindrop is normally not considered before 40 μm -100 μm (Seifert and Beheng, 2006).

Rain formation requires an efficient collision-coalescence process (Lamb and Verlinde, 2011). As cloud droplets grow by condensation they gain mass and reach sizes large enough to fall through the cloud. While falling they collide with other cloud droplets and fuse. Some drops then gain more mass and will fall faster, growing very rapidly by this process. This initial part is the process of making drizzle (small raindrops), further collision-coalescence processes lead to larger raindrops forming. The efficiency depends on the collector droplet size (larger than 5 μm (Lamb and Verlinde, 2011)) and the small drop radius getting collected. Coalescence is more likely with smaller droplets while colliding in the first place happens more frequently with larger droplets. The collection process is exponentially dependent on time and is a rapid way of forming drizzle and rain.

The aerosol impact on rain formation is named the 2nd indirect effect (lifetime effect). It describes the lifetime increase for polluted clouds due to an inhibition of rain formation (Albrecht, 1989). With more small droplets the collection mechanism is less efficient and the result is a suppression of rain formation. This effect is considered in a

vapour-limited situation where the droplets compete for the same amount of vapour for condensational growth.

Warm rain processes are parameterised by Seifert and Beheng (2006). Autoconversion is the term used in the model for parameterising the rain formation. This is followed by accretion and self-collection. Autoconversion transfers cloud droplets to drizzle droplets without taking collision-coalescence explicitly into account. Accretion is the collection mechanism by raindrops, enabling rapid growth into large raindrops. Self-collection is the aggregation of raindrops. A breakup of raindrops is also included whereby large raindrops ($> 300 \mu\text{m}$) can split into fragments, this is further covered in Chapter 3.2.2.

The warm rain processes are called after all sources and sinks of cold processes have been calculated. After the rain evaporation is called, the microphysics routine for that height level and time step is finished and a second saturation adjustment is called. This order of calls for microphysics allows for the activation of cloud droplets that then freeze through heterogeneous processes, growing by deposition and colliding with other species in the same time step. Rain however can not form and freeze within the same microphysics call as it is called after the rain freeze mechanism. Calling the rain process last ensures that an unreasonably large amount of rain freeze is not possible which might have been possible with a scheme that calls rain straight after activation. The immersion freezing would also suffer greatly in this regard.

3.2.2 Cold Processes

This section introduces cold clouds, clouds existing at temperatures colder than 0°C .

Primary Ice Formation

In the cold phase, clouds may contain cloud ice, snow, graupel, hail, and supercooled liquid droplets. The cloud ice category includes small crystals that are just frozen droplets, with sizes on the order of $1\text{-}10 \mu\text{m}$ (Lamb and Verlinde, 2011) (Fig. 1.24). To form ice it is not enough to simply acquire temperatures below 0°C . Liquid droplets may stay in their phase at subzero temperatures when there is no efficient freezing mechanism. This is highly dependent on their size (Ickes et al., 2015). These are called supercooled liquid droplets (SLD). However, at temperatures colder than approximately -38°C , water droplets, as well as dissolved aerosol particles, freeze on their own through homogeneous freezing (Hoose and Möhler, 2012). At temperatures warmer than -38°C , ice nucleating particles (INP) are required. Acting as a seed for ice formation, these INPs enable ice formation.

Four heterogeneous (requiring an INP) pathways have been hypothesised; deposition nucleation, condensation freezing, immersion freezing, and contact nucleation (Hoose and Möhler, 2012). These are shown in Fig. 3.3. We here make the note that freezing is a type of nucleation, where the initial stage of the nucleation occurs through the

liquid phase. Immersion freezing is the phase change of a cloud droplet that has an INP immersed within. The drop then freezes at temperatures depending on the chemical character of the particle and its size. Condensation freezing is a similar pathway but considers the adsorption of vapour onto an INP until it forms a supercooled liquid droplet which then immediately freezes. Deposition nucleation is the vapour accumulation onto an INP, whereby after critical layering of water molecules the particle freezes (Roudsari et al., 2023). The final heterogeneous pathway, contact nucleation, is described by its name, where a supercooled liquid droplet freezes upon contact with an ice particle (Ladino Moreno et al., 2013).

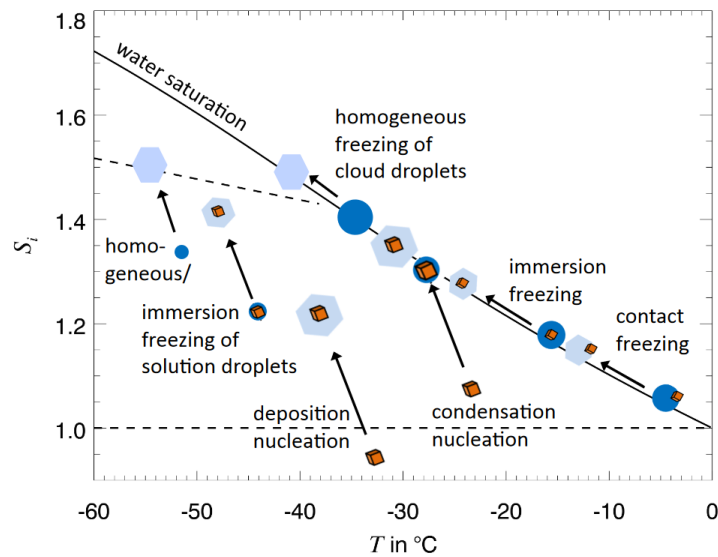


Figure 3.3: Nucleation pathways with supersaturation and temperature. From Hoose et al. (2012), used under the Creative Commons CC-BY license.

At temperatures colder than -38°C , nucleation is possible without the presence of an INP via the process of homogeneous nucleation. Homogeneous nucleation follows the classical nucleation theory (CNT) quite well and the rate of nucleation can be generalised from this (Pruppacher and Klett, 1979; Ickes et al., 2015). The energy barrier for activation depends on the degree of supercooling and with higher values (colder temperatures) the smaller the activation barrier (Lamb and Verlinde, 2011).

In ICON, we may describe the microphysics using different moments of the size distribution. For a 1-moment scheme, the mass concentration is traced in time while in a 2-moment scheme, both mass and number concentrations are prognostic variables.

For the 1-moment microphysics (in ICON), the cloud ice number concentration, N_{ice} , is represented by the Cooper (1986) parameterisation;

$$N_{ice} = 5 \exp\{0.304 \cdot (273.15 - T)\} \quad (3.15)$$

where T is the temperature with an imposed threshold at $T < 267.15$ K. This quantity is not traced in time but is used to calculate the mass concentration at each level and time step.

In the 2-moment scheme, more pathways are represented, to, ideally, better represent the actual processes in the cloud. The microphysics is called following the outline in Chapter 3.1.1. The immersion freezing requires the presence of cloud droplets, the correct temperature range, and ice supersaturation. In this study, we use the Hande parameterisation for immersion freezing (Hande et al., 2015), which similarly to other parameterisations is constrained by temperature. The parameterisation was developed based on dust simulations over Europe using COSMO-MUSCAT. The simulated Saharan dust was filtered for potential INPs using the dust parameterisation by Niemand et al. (2012) and evaluated using a best-fit against multiple data sets. It is parameterised by;

$$N_{imm}(T) = a \cdot \exp\{-b \cdot (T - T_{min})^c\} \quad (3.16)$$

where the ice crystals, N_{imm} , per m^{-3} is given by the model temperature T . T_{min} is the imposed lower temperature limit of the freezing at 237.15 K (-36°C) and letters a-c are fitting parameters to the median INP profiles. The parameterisation is used in this study as a reference and a base for a new parameterisation more appropriate for the Arctic environment. The upper-temperature limit is (here) 261.15 K, following the chemical characteristics (and size) of the dust particles parameterised.

Deposition nucleation is also parameterised using Hande et al. (2015) and is called outside of the physical limits of immersion freezing; when there is less than 10^{-20} kgkg^{-1} mass concentration of cloud droplets. Further constraints include ice supersaturation and temperature thresholds between $-50^\circ\text{C} < T < -20^\circ\text{C}$. The parameterisation follows

$$N_{dep}(T, RH_i) \approx INP_{imm}(T) \cdot DSF(RH_i) \quad (3.17)$$

where the INPs activating through deposition nucleation, INP_{dep} , depends on both the local temperature, T , and the relative humidity over ice, RH_i . A scaling factor is introduced, DSF , defined as

$$DSF = a \cdot \arctan(b \cdot (RH_i - 100) + c) + d \quad (3.18)$$

where coefficients, a , b , c , and d are determined from a best-fit.

Homogeneous nucleation of liquid aerosols (deliquesced aerosols) requires a critical supersaturation over ice depending on temperature (~ 1.44 at 235 K, ~ 1.50 at 220 K). It is further constrained by updraft speed and a temperature threshold below -38° (Kärcher and Lohmann, 2002; Kärcher et al., 2006). The homogeneous freezing of cloud

droplets, (may be pure water droplets but often contain aerosols) is parameterised using the degree of supercooling ($\Delta T_s = 273.15 - T$, where T is the actual temperature) (Jeffery and Austin, 1997), with thresholds on cloud droplet mass concentration and temperatures threshold at -30° . To be noted, below -50° everything freezes instantaneously.

The freezing of raindrops is called after the other primary ice formations but as it implicitly contains many INPs, it is included here for completeness. Rain freeze is the pathway for raindrops to form ice particles, this is parameterised based on probabilities of freezing depending on the volume of the droplet and temperature (Bigg, 1953b). Below -40° , everything freezes immediately. At temperatures above this but below freezing, raindrops will freeze into ice, graupel, or hail depending on their size; smaller than 0.5 mm become ice and larger than 1.25 mm become hail. Sizes in-between end up in the graupel category. Requirements include mass content of rain above 10^{-6} kgkg $^{-1}$.

As a final note on primary ice formation, contact freezing is not considered in the model.

Mixed-phase clouds

Mixed-phase clouds act somewhat differently from single-phase clouds. The supersaturation, s , development, gains an extra term (Lamb and Verlinde, 2011);

$$\frac{ds}{dt} = Q_1 w - Q_2 \frac{dq_l}{dt} - Q_3 \frac{dq_i}{dt} \quad (3.19)$$

where the loss of supersaturation due to vapour deposition on ice (dq_i/dt) acts as a sink for supersaturation with coefficient Q_3 slowly varying in time. Equation 3.19 also gives the limits to the WBF mechanism (Wegener, 1911; Bergeron, 1928; Findeisen, 1938) where the thresholds for ice growth at the expense of liquid droplets and the updraft threshold above which both grow can be determined assuming a steady-state. For high updrafts, both ice particles and cloud droplets grow simultaneously while for low updrafts or a high number concentration and/or radial size of cloud ice particles, the WBF process is active and ice grows preferentially. The WBF process is more common in downdrafts, as the lower threshold is determined by the liquid droplet properties (larger number concentrations in general, though sizes are smaller). For Arctic clouds, vertical velocities are generally low and WBF occurs in the small range of just above 0 ms^{-1} to -1 ms^{-1} (Fan et al., 2011).

In the model, the vapour deposition onto frozen particles is parameterised by Morrison et al. (2005a) and the deposition is constrained by a vapour gradient larger than 10^{-20} kgkg $^{-1}$. The evaporation of cloud droplets is treated implicitly by the saturation adjustment.

Growth of Ice Particles

Ice particles nucleating through the processes detailed above may grow by vapour deposition: through the WBF process in a mixed-phase cloud, in updrafts where both liquid droplets and cloud ice grow, or in an ice cloud that is supersaturated with respect to ice. Other pathways to growth include aggregation and riming.

Snow particles are ice crystals that have been through substantial vapour deposition into habits such as plates, columns, and dendrites. Snow may also grow by aggregation, where snow crystals collide and stick together. The most famous ice type; the snowflake, is simply an aggregate of snow crystals (Pruppacher and Klett, 1979) and can reach sizes up to a few centimetres (Lamb and Verlinde, 2011). Ice and graupel can grow in a similar fashion through the collision and subsequent collection of particles. The aggregation of particles can quickly increase the mass of a particles, causing precipitation.

In the model, aggregation, parameterised by Seifert and Beheng (2006), further add mass to the frozen hydrometeors. The efficiency of the process depends on the particle mass and their relative fall speed. These aggregation mechanisms are (excluding the hail products);

- Ice-ice aggregation to snow when mass of ice particles exceed 10^{-6} kgkg⁻¹ and the diameters of colliding ice crystals exceed 5 μ m.
- Snow-snow aggregation to snow based on sticking efficiency
- Graupel-graupel aggregation to larger graupel.
- Particle-particle aggregation; snow+ice to snow, graupel+ice to graupel, and graupel+snow to graupel.

Another efficient growth mechanism is the riming process, whereby liquid (super-cooled) cloud droplets or raindrops collide and adhere to an ice particle. This mechanism of course requires a mixed-phase cloud (Pruppacher and Klett, 1979). Riming depends on various atmospheric variables such as temperature (Kneifel and Moisseev, 2020) and size (Ávila et al., 2009). Cloud droplets should be larger than 10 μ m for efficient riming (Wang and Ji, 2000) but the riming efficiency increases quickly with larger sizes (Kneifel and Moisseev, 2020).

Riming can heavily alter the original ice particle. When the initial particle features are no longer distinguishable, the particle is defined as a graupel particle and obtains a conical shape (Pruppacher and Klett, 1979). This process also leads to rime-splintering in the temperature range $-8^{\circ}\text{C} < T < -3^{\circ}\text{C}$ (see the section below).

In the model, riming is parameterised by Seifert and Beheng (2006). Ice rimed by cloud droplets stays as ice crystals while the number and mass concentration of the cloud droplets are lost. A mass threshold of 10^{-6} kgkg⁻¹ is imposed together with a

diameter threshold of at least $10\ \mu\text{m}$ for both the colliding ice particle and the cloud droplets. For riming by rain, pre-requisites include an ice crystal diameter $> 100\ \mu\text{m}$ and mass content of ice particles above $10^{-6}\ \text{kgkg}^{-1}$ as for riming by cloud droplets. When the ice crystal is in sub-saturated environments or the depositional growth is smaller than the riming rate, ice may be heavily rimed and convert into the graupel category. The riming of snow follows similarly with the same size threshold as for ice crystals. The riming of graupel requires the same thresholds but is simplified as no conversion to other categories may be done.

At temperatures above freezing the hydrometeors start to melt. Ice can either melt to cloud droplets or rain depending on if the size of the ice crystal is smaller or larger than the maximum cloud droplet size while snow, graupel, and hail only melt into rain.

Secondary Ice Production

In the mixed-phase regime, secondary ice production (SIP) is another aspect of ice formation, or rather, ice multiplication, as these processes require ice to be initially present. SIP supplies additional cloud ice within certain temperature ranges depending on the process in question and is commonly thought of as a mechanism to "make up" missing ice in models (Sotiropoulou et al., 2020; Zhao and Liu, 2022) as SIP is commonly not included in most models. SIP has been successfully studied in laboratories (Korolev and Leisner, 2020) but its atmospheric relevance remains unclear. Out of the six hypothesised mechanisms, three have been identified as possible major contributors in models and include rime-splintering (Hallet-Mossop) (Hallet and Mossop S.C, 1974; Seidel et al., 2024), collisional breakup upon ice-ice collision (Vardiman, 1978; Takahashi et al., 1995; Knight, 2012) and droplet freezing and shattering (Mason and Maybank, 1960; Lauber et al.; Kleinheins et al., 2021). The other three mechanisms so far hypothesised are ice fragmentation during thermal shock, sublimation fragmentation, and INP activation in transient supersaturations (Korolev and Leisner, 2020) but will not be further discussed here due to the lack of current parameterisations. The three major SIP processes are sketched in Fig. 3.4.

Rime-splintering, discovered by Hallet and Mossop (1974) and Mossop (1976), is implemented in several global models (Komurcu et al., 2014) and many cloud-resolving models (Klein et al., 2009; Morrison et al., 2009; Fu et al., 2019; Schäfer et al., 2024), and describes the process where the riming of ice particles result in smaller ice fragments. While rime-splintering is already included in the reference setup for ICON, this process has been found to be weak when acting alone. However, in combination with ice multiplication from breakup collisions, it has been shown to have a considerable impact on the ice number concentration of Arctic clouds (Sotiropoulou et al., 2020). The parameterisation in ICON covers the temperature range of $265\ \text{K}-270\ \text{K}$ ($-8^\circ\text{C} < T < -3^\circ\text{C}$) and fragments are generated by

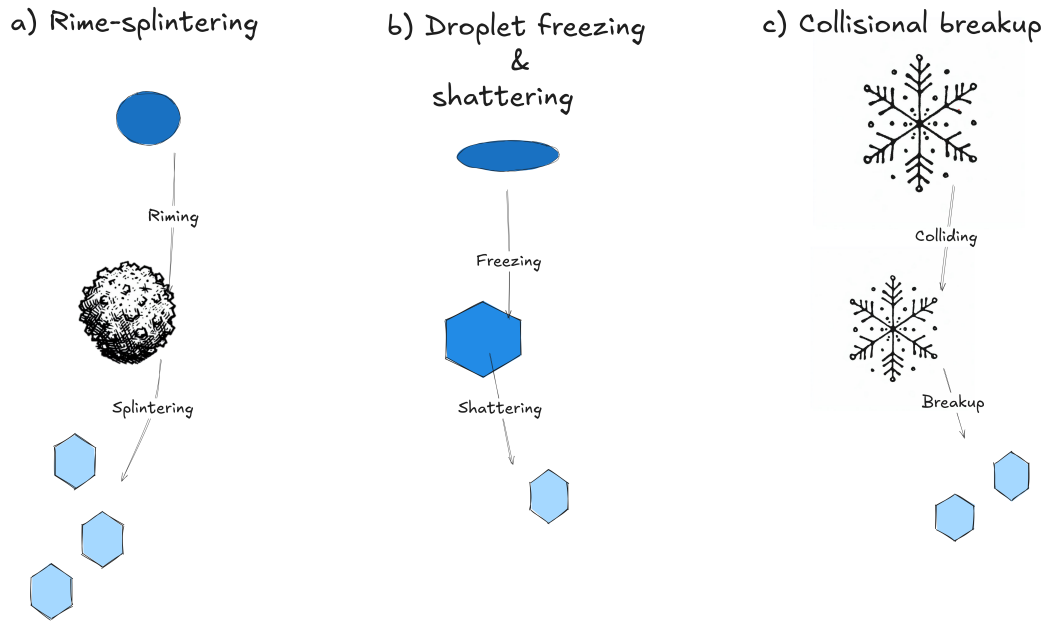


Figure 3.4: The three SIP processes introduced to the model. a) Rime-splintering, occurring at temperatures between $-8^{\circ}\text{C} < T < -3^{\circ}\text{C}$, b) droplet freezing and shattering, occurs at sub-zero temperatures, and c) breakup upon ice-ice collision, which occurs down to 252 K with a peak at 257 K.

$$\frac{\partial N_{ice}}{\partial t} = F_{RS} \times w_{RS}(T) \times q_{rime} \quad (3.20)$$

where the N_{ice} is the number concentration of generated ice splinters and q_{rime} is the mixing ratio of the rimed particle. The prefactors include a constant F_{RS} set to 3.5×10^8 and a temperature weighted coefficient w_{RS} computed as

$$w_{RS} = \begin{cases} 0, & T < 265K \text{ and } T > 270K \\ \frac{T-265K}{3K} \frac{T-270K}{-2K}, & 265K < T < 270K \end{cases} \quad (3.21)$$

giving a maximum efficiency at a temperature of 268 K. The rime-splintering is included in the calls for the riming of ice, snow, and graupel by cloud droplets and raindrops.

The collisional breakup mechanism describes the fracturing of frozen hydrometeors upon collisions with other frozen particles. It is a mechanical fragmentation and the number of fragments generated is a function of the change in momentum upon collision, degree of riming and crystal type (Vardiman, 1978). Takahashi et al. (1995) explored the graupel-graupel collisions by colliding graupel particles constrained to rotating rods, where the rotating speeds were varied to simulate large particles colliding with smaller ones. By growing graupel particles on the rods to 1.8 cm large particles, the collisional breakup mechanism was found to peak at -16°C with a maximum ice generation rate of

800 particles per collision. The breakup collision mechanism is investigated in this thesis using the parameterisation developed for COSMO by Sullivan et al. (2018) based on the laboratory work of Takahashi et al. (1995). The ice splinter number concentration, N_{ice}

$$\left. \frac{N_{ice}}{dt} \right|_{BR_{jk}} = \eta_{BR} \cdot \left. \frac{\partial N_j}{\partial t} \right|_{coll_{j,k}} \quad (3.22)$$

with the collision tendency, $\left. \frac{\partial N_j}{\partial t} \right|_{coll_{j,k}}$, and the fragment number concentration, η_{BR} , described as

$$\eta_{BR} = F_{BR} \cdot (T - T_{min})^{1.2} \exp\left\{ \frac{-(T - T_{min})}{\gamma_{BR}} \right\} \quad (3.23)$$

where T_{min} is set to 252 K. F_{BR} is a coefficient and γ_{BR} is the decay rate, set to 50 and 5 respectively. These are poorly constrained and have been investigated to better-fit case studies of clouds (e.g., Dedekind et al., 2021; Sotiropoulou et al., 2020) but without a consensus on the improvement. The Takahashi et al. (1995) parameterisation has been questioned for its atmospheric efficiency (too efficient) (Han et al., 2024; Sotiropoulou et al., 2021; Dedekind et al., 2021), due to the original experiment being conducted with large (1.8 cm diameter) colliding particles. To remove the dependency on the original experiment, a diameter scaling is used in multiple studies (e.g., Sotiropoulou et al., 2021; Georgakaki et al., 2022; Han et al., 2024). This scaling may be added to the Takahashi et al. (1995) parameterisation to reduce the large impact of the breakup collision through an addition to the η_{BR} term,

$$\eta_{BR} = F_{BR} \cdot (T - T_{min})^{1.2} \exp\left\{ \frac{-(T - T_{min})}{\gamma_{BR}} \right\} \cdot \frac{D_p}{D_{taka}} \quad (3.24)$$

where D_p is the colliding particle diameter and D_{taka} is the original diameter of 1.8 cm. The original parameterisation and three diameters of colliding particles (100 μm , 1 mm, and 1 cm) are shown in Fig.3.5.

The droplet freezing and shattering mechanism describes the process where freezing raindrops may eject ice crystals during their phase change due to pressure build-up from inside the freezing drop and is largely dependent on temperature (Mason and Maybank, 1960; Kleinheins et al., 2021). This process is parameterised by Sullivan et al. (2018) through

$$\left. \frac{\partial N_{ice}}{\partial t} \right|_{DS} = [1 + p_{DS} \cdot \eta_{DS}] \cdot \left. \frac{\partial N_{fr}}{\partial t} \right|_{DS} \quad (3.25)$$

where the number concentration of ice splinters produced, N_{ice} , is the product of a shattering probability, p_{DS} , based on a normal distribution in temperature, and the

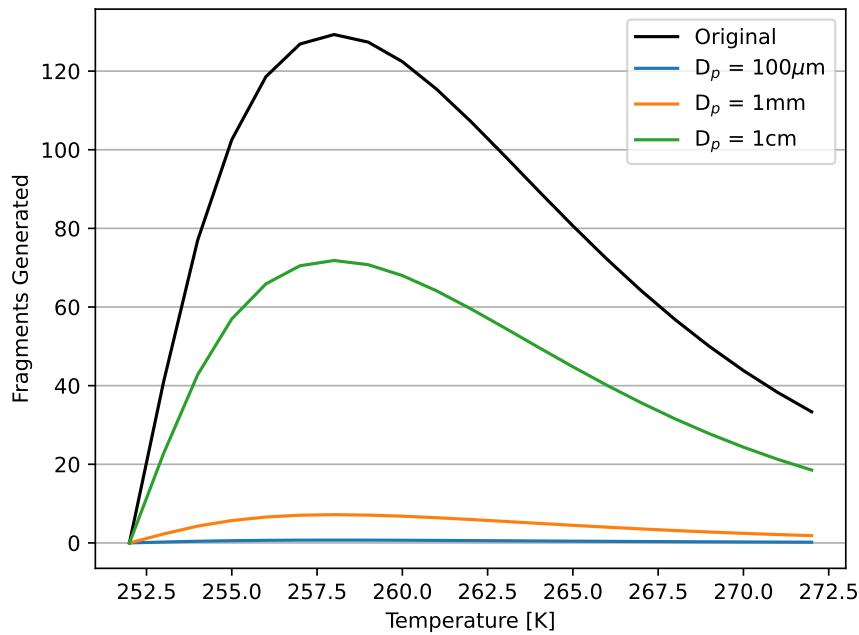


Figure 3.5: Breakup collision parameterisation based on Takahashi et al. (1995) for the original parameterisation implemented by Sullivan et al. (2018) in black and the diameter scaled version implemented by Han et al. (2024) for three colliding particles of sizes $100\ \mu\text{m}$, $1\ \text{mm}$, and $1\ \text{cm}$ respectively.

droplet freezing tendency, $\frac{\partial N_{fr}}{\partial t}$ predicted by Bigg (1953a). η_{DS} is the ejected fragment number and is kept constant at 10.

For all three multiplication processes implemented in ICON, a cascading effect is included, where the fragments generated are capable of colliding and generating new fragments.

Seeder-Feeder Mechanism

One of the more interesting phenomena in regards to MLCs is the possibility of the seeder-feeder mechanism (Bergeron, 1949) whereby frozen precipitation from an upper cloud layer can fall into and seed a lower cloud. Here, a seed may be referred to as a catalyst for ice formation akin to INPs, granted they survive the sub-saturated layer between the cloud layers. This seeding may initiate glaciation in a supercooled liquid or mixed-phase cloud, whereupon the Wegener-Bergeron-Findeisen (WBF) mechanism efficiently evaporates liquid cloud droplets in favour of vapour deposition onto ice particles. This seeding effect is most commonly identified by an increase in precipitation from the lower cloud, this may be ice derivatives such as cloud ice, snow, graupel, hail, or rain. Seeding was first ascribed to the increase in precipitation in orographic clouds (Roe, 2005) and has since been investigated for both internal (seeding within the same cloud) and external seeding for multilayer clouds over the Swiss Alps (Proske et al., 2021; Dedekind et al., 2024) and in the Arctic (Vassel et al., 2019). Vassel et al. (2019),

investigated the occurrence of seeding MLCs on Svalbard using sublimation calculations with variables derived from radiosoundings, and they found a seeding occurrence of 23%. In studies over the Swiss Alps, Proske et al. (2021) found a seeding frequency of 31% for cirrus clouds overlaying lower clouds, investigated using DARDAR, while Dedekind et al. (2024) found a 10% occurrence frequency of seeding for a modelled case study also over the Swiss Alps. They report an 8.5% decrease in surface precipitation and a 3.9% decrease in riming when seeding was inhibited. This mechanism is also attributed to the dissipation of lower multilayer cloud layers (Chen et al., 2020). As the precipitating hydrometeors fall through the sub-cloud layer, sub-saturated conditions prevail causing sublimation. The distance between the cloud layers thus greatly impacts the possibility of seeding. Proske et al. (2021) found a survival percentage of 10%-20% when the distance between cloud layers was 2 km, with a large dependence on shape assumptions.

3.3 Cloud-Radiation Interaction

Clouds interact with radiation, both in the longwave (LW) (wavelengths larger than $4 \mu\text{m}$) and shortwave (SW) (wavelengths smaller than $4 \mu\text{m}$) spectra (Lamb and Verlinde, 2011). In general, clouds are assumed to be graybodies, emitting thermal radiation (LW) with an emissivity close to 1. Following Stefan-Boltzmann's law (Petty, 2004) they would thus only have a temperature dependency on their thermal emission which would be proportional to T^4 . According to Kirchoff's law, they then absorb longwave radiation equally efficiently. The emission of longwave radiation acts to cool the cloud while the absorption has the opposite effect. The generalisation of clouds as grey bodies is only valid for clouds with cloud mass larger than 30 gm^{-2} (Shupe and Intrieri, 2003), which renders the clouds optically thick. Emissivity, while close to one for all clouds, differs for clouds depending on their optical character. This is modulated by the optical depth (Liou, 1980), which in turn depends on the microphysics of the clouds (Twomey, 1977; Wood, 2015), including the effective radii and the number and mass concentration. Thus, thick liquid clouds with an abundance of droplets efficiently radiate, while ice clouds with lower concentrations and larger effective radii have a lower emissivity.

Clouds also scatter and absorb radiation from the sun, emitted in the SW. This efficiently reduces the amount of radiation reaching the surface of the Earth. Clouds that scatter more SW are considered to be optically thick (Cesana et al., 2023). The altitude, location, and phase of the cloud influence the radiative interactions with clouds. The global net effect of clouds present, however, is cooling (Boucher et al., 2013).

In a liquid cloud, the number of cloud droplets determines the level of SW scattering, thus clean clouds (less CCN) scatter less SW than polluted clouds (more CCN). This is the Twomey effect or the 1st indirect effect of aerosols (Twomey, 1974). Thin, high,

cirrus clouds, with a cold cloud-top temperature, tend to be invisible to SW radiation. This significantly reduces the net cooling in the atmosphere, as they absorb longwave radiation emitted from lower clouds and the Earth while they emit very little (T^4 dependency). This is commonly known as the greenhouse effect.

Measured surface radiation in the longwave and shortwave bands can be combined into a net surface radiation term, F_{net} , and is calculated as

$$F_{net} = (F_{LW}^{\downarrow} + F_{SW}^{\downarrow}) - (F_{LW}^{\uparrow} + F_{SW}^{\uparrow}) \quad (3.26)$$

where \downarrow (\uparrow) indicates the downwelling (upwelling) direction of the radiation flux at the surface (units Wm^{-2}). We may further introduce the cloud radiative effect (CRE) (Ramanathan, 1987) which quantifies the impact of the presence of clouds compared to a clear sky. It is defined as

$$CRE = F_{cloudy}^{net} - F_{clear}^{net} \quad (3.27)$$

where the F_{clear}^{net} indicate the net radiation flux in a hypothetical cloud-free atmosphere and F_{cloudy}^{net} is the actual net radiation flux. This can be further decomposed into a shortwave and longwave component $CRE = CRE_{SW} + CRE_{LW}$, where

$$CRE_{SW} = (F_{cloudy,SW}^{\downarrow} - F_{cloudy,SW}^{\uparrow}) - (F_{clear,SW}^{\downarrow} - F_{clear,SW}^{\uparrow}) \quad (3.28)$$

with CRE_{LW} similarly decomposed (Li et al., 2011). A negative (surface) CRE indicates surface cooling compared to clear skies, i.e. the clouds have a net cooling effect. Longwave CRE has been shown to depend more on the microphysics, including the temperature and emissivity of the cloud. Shortwave CRE depends on cloud transmissivity while also governed by external factors such as the solar zenith angle and surface albedo (Shupe and Intrieri, 2003). On the scale of an individual cloud, the cloud-top is cooled by longwave radiation while heated by shortwave absorption (and possibly by LW radiation emitted by overlaying clouds). These effects are termed cloud radiative heating (CRH) and refer to the localised impact of the cloud with respect to its environment. We may think of this as CRE but in the atmosphere, however, CRE is defined as a flux in units of Wm^{-2} while CRH is a flux divergence K day^{-1} (Harrop and Hartmann, 2016). The CRH is calculated using;

$$CRH = \frac{\partial T}{\partial t} = \frac{1}{\rho c_p} \frac{\partial}{\partial z} (F_{cloudy} - F_{clear}) \quad (3.29)$$

where ρ is the density of the air, c_p , the heat capacity at constant pressure. A shortwave and longwave component can be decomposed using the nomenclature from above.

The Longwave Radiative Cooling Suppression in the Multilayer Cloud System

In the multilayer cloud system, a longwave cooling suppression of an underlying cloud has been found to occur as an upper cloud layer heats the atmosphere below it by trapping longwave radiation from the lower cloud. This phenomenon has been seen in satellite studies (Christensen et al., 2013; Adebisi et al., 2020; Jian et al., 2022), observational case studies in the Arctic (Shupe et al., 2013; Turner et al., 2018; Lonardi et al., 2022), and idealised modelling studies (Chen and Cotton, 1987; Luo et al., 2008; Chen et al., 2020). In a detailed study by Christensen et al. (2013) the impact of free-tropospheric clouds overlaying marine stratocumuli was investigated, where they found a strong correlation between the presence of an upper layer and a decrease in longwave cooling of the lower layer, with a large dependency on the height of the upper layer. Cloud top heights (of the lower layer) were suppressed together with turbulent kinetic energy, entrainment and nighttime precipitation. The relative decrease in longwave radiative cooling with an overlaying cloud amounted to 4.2 K day^{-1} during nighttime. Similar characteristics were confirmed by Jian et al. (2022) who quantified the reduction of cloud-top LW cooling for clouds overlaying stratocumuli to 5 K day^{-1} , however, their results were independent of the time of the day. In another satellite study, Adebisi et al. (2020), show a 10 K day^{-1} reduction by mid-level Atlantic clouds, including all observations (day and night). These newer findings are quite contrary to Christensen et al. (2013) who argue that the increase in the number of cloud layers reduces the incoming SW radiation which allows for a stronger LW radiative cooling during the day for cloud layers shielded by upper layers. Thus, Christensen et al. (2013) report a daytime increase in LW radiative cooling for multilayered clouds of 2.4 K day^{-1} .

Turner et al. (2018), provide the only long-term comparison of multilayer clouds in the Arctic region. They investigated the radiative heating and cooling of clouds on the northern slopes of Alaska and found a strong radiative cooling suppression. Circa 7 times lower cooling rates for a lower layer cloud compared to a single layer cloud with a similar (high) LWP were found, efficiently reducing the cloud-top cooling from about 70 K day^{-1} to 10 K day^{-1} . Liquid-bearing clouds beneath ice clouds were reduced but to a smaller extent (about 5 K day^{-1}). The level of cooling of the lower cloud is directly related to the cloud mass (optical thickness) of the upper cloud, allowing more cooling for shallower overlaying cloud layers. This trend can be seen for all clouds but is more evident for liquid-bearing upper layers. In observational studies in the high-Arctic, the impact of an overlaying cloud has been noted (Shupe et al., 2013; Lonardi et al., 2022) but has not yet been quantified in a long-term study.

Model Parameterisation

In the model, the radiation is parameterised using the ecRad scheme (Hogan and Bozzo, 2018). ecRad is a fully modular system allowing for different components of the radiation to be interchanged. A radiation solver is used to calculate SW and LW

irradiance profiles (F_{SW} and F_{LW}). Fed to the radiation solver is the cloud cover (the cloud fraction) and the effective radii of liquid droplets and ice crystals. The cloud optical parameterisations for liquid water droplets (Edwards and Slingo, 1996) and ice crystals (Fu, 1996) calculate the extinction coefficients based on effective radii, calculated within the microphysics. The SW and LW radiation solver used here is the Monte Carlo Integration of the Independent Column Approximation (McICA) (Pincus et al., 2003). McIca is a 2-stream radiation transfer module, where only vertical directions are solved, disregarding any 3D effects of scattering.

Clouds overlapping need special consideration when it comes to radiation as the level of overlap between the layers impacts the amount of radiation absorbed and scattered by the individual layers. Cloud overlap is a large topic of research where assumptions of overlap for each cloudy model level form the base for parameterising the cloud cover. For discontinuous or non-contiguous clouds, i.e. multilayer clouds, the overlap is best represented as random (Hogan and Illingworth, 2000; Tompkins and Di Giuseppe, 2015) but this scheme underestimates the cloud fraction over stratocumulus regions (Li et al., 2015). In the operational setup for ICON a hybrid version is used, the exponential-random overlap assumption by Hogan and Illingworth (2000) where the overlap for multilayer clouds is considered to be uncorrelated (random) and the decorrelation length scale, z_D , is set to 2 km as a default. This length scale defines the amount of overlap, by

$$\alpha = \exp\left(-\frac{\Delta z}{z_D}\right) \quad (3.30)$$

where α is the amount of overlap, ($\alpha=1$ when completely overlapping and $\alpha=0$ when only randomly overlapping), this tends to zero for larger layer separation Δz , indicating that the clouds are less likely to overlap for larger separation.

3.4 The Arctic System

The Arctic is the region enclosing the North Pole. Various definitions of its extent exist but here we use the definition of pole-wards of 60°N . The Arctic participates in global circulation through the polar cell, the smallest and weakest of the circulation cells. The polar cell extends from about 60°N to the pole and creates a subsidence region, an area of sinking air, at the pole affecting the clouds residing in this area (Young et al., 2018). It transports warm air from the midlatitudes to the Arctic, where it is gradually cooled down and dried and transported southwards. The Arctic system is highly governed by the mid-latitudes (Kokhanovsky and Tomasi, 2020). Warm air intrusions frequently occur in the Arctic and are governed by large-scale synoptic systems extending from mid-latitudes to the Arctic sector (Pithan et al., 2018; Svensson et al., 2023). A warmer air mass advected northward cools down through contact with the icy

surface and forms a fog (Dimitrelos et al., 2020; You et al., 2021), which transforms into the low clouds we commonly see in the Arctic. The impact of Arctic air mass transformation and cloud formation has been thoroughly studied (e.g. Curry, 1983; Pithan et al., 2018; Dimitrelos et al., 2020; You et al., 2021; Silber and Shupe, 2022; Svensson et al., 2023).

The region has seen a rapid change in the last decades due to the increase in global greenhouse gases and the local temperature is rising two (Overland et al., 2019) up to four times (Rantanen et al., 2022) as fast as the global mean. One of the more dominant feedback loops pertains to the sea ice and its melting, where the increase in temperature leads to melting sea ice, this darkens the surface allowing for more radiation to be absorbed which leads to higher surface temperatures (Serreze and Barry, 2011). The more rapid warming of the Arctic compared to the rest of the Northern Hemisphere, is named Arctic Amplification and while some impacts seem clear, many feedbacks are still to be identified. The cloud feedback and its role is one of them (Taylor and Monroe, 2023).

Temperature inversions frequently occur in the region (88 % in the summer Arctic (Palo et al., 2017)) due to a combination of surface radiative cooling, warm air advection, cloud-top cooling and subsidence (Siebesma et al., 2020; Palo et al., 2017). Subsidence, in particular, allows for more thermodynamically stable conditions. Humidity inversions are often found together with the temperature inversion which is, in general, formed due to transport with a warm airmass from the south (Siebesma et al., 2020).

Arctic Cloud Features

The Arctic is a cloudy place, with yearly mean cloudiness above 50% (Intrieri et al., 2002b; Shupe et al., 2022; Jiang et al., 2024) and reaching 80% during the summer (Jiang et al., 2024). Low, stratiform (Stratocumulus, Sc), clouds are the most frequent summer clouds in the Arctic region (Eastman and Warren, 2010). While vertically constrained by the subsidence in the region, they are generally formed by the advection of warm and moist air (Siebesma et al., 2020).

Overall the dynamics of Arctic stratocumulus are similar to the marine kind. The generation and persistence of the Sc cloud come from its strong cooling by longwave radiation (Wood, 2015). Cooling occurs heavily in the supercooled liquid layer of the cloud and is an important feature for sustenance. As the cloud top cools, normally located at the bottom of a temperature inversion, it cools upward to space but also downwards. The rest of the cloud is at a warmer temperature than the top which produces negatively buoyant parcels. This downward displacement of air initiates upward buoyancy flux that fills the "empty space" further initiating turbulent motions. These turbulent eddies extend above the cloud top where atmospheric air is drawn into the cloud through entrainment. The eddies are further strengthened by latent heating,

from condensation, in updrafts while downdrafts force the evaporative cooling (cloud droplets evaporating) (Wood, 2015). For most marine Sc clouds, warm and dry air is entrained. The warm air cause local evaporation which in turn cools the environment due to evaporative cooling, causing a negative feedback loop for the cloud persistence, leading to its decay (Lilly, 1968; Van Der Dussen et al., 2014).

In the Arctic, moisture inversions, mentioned above, enable further cloud deepening through moist entrainment at cloud top (Egerer et al., 2021). A perfectly stable cloud top (no rising or sinking motion) indicates that cloud top entrainment is approximately balanced by large-scale subsidence. The moisture inversion in the Arctic is thus maintaining the cloud through two survival mechanisms; 1. cancelling the effects of high subsidence that causes cloud thinning (Siebesma et al., 2020), 2. acting as a moisture source; marine Sc has an endless supply of moisture from the ocean resupplying the cloud. With an ice-covered surface, this moisture source is cut off, often rendering the clouds thermodynamically decoupled from the surface (Sotiropoulou et al., 2014). An abundance of CCN has also been found to occur above the cloud-top, entraining into the cloud with the moisture (Sterzinger and Igel, 2024). These Arctic Sc clouds can persist for days (Morrison et al., 2012) which, when taking the unstable character of mixed-phase clouds into account, is quite surprising. The persistence of mixed-phase Arctic clouds is still a question of research.

Arctic clouds have, for most of the year, an opposite cloud-radiative effect than the global mean. Due to the reflective character of the ice-covered surface, the albedo of the clouds is less than the surface and in the absence of clouds, more sunlight is scattered back to space. This induces an additional warming effect from the clouds on top of the longwave absorption. However, in summer, with the sea ice melting, the surface albedo is greatly reduced and the low clouds are found to be cooling the surface (Shupe and Intrieri, 2003). The temperature inversions often present, allow clouds to emit longwave radiation at a higher temperature than the surface and together with a dry atmosphere (less absorption by water vapour) the cloud radiation impact is larger than in the Arctic than in midlatitudes (Shupe and Intrieri, 2003). Investigating the transition period in autumn, when the solar radiation is greatly reduced, may give net heating or cooling depending on the cloud microphysics, water vapour, and solar zenith angle.

Arctic Multilayer Clouds

The formation and dissipation of these multiple cloud layers in the Arctic have been accredited to many explanations. Figure 3.6 shows sketches of some of the formation mechanisms proposed. Herman and Goody (1976) suggested the formation of two layers from the splitting of an Arctic stratus due to the incomplete dissipation of the layer, induced by shortwave absorption (Fig. 3.6c). Radiative cooling at an existing temperature inversion causing mixing and lifting whereby a lower inversion may form due to surface air cooling by the sea ice was proposed by McInnes and Curry (1995,

Fig. 3.6d). Other authors propose independent formation mechanisms for the layers, such as an upper cloud formed by weak ascent or moist entrainment while a bottom cloud is initiated by advection (Tsay and Jayaweera, 1984) (Fig. 3.6a). More recent studies from the M-PACE campaign show a dependency on large-scale advection on both the formation and the persistence of the upper layers (Luo et al., 2008; Morrison et al., 2009). Luo et al. (2008) modelled a real case of multilayer clouds using a two-dimensional cloud-resolving model. They showed that the formation of two layers was initiated by large-scale advection and radiative heating below the upper cloud. Sensitivity studies, such as turning off longwave cooling completely and removing large-scale advection revealed the inhibition of the formation of the upper cloud layer. They further suggest surface fluxes are required for the formation of the lower layer. Harrington et al. (1999) proposed a lower layer forming due to cooling and moistening of the atmosphere due to ice sublimation whereby a slow condensation keeps the layers intact due to radiative cooling. This cloud layer then slowly forms an inversion and a mixed layer (Fig. 3.6b). This was further theorised by Sotiropoulou et al. (2014) where this evaporation may enhance decoupling from the surface.

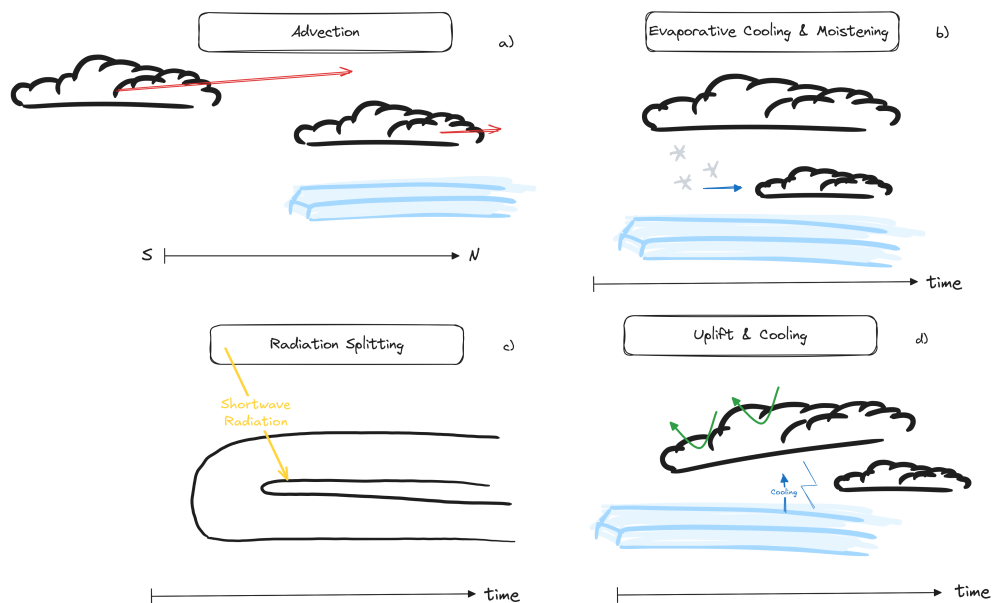


Figure 3.6: Hypothesised multilayer cloud formation mechanisms. a) The advection hypothesis, whereby one or more cloud layers are independently advected to overlap with each other. b) The formation of a lower layer due to the evaporative cooling and moistening from precipitation which initiates radiative cooling enabling cloud droplet formation. c) The radiation splitting hypothesis, a single-layer stratocumulus cloud absorbs shortwave radiation unevenly through the cloud which leads to the evaporation of cloud droplets and splitting of the cloud layer into two. d) The strong radiative cooling at the cloud top forces the rising motion of the cloud, this is followed by the formation of a surface inversion due to the low thermal conductivity of snow which enables a cloud to form below the upper cloud through continuous cooling.

Cloud Microphysics of Arctic Clouds

Phase partitioning in Arctic single-layer mixed-phase clouds is commonly observed as a liquid cloud layer precipitating ice (Hobbs and Rangno, 1998; Morrison et al., 2012; Solomon et al., 2018). In general, Arctic cloud IWP is consistently underrepresented in models (Morrison et al., 2009; Fridlind and Ackerman, 2017; Stevens et al., 2018) while LWP may be adequately captured. Immersion freezing has been deemed the dominant primary ice nucleation pathway (Fridlind and Ackerman, 2017) while some studies claim it is too soon to not consider contact freezing for Arctic mixed-phase clouds (Morrison et al., 2005b; Schäfer et al., 2024). A multitude of modelling studies have been performed with results indicating that we still don't fully understand how these clouds respond to perturbations. Non-linear effects have been seen when perturbing CCN (Solomon et al., 2018) but most studies see an increase in LWP with CCN as known from other regions. This is also seen for idealised multilayer clouds (Bulatovic et al., 2021). A drizzle suppression when the CCN is high, due to the competition for vapour, has been recorded for Arctic clouds as well (Stevens et al., 2018), with a large spread of impacts on the clouds. In a low CCN regime (CCN concentration $< 10 \text{ cm}^{-3}$), the clouds become CCN limited (tenuous cloud regime), which may force the dissipation of the layer (Mauritsen et al., 2011; Stevens et al., 2018; Sterzinger et al., 2022).

Concerning cloud ice, both an increase (Solomon et al., 2018) and a decrease (Morrison et al., 2008) in IWP, when more CCN are introduced, have been noted. More IWP is in general found with a higher INP concentration (Stevens et al., 2018) followed by a decrease in LWP due to the WBF process. Glaciation may (Harrington et al., 1999) and may not (Stevens et al., 2018; Morrison et al., 2011) occur with the WBF process active. Furthermore, the way Arctic INPs are treated in the model may be improved by using prognostic aerosol models (Solomon et al., 2018). Similarly, the recycling of INPs in the sub-cloud layer, such that INPs sedimenting out of the cloud through precipitation may re-enter the cloud and enhance the ice formation, has been shown to be important for Arctic mixed-phase clouds (Solomon et al., 2015) and Arctic multilayer clouds (Fu et al., 2019). Another aspect of INP activation concerns instant versus time-dependent activation. This is not a new topic but has still not received much traction in the community. The inclusion of time-dependence may have a large impact on how models simulate INP activation (Jakobsson et al., 2022) which could be important for the persistent Arctic mixed-phase clouds.

With a general misrepresentation of cloud ice in models (Morrison et al., 2009; Fridlind and Ackerman, 2017) it is probable SIP is present. SIP is far from something we understand, however, it likely has a large impact on Arctic clouds. The observational study by Pasquier et al. (2022) showed a 40% occurrence frequency of SIP during a campaign over Ny Ålesund with number concentrations of ice crystals up to 10 L^{-1} . The dominant process was found to be droplet freezing and shattering followed by breakup upon ice-ice collisions. This is quite contrary to the results from the modelling

work that shows the dominance of the breakup upon ice-ice collision process for Arctic (single-layer) clouds (Sotiropoulou et al., 2020; Schäfer et al., 2024; Sotiropoulou et al., 2024). This process is, however, badly constrained by assumed pre-factors (Sotiropoulou et al., 2020) and parameterisations. Other studies showed the importance of droplet freezing and shattering for multilayer clouds (Fu et al., 2019) and single-layer clouds (Zhao et al., 2021). The rime-splintering mechanism seems to be redundant but may initiate the breakup collision by creating smaller ice crystals (Sotiropoulou et al., 2020). Enhancement factors, the increase in number concentration of cloud ice with SIP included, reach 10^2 (Sotiropoulou et al., 2020) and 10^4 (Zhao et al., 2021).

4 | DATA AND METHODS

This chapter introduces the methods we employ in this thesis: the model setup, statistical measures, diagnostics, and the observational datasets used for model constraint and evaluation.

4.1 General Model Setup

Here a general setup of the ICON model is presented. This covers the parameterisations that are common for all chapters. In each result chapter more specific changes are given to facilitate understanding and readability.

For this thesis, we use the ICON model versions 2.6.5 (Chapter 5 and Chapter 6) and 2.6.6 (Chapter 7 and Chapter 8). For the parameterisations of interest in this thesis, the model versions are comparable. An overview of the implementations of the different chapters is provided in Table 4.1.

	Chapter 5	Chapter 6	Chapter 7 & 8
Model Version	2.6.5	2.6.5	2.6.6
Domain Extent	60°N-90°N, 85°N-90°N, 1°radius, 0.3°radius	85°N-90°N	71°N - 90°N
Nests	6 km, 1.6 km, 400 m, 100 m	1.6 km (driven by 6 km)	2.5 km
Vertical Levels	90, 90, 150, 200	90	120
Δt	50 s, 12 s, 4 s, and 0.8 s	12 s	20 s

Table 4.1: Overview of setups for the different result chapters. Δt signifies the time step of the fast physics.

Limited Area Simulations

To study clouds we set up the model in a limited-area mode. This implies that we do not simulate the entire globe but choose a smaller area, a domain, to perform the

simulations on. In turn, this allows us to study the clouds at a higher resolution as we may make the grid spacing smaller. A smaller grid spacing is possible only due to the choice of a smaller domain, as we are still limited by computational power. The clouds in this thesis are studied through a real set-up, meaning we use analysis data to force the boundaries and initialise the model. The analysis data is the global ICON model analysis. This is the global version of ICON which runs with a 1-moment microphysics scheme at 13 km grid spacing. The analysis is the product of a model run using assimilated data. Every three hours, a data-assimilation cycle begins, incorporating global observations into the model to obtain the best state of the atmosphere, which is called the analysis. The analysis includes atmospheric variables such as temperature, winds, and pressure but also cloud variables (mass concentration). DWD assimilated the ascending and descending radiosondes from MOSAiC and thus at initialisation, the model should be close to observed values. We initialise our model at 00 UTC, across the full domain. Similarly, boundary conditions update the boundaries of the limited-area domain.

Initially, our system is identical to the 13 km analysis. However, it is remapped onto a finer grid spacing. The domain extent and grid spacing change between the chapters and for this reason they are now introduced separately.

Domain Extent

For Chapter 5 and Chapter 6, a nested strategy is adopted. This is a method to gradually increase the horizontal grid spacing to avoid too large jumps in what is resolved. From the ICON analysis, we remap the variables onto a 6 km nest outlined in dotted lines in Fig. 4.1 and further use the output to initialise and update boundaries for a higher resolution domain at 1.6 km. This method is further repeated for a 400 m nest and a 100 m nest, all outlined in Fig. 4.1. The model is initialised at 00UTC for the 6km nest and the other nests are initialised at 4UTC, 6UTC, and 8UTC respectively to let the model spin up at a higher resolution before further increasing the horizontal and vertical resolution. This relatively short spin-up time was deemed necessary to still capture the local thermodynamic state. The 400 m nests and subsequent 100 m are initialised by the 1.6 km (with prescribed INP concentration at 1L^{-1}) simulation (see Chapter 5). Appendix A.1 shows that further increases in resolution from the 1.6 km have only small impacts on the cloud systems, and thus the 1.6 km grid spacing is a good compromise between resolution and computational costs. The model is left to run for 48 h and 24 h for a case study between the 1st-2nd September and 3rd of September 2020 respectively.

For Chapter 7 & 8 no nesting was adopted. Simulations are performed at a horizontal grid spacing of 2.5 km which was deemed the largest Arctic domain we could stably simulate. This grid spacing is within the limit of jumps in resolution (less than a factor of 10) from the global simulation at 13 km. This domain, extending from 71°N to 90°N , covering a radius of 2100 km, centred on 90°N , and extending over 2.4 million

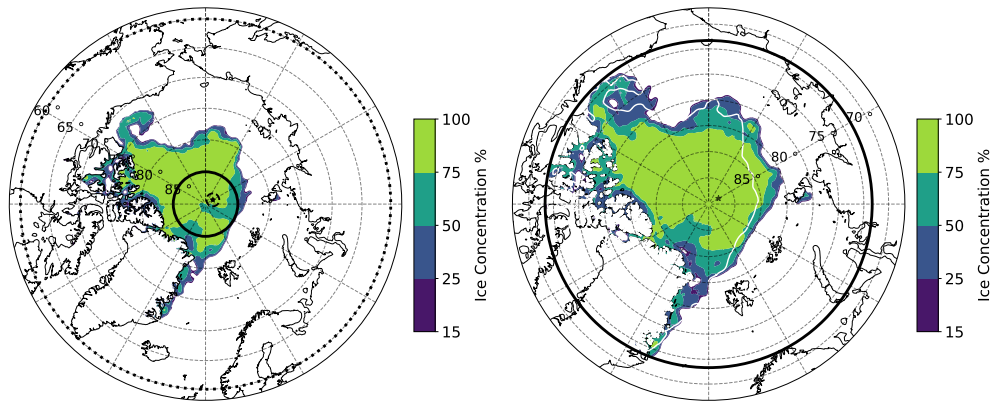


Figure 4.1: Left plot: Nested domains used in Chapter 5 and Chapter 6. The 6 km nest in dotted lines reaching from 60°N-90°N, solid line marking the 1.6 km nest used for most analysis and the high-resolution domain at 400 m in dashed lines. The 100 m domain is too small to show up next to the average daily ship position (1st of September 2020) presented with a star. Colours show the sea ice concentration above 15% on the same day. The figure is reprinted from Wallentin et al. (2024) under the licence. Right plot: Domain extent marked in black for the long-term simulations performed in Chapter 7 & 8. The sea ice concentration during the first (last) simulation is shown in filled contours (15% concentration in a white line).

grid cells, was determined to be the largest the radiation scheme could handle on the high-performance computer (HPC) HoreKa and is plotted in Fig. 4.1. This is likely due to memory issues as larger domains using ICON have been used for other studies. The model is initialised at 00UTC and runs for 24 hours. We simulate 32 days, between the 22nd of August 2020 and the 22nd of September 2020.

Parameterisations

High-resolution nests (finer than 3 km) are run with the two-moment microphysics by Seifert and Beheng (2006) with six hydrometeor classes: cloud droplets, rain, graupel, hail, snow, and cloud ice. With the 2-moment microphysics, more microphysical pathways are included and we make use of the more sophisticated schemes. At a grid spacing of 6 km (largest nest in Chapter 5), convection, the vertical transfer of heat when air parcels are less dense than their environment, is parameterised (Tiedtke, 1989; Bechtold et al., 2008). At finer grid spacings, both deep and shallow convection are considered explicitly resolved. This is evaluated over the Arctic domain with negligible differences when including shallow convection (not shown). The radiation is described by the ecRad radiation scheme (Hogan and Bozzo, 2018) introduced in Chapter 3.3. For all simulations except the 100 m nest in Chapter 5, turbulence is described by a 2nd order turbulence parameterisation (Raschendorfer, 2001). At 100 m grid spacing, the turbulence is parameterised using the Lilly- Smagorinsky parameterisation (Smagorinsky, 1963; Lilly, 1962). The turbulence schemes are introduced in Chapter 3.1.1.

Call Frequency

In the model the schemes are called at certain intervals, the fast physics (including microphysics, turbulent diffusion, and saturation adjustments) time step is set to 50 s, 12 s, 4 s, and 0.8 s for Chapter 5 and Chapter 6 while for Chapter 7 & 8 it is set to 20 s. These have been thoroughly tested for optimal computational usage and to not exceed the Courant-Friedrich-Lewy criterion for computational stability ($0 \leq c \frac{\Delta t}{\Delta x} \leq 1$, where c is a translation velocity, typically the maximum wind speed within the domain, Δx is the grid spacing defined in Eq. 3.2 and the time step Δt of the fast physics). The radiation is called every 12 minutes for Chapter 7 & 8, in comparison with every 144 s for the other chapters. This is to reduce the cost of the large simulation in Chapter 7 & 8. In Chapter 6 we are specifically interested in the radiation interaction and thus increase the call frequency to the radiation scheme.

Vertical Levels

We have noticed the importance of high vertical grid spacing throughout our work. For Chapter 5 and Chapter 6 this is explored within the nested strategy and the 6 km and 1.6 km runs are kept to 90 levels while the 400 m (100 m) run is increased to 150 (200) vertical levels. For Chapter 7 & 8 the vertical levels are set to 120. The model top is consistently set to 23 km while sleeve coordinates distribute model levels vertically to keep the highest density of model levels in the lowest kilometres.

Aerosol Constraint

The main focus of this thesis is the microphysical interactions within the clouds. To understand these better we perform microphysical perturbations. These can be thought of as a small change in a parameterisation, such as the immersion freezing parameterisation, where we decrease the number of ice nucleating particles (INP) and simulate the cloud system again. This is to systematically explore how the clouds react to changes. Through this method, we can investigate how important different perturbations are, such as changing the temperature at which the INP activate and quantify the impact. As a diagnostics tool, accumulated microphysical process rates in time are collected with the model output and are used as indicators for which processes contribute to layer growth as well as cloud phase partitioning. The model tunings for INPs and the implementation differ in each chapter and will thus be introduced there to increase readability.

A CCN tuning to the Hande et al. (2016) parameterisation has been done to better capture the Arctic aerosol distribution. In Chapter 5 and Chapter 6 a tuning factor of 1/10 is applied to Eq. 3.12. The tuning factor is based on the evaluation of vertical velocities in the model and the CCN data from the MOSAiC campaign (see the introduction to observational data sets in Ch. 4.2.1, Fig. 4.4). For Chapter 7 &

8 a larger tuning is applied. We compare data from the MOSAiC campaign with the MOCCHA campaign (see Chapter 4.2.2) and find a tuning factor of 0.01 is justified for the vertical velocities found within the domain. This scaling considers that the advection into the domain is one of the major sources of cloud liquid in the simulation and we thus limit the local activation further. The original parameterisation and the tuned ones (by 1/10 and 1/100) are shown in Fig. 4.2.

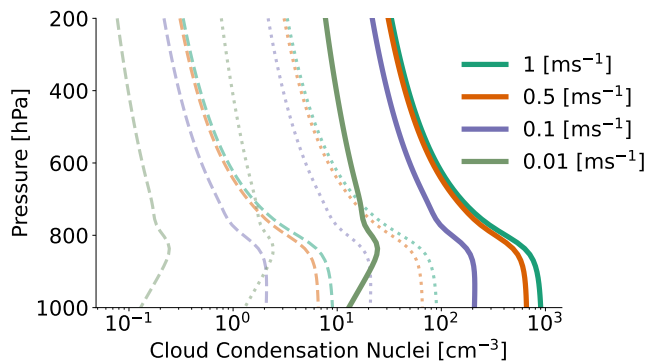


Figure 4.2: CCN parameterisation by Hande et al. (2016) (solid lines) giving CCN concentration (cm^{-3}) for each pressure level parameterised with respect to the vertical velocity. The observational mean value at 1 % supersaturation (Koontz et al., 2020) is marked with a *. The tuned parameterisations, divided by 10 and 100, are marked in dotted lines and dashed lines respectively.

4.1.1 COOKIE Implementation

To explore the cloud-radiative impact on multilayer clouds, we employ the Cloud On-Off Climate Model Intercomparison Experiment (COOKIE) method (Hunt, 1978; Stevens et al., 2012) in Chapter 6. This is realised by controlling which clouds are allowed to interact with radiation, effectively making clouds transparent (to radiation). This method has previously been used to study topics such as the cloud-radiative impact on climate (Voigt et al., 2021), high clouds (Haslehner et al., 2024), extratropical cyclones (Keshtgar, 2024), and extreme precipitation (Medeiros et al., 2021). Here, we employ the COOKIE method to study the radiative impact on the individual clouds and the role of radiative heating in the formation of multilayer clouds.

In the COOKIE method, two simulations are needed: one simulation with cloudy sky radiative heating (Clouds-On) and one simulation in which clouds are set to zero in the radiation calculation and only the clear-sky radiative heating is calculated (Clouds-Off). To implement this method, we follow the implementation of Schäfer and Voigt (2018) and Keshtgar (2024) that made slight changes to the method to preserve the radiative impact of clouds at the surface to avoid abrupt changes in the surface temperature. We add a further limitation to where in the vertical column the clear sky replaces the cloudy fluxes similar to the implementation by Voigt et al. (2023). Here, the clouds of interest have a natural separation at 1 km, and thus this is used as a border for the CRH. This

may introduce strong gradients in radiative heating at this border and we keep this in mind for the evaluation. Two sensitivity experiments are performed, where the clouds at different levels are made invisible to radiation. This implies that a cloud in a region where radiation is "turned off" does not have any CRH; i.e. it does not scatter SW nor does it emit LW radiation. Three simulations are performed in total, a reference and for the sensitivity study; one allows CRH above 1 km (*Below Off*) while the other only allows CRH below 1 km (*Above Off*). For clarity, these are visualised in Fig. 4.3.

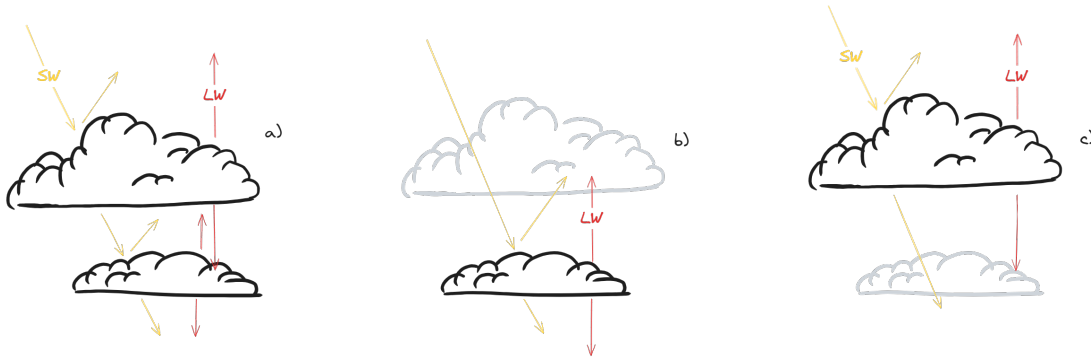


Figure 4.3: The three sensitivity simulations performed in Chapter 6. a) The reference with all cloud radiative heating/cooling allowed, b) *Above Off* simulation where clouds above 1 km are transparent to radiation, and c) *Below Off* simulations where clouds below 1 km are made transparent to radiation.

4.1.2 Diagnostics

A few metrics are used to quantify and process the microphysical output. These are defined here.

Supercooled Liquid Fraction

We may define the supercooled liquid fraction (SLF) as the ratio of liquid water to hydrometeors in the cloud

$$SLF = \frac{LWC}{LWC + IWC} \quad (4.1)$$

where IWC includes all frozen hydrometeors ($IWC+SWC+GWC$). Hail is considered negligible. An SLF of 1 (0) indicates a fully liquid (ice) cloud while numbers in between gauge the level of mixed phase.

Ice Enhancement Factor

To quantify the impact of SIP, an ice enhancement factor may be defined as

$$N_{SIP}/N_{PIP} \quad (4.2)$$

where N is the number concentration of cloud ice for a simulation with SIP and a simulation with only primary ice production, PIP. As most studies comparing these values are highly idealised they may use the domain integrated number concentration. For our simulations, we instead use the spatial average surrounding the ship and take the maximum column integrated number concentration with time, termed the maximum enhancement.

Multilayer Algorithm for Model Data

In Chapters 6 and 8 we identify the multilayer cloud occurrence at the MOSAiC site as well as regionally. Here, the algorithm to identify these layers is outlined, Appendix C.1 further provides a detailed evaluation of the mass and relative humidity thresholds

We define a cloud by a cloud mass threshold defined as LWC plus IWC exceeding 10^{-9} kgkg⁻¹. This is in line with the radiation solver's definition of when a cloud interacts with radiation (Rieger, 2019). A mass threshold is otherwise a limiting factor. We thus provide an evaluation of the mass threshold in terms of changes in cloud layer distribution in Appendix C.1 using model output collected from Chapter 8. Secondly, a saturation clause is introduced such that a cloud layer requires supersaturation with respect to liquid water or ice. This is to ensure the exclusion of seeding layers, as these may exceed the mass threshold. Fluctuations in relative humidity seem to occur between time steps rendering a proportion of cloud layers with appreciable cloud mass in the "no cloud" category, potentially due to temperature fluctuations. An evaluation of the relative humidity threshold over ice is given in Appendix C.1 to investigate the impact of this potential problem. Thirdly, layers that are within 100 m of each other will be merged into one cloud, this is iterated over all model levels. Cloud layers existing without neighbouring cloud layers may be less than 100 m thick.

Seeding Definition

The seeding frequency for the model is determined by identifying the cloud top in the model algorithm outlined above, where the relative humidity over ice or water is above 100% and the LWC+IWC exceeds 10^{-9} kgkg⁻¹. The model layer above the cloud top is defined as a "feeder layer". If the combined mass of graupel, snow, and cloud ice exceeds 10^{-9} kgkg⁻¹ in this layer (while in a sub-saturated environment) this layer is flagged as being seeded. This is further combined with a check if the cloud above it, the seeder cloud, has a model layer beneath the cloud base precipitating ice, snow, and graupel above 10^{-9} kgkg⁻¹, the "seeder layer". Therefore, layers above the cloud-tops with sporadically high water contents (such as those resulting from supersaturation fluctuations), can be mostly filtered out. The choice of mass threshold still presents a limitation. We do not check for the continuous presence of precipitating ice between the layers, only at the model layer above the cloud layer in question and beneath the layer above. Additionally, cloud layer gap calculations, which may restrict the seeding

possibility for larger cloud gaps, are not currently implemented. This is a topic for future research.

Model Evaluation

With a non-stationary observational site, discrepancies in the spatial dimension can be expected when compared to the model output. Here, we use a spatial average over a 15 km radius surrounding the daily average ship position to accommodate for the daily drift. If nothing else is reported this is how the spatial dimension is handled. For the long-term study in Chapter 7 & 8, we make use of meteograms. Meteograms are specified at a latitude and longitude whereupon the model uses the closest grid box. This version of the output fields greatly reduces the storage requirement as they now only contain 2D (and 1D, surface) variables and enables us to store output with a high temporal frequency of 1 min, comparable to observations.

4.2 Observational Data

This section introduces the observational datasets used for model comparison and constraint. Bear in mind it is a brief overview and full details concerning quality controls and overall features will not be given here.

4.2.1 The MOSAiC Campaign

The observational data, used for model comparison and aerosol constraint in the high-Arctic, is collected from the Multidisciplinary Drifting Observatory for the Study of Arctic Climate (MOSAiC) campaign (Shupe et al., 2022) where the ice breaker *RV Polarstern* (Knust, 2017) was moored to an ice shelf in the high Arctic during 2019/2020. As the second-ever full-year Arctic campaign, and the only one in this century with modern instruments and techniques, the MOSAiC campaign was a feat without likeness. Unique datasets now exist spanning multidisciplinary fields. We make use of this dataset to further develop and evaluate our model.

Microphysical Retrievals

Cloud variables, such as LWC, IWC, and IWP, are collected from two retrieval algorithms. One is from the Cloudnet database (Engelmann et al., 2024) retrieved through the approach by Illingworth (2007) using cloud radars, lidar, microwave radiometer, and radiosondes specified in Table 4.2. The other is the ShupeTurner algorithm (Shupe et al., 2015), which was specifically developed for microphysics retrievals in the Arctic region and utilises radiosondes, radar, lidar, microwave radiometer, and infrared radiometer to derive retrieved liquid water content and ice water content. The infrared radiometer is used for thin clouds while the radar mostly sees larger particles such as ice particles. The

Instrument	Specification	Usage
RPG Humidity And Temperature PROfiler (HATPRO) G5	Passive microwave radiometer, multichannel 22.24 GHz and 60 GHz	LWP, integrated water vapour (IWV)
Microwave Radar for Arctic Clouds (MiRAC)	89 GHz	IWV
Ka-band ARM Zenith Radar (KAZR)	35 GHz	Cloud profiles, microphysics retrieval
Raman lidar Polly ^{XT}	Wavelengths 355, 532, 1064 nm	Microphysics retrieval
Radiosondes RS41 Vaisala	Launch every 6 hours	Temperature, pressure, moisture, and wind
Pyranometer Kipp and Zonen CMP21		Solar irradiance
Pygeometer Kipp and Zonen CGR4		Terrestrial irradiance
Met Tower	at Met City, 10 m mast	Pressure (2 m), temperature, relative humidity, surface skin temperature, and sonic anemometer winds
Total aerosol filters	Offline analysis using the ice spectrometer	Immersion freezing INPs
Cloud condensation nucleus counter	2 column (CCN200), supersaturation at 0.4% and scanning from 0 to 0.8%	CCN concentration
Condensation particle counter (CPC)	Total particle number concentration >10 nm	Pollution mask
Atmospheric Surface Flux Stations (ASFS)	2 stations in the distributed network	Upward and downward, broadband solar and terrestrial radiation

Table 4.2: Instruments used from the MOSAiC campaign, specifications from Shupe et al. (2022) and Griesche et al. (2024).

microwave radiometer measures the integrated liquid water path but does not provide a vertical liquid distribution. In contrast, the lidar observes the cloud base and is more sensitive to smaller particles such as cloud droplets. Liquid water content is calculated adiabatically where the classification algorithm flags liquid water and liquid water path is measured by the Microwave Radiometer. The uncertainty on the LWC is 15-25% (Frisch, 1998; Griesche et al., 2021) and for LWP a standard deviation.

One of the main differences in the microphysical retrieval approaches is the temperature assumption. While the Cloudnet product is calculated using a model temperature the ShupeTurner algorithm uses interpolated radiosonde data. The ice water content, in Cloudnet, is calculated from the 35GHz radar reflectivity factor and temperature from a forecast model using the approach by Hogan et al. (2006) with an associated uncertainty of +40% and -30% by the equation

$$\log_{10}(IWC) = 0.000242 * Z * T + 0.0699 * Z - 0.0186 * T - 1.63 \quad (4.3)$$

where Z is the radar reflectivity (in dBz) and T the model temperature in °C. The ShupeTurner algorithm instead calculates IWC based on a power law (detailed and evaluated in (Shupe et al., 2005) based on Matrosov (1999))

$$IWC = aZ^b \quad (4.4)$$

where the coefficients are tuned for each radar profile based on cloud optical thickness and ice water path obtained from layer-mean radar reflectivity (Matrosov, 1999). b is 0.63 while a is a measure of the particle size, which is affected by optical depth and temperature and thus has a seasonal variance (Shupe et al., 2005) between 0.05 (in summer) and 0.1 (winter). The radar reflectivity, Z , in Eq. 4.4 has units mm^6m^{-3} .

Atmospheric Variables

Vertical atmospheric variables such as temperature, moisture, and relative humidity are taken from level 3 Vaisala RS41 6-hourly radiosondes (Maturilli et al., 2022b). These radiosondes give vertical information about the thermodynamic structure and are used for model comparison and multilayer cloud detection. Atmospheric surface variables, including temperature, wind, pressure, and irradiance are collected from the Met Tower (Cox et al., 2023), at the so-called Met City, a 10 m mast raised on the ice floe at 375 m away from the ship, at a location deemed far enough to not be impacted by the ship itself (Shupe et al., 2022). Integrated water vapour is retrieved from Walbröl et al. (2024). They combine two microwave radiometers; HATPRO and MiRAC-P to derive the IWV.

Radiation

To investigate the radiative impact of multilayer clouds we make use of surface radiation measurements. These include broadband pyranometers (SW) and pyrgeometers (LW) by the Met City mast and ASFS, measuring upward and downward, broadband solar and terrestrial radiation. These were placed further away from the ship (at least 200 m) to exclude any turbulence effects from the ship itself.

Aerosols

Cloud condensation nuclei and ice nucleating particle concentrations are used to tune the model representation of cloud droplet activation and heterogeneous freezing. Aerosol data are obtained from measurements from the American Atmospheric Radiation Measurements (ARM) site (Creamean et al., 2021a; Koontz et al., 2020). The number concentration of CCN was measured using a continuous flow chamber scanning from 0 to 0.8 % supersaturation (Shupe et al., 2022; Koontz et al., 2020). Particle number concentrations, collected from the condensation particle counter from the Swiss aerosol container, are used for the associated pollution flag (Beck et al., 2022). Surface-based measurements of CCN concentrations suffer from local ship emissions (due to the sampling close to the ship plume) and were thus filtered using a pollution mask from Beck et al. (2022). The raw data and the filtered CCN concentrations at less than 0.5 % supersaturations from August to September 2020 are plotted in Fig. 4.4.

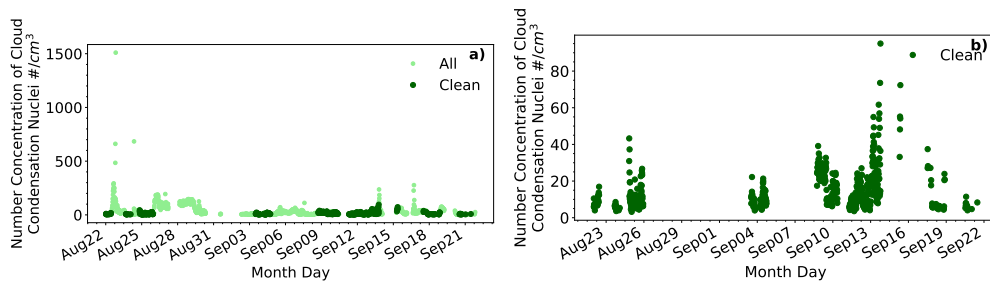


Figure 4.4: Cloud condensation nuclei concentrations at supersaturations less than 0.5 %, a) the raw dataset from ARM (Koontz et al., 2020), b) the filtered data set using the pollution mask from Beck et al. (2022). Approximately 60% of the data is removed through this step.

Total INP concentrations during MOSAiC were measured using total aerosol filters. Samples were collected over 72 hours through a vacuum pump, with single-use sterile filter units (NalgeneTM Sterile Analytical Filter Units) secured to a container railing while shielded from precipitation and blowing snow (Creamean et al., 2022). Samples were then placed in a Petri dish and kept frozen until analyses were performed offline using the CSU Ice Spectrometer (IS). The IS cools at $0.33^{\circ}\text{C min}^{-1}$ until -30°C and the freezing was recorded every 0.5°C with a camera (CCD) (Creamean et al., 2021a). The INP concentration per litre of air is then calculated through the equation by Vali et al.

(1971). The data and the respective tunings performed for each chapter are introduced within the chapters themselves.

4.2.2 Additional Aerosol Measurements

In Chapter 7 & 8 a long-term simulation approach is used. To capture the Arctic aerosol concentrations better, we compare the MOSAiC dataset with previous campaigns and station data.

For CCN we use data from the Microbiology-Ocean-Cloud-Coupling in the High Arctic (MOCCHA) campaign (Vüllers et al., 2021) during August-September 2018. This campaign covered a similar area as the MOSAiC campaign and thus we use this as a comparison, to ensure that the MOSAiC measured aerosols were in the normal range for the high-Arctic. The CCN data from MOCCHA (Duplessis et al., 2023) and MOSAiC (Koontz et al., 2020) are shown in Fig. 4.5. The mean number concentration of the MOSAiC and MOCCHA campaigns at 1% supersaturation amounts to 25 cm^{-3} and 19 cm^{-3} , respectively.

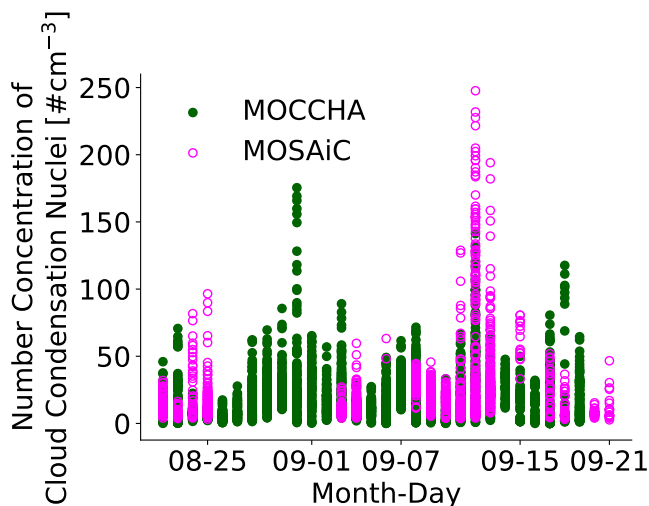


Figure 4.5: Cloud condensation nuclei data during August and September from the MOCCHA 2018 (Duplessis et al., 2023) and MOSAiC 2020 (Koontz et al., 2020) campaigns at all measured supersaturations.

For INPs, in Chapter 7 & 8, we also employ a multi-dataset evaluation. In Fig. 4.6 the locations of the campaigns and stations used for evaluation are shown. On top of INPs measured during MOSAiC (Creamean et al., 2022) and MOCCHA (Porter et al., 2022), we use data from the Ice Nucleation over the ARctic Ocean (INARCO) campaign in September 2017. Furthermore, station data has been evaluated. The Atmospheric Radiation Measurement (ARM) site at Utqiavik, Alaska, during the ARctic Study of Permafrost Ice Nucleation (ARCSPIN) campaign September 2021 (Barry, 2023), the Greenland research site Villum (Sze et al., 2023), Canadian Archipelago station Alert (Wex et al., 2019), and two datasets from the Zeppelin station on Svalbard, Norway

(Wex et al., 2019; Freitas et al., 2023). The data evaluated here only includes INPs collected between the 22nd of August and the 22nd of September.

The INP curves are shown in Chapter 7 (Fig. 7.1) together with an evaluation of three parameterisations created.

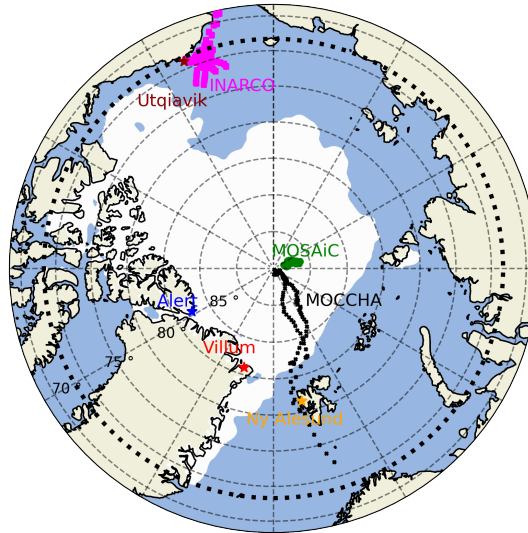


Figure 4.6: Spatial distribution of the stations used for the INP parameterisation development. For the ship-based campaigns; MOSAiC total aerosol filters (Creamean et al., 2022) in green, MOCCHA (Porter et al., 2022) in black, the INARCO campaign (Creamean, 2019) in magenta. The stations; Utqiavik (ARCSPIN campaign) (Barry, 2023), Alert (Wex et al., 2019), Villum (Sze et al., 2023), Svalbard 2012 (Wex et al., 2019) and 2017-2020 (Freitas et al., 2023). All datasets only contain measurements during August-September.

4.2.3 Observational Multilayer Cloud Algorithm

To compare with model output, we use the observational MLC algorithm developed by Vassel et al. 2019. It is based on the radiosondes as the major input data and is thus constrained temporally by the radiosonde launches. During MOSAiC, these are launched 6-hourly. The algorithm determines the number of layers present in a radiosonde profile by identifying sub-saturated layers in the calculated (from relative humidity and temperature) relative humidity over ice. The minimum thickness of a layer is set to 100 m. Radar reflectivity is used as a validation to ensure a cloud layer is present and not simply a supersaturated layer. The algorithm only considers cloud layers with sub-saturated layers of temperatures below 0°C as it was developed with a focus on the seeder-feeder mechanism. This introduces a bias in the warmer months where the actual MLCs occurrence may be higher due to this limitation. For the MLC characterisation, the radiosonde uncertainty is large; temperature and relative humidity measurements have 0.3°C and 4% uncertainty respectively (Vaisala Radiosonde RS41 Measurement Performance). The uncertainty in the temporal dimension, however, due

to drifting radiosondes and advected clouds at lower levels is not possible to quantify and we simply bear this in mind.

The seeding occurrence is based on sublimation calculations using Maxwell's growth law replacing the droplet radius, r , with a capacitance, C , which describes the ice crystal shape while acting as a size parameter. For this study, they were mostly interested in cloud ice with the shape of hexagonal plates. The equation follows as

$$\frac{dm}{dt} = 4\pi C \rho_i G_i s_i \quad (4.5)$$

where the loss of (ice) mass in time is defined by the density of ice, ρ_i , supersaturation over ice, s_i , and the growth parameter G_i (Lamb and Verlinde, 2011). Using a mass-diameter power-law, the diameter is determined which is further used to calculate the fall velocity for the particle. Initial crystal sizes were assumed at 400 μm , 200 μm , and 100 μm . A margin of error is allowed when the seeding fall height ends within the vertical spacing of the radar.

4.3 Analysis Methods

4.3.1 Methods for Model Evaluation

From the inherent structure of the observational MLC algorithm outlined above, the occurrence frequency is tied to the radiosonde launches. To compare with the model, atmospheric variables from the MOSAiC site are collocated in time to the radiosonde launch and taken as a 2-hour mean from the time of the launch. Thus, average profiles are used from the observations. The model MLC occurrence is derived from the model output using the abovementioned model algorithm. The model data is also collocated in time with the radiosonde launch to better compare with the observations. As the model produces 2D (meteogram output) fields at all time steps, a mean over two hours is not a feasible comparison. Instead, all profiles within 2 hours of the radiosonde launch are classified and variables are plotted with regard to the profile, MLC or SLC, character. This means the model has a larger number of data points compared to the observations.

4.3.2 Trajectories

The back trajectory tool Lagranto (Wernli and Davies, 1997; Sprenger and Wernli, 2015) allows us to study the upstream formation of the clouds. Back trajectories are based on tracing the 3D wind fields back in time to find the path an air mass took. The trajectories are initialised at the ship location and are traced back in time, following the output of the model. We use this approach for Chapter 5 and Chapter 6. Trajectories are initialised hourly between 10 UTC and 12 UTC near the ship location every 6 km within 114°E-120°E and 88.3°N-88.5°N on the 1st and within 118°E-120°E and 88.5°N-89°N

on the 3rd. Vertical trajectory starting positions are set to every 250 m in the lowest 2 km, every 500 m between 2 to 7 km height, and finally every 1 km up to 10 km height.

To further study the evolution of the clouds, pseudo-trajectories have been utilised. These are defined as the longitudinal mean over the longitudes the back-trajectories of interest cover. Thus a mean state for each latitude can be determined. As air masses flow northward towards the ship location this can be thought of as an upstream pathway and cloud variables can be evaluated along this track.

We further calculate the temperature advection by the wind from the model output via

$$-\mathbf{u} * \nabla T = -(u \cdot \frac{\partial T}{\partial x} + v \cdot \frac{\partial T}{\partial y} + w \cdot \frac{\partial T}{\partial z}) \quad (4.6)$$

where \mathbf{u} signifies the 3D wind vector containing horizontal velocities u and v , and vertical velocity w . T is the temperature.

4.3.3 Statistical Metrics

Mean Absolute Error

The Mean Absolute Error (MAE) is an intuitive statistical measure used to compare the model output with observed quantities. It is defined as

$$MAE = \frac{1}{n} \sum_{i=1}^n |y_i - x_i| \quad (4.7)$$

where the MAE is the sum of the absolute error between the model, y_i , and the observations, x_i , divided by the sample size, giving a mean error of the entire sample.


Spearman Correlation Coefficient

Calculating the Spearman Correlation Coefficient (ρ) is an efficient way to determine the strength of a relationship between the model and observations. The coefficient measures the monotonic relationship of non-normal distributed data through the rank by

$$\rho = 1 - \frac{6 \sum d_i^2}{n(n^2 - 1)} \quad (4.8)$$

where $d_i = R[x_i] - R[y_i]$, the difference between the ranks of the observations and the model, divided by the total number of data points (here time steps). ρ ranges from -1 and 1 where the sign indicates the direction of association. For example, if the observed temperature increases, a positive sign shows that the modelled temperatures also follow the same trend. A larger value (up to 1) indicates a stronger (monotonic) relationship.

5 | CASE STUDY ON THE MICROPHYSICAL INTERACTIONS OF ARCTIC MULTILAYER CLOUDS

In this chapter, we explore two multilayer cloud systems in detail with a focus on their thermodynamical and microphysical representation in ICON and how to improve the modelling of these cloud systems. A three-day case study was chosen from the MOSAiC campaign, where two days showed very different multilayer cloud systems. This chapter is based on the paper submitted to ACP by Wallentin et al. (2024) and is reused here under a  Creative Commons Attribution 4.0 International License (<https://creativecommons.org/licenses/by/4.0/legalcode>).

This study aims to build on the existing knowledge of Arctic multilayer clouds and to further investigate these cloud systems in a detailed and realistic perspective. We investigate the limits to accurately model the layering of the clouds in a remote region, evaluated with the observations from the MOSAiC campaign. We further use the observed aerosol concentrations to constrain the CCN and INP parameterisations to better represent the Arctic aerosols. SIP are explored and the impacts of seeding and glaciation due to the WBF mechanism are discussed. The model is run at 6 km grid spacing, and further offline nests are applied to reach 1.6 km, 400 m, and 100 m. Appendix A.1 details the high-resolution (400 m and 100 m) simulations performed. The high computational demand of running simulations at a fine resolution means that improvements, in particular with regard to cloud ice, were insufficient to justify further study of microphysical perturbations with these configurations. It is hence concluded that the 1.6-km grid spacing is a good compromise between resolution and computational costs. The general model setup was introduced in Chapter 4.1 and the observational data, used for comparison, was presented in Chapter 4.2.

5.1 Aerosol Constraints

The phase partitioning of a cloud is highly dependent on the microphysical parameterisations. The CCN constraint applied was presented in Chapter 4.1.

We hypothesise that the INPs must be adequately represented so as not to overestimate the impact of heterogeneous ice nucleation on ice clouds at low temperatures. Similarly, the INP species active at higher temperatures need to be included to achieve a mixed-phase state at warmer, but sub-zero, temperatures. The ways ICON parameterise the immersion freezing are outlined in Ch. 3.2.2. In the 6 km simulation, using a 1-moment microphysics scheme, the ice crystal number concentration is simply parameterised by an exponential function depending on temperature (1-moment curve in Fig. 5.1 by Cooper et al. (1986)) while in the 2-moment microphysics scheme, the immersion freezing is explicitly used as a nucleation routine. Figure 5.1 shows these two parameterisations where in the 2-moment microphysics we use the parameterisation by Hande et al. (2015). The measured INP concentration during these three days is plotted therein.

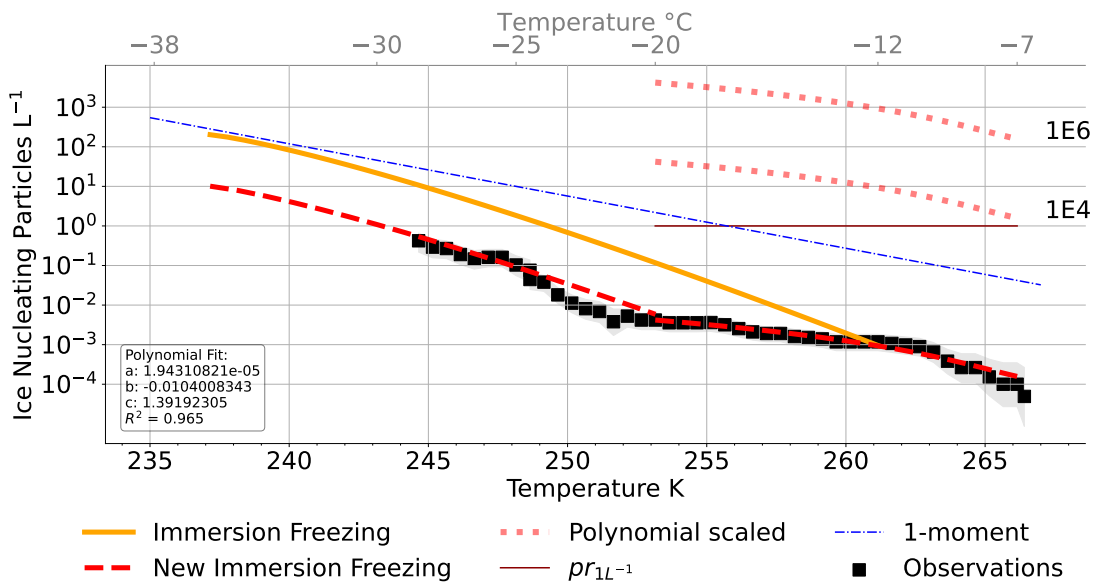


Figure 5.1: Ice nucleating particle concentration (L^{-1}) plotted against temperature. The immersion freezing parameterisation by Hande et al. (2015) is marked with solid orange and the observational data set (Creamean et al., 2022) in black squares with its confidence intervals indicated in shading. The observationally constrained parameterisation is shown (dashed red) where at temperatures below $-20^{\circ}C$ the original immersion parameterisation is scaled down by 0.05 while at high temperatures $-20^{\circ}C < T < -7^{\circ}C$ a polynomial fit to the observational data is used with parameters indicated in the box. Perturbations to the warm INPs are shown (small dotted red) marked with $1E4$ and $1E6$ and a prescribed $1 L^{-1}$ in solid red. The 1-moment cloud ice parameterisation by Cooper (1986) is shown in dashed blue. The figure is reprinted from Wallentin et al. (2024) under the CC BY licence.

Large discrepancies between the observed INP and the current parameterisation can be seen. At cold temperatures, the INPs are overestimated by the parameterisation by more than one order of magnitude while at warmer temperatures ($T > -12^{\circ}C$), the model does not have active nucleation whereas the observed INP concentration reaches $10^{-3} L^{-1}$. We thus constrain the three heterogeneous freezing parameterisations;

deposition nucleation, immersion freezing and rain freeze. These parameterisations act at different temperatures as specified in Ch. 3.2.2. At cold temperatures, ($T < -20^\circ\text{C}$), all three are active and are thus scaled similarly. A factor of 0.05 is applied to the parameterisations for rain freeze, deposition nucleation and immersion freezing, following the comparison to the observational values of INPs (see Fig. 5.1) at these temperatures ($T < -20^\circ\text{C}$). At warmer temperatures, ($T > -20^\circ\text{C}$) only immersion freezing and rain freeze may be active. To better represent warm mixed-phase clouds we adjust the immersion freezing parameterisation and add INPs at high temperatures ($-20^\circ\text{C} < T < -7^\circ\text{C}$), fitting a second-order polynomial to the observed INP. Rain freeze is, however, kept scaled down for all temperatures to limit the impact of the increased rain production for scaled CCN concentrations. INPs activating as immersion nuclei at temperatures above (below) -20°C will from now on be called warm (cold) INPs. To summarise, the parameterisations for deposition nucleation and rain freeze are scaled down throughout their active temperature range while immersion freezing is treated differently for cold (scaled down) and warm (fitted polynomial) temperatures.

Sensitivity Studies Performed

Sensitivity studies have been performed to investigate whether the above-mentioned constraints are appropriate. These are tabulated in Table 5.1. The perturbations are applied to the nest with a grid spacing of 1.6 km, initialised and updated through the boundaries with the output from the 6 km simulation.

Name	INP	CCN	SIP	Day
1.6km	original			1st & 3rd
INP	constrained			1st & 3rd
pr_{1L-1}	1 L^{-1} at warm T			1st & 3rd
$pr_{1L-1} + \text{CCN}$	1 L^{-1} at warm T	0.1		3rd
INPx1E4	constrained + warmx1E4			3rd
INPx1E6	constrained + warmx1E6			3rd
1.6km + SIP	original		BR & DS	3rd
SIP	constrained		BR & DS	3rd
SIP scaled	constrained		BR scaled & DS	3rd
$pr_{1L-1} + \text{SIP}$	1 L^{-1} at warm T		BR & DS	3rd
INP+CCN+SIP scaled	constrained	0.1	BR scaled & DS	3rd

Table 5.1: Sensitivity simulations on the 1st and 3rd of September 2020 at 1.6 km grid spacing. BR and DS signify the SIP breakup upon collision and droplet shattering respectively while rime splintering is included in all simulations. "Warm" refers to the temperature range $-20^\circ\text{C} < T < -7^\circ\text{C}$. For more details please refer to the text.

Sensitivity tests on the immersion freezing include the constrained parameterisation introduced above named "INP" in Table 5.1 and further scalings to the polynomial fit

at warm temperatures, these are indicated by "warm" in the table. A factor of 1E4 and 1E6 is applied to the polynomial, increasing the immersion freezing at temperatures between $-20^{\circ}\text{C} < T < -7^{\circ}\text{C}$. Furthermore, a prescribed INP concentration of 1 L^{-1} ($pr_{1L^{-1}}$ simulation) has also been applied for a uniform immersion nuclei concentration at "warm temperatures" of $-20^{\circ}\text{C} < T < -7^{\circ}\text{C}$. Meanwhile, at cold temperatures the heterogeneous processes are scaled down (by 10^{-3} , effectively to zero), this setup is further studied with a CCN scaling to explore the sensitivity to cloud droplet activation ($pr_{1L^{-1}} + \text{CCN}$).

Secondary ice processes are also explored through various SIP simulations. The five SIP simulations tabulated include droplet shattering and collisional breakup (with all simulations including rime-splintering). For the breakup upon collision mechanism, we apply the parameterisation by Takahashi et al. (1995) and further explore the diameter scaling introduced in Ch. 3.2.2. The first SIP simulation is performed with the original primary ice parameterisations (1.6km + SIP). Three other SIP setups are performed using the new INP parameterisation for primary ice production (SIP, SIP scaled, INP+CCN+SIP scaled). This includes the SIP addition on the constrained INP simulation (SIP simulation) and a similar setup with a diameter scaling within the breakup routine (SIP scaled). We further explore a CCN scaling to this setup (constrained INP and scaled breakup upon ice-ice collisions) to explore the impact of large supercooled droplets on the droplet shattering mechanism (INP+CCN+SIP scaled). To be emphasised here, the droplet shattering mechanism is tuned down due to the tuning of the rain freeze mechanism, where the droplet shattering is implemented. To investigate the primary ice impact on SIP we further use a prescribed INP concentration of 1 L^{-1} (at $-20^{\circ}\text{C} < T < -7^{\circ}\text{C}$) and apply the Takahashi et al. (1995) breakup parameterisation ($pr_{1L^{-1}} + \text{SIP}$).

5.1.1 Case Description

The 1st to the 3rd of September 2020 (from now on called the 1st, 2nd, and 3rd), during the MOSAiC campaign, were chosen to investigate two different multilayer cloud systems. On the 1st, a high ice cloud overlaying a mixed-phase boundary layer cloud can be seen in Fig. 5.2a showing the derived LWC and IWC products from Cloudnet (Engelmann et al., 2023). The 2nd comes with a shallow lower layer and a shorter mixed-phase cloud overlapping. On the 3rd, a double-layered system can be seen in the lowest kilometre of the atmosphere with some sporadic third layers (around 2-4 km). Crosses (circles), in Fig. 5.2a, mark the cloud base (top) for each layer identified using the MLC algorithm (Chapter 4.2.3) by Vassel et al. (2019). This algorithm uses radiosonde data and radar input to determine if a profile contains multiple layers (see Sect. 4.2.3) and can distinguish cloud layers remarkably well. Discrepancies may be due to drifting radiosondes and precipitation (falling ice crystals), which complicates the determination of cloud boundaries.

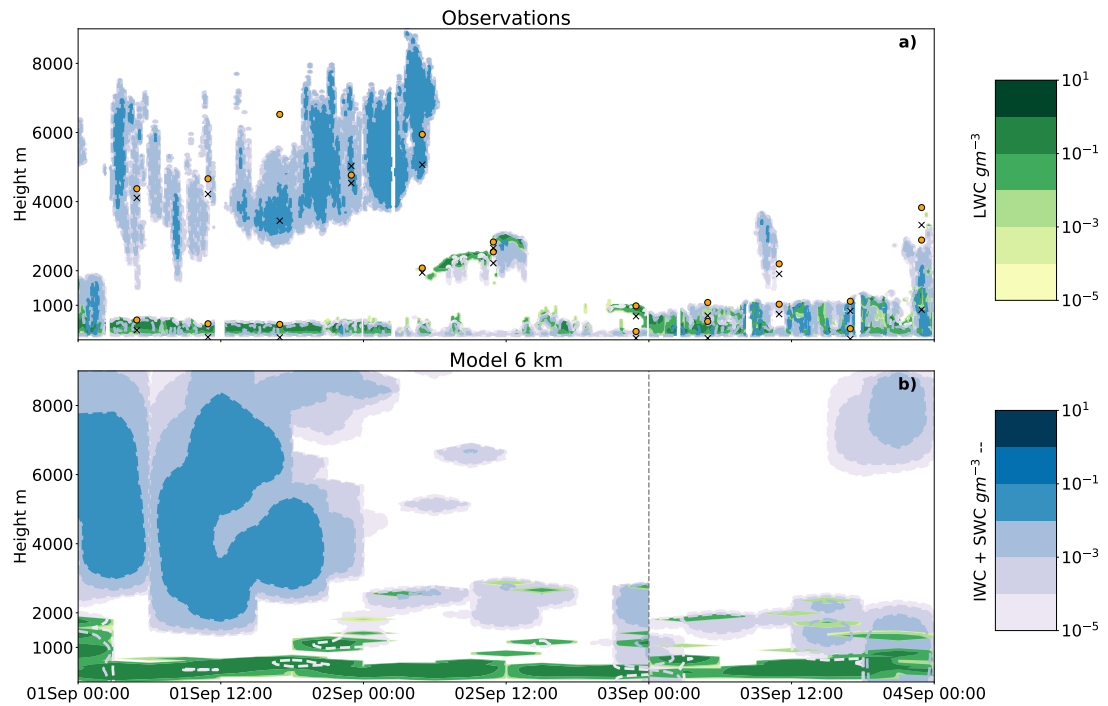



Figure 5.2: 3-day case study in September 2020, with the liquid water mass content (green) and cloud ice water mass content (filled contours in blue and dashed outlines). (a) 10 min observational mean, (b) 3-hourly model output at 6 km grid spacing, here also the snow water content from the model is included. The vertical line partitions the two simulations performed. Crosses (circles) in (a) mark the cloud base (top) for each layer identified using the MLC algorithm by Vassel et al. (2019). The missing circle on the 2nd at 00UTC exceeds the plotted region. The figure is reprinted from Wallentin et al. (2024) under the  licence.

Synoptic Situation

The synoptic situation from the model output at 00UTC on the 1st can be seen in Fig. 5.3. Temperatures are usual for the time of the year with the sea ice temperature locked to 273 K due to the melting of the sea ice and mean sea level pressure is shown in contours. To understand air mass origin, 10-h backward trajectories are calculated with LAGRANTO (Wernli and Davies, 1997; Sprenger and Wernli, 2015) based on hourly 3D wind fields from the 6 km simulation. Trajectories are initialised hourly between 10 UTC and 12 UTC near the ship location every 6 km within 114°E - 120°E and 88.3°N - 88.5°N on the 1st and within 118°E - 120°E and 88.5°N - 89°N on the 3rd. Vertical trajectory starting positions are set to every 250 m in the lowest 2 km, every 500 m between 2 to 7 km height, and finally every 1 km up to 10 km height. Back trajectories initialised at 12 UTC on the 1st (Fig. 5.3) show upper-level air parcels moving faster towards the ship compared to the < 4 km trajectories, which spend more time over the pack-ice. Interestingly, on the 3rd air parcel trajectories below 2 km height move faster and originate from further away than trajectories at higher altitudes, which is likely related to the presence of low-level jets (López-García et al., 2022). Low-level

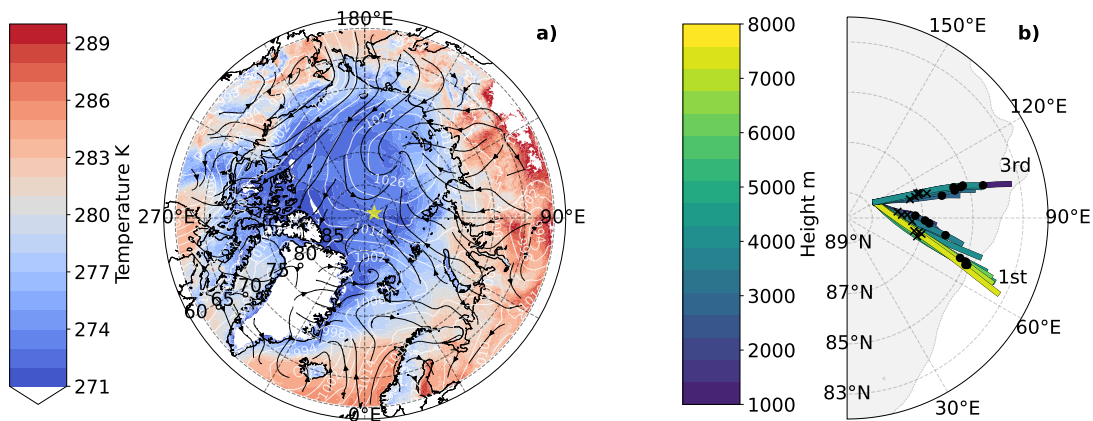



Figure 5.3: (a) Modelled synoptic situation on the 1st September. Mean sea level pressure contours are marked in white with wind streamlines (black arrows) showing the relative magnitude and direction of the wind at 10 m. The filled contours show surface temperature. The average daily location of the ship is shown with a star (*) (1st; 88.3°N, 117°E, 3rd; 88.7°N, 120°E). (b) Back trajectories initialised at the daily average ship location at 12 UTC for the 1st and 3rd of September, the dates are marked at the end of the trajectory cluster. Colours indicate the height at which the back trajectory is initialised and crosses (dots) mark 8 UTC (4 UTC). For the 3rd, only trajectories initialised at 4 km or lower are shown because of the low clouds simulated. Additionally, the extent of the sea ice concentration (>15%) is shown with a grey contour. The figure is reprinted from Wallentin et al. (2024) under the  licence.

winds, with magnitudes in the lowest km of up to 15 ms^{-1} , primarily flow towards the ship location from the Siberian coast, shifting from approximately parallel to the 70°E meridian on the 1st to 100°E meridian on the 3rd.

5.2 Evaluating the Coarse Simulations of MLCs

A first reference simulation is performed at 6 km grid spacing to evaluate the model against observations. Although a side-by-side comparison is difficult due to differences in spatial and temporal output, general features can be assessed. Figure 5.2 showed a time-height cross-section from an Eulerian perspective. The water content derived from the observations (Fig. 5.2a) can be compared to the model output (Fig. 5.2b). The model runs from 00 UTC on the 1st of Sept until 00 UTC on the 3rd. Another simulation is then initialised at 00 UTC on the 3rd to prevent the model from deviating too far from the global analysis. The first 6 hours are considered spin-up and are not included in mean state analyses but are shown here for initialisation comparison. The mean state is calculated for grid points within a radius of 15 km of the ship to account for the daily drift of the ship and spatial variability. Overall, the location and timing of cloud formation in the simulation agree well with the observations. The boundary layer cloud on the 1st is well represented, although the phase is predominantly liquid, unlike the observed mixed-phase character. The large vertical extent of the upper cloud on

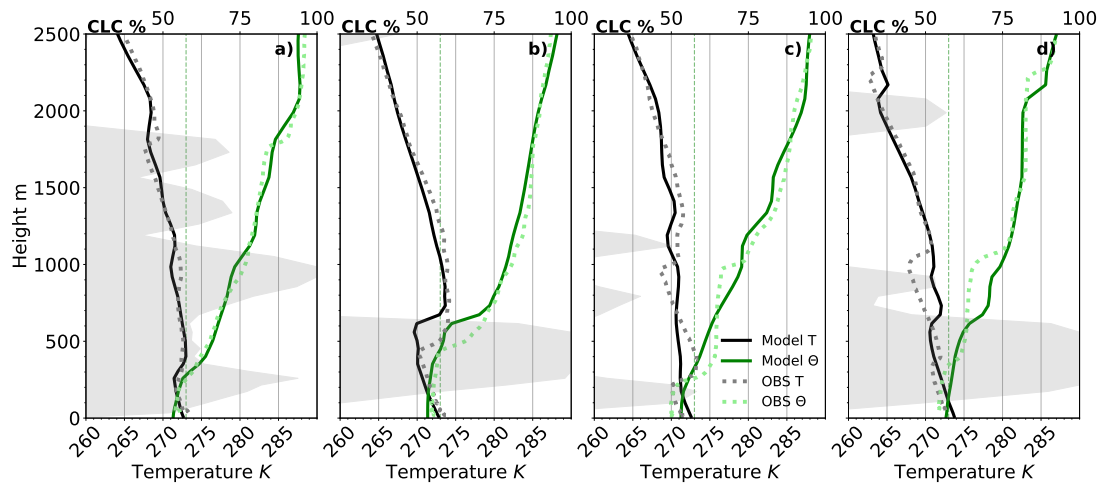


Figure 5.4: Vertical profiles of the lowest layer(s) for temperature (black), potential temperature (θ) (green), and the modelled cloud cover (CLC) (contours in temperature plot) signifying the cloud layers. (a) 1st at initialisation time 00UTC, (b) 1st at 12UTC, (c) 3rd at initialisation time 00UTC, and (d) 3rd at 12UTC. The observational data (in dots) are from the radiosondes (Maturilli et al., 2022b) and the model data (solid lines) are the 6 km grid spacing simulation, averaged over two grid cells within the 15 km radius of the daily average ship position. The dotted vertical line marks 273 K. The figure is reprinted from Wallentin et al. (2024) under the licence.

the 1st may be the result of sparse vertical levels at altitudes above 7 km together with a lack of precipitation formation (few sinks). Moisture profiles compare well with the observations (Fig. A.5a-b). During the 2nd, the cloud layers are less persistent in the model compared to the observations but the layers are captured at adequate heights. Due to the brief overlap of the cloud layers, this day will not be further studied in this chapter, it is, however, studied further in regards to its radiation interaction in Chapter 6. On the 3rd, two layers of clouds are simulated, one at around 600 m and the second at approximately 2 km. The lower layer cloud is well constrained to the boundary layer but liquid dominated while the upper cloud is placed 1 km higher than the observations. In general, the 6 km simulation accurately represents the clouds but falls short in representing the phase partitioning. Constraints have been implemented in the microphysical parameterisations to address this issue (see next section).

The placement of these layers depends on the initialisation of the model. DWD assimilated the radiosondes from MOSAiC including the temperature, wind profiles, and relative humidity. However, data assimilation is a difficult field and capturing a perfect vertical thermodynamic profile is challenging. On the 1st (Fig 5.4a), the model quite accurately captures three low-temperature inversions (at 300 m, 1000 m, and 1800 m) and correctly predicts the loss of the upper two in favour of a persistent layer at 600 m in the 12UTC radiosonde profile (Fig. 5.4b). The 3rd (Fig. 5.4c) is initialised with a smoother profile than observed and inversions are less accurately captured. The temperature profile at 12 UTC on the 3rd (Fig. 5.4d) deviates quite radically

from the observed radiosonde profile. ICON is found to place inversions too high in comparison with observations, a similar error has been found to be due to excessive vertical mixing in the European Centre for Medium-Range Weather Forecasts (ECMWF) Integrated Forecast System (IFS) model (Sandu et al., 2013). Moisture content and relative humidity with respect to liquid water are shown in Fig. A.5 for completeness. Subsequent high-resolution simulations (see Appendix A.1) do not improve on the main layering (some spurious intermittent layers may occur with higher vertical resolution), as this is mostly governed by the initial state.

5.3 Microphysical Sensitivity Simulations

5.3.1 1.6 km Simulations for 1st of September

The 1st of September 2020 is further simulated with a higher resolution nest at 1.6 km, where the boundary conditions (and initialisation) are provided with input from the 6 km simulation. We make use of the 2-moment microphysics and aerosol constraints laid out in Chapter 5.1. The high-resolution simulation, similarly to the 6 km simulation, produces a thick ice cloud and a fully liquid lower layer, found at a temperature just below 0°C. A vertical cross-section of hydrometeors with time is shown in Fig. 5.5 for the original setup at 1.6 km (Fig. 5.5b) and the simulation with constrained INP (Fig. 5.5c). Compared to the observations (Fig. 5.5a), the model in its original setup produces too much ice in the upper layer while the lower layer is dominantly liquid compared to the observational mixed-phase character (mostly visible in Fig. 5.2).

With the INP constraint at cold temperatures (including the reduction of immersion freezing, deposition nucleation and rain freeze) and additions to the immersion freezing routine for warm INPs, surprisingly, no large impacts can be seen (Fig. 5.5c). The upper layer shows small changes due to the scalings of the heterogeneous parameterisations. A reduction in INPs (at cold temperatures above 4 km, see Fig. 5.6e) induces small reductions in ice mass concentration in the upper levels of the upper cloud (above 4 km). This amounts to a time-averaged (10 UTC-12 UTC) reduction by a factor of 0.5 in the ice mass concentration (Fig. A.4c). In the lower levels of the upper cloud (at warmer temperatures), an increase is noted. The time-averaged difference in the ice mass concentration amounts to an increase by a factor of 1.4. The ice number concentration for the INP simulation across the upper layer is decreased by a factor of 8 and reaches a maximum value of 0.4 L^{-1} (Fig. A.4d). The lower layer is unaffected by the changes due to its relatively warm temperature (Fig. 5.4a,b). Prescribing INPs at 1 L^{-1} , ($pr_{1L^{-1}}$, Fig. 5.5d), effectively increasing the immersion freezing at the bottom of the upper layer while reducing INPs at colder temperatures, renders similar cloud features with the largest difference being the increase in precipitation during 10 UTC-12 UTC.

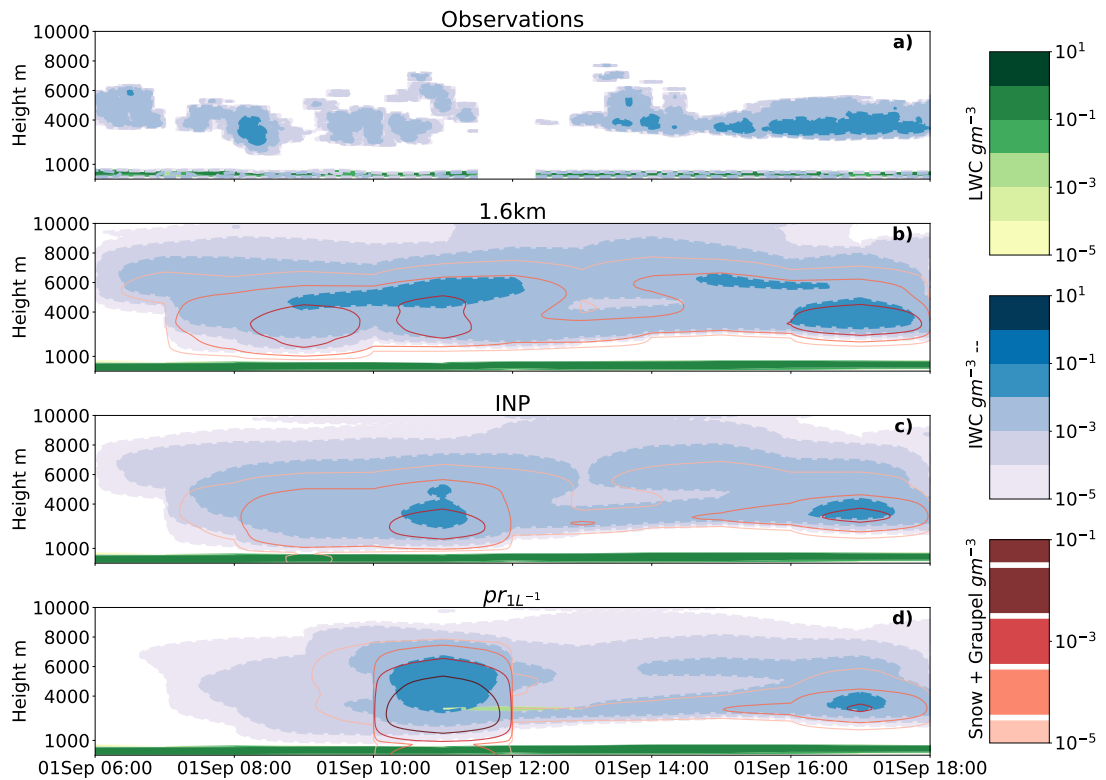


Figure 5.5: Vertical cross-section on 1st September 2020, with the liquid water mass content (green) and cloud ice water mass content (filled contours in blue and dashed outlines) in (a) 10 min observational mean together with (b) reference simulation, hourly model output at 1.6 km grid spacing, (c) the constrained INP simulation, and (d) the prescribed $1L^{-1}$ INP at warm temperatures. Additional model parameters shown are the graupel and snow mass content in red (solid lines). The figure is reprinted from Wallentin et al. (2024) under the [CC BY](https://creativecommons.org/licenses/by/4.0/) licence.

The ice number concentration for the $pr_{1L^{-1}}$ simulation reach a maximum value of $25 L^{-1}$ (Fig. A.4d). A decrease in ice number concentration below 4000 m together with an increase in ice mass concentration (Fig. A.4c) shows the impact of increased vapour deposition (Fig. 5.6c) onto cloud ice rendering larger particles capable of efficient aggregation into snow. Ice-ice collisions result in particles assigned to the snow category, while ice-snow collisions aggregate into larger snow particles (Fig. 5.6f). The snow produced in the lower part of the upper cloud seed the lower cloud but not efficiently enough to glaciate or strengthen it. The snow particles seemingly fall through the lower layer with negligible interactions (Fig. 5.5d). Due to its warm cloud top temperature, the lower layer may only become mixed-phase with the presence of seeding, however, glaciation is also inefficient at these high temperatures. We do not observe local seeding in the observations and we must assume that previous seeding of the lower layer has occurred and that we are unable to recreate this with the perturbations performed here. Due to its high temperature, further studies on primary and secondary ice processes in the lower cloud layer are deemed redundant.

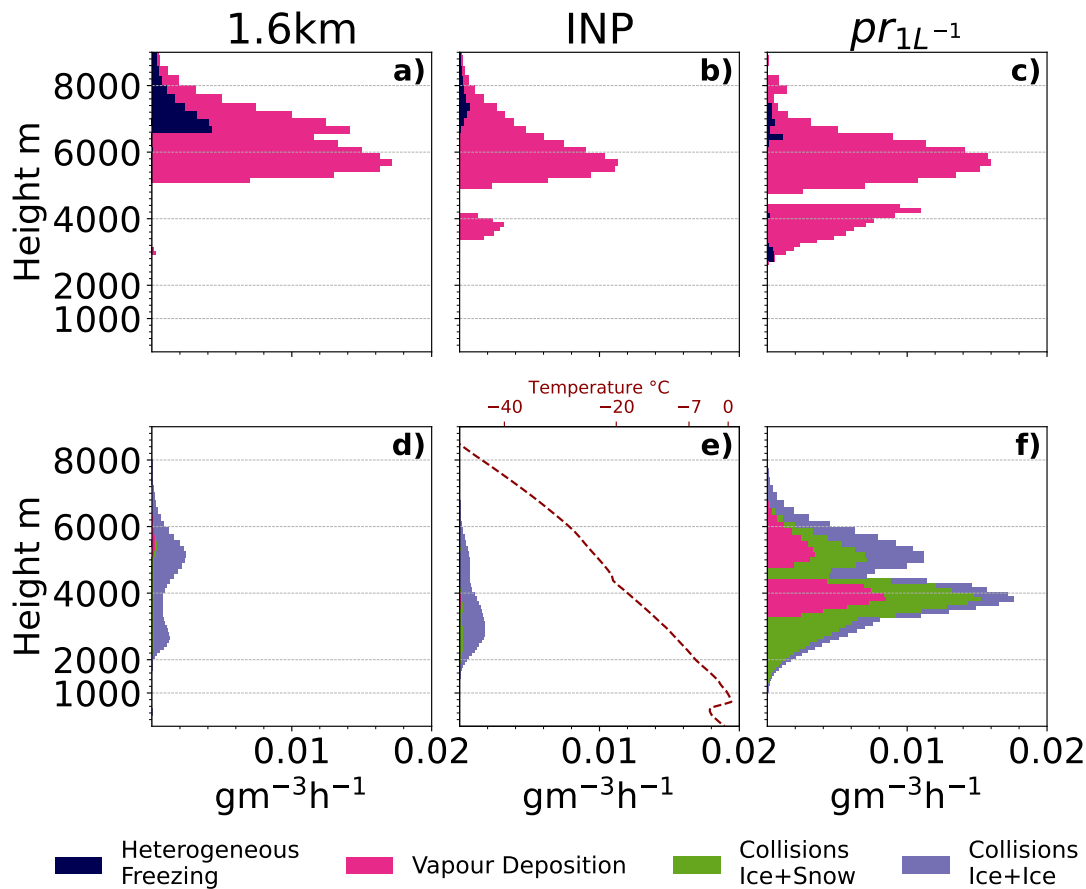


Figure 5.6: Microphysical process rates hourly accumulated during the simulation and here taken as a mean between 10-12UTC on the 1st of September. a-c) show processes for cloud ice, and d-f) for snow. Colours correspond to the various process rates defined in the legend. Collisions lead to aggregation where ice+ice and ice+snow give snow aggregates. Additionally, a temperature profile is provided in (e) to more easily distinguish between temperature regions of cold ($T < -20^{\circ}\text{C}$) and warm ($-20^{\circ}\text{C} < T < -7^{\circ}\text{C}$) INP scalings within the parameterisations for primary ice production. The figure is reprinted from Wallentin et al. (2024) under the licence.

5.3.2 1.6 km Simulations for 3rd of September

The 3rd of September 2020 is also simulated at a higher grid spacing of 1.6 km using the 2-moment microphysics. The time-height contours of the 3rd are shown in Fig. 5.7, where the reference at 1.6 km (Fig. 5.7b) and the constrained INP simulation (Fig. 5.7c) are shown together with the observations.

As previously discussed, the model layers the clouds at the wrong heights, but more striking is the lack of ice in the model. At a mean cloud-top temperature of -8°C (Fig. 5.4d), the only primary ice parameterisation active in the reference is rain freeze, however, the addition of warm INPs (Fig. 5.7c) does little to increase the ice mass concentration. Blue contours marking the cloud ice mass concentration can be seen to only slightly increase (mostly just after 06 UTC) when including warm INPs.

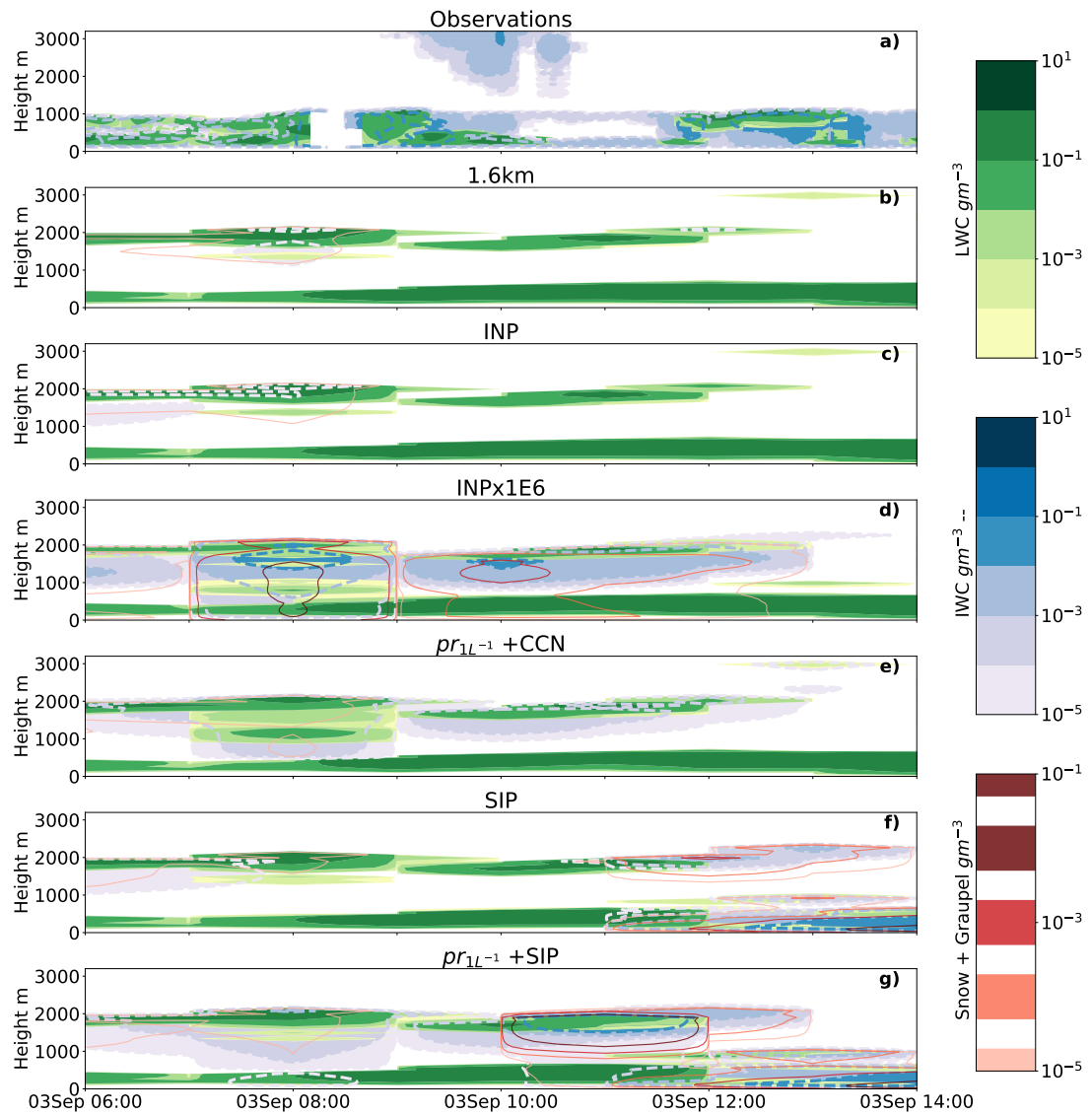


Figure 5.7: Time height plot of hydrometeors from the 3rd of September with liquid water mass content (green) and cloud ice water mass content (filled contours in blue and dashed outlines). (a) Observations 10 min mean, (b) reference simulation, (c) INP constrained simulation, (d) warm INP perturbation by 10^6 , (e) a prescribed INP concentration of $1L^{-1}$ at warm temperatures combined with a CCN scaling of 0.1, (f) SIP using the same primary ice nucleation as the INP simulation with added droplet freezing and shattering and breakup upon ice-ice collisions, (g) prescribed INP at $1L^{-1}$ with added droplet freezing and shattering and breakup upon ice-ice collisions. Additional model parameters are the snow and graupel mass content in red (solid line). For clarification on the perturbations please refer to the text and Fig. 5.1. The figure is reprinted from Wallentin et al. (2024) under the licence.

Time-averaged (06 UTC-12 UTC) maximum ice mass concentration increases by a factor of 1.5 (for vertical profiles see Fig. A.2d). This small impact does not reach the observed levels of ice. Thus, we explore the scalings of the primary ice parameterisations in the model. Multiplying the warm INP polynomial (Fig. 5.1) by $1E4$ (Fig. A.1a) and $1E6$ (Fig. 5.7d), give rise to more similar values to the observations. These are very extreme

scalings, but as the observed INP concentration is low, this gives INP concentrations between $1\text{-}100\text{ L}^{-1}$, on the upper end in midlatitudes and very high for Arctic clouds (Porter et al., 2022; Raif et al., 2024). With this high INP concentration, the ice number concentration increases as well. Time-averaged (06 UTC-12 UTC) maximum ice number concentrations in the upper cloud layer reach 0.22 L^{-1} and 6.7 L^{-1} for the INPx1E4 and INPx1E6 simulations respectively (Fig. 5.9e). This is compared to 0.0008 L^{-1} for the INP simulation (Fig. 5.9e), an increase of more than two and almost four orders of magnitude respectively. However, irrespective of this substantial increase in ice number concentration, these values do not necessarily lead to the glaciation of the cloud, as seen here and in previous studies (Stevens et al., 2018; Solomon et al., 2018).

As a scaling of 1E4 to 1E6 is needed to create appreciable ice content in the clouds we further explore a prescribed INP concentration at warm temperatures of 1 per L ($pr_{1L^{-1}}$). The prescribed INP compare well with the 1E4 scaling, with slightly lower values for cloud ice (Fig. A.1c). To investigate the impacts of the cloud droplet activation on the too-thick modelled liquid layer, a sensitivity experiment with a decreased cloud droplet activation rate ($pr_{1L^{-1}} + \text{CCN}$) is performed (Fig. 5.7e). The cloud structure changes during 07 UTC -09 UTC where the presence of a third layer is evident, similar to the INPx1E6 simulation.

To better compare with the observed values we look at the column integrated values where we include graupel and snow together with ice in a frozen water path (FWP) category. Figure 5.8 shows the time-averaged (06 UTC-12 UTC) FWP vs LWP.

The large underestimation (more than two orders of magnitude) of FWP in the 1.6 km simulation (circle in Fig. 5.8) compared to observed values (diamond) is quite evident while the LWP is approximately four times too high in the model. The small change using the new INP parameterisation (INP simulation, square) gives an increase in FWP with a preference for cloud ice. The prescribed INP simulation ($pr_{1L^{-1}}$, tilted cross) looks similar in the contours to the 1E4 scaling (right-pointing triangle) but gives a three times lower FWP. This corresponds nicely to the almost three times lower INP concentrations for the prescribed INP simulation at minimum cloud-top temperatures (about -9°C).

As expected with a lower CCN concentration ($pr_{1L^{-1}} + \text{CCN}$, tilted hexagon), we see an increase in rain (colour bar of Fig. 5.8a). With a lower activation rate of CCN, the cloud droplets may grow to larger sizes due to less competition for vapour and convert more efficiently to rain through autoconversion. With the presence of more cloud liquid, due to the presence of a third cloud layer (Fig. 5.7e), condensation increases due to the saturation adjustment within this layer (Fig. A.2e) and the resulting impact of the CCN scaling is small. When reducing the CCN by a factor of 10, the LWP only drops by a factor of 1.28. The presence of the sub-cloud layer with adequately large cloud droplets that may convert into rain increases the riming rate and the possibility of rime-splintering,

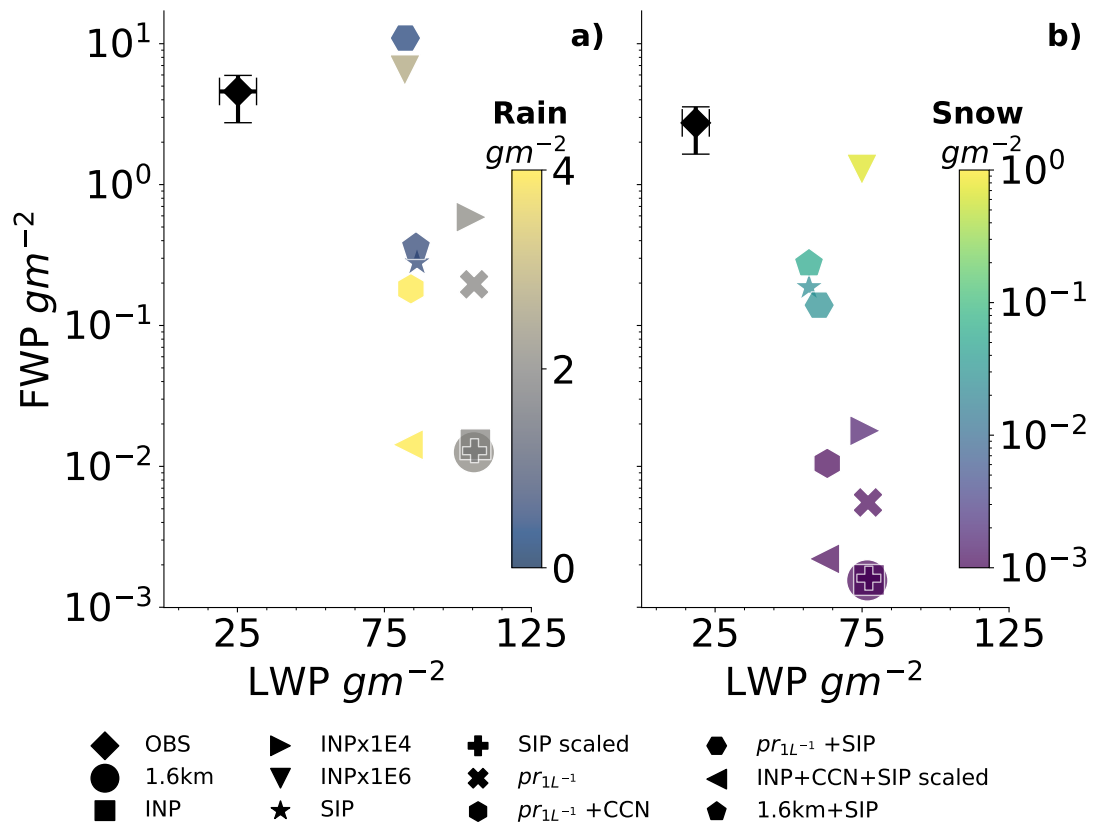


Figure 5.8: Frozen hydrometeor water path (FWP) the vertically integrated sum of cloud ice, snow, graupel and hail, over liquid water path (LWP) for all perturbations on the 1.6 km resolution on the 3rd of September between 06UTC-12UTC,. (a) The column integrated FWP vs LWP with colours indicating the precipitation contribution from the rain in gm^{-2} . The observations are integrated up to 1.1 km to exclude the upper ice cloud during this time. (b) FWP and LWP are integrated over the modelled lower layer with an imposed upper threshold at 750 m. The colour bar in (b) shows the snow falling from the lower layer (graupel is negligible). The figure is reprinted from Wallentin et al. (2024) under the licence.

granted the cloud exists within the temperature range of $-8^{\circ}C < T < -3^{\circ}C$. Thus graupel forms and seeds the lower layer. The increase in the mass-accumulated riming rate of graupel can be seen in Fig. A.6q and the small impact from rime-splintering in Fig. 5.9b. These processes are not strong enough to glaciare the lower layer, nor any classical seeder-feeder impacts can be seen. Compared to the pr_{1L-1} simulation (Fig. 5.8, tilted cross) no impacts on the FWP can be seen, indicating that the CCN scaling and the increase in the riming of graupel do not impact the column integrated values, thus the negligible impact on the lower layer may be expected. In terms of droplet number concentration, time-averaged (06 UTC-12 UTC) maximum values reach 40 cm^{-3} for the pr_{1L-1} simulation while a reduction by a factor of three is noted for the $pr_{1L-1} + CCN$ simulation (Fig. A.2a).

The large scalings of warm INPs (INPx1E4 and INPx1E6) thoroughly increase the FWP, however highly non-linearly with a 40 (450) times increase between INP and

INPx1E4 (INPx1E6). Here, we notice that the lack of glaciation in Fig. 5.7d may not show the full story. When we look at the integrated values a 77% decrease in LWP in the upper layer between the 1.6 km and the INPx1E6 (down-pointing triangle) simulation can be seen, showing the WBF process in action together with an increase in riming by cloud droplets (Fig. A.6a-b). An increase in riming may be due to the sheer number of ice particles now present in the cloud.

Looking at the lower layer only, Fig. 5.8b, similar trends to the full integration can be seen with a next-to-none impact of simply adding the warm INPs (INP simulation). The scaling of warm INPs (simulations INPx1E4 and INPx1E6) both increase the FWP in the lower layer. As this layer is found at a temperature just below 0°C, this increase is due to seeding from above. An increase in precipitation from the lower layer can also be seen with the highest INP scaling (INPx1E6), where snow precipitation increases by three orders of magnitude, showing the seeder-feeder mechanism in play. Interestingly, the 1E4 scaling does not show a similar pattern of precipitation increase. Instead, this simulation shows only a large increase in ice mass concentration. Lower layer ice number concentrations (time-averaged between 06 UTC-12 UTC, Fig. 5.9e) reach values of 0.002 L^{-1} and 0.02 L^{-1} for the INPx1E4 and INPx1E6 simulations respectively. With a larger amount of ice crystals, they largely occupy the same space and increasing the number of ice crystals in the same volume makes collisions more likely (the collision process rates, where ice collides with ice or snow to form snow are shown in Fig. A.6g-h). Snow, with a larger size, tends to fall more readily and allows for seeding of the lower layer, explaining the larger amount of snow (and thus FWP) for INPx1E6 in Fig. 5.8.

5.3.3 Can the Lack of Cloud Ice be Explained by SIP?

Secondary ice processes may be the missing link between the observed INP concentrations and the frozen water path, which is underestimated by the simulations discussed so far. We investigate whether the required warm INP scaling of 1E6 detailed above could be replaced by a (potentially) more realistic pathway. On top of the rime-splintering already implemented in the reference, we add breakup upon ice-ice collisions as well as droplet freezing and shattering and investigate the impact of different INP concentrations available for primary ice production. With a mean cloud top temperature of -1.5°C (between 06 UTC-12 UTC) for the lower layer on the 3rd, two out of three SIP (collisional breakup and droplet shattering) may be active, while the upper layer at a mean cloud top temperature of -8.5°C, overlaps with the temperature range for all three (including rime-splintering).

Five simulations have been performed and are tabulated in Table 5.1. Three simulations explore the primary ice impact on the SIP where the INP concentration is changed from the original (1.6km+SIP) to the constrained primary ice production (SIP simulation), and finally, set to 1 per L ($pr_{1L^{-1}}$ + SIP). The final two simulations explore a scaled breakup parameterisation, using Takahashi et al. (1995) scaled by the colliding

particle diameters (Han et al., 2024). A CCN scaling is performed on top of this to explore its impact on the droplet shattering mechanism.

We start by exploring the impact of primary ice production on SIP. The SIP simulation (Fig. 5.7f) and the 1.6km+SIP simulation display comparable cloud structures and column-integrated values (Fig. A.1e, Fig. 5.8). The pr_{1L-1} +SIP shows similar features but with more pronounced ice mass concentration throughout the simulation. All SIP implementations almost fully glaciate the lower layer just after 12 UTC, some liquid persists while the upper layer dissipates similarly to the other experiments (Fig. 5.7a-e). Figure 5.9 shows time-averaged (06 UTC-12 UTC) process rates for secondary ice production (Fig. 5.9a-d). The full impact on cloud ice mass concentration is shown in Fig. 5.9a while Fig. 5.9b-d show the respective impacts on the cloud ice mass growth from rime splintering, droplet shattering, and breakup upon ice-ice collisions respectively. Ice number concentration is shown in Fig. 5.9e and the ice enhancement factor (IEF, see below) is shown in Fig. 5.9f. The maximum ice number concentrations, Fig. 5.9e, in the lower cloud layer reach 484 L^{-1} , 396 L^{-1} , and 156 L^{-1} for the 1.6km+SIP, SIP, and pr_{1L-1} +SIP simulations respectively.

The large increase in ice number concentration drives the increase in vapour deposition through the WBF process (Fig. A.6c,f,h) resulting in the glaciation of the lower layer. We find the breakup upon ice-ice collisions to be the dominant mechanism for this increase in ice number and mass concentrations (Fig. 5.9d). The major contributions are from small ice crystals colliding with snow or snow-snow collisions (crosses and circles in Fig. 5.9d). The ice-snow collisions are the most active in-cloud while snow-snow collisions dominate throughout the sub-cloud layer. The rime splintering and droplet shattering show only small contributions (Fig. 5.9b-c). The breakup upon ice-ice collision parameterisation is highly sensitive to temperature fluctuations and the sudden onset of glaciation through ice particles generated by SIP is due to a drop in temperature of the lower layer (not shown).

One of the main differences between the SIP and pr_{1L-1} +SIP simulations is the seeding seen with a higher baseline of INPs. The seeding into the lower layer, seen in Fig. 5.7g, has a surprisingly small impact on the cloud layer during the time window 06 UTC-12 UTC, referring back to Fig. 5.8b. The simulations with SIP implementations do not largely differ in LWP nor FWP in the lower layer, showing the lack of interaction with the falling hydrometeors from the upper layer. The initiation of seeding is explained by the higher collision rates as previously discussed for a larger amount of small ice crystals (Fig. A.6i,l). The mean hourly collisional rate increase between the pr_{1L-1} +SIP and pr_{1L-1} (without SIP) is five orders of magnitude while the difference between the INP and SIP simulations reaches six orders of magnitude. This increase in collisions increases the collisional breakup, especially between ice and snow and between small ice crystals, leading to a large contribution from this scheme (Fig. 5.9d).

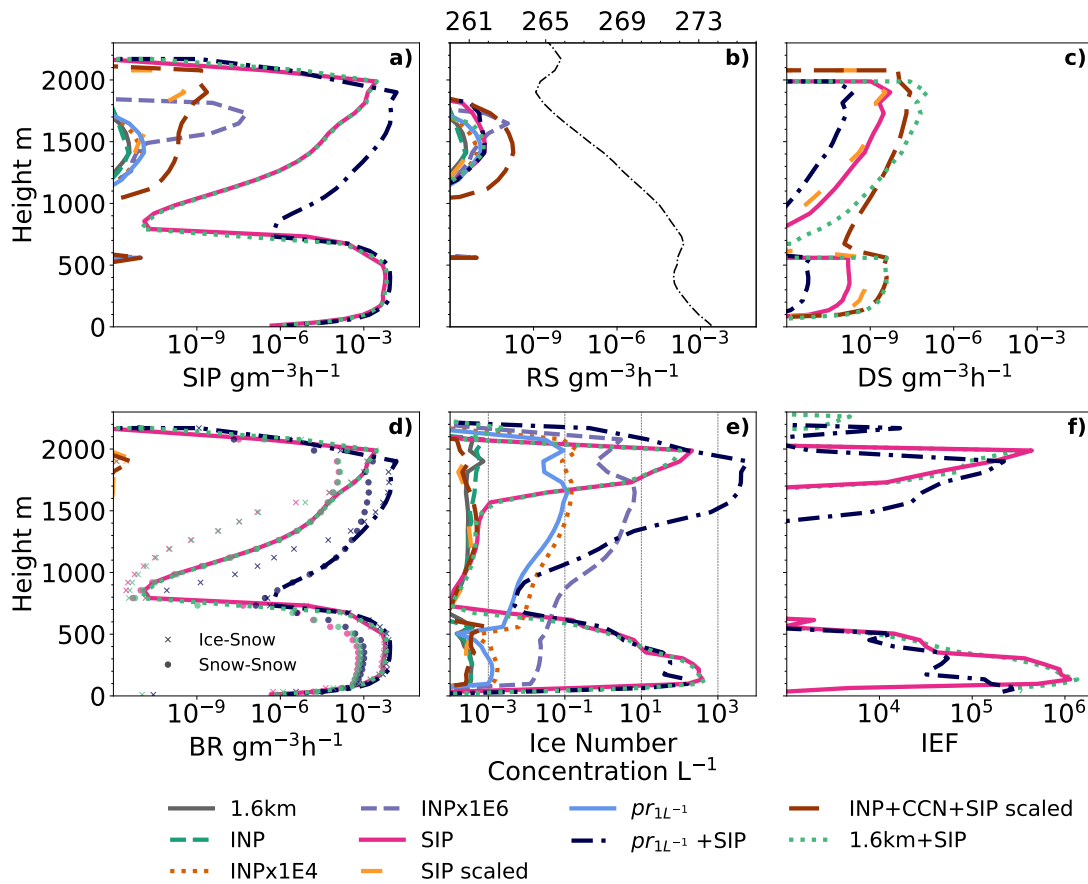


Figure 5.9: Average secondary ice production rates and ice number concentration shown for selected sensitivity studies on the 3rd of September 2020 between 06 UTC-12 UTC (before glaciation). (a) All SIP, (b) rime-splintering contribution, (c) droplet freezing and shattering, (d) breakup upon ice-ice collisions with the major contributions snow-ice collisions and snow-snow collisions marked in crosses and circles respectively. Panel (e) shows the ice number concentration used to calculate the ice enhancement factor (IEF) in panel (f). Panels (c) and (d) only show the five SIP simulations; 1.6km+SIP, SIP, SIP scaled, $pr_{1L^{-1}} + \text{SIP}$, INP+CCN+SIP scaled, wherein (d) the scaled SIP runs only show an impact at 1900 m. A temperature profile is added to panel (b) to distinguish the locations of the cloud layers.

We find that breakup upon ice-ice collision is the dominating SIP. To explore more realistic implementations of this we investigate the scaling of the breakup collision parameterisation (SIP scaled), to reduce the large increase in ice crystals forming from the collisions. We find that this scaling is too substantial and brings down the SIP impact to zero and no difference compared to the reference can be found (Fig. 5.8 and contours in Fig. A.1b). This might be due to very small frozen hydrometeor sizes that scale down this collisional rate too much or the lack of ice habit representation. A further study, using scaled breakup upon ice-ice collision, investigates whether scaling of the CCN concentration has an impact on the droplet shattering mechanism (INP+CCN+SIP scaled). This simulation is also shown in Fig. 5.8 (contours are shown in Fig. A.1d) and shows no large impact (on the frozen water path) from an increased droplet shattering

with larger droplets (Fig. 5.9b). Similarly to the $pr_{1L-1} + \text{CCN}$ simulation, a decrease in LWP is seen together with an increase in rain formation. A small rise in FWP can be seen in the lower layer (Fig. 5.8b) however, it is not substantial enough to impact the cloud phase further.

An ice enhancement factor, the increase in the number concentration of cloud ice due to SIP, can only be used for a constrained LES simulation where all ice within the domain has been formed during the simulation. Here, as we are dealing with a real setup, some of the cloud ice within the domain is supplied from the continuous advection of cloud hydrometeors through the domain boundaries. To gauge the impact of the SIP however, we may calculate the ratio between the simulations with and without SIP (apart from the rime-splintering which is included in all simulations but has a small impact) by N_{SIP}/N_{Ref} , where N is the number concentration of cloud ice and "SIP" and "Ref" refer to the simulation with and without SIP (with the same initial primary ice). We use maximum time-averaged (06 UTC-12 UTC) ice number concentrations (shown in Fig. 5.9e) to gauge the impact of SIP and calculate the ratio between SIP implementations and their respective reference. The average ice number concentration enhancement ratio, shown vertically in Fig. 5.9f, amounts to 10^5 for the lower INP simulations (1.6km+SIP vs 1.6km and SIP vs INP). For a larger initial INP concentration (pr_{1L-1}) the average ice enhancement is 10^4 . This indicates a higher efficiency of the addition of SIP for a lower initial primary ice, as previously seen in the LES simulations by Sotiropoulou et al. (2020).

5.4 Summary & Discussion

In this chapter, we investigate the microphysical sensitivity of Arctic mixed-phase multilayer clouds via the example of two cases observed during the MOSAiC campaign. Sensitivity simulations on cloud droplet activation, primary ice, and secondary ice processes were performed for two multilayer cloud systems in September 2020. The focus of this chapter is two-fold, 1) to show that multilayer clouds can be accurately modelled providing a ground for further analysis into how these cloud systems form and evolve, and 2) to evaluate the microphysical sensitivities, in particular, the primary ice production and its impact on secondary ice production (SIP), while constraining the parameterisations to the observed ground-based measurements to better represent cloud phase.

Using the ICON model, a nested setup is adopted and through our analysis, we find that high-resolution (grid spacing finer than 1.6 km) simulations do not substantially improve the representation of the clouds. However, we acknowledge that finer resolutions than the 100 m studied here may be beneficial for many purposes (such as detailed studies of entrainment and turbulence, and especially idealised studies). We set up our

model as a real case, with initial and boundary conditions from ICON Global 13 km analysis. The clouds are adequately represented in terms of vertical placement. However, during days when the local thermodynamic structure is not captured in the initial conditions, the model suffers from incorrectly placed cloud layers (vertical layering). The local structure and layering do not improve with higher resolution; these real-case setups suffer from carrying over large-scale biases in the initial and boundary conditions, which do not improve upon decreasing the grid spacing. Improvements in data assimilation may thus be crucial for accurately representing these clouds.

Switching from a 1-moment microphysics scheme to a 2-moment scheme facilitates comparisons with the real world, as the primary ice is represented using more explicit nucleation pathways. With the 2-moment microphysics and a 1.6 km grid spacing, we perform microphysical perturbations by constraining the model parameterisations with measured data. An immersion freezing parameterisation is created based on the surface-measured INPs to better represent the Arctic INP population. Accurate representation of these clouds is challenging and to adequately represent the observed ice mass concentration at warmer temperatures ($T > -19^{\circ}\text{C}$), large scalings to the measurement-constrained immersion freezing parameterisation are needed, amounting to a factor between $1\text{E}4$ - $1\text{E}6$, which corresponds to prescribed INPs in the range of 1 - 100 L^{-1} . We hypothesise that the addition of the measured INPs is still too low to initiate further ice-phase processes, such as growth by deposition, and a larger scaling is required to get a response. The seeder-feeder mechanism, whereby frozen precipitation falls into a lower layer, was found to occur in the simulation with the highest INP concentration ($\text{INP} \times 1\text{E}6$). Falling snow from the lower layer increases by three orders of magnitude compared to reference simulations.

As the model produced too much liquid water, a CCN scaling of 0.1 was performed. The reduction of CCN concentration results in an expected rain enhancement due to the formation of larger droplets. This has no further impacts on the cloud ice due to the low rates of riming. With a prescribed CCN concentration and relatively coarse horizontal grid spacing, capturing realistic cloud droplet activation is challenging. Prognostic aerosols using a dynamic aerosol model such as ICON-ART (Aerosol and Reactive Trace gases module) would improve the representation of the local CCN concentrations and provide a more realistic cloud droplet activation. Furthermore, accurate representation of updrafts ensures a more realistic simulation of cloud droplet activation, ultimately enhancing the overall predictability of cloud properties.

SIP has been investigated as these mechanisms are hypothesised to fill the gap in cloud ice number concentrations between models and observations. We find that the parameterisation for breakup upon ice-ice collisions (Sullivan et al., 2018) based on laboratory work by Takahashi et al. (1995) is very active, successfully glaciating the lower layer through the increase in small ice crystals and snow formation. This follows the findings by Sotiropolou et al. (2024) who show the dominance of collisional breakup

for modelled Arctic clouds. The maximum enhancement in the integrated cloud ice number concentration between simulations with and without SIP amounts to 10^4 - 10^5 , for a high and low initial INP concentration respectively. These factors are on the larger side but compare well to other Arctic studies that found ice enhancement up to 10^2 (Sotiropoulou et al., 2020) and 10^4 (Zhao et al., 2021). However, the enhancement from SIP is highly fluctuating with time, making a concrete analysis into whether or not the parameterisation is correctly representing the processes challenging. Scaling the breakup collision process by the particle diameter (Sotiropoulou et al., 2021; Georgakaki et al., 2022; Han et al., 2024) scales down the process such that no SIP impacts can be seen. Further sensitivity studies, such as scaling the pre-factor in the parameterisation for breakup upon ice-ice collisions, as other studies have done (e.g. Sotiropoulou et al., 2020; Dedekind et al., 2021) may tune the collisional breakup rates to avoid the complete glaciation. Here, we will settle on the possibility that breakup may be a missing factor in these cloud layers and that we may not have the parameterisations available to properly explain the discrepancies. Droplet shattering was shown by Pasquier (2022) to be the dominant SIP during their observational study on Svalbard. The negligible impact from the droplet shattering routine in this work may be due to the lack of adequate parameterisation. Improvements in the representation of cloud droplets and their freezing mechanisms might be crucial to better simulate the droplet freezing and shattering process. The dependency on initial INP concentration alludes to the misrepresentation of the INPs through our measurement-constrained parameterisation and we conclude that the developed immersion freezing parameterisation is inadequate to capture the observed cloud ice mass concentration. Secondary ice production combined with increased primary ice production is required to reach observed levels of ice.

In general, INP distributions are hard to capture with both models and with measurements (Burrows et al., 2022). Only ground-based measurements are available, which do not always correlate with INPs at cloud base (Creamean et al., 2021b), and this may be part of the explanation. Another aspect is the lack of INP recycling in the model, whereupon INPs in the sub-cloud layer, deposited by precipitating ice, can re-enter the cloud and activate with possible time-dependent freezing rates, which is important for Arctic mixed-phase clouds (Solomon et al., 2015; Fu et al., 2019).

6 | CASE STUDY ON THE RADIATIVE INTERACTIONS OF MULTILAYER CLOUDS

This chapter introduces other aspects of the case study presented in Chapter 5. Here, the focus is on the formation of a double-layered structure and the radiative interactions between MLCs. We further explore the hypothesis of a strong radiative cooling suppression of multilayer clouds over the entire domain of this case study (85°N- 90°N), to validate observational studies and to deepen our understanding of this mechanism.

The general setup of the model was introduced in Chapter 4. The specific setup adopted here is the pr_{1L-1} sensitivity study performed in Chapter 5, which encompasses warm-temperature INPs at a concentration of 1 L^{-1} between $-20^\circ\text{C} < T < -7^\circ\text{C}$. At colder temperatures, the original INP parameterisation is reduced by a factor of 10^{-3} . Detailed discussions on microphysics, cloud phase, and why the model cannot produce a low mixed-phase cloud during the 1st of September 2020 are covered in Chapter 5. The reason to use the quite high INP concentration present within the pr_{1L-1} simulation is to capture a larger cloud ice concentration at warmer temperatures such that mixed-phase clouds are present within the domain.

To study the split of a layer into two and to gauge the importance of radiation in this mechanism, we employ a radiative interaction approach called COOKIE (introduced in Chapter 4.1.1) where cloud layers are made transparent to radiation to study the impact on the layers themselves and the response on the other cloud layers present.

The mean state is defined here as the temporal and spatial mean over an area spanning a 7.5 km radius from the average daily ship location (88.5°N, 118°E).

6.1 COOKIE Setup

Three sensitivity studies are performed to investigate the radiative impact on the split of a double-layered cloud system. The COOKIE setup was introduced in Chapter 4.1.1. The radiative differences of the three sensitivity runs, sketched in Fig. 4.3, are shown in Fig. 6.1. The longwave radiative cooling (Fig. 6.1a-c) and shortwave heating (Fig. 6.1d-e)

can be seen to differ between the sensitivity runs as expected. The (vertical) location of the cloud mass (LWC+IWC) is shown in contours, showing the difference between the runs due to the cloud radiative impact being turned off in parts of the atmosphere. A clear cut-off at 1 km for panels b and e can be seen, signifying the radiation to be turned off above this (*Above Off* simulation). Panels c and f show the opposite behaviour (cloud radiative impacts turned off below 1 km, *Below Off* simulation). As expected, the shortwave heating plays a small role with about an order of magnitude lower heating rates than the absolute longwave radiative cooling of the clouds, even considering the simulations were performed in September during the polar day and thus the sun is still appreciably powerful with a clear-sky local maximum (at 04UTC) of about 120 Wm^{-2} . Due to the implementation of the COOKIE setup, no surface responses are taken into account with a change in CRH. The surface records the same cloud systems in the sensitivity studies as the reference and thus, no evaluation of the surface temperature impacts may be performed (only CRE within the atmosphere).

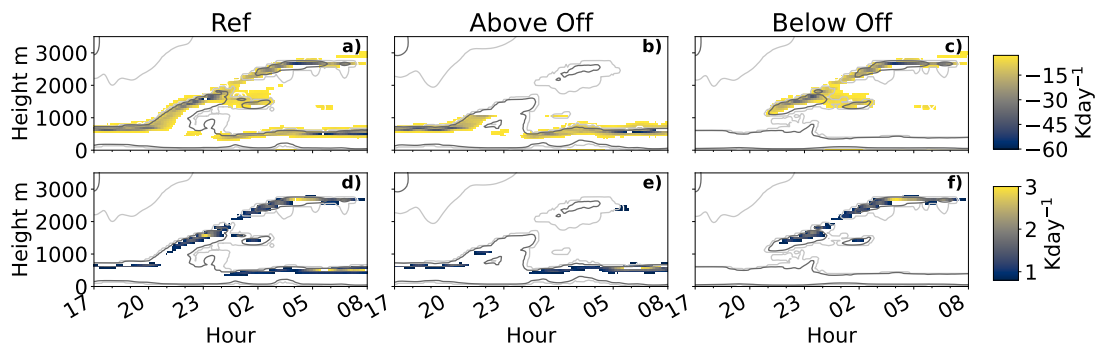


Figure 6.1: Cloud radiative heating (CRH) rates in K day^{-1} . Longwave radiative cooling (a-c) and shortwave heating (d-e) of the clouds for each sensitivity experiment. In the *Above Off* simulation, the cloud radiation interaction is turned off above 1 km while the opposite is true for the *Below Off* simulation. The (vertical) location of the cloud mass (LWC+IWC) is shown in contours.

6.2 Case Description

The simulated case study is shown in Fig. 6.2 along with the observations. The model captures the upper ice cloud as seen in the observations. However, the model overestimates the cloud thickness compared to the observations. The sparse model levels together with a moist upper troposphere seem to be the main reasons for this, this is further discussed in Chapter 5. The boundary layer is purely liquid compared to the observed mixed-phase state, which is also discussed in detail in Chapter 5. The most interesting part of this case is the split of the lower layer at 20UTC into two layers, of which the upper layer then quickly rises to form a stable mixed-phase cloud at 01UTC. In the observations, the split is not observed. The overall layering is quite accurately modelled, although the model forms the upper layers on the 2nd earlier than observed.

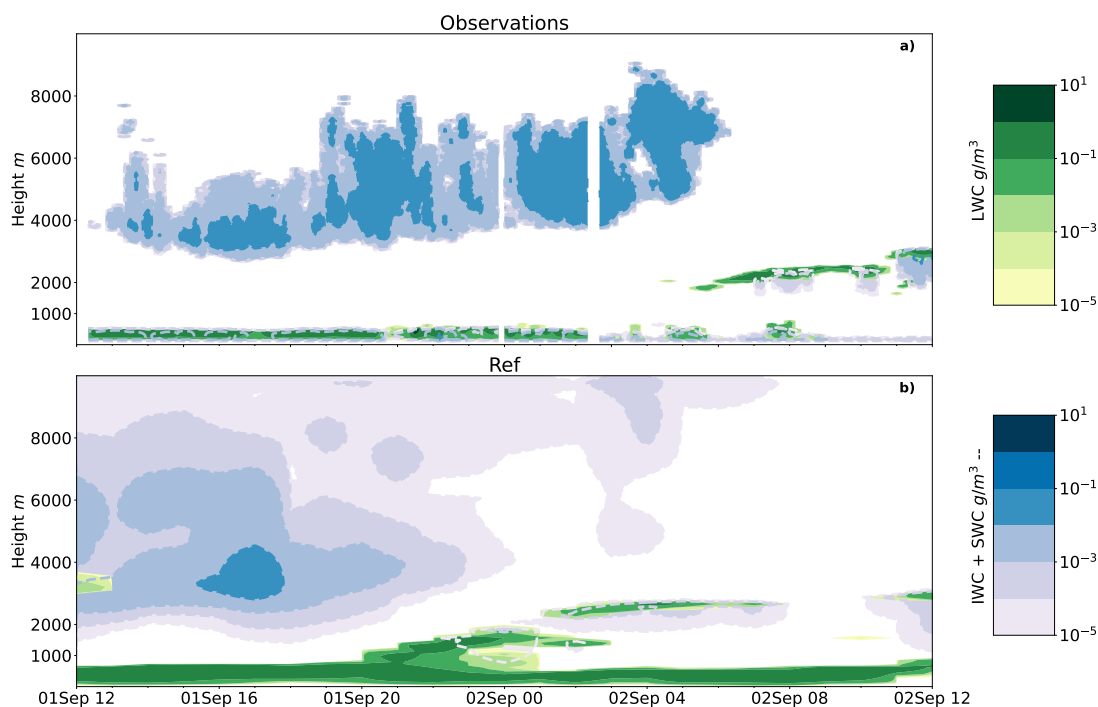


Figure 6.2: Time-height contours of observations (a) and the reference simulation (b) for liquid water content (LWC) in green contours and ice and snow water contents (IWC and SWC respectively) in blue.

6.3 The Radiative Impact of Overlapping Layers

The results of the removal of the radiative impact of the upper and lower layer on the cloud mass are shown more explicitly in Fig. 6.3. At first glance, the *Above Off* simulation (Fig 6.3c) does not differ much from the reference when observing the clouds until the split (21UTC), indicating that the upper layer exerts minimal radiative impact on the lower layer. The split occurs as in the reference, however, it is slightly delayed (by about an hour) and is suppressed in height. The splitting mechanism will be discussed in detail in Chapter 6.4. From 01UTC and onwards, the situation differs more, the middle layer, forming in the reference just above 1 km, does not form in the *Above Off* simulation and the upper cloud dissipates more quickly. When the radiative impact is disabled at an altitude of 1 km and above, these layers are unable to cool radiatively, which results in a more rapid dissipation. This may be the underlying cause of the absence of a third layer at 01UTC.

Removing cooling from the lower layer (*Below Off*, Fig 6.3d), has a large impact on the lower layer which is now suppressed in cloud top height by 300 m between 12UTC and 18UTC on the 1st. The split also changes quite radically; the layers above form similarly to the reference but the smooth transition from the lower layer to a rising layer is no longer observed. This indicates a dependency on radiation for this transition but also ensures that the upper layer forming at 21UTC is not driven by longwave radiative cooling of the lower layer. The third layer, at 01UTC, is again present when we allow

this layer to cool, and the lower layer during the later stages of the day is continuously suppressed in height. Still, it persists throughout the day, indicating that longwave radiative cooling is *not* required for the sustenance of the layer. The upper layer in the *Below Off* simulation is very similar to the reference, following the established theory that the presence or absence of longwave radiative cooling of a lower layer has minimal impact on an upper cloud as the temperature of the surface below is comparable to that of the cloud.

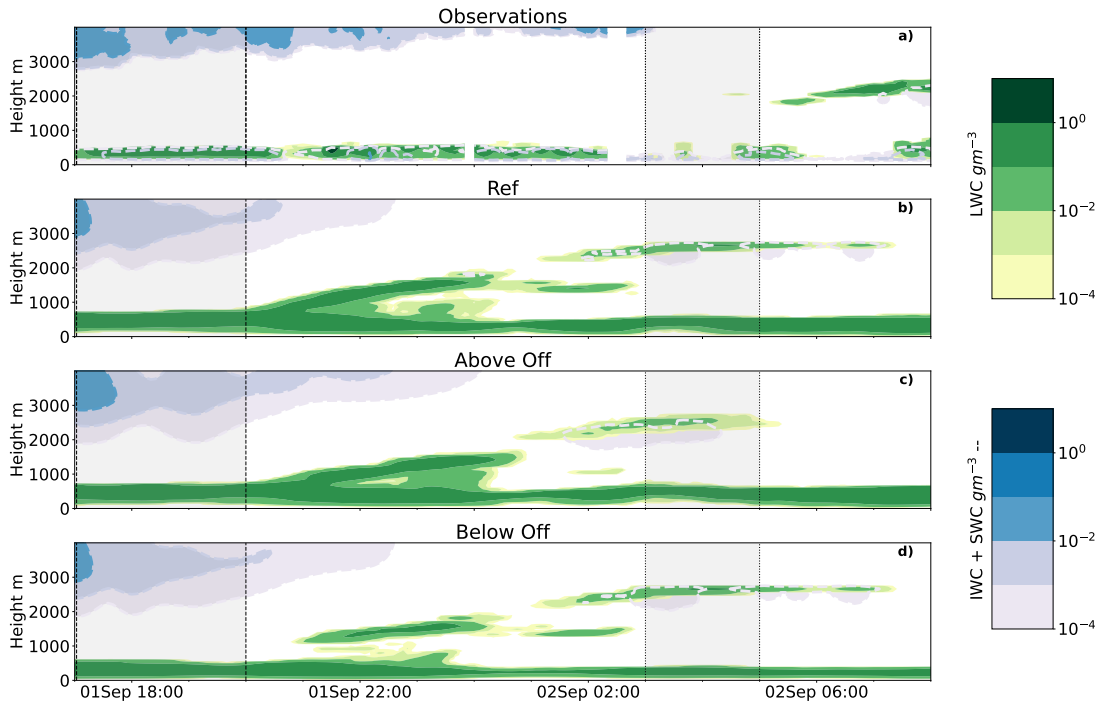


Figure 6.3: Time-height contours of observations (a), the reference simulation (b), (c) the simulation with cloud radiative heating turned off above 1 km, and (d) the simulation with cloud radiative heating turned off below 1 km. Liquid water content (LWC) is shown in green contours and ice and snow water contents (IWC and SWC respectively) are in blue. Shaded areas signify the evaluation regions for later analysis, 17UTC-20UTC and 03UTC-05UTC.

For a more detailed look at the impact of the upper ice cloud on the lower layer, in Fig. 6.4 vertical profiles of the mean heating rates between 17UTC and 20UTC (first shaded area in Fig. 6.3) on the 1st are shown. Only clear-sky impact can be seen at heights above 1 km when the cloud radiation interaction is turned off (*Above Off*). Noticing the small differences in the mean between this simulation and the reference at heights above 1 km in Fig. 6.4a, indicates that the large ice cloud cools inefficiently. A low rate of radiative cooling can be expected from an ice cloud due to both its smaller optical thickness (Turner et al., 2018), brought on by a lower cloud mass concentration and larger effective radii, and a cold cloud-top temperature. The inset in Fig. 6.4a shows a zoom-in on the lower layer. Here, we notice a small increase in the longwave radiative cooling rate when the upper cloud is made invisible to radiation (*Above Off*), with a

19.3% (absolute values) increase in maximum longwave radiative cooling compared to the reference (0.23 K hour^{-1} , 5.4 K day^{-1} increase in *Above Off*). The mass content in the lower layer is similar to the reference (0.2% increase compared to the reference).

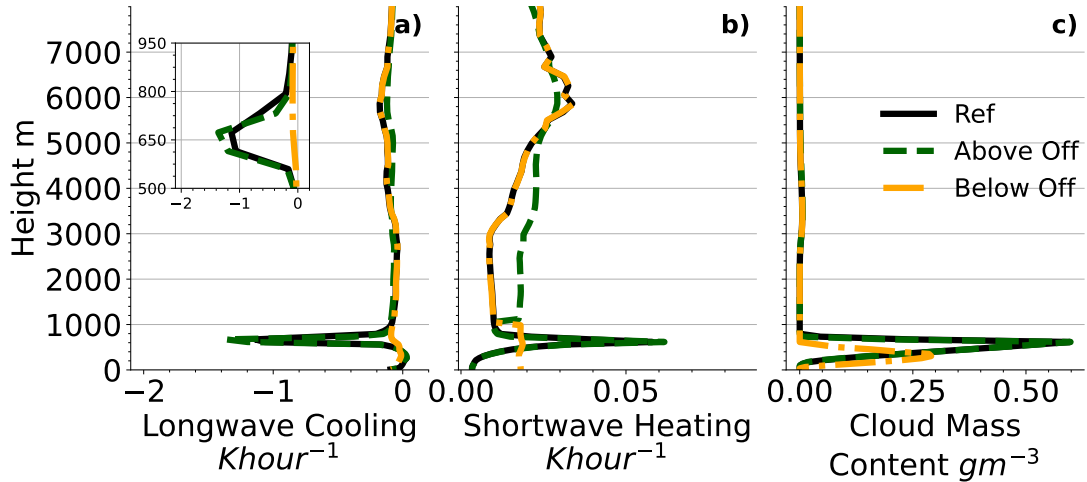


Figure 6.4: Mean vertical profiles between 17UTC-20UTC on the 1st of September. (a) longwave radiative cooling rates, (b) shortwave radiative heating rates, and (c) cloud water and cloud ice mass content in g m^{-3} for the reference in black and the two sensitivity experiments. The inset in (a) shows the lower layer only longwave radiative cooling rates.

Shortwave impacts are minimal, with less than 0.7 K hour^{-1} cloud SW heating by absorption (Fig. 6.4b). The lower layer sees only a small difference in shortwave absorption (6% increase between *Above Off* and the reference), while the atmosphere above 1 km heats more through SW absorption by atmospheric gases such as water vapour as the cloud is no longer interacting. The cloud top can be seen in the shortwave radiation for the reference around 6000 m where the ice crystals interact with the incoming shortwave radiation.

Without a cooling mechanism in the lower layer (*Below Off*), the cloud mass is reduced by a factor of two (LWP: 85 g m^{-2} , IWP: 5.9 g m^{-2}) and the cloud top height is suppressed. This is brought on by the removal of cloud-top longwave cooling which reduces the convective overturning within the cloud, efficiently minimises in-cloud turbulence and updrafts responsible for further cloud droplet activation. This layer also does not absorb shortwave radiation. Thus, a 69% decrease in shortwave heating in the lower layer is noted. The implementation does not allow for a surface impact to be quantified. However, at 10 m, the lack of a lower layer induces $0.015 \text{ K hour}^{-1}$ heating. Negligible differences ($\Delta\text{LW} < 0.01 \text{ K hour}^{-1}$) can be seen in the upper layer when the lower cloud is made transparent to radiation.

The difference in the liquid cloud mass is minimal between the reference and *Above Off* (LWP: 156 g m^{-2}). There are, however, differences in the ice water path. These processes are shown in Fig. 6.5. The mean IWP amount to 5.5 g m^{-2} and 9.6 g m^{-2} for

the reference and *Above Off* respectively, while median values show smaller differences (2.5 g m^{-2} , 3.6 g m^{-2}). This is quite contrary to other findings that show an increase in cloud ice with longwave radiative cooling (Sullivan et al., 2023). We find a similar increase in the ice number concentration (Fig. 6.5b) and a following increase in vapour deposition and sublimation rates (Fig. 6.5d). Ice number concentration changes are governed by ice nucleation, acting as a source of ice crystals, and sinks, such as riming, aggregation, and melting which transfer the ice crystals to other hydrometeor categories. Local ice nucleation rates are similar (Fig. 6.5c), however, which points to changes further upstream. We may further investigate the differences between the reference and *Above Off* across the domain. The spatial difference in IWP is shown in Fig. B.2. The lack of longwave radiative cooling in the upper atmosphere has huge implications on the IWP across the domain and can be seen to cause absolute differences up to 100 g m^{-2} . Following this, the column-integrated ice nucleation rate is shown spatially in Fig. B.3 and can be seen to differ similarly between the reference and the *Above Off* simulation. However, no bias can be found in ice nucleation and IWP differences that would point to a clear conclusion. In the mean IWP over the domain and through the simulation period a 9% increase in IWP is recorded for the *Above Off* simulation. Interestingly, the air mass flows northward from the Siberian coast, where the IWP and ice nucleation differences are negative, indicating that the reference has higher values. Further in from the domain boundary, the values turn more positive, indicating that the *Above Off* simulation now has larger rates. From this we may hypothesise the presence of temporal effects due to the lack of longwave radiative cooling that grows with time. The split was seen to be delayed by about an hour in the *Above Off* simulation which may further point to temporal differences. The presence of seeding between the layers, which increases the column-integrated IWP may be another factor that drives the differences. Disentangling these dependencies and lack thereof is a challenging task and reasons as to why this increase in IWP is seen for the *Above Off* simulation are left for further investigation in the future.

In Fig. 6.5d, the differences in longwave radiative cooling of the upper ice cloud between the reference and *Above Off* are clearer. We can see a lack of longwave radiative cooling by the cloud at altitudes 4-6 km as the difference between the reference and the *Above Off* simulations (only clear sky impacts), amounting to $\sim 0.1 \text{ K hour}^{-1}$ difference. The LW warming by the cloud can be seen between 1-3 km, with a smaller impact of $\sim 0.02 \text{ K hour}^{-1}$. This difference in the lower levels is what drives the suppression in longwave radiative cooling in the lower layer in the reference (Fig. 6.4).

The shorter period of a mixed-phase cloud that overlaps a liquid layer in all three simulations, between 03UTC-05UTC on the 2nd (second shaded area in Fig. 6.3), is shown in Fig. 6.6. Here, the clouds are perturbed by differences in the splitting mechanism, making these clouds somewhat different from the reference as seen in Fig. 6.3. When making the upper layer radiatively transparent (*Above Off*) the lower

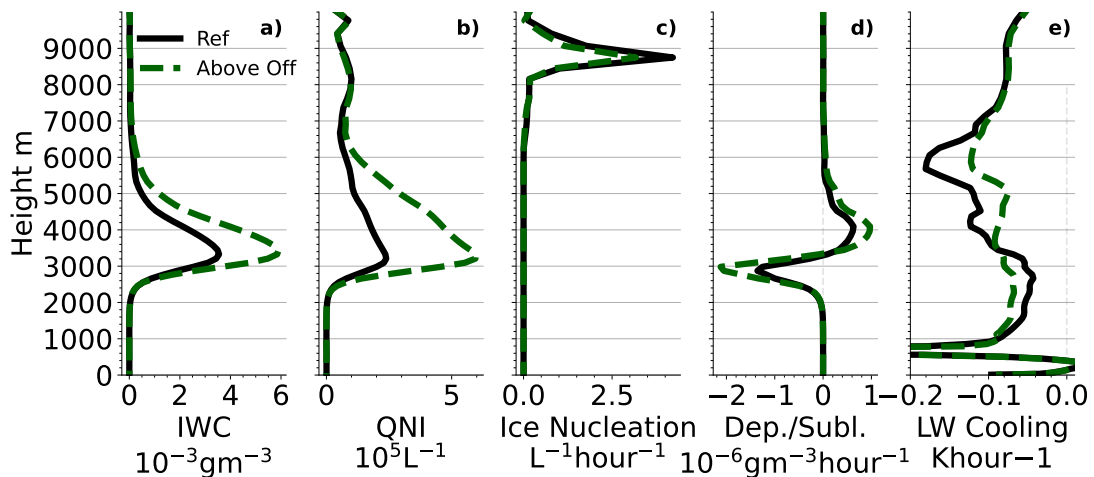


Figure 6.5: Comparison of the mean state of the reference and *Above Off* simulations between 17UTC-20UTC on the 1st. (a) Ice water content (IWC), (b) ice number concentration, (c) ice nucleation (heterogeneous and homogeneous) (d) deposition (positive values) and sublimation (negative values), and (e) longwave radiative cooling, zoomed-in on the upper layer impacts.

layer contains 26% less cloud water than the reference, and a reduction in longwave radiative cooling can be seen (-33%). The cloud mass content is also severely decreased in the upper layer (-83%) explained by the lack of longwave radiative cooling that contributes to growth. This does not impact the changes in the lower layer as this layer is radiatively oblivious to the upper one. Shortwave absorption is similar to the reference even with the 26% reduction in cloud mass. A small cloud-top height difference can be seen with 52 m elevation in the *Above Off* simulation.

For the *Below Off* simulation, an even larger reduction in cloud top height and cloud mass in the lower layer can be seen with a 50% reduction in cloud mass and close to 200 m cloud-top height depression. As the lower cloud has a similar temperature as the surface the upper cloud is not impacted when making the lower cloud transparent (*Below Off*), even with this quite small vertical separation (2 km).

6.4 The Radiative Impact on the Splitting of a Cloud

The split of the cloud layers, in the reference at 20UTC, differs between the runs, indicating some influence of radiation on the evolution of the cloud layers. However, the differences are small and the final cloud layers are similar between the runs, demonstrating the impact of non-local effects such as large-scale advection. To explore the advection aspect, back-trajectories have been performed using Lagranto (Wernli and Davies, 1997; Sprenger and Wernli, 2015). The trajectories, starting at 21UTC, are traced back for 10 hours and are shown in Fig. B.1. These are the mean positions of trajectories initialised surrounding the average ship position during these two days based on the 6 km model

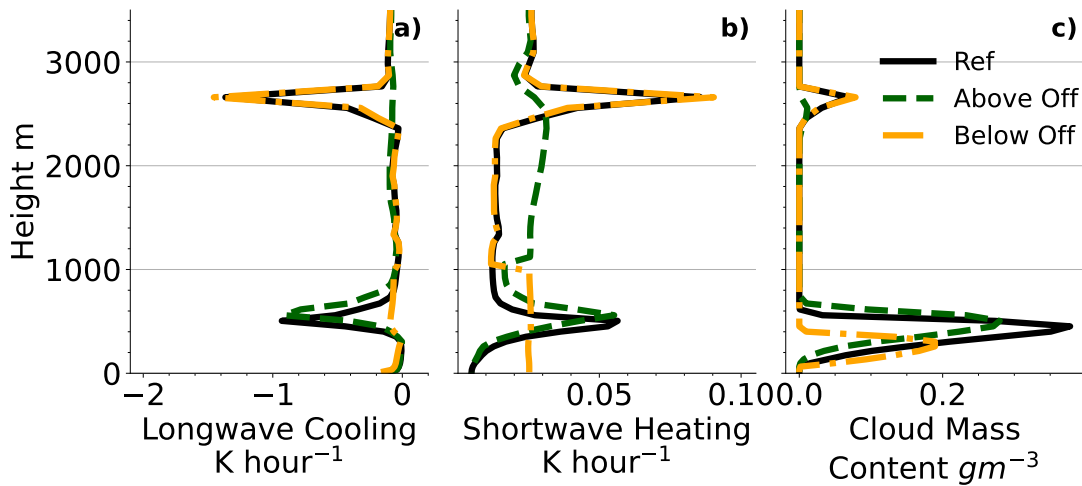


Figure 6.6: As in Fig. 6.4 with mean vertical profiles between 03UTC and 05UTC on the 2nd of September.

output spanning to 60°N . Through the evening hours, the airmass slightly changes direction and slows down. From these back trajectories, we can define pseudotrajectories following the mean state. Figure 6.7 shows the cross-section of clouds and wind with latitudes. These are calculated as the average over the longitudes the trajectories span, to obtain an upstream path.

The "split" can be seen to be advected up from the boundary region (85°N) with an average speed of 10 m s^{-1} . We also notice the lack of a split for the *Below Off* simulations (Fig. 6.7o-u), where a separate upper layer is instead advected northwards. The wind is very similar for the three cases, at this scale. The cloud layers coming over to the ship around midnight just above 2 km can be seen to travel northward at a similar speed. This layer tends to be drying and slowly descends towards the ship. In the *Above Off* simulation (Fig. 6.7h-k), the layer (just above 2 km) dissipates faster, followed by a small re-initiation in panel m. Astonishingly, the clouds persist for the 8.5 h travel it takes to get to the ship. Even the clouds in a non-radiative state, where the cloud-radiation interaction is turned off, do not diminish. We hypothesise that this is due to the boundary conditions (at 85°N) supplying a large amount of liquid water (as can be seen in Fig. 6.7). This coupled with the absence of cloud water sinks, such as drizzle formation, mixed-phase processes (riming and immersion freezing) or dissipation due to drying, leads to dynamically passive, surviving clouds. An additional model feature is the constant replenishing of aerosols. This set-up has not been tuned for CCNs and we thus see an activation of cloud droplets (depending on updrafts) comparable to Europe which further limits the precipitation possibility of the cloud layers. However, the updrafts here are not substantial enough ($\sim 0.5 \text{ cm s}^{-1}$) to add any significant cloud liquid. Similarly, the upper ice cloud is very robust and has almost an identical structure between the simulations. The descent towards the pole is quite an interesting feature however and might point to a high subsidence rate.

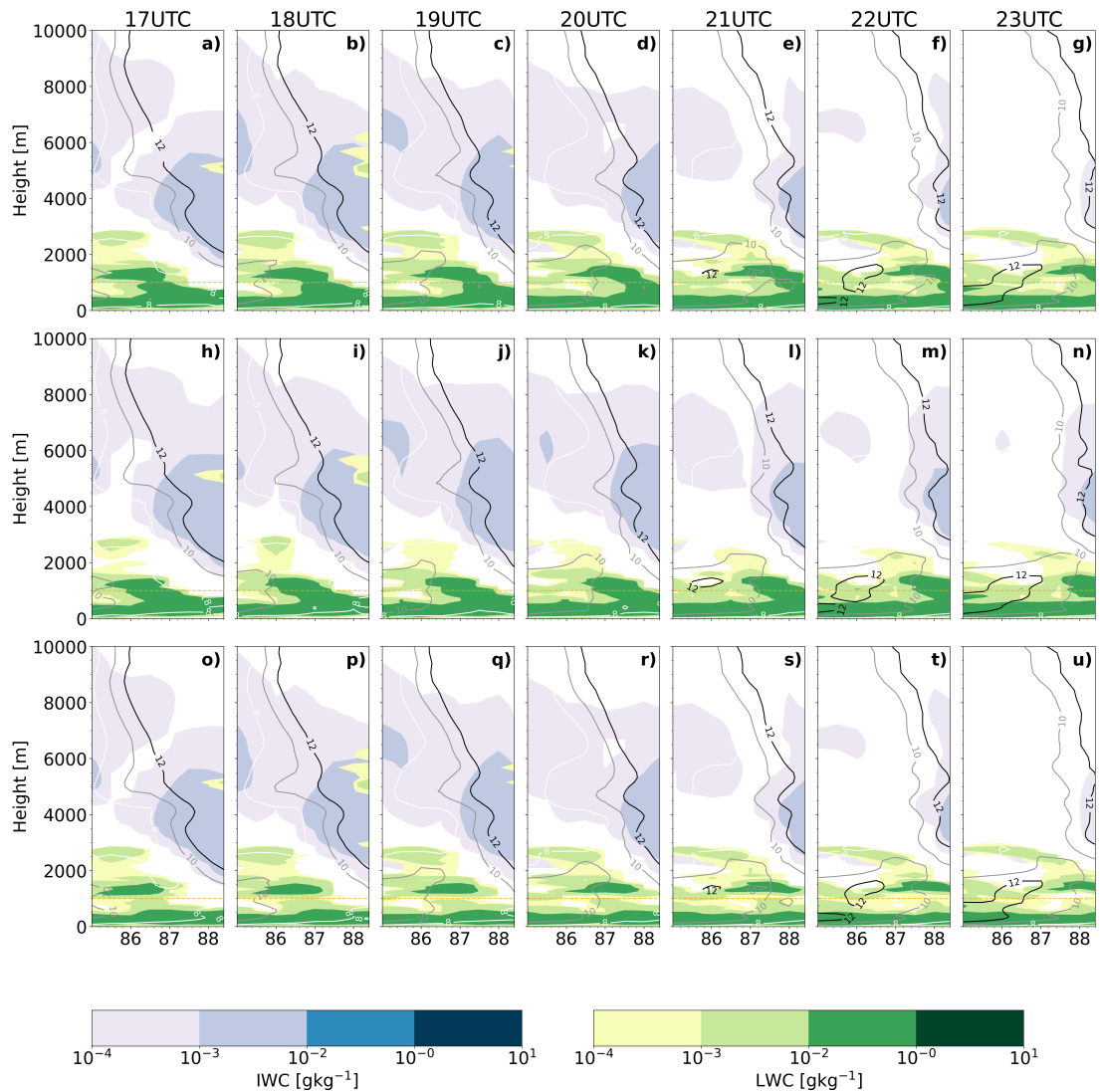


Figure 6.7: Pseudotrajectories following the mean state. Cross-section of clouds and wind taken as the average over the longitudes the trajectories span, to obtain an upstream path. The ship is located on the very right at 88.3°N . Shown are the reference (upper panels), *Above Off* (middle panels), and *Below Off* (lower panels). The hour on the 1st of September 2020 is shown at the top and LWC is shown in green contours while IWC is shown in blue. The wind speed is also shown in grey contours marked with their respective speed.

Even though the clouds seem to be governed by advection from the south, we are also interested in this local, smooth, transition from a single layer to a double-layered structure and notice that when the lower cloud is not cooling by longwave radiation the smooth transition does not occur (Fig. 6.3d). Looking in more detail we also see that in the *Above Off* simulation, the split is delayed by about an hour and is vertically suppressed. This is likely due to the removal of longwave radiative cooling at the cloud top as the cloud transitions at 21UTC. Figure 6.8, shows a temporal evolution for all three simulations between 17UTC- 23UTC. A smooth transition can be seen in the temperature (Fig. 6.8a,f) and cloud mass (Fig. 6.8e,j) for the reference and *Above Off* simulations, from a stable low cloud centred at 600 m to the two-layered structure (upper cloud ending at 1250 m, lower is slightly suppressed to 400 m). Essentially, we are watching a cloud system pass through (as seen in Fig. 6.7) with a temperature between the upper and lower end of the 600 m inversion. This temperature inversion is gradually heated by an average 0.5 K hour^{-1} (up to 1.5 K hour^{-1}) while the cloud (coming in) has a lower mass. Meanwhile, the upper end of the inversion (around 800 m) gradually cools down and an upper cloud layer arrives.

From the temperature advection term (Fig. 6.8c,h), we can see the heating (up to 2 K hour^{-1}) corresponding to the temperature inversion losing strength while a gradual cooling of the upper air (by up to -2 K hour^{-1}) renders the second structure. The cooling by longwave radiation, during the initial hours of the split ($\sim -1.4 \text{ K hour}^{-1}$), offsets the heating ($\sim 1.2 \text{ K hour}^{-1}$) by advection but the advection dominates at later time steps as the cloud cools less. This could be due to either less cloud mass or downwelling radiation from the upper cloud. Disentangling these two causes is challenging as the layers start to split below 1 km. A low-level jet, determined by the method used in Lopez-Garcia et al. (2022), is induced for the reference and *Above Off* simulation at 750 m (Fig. 6.8b,g). This is based on the identification of a wind speed maximum, at least 25% larger than the minimum above it, within the lowest 1500 m. Potentially produced or reinforced by the longwave radiative cooling from the lower layer, it seems this jet is enforcing the advection of the upper cloud layer. This is beyond the scope of our current study but could be further investigated in future work.

6.5 Regional Signal in the Suppression of Cloud-top Long-wave Radiative Cooling

With the reference simulation performed, we make further use of the extent of the domain (85° - 90° N, Fig. 4.1) to study the radiative impact of multilayer clouds across this region. Here, we are interested in the study of cloud-top longwave radiative cooling suppression, as seen by previous studies when an overlaying cloud is present (Chen and Cotton, 1987; Christensen et al., 2013; Turner et al., 2018; Jian et al., 2022). To investigate the LW radiative cooling across the domain we use the reference simulation

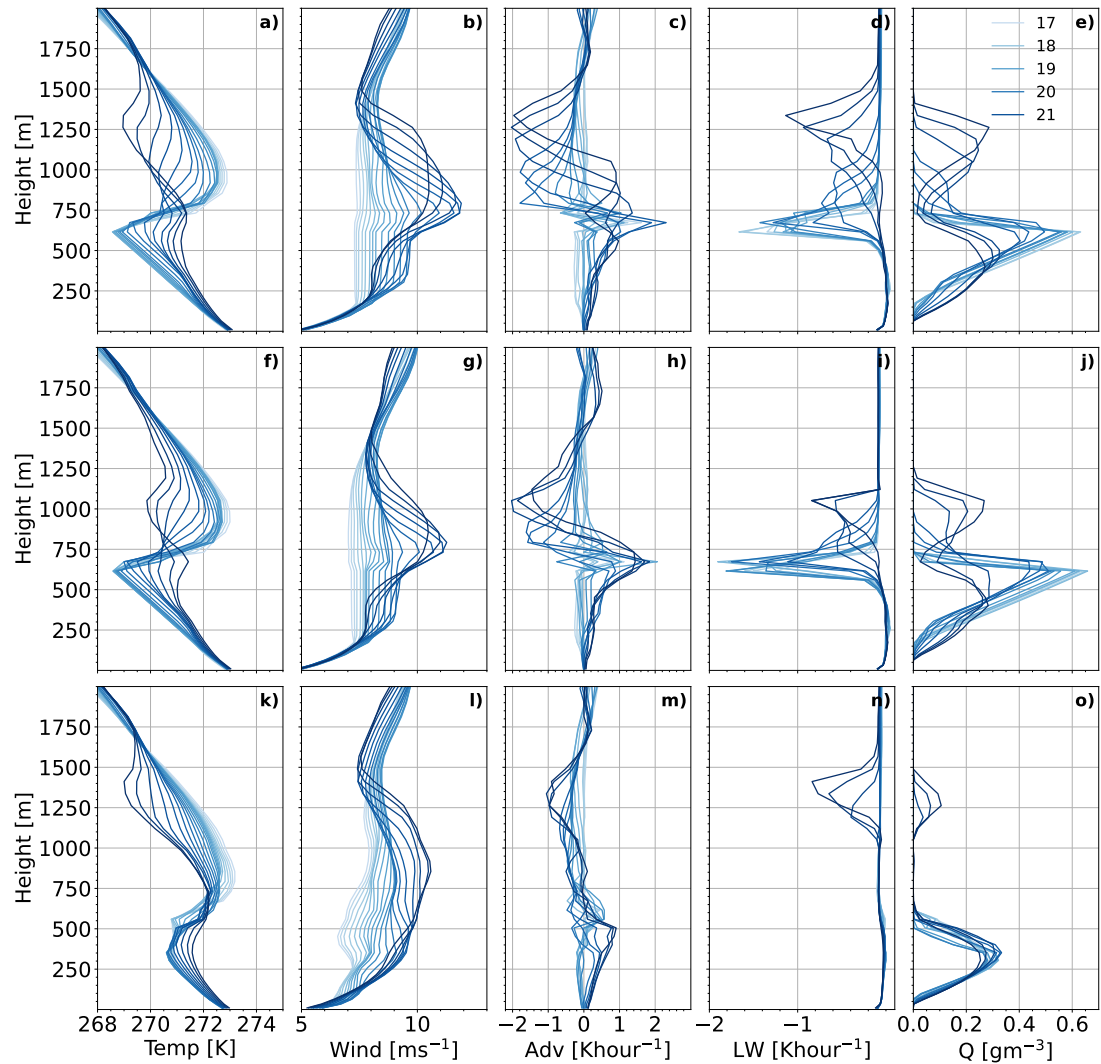


Figure 6.8: Vertical profiles for the reference simulation during the split shown in Fig. 6.3b. Gradual blue shades show the progression from 17UTC until 22UTC with 15-minute outputs. Shown are temperature, wind, advection, radiative cooling rates, and cloud mass including cloud ice and cloud water for the (a-e) reference, (f-j) *Above Off* (k-o) *Below Off*.

and apply the MLC algorithm defined and outlined in Chapter 4.1.2. The algorithm quantifies the number of layers and extracts cloud-top CRH, phase, and temperature using relative humidity and a cloud mass threshold.

The cloud-top temperature tendency from longwave radiative cooling for multilayer and single-layer clouds is presented in Fig. 6.9. All profiles of MLCs and single-layer clouds (SLCs) have been identified across the domain. Furthermore, we isolate the lowermost MLC, named the 1st layer MLC, to further study the impacts of an overlaying cloud compared to SLCs. The median cloud-top LW radiative cooling rates for MLC, 1st layer MLC, and SLC are $-0.12 \text{ K hour}^{-1}$, $-0.19 \text{ K hour}^{-1}$, $-0.16 \text{ K hour}^{-1}$ respectively. Thus, in the median, no suppression in the longwave radiative cooling is simulated. Instead, considering the mean state; values are $-0.42 \text{ K hour}^{-1}$, $-0.45 \text{ K hour}^{-1}$, and $-0.85 \text{ K hour}^{-1}$ respectively. Even though the distributions are skewed, the mean state might be more representative here as many cloud tops represent thin and cold cloud layers which do not cool very efficiently. The mean state better reflects the comparatively larger radiative cooling rates of the warmer and thicker cloud tops. Thus, when considering the mean state, a suppression of 0.4 K hour^{-1} is simulated between the 1st layer MLC and SLC in the longwave radiative cooling.

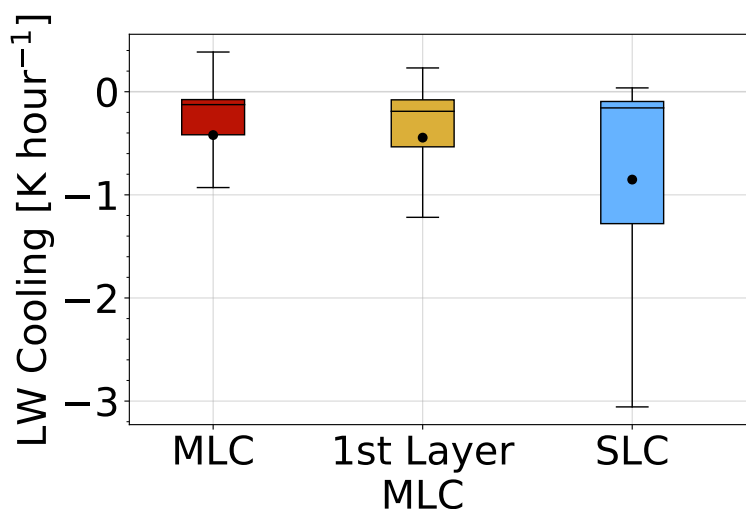


Figure 6.9: The longwave radiative cooling of the cloud tops identified as MLC, 1st layer MLC, and SLC over the entire domain ($85^{\circ}\text{N} - 90^{\circ}\text{N}$) during 04UTC 1st September to 00UTC 3rd September.

The lack of suppression in the median values of cloud-top longwave radiative cooling might be due to low radiative cooling tendencies in general as LW cooling in the range of 0.2 K hour^{-1} ($\sim 5 \text{ K day}^{-1}$) is very low for Arctic mixed-phase clouds (Turner et al., 2018). Turner et al. (2018) reported LW cooling of clouds with respect to their phase. Single-layer ice clouds in their study with IWP in the range of $1\text{-}10 \text{ g m}^{-2}$ have LW signals of $1.5\text{-}4 \text{ K day}^{-1}$ (absolute values) while liquid (single layer) clouds had signals highly depending on the LWP. Clouds corresponding to an LWP of $\sim 150 \text{ g m}^{-2}$

would have absolute values of radiative cooling of $\sim 80 \text{ K day}^{-1}$. Thus, our signal may be skewed due to the lack of pre-sampling for liquid-containing (mixed-phase) clouds that have warmer cloud-top temperatures and are in general optically thicker, allowing for higher LW radiative cooling rates. We approach this by exploring the correlation between the cloud-top phase and absolute values of LW radiative cooling. In the Arctic, a predominance of liquid and mixed-phase cloud tops with frozen precipitation has been found. Based on this vertical distribution of the cloud phase, we may hypothesise that clouds with a cloud top in the ice phase may be assumed to be fully in the ice phase and thus, experience a low rate of LW radiative cooling. To explore this, we filter for liquid-only, ice-only, and mixed-phase cloud tops using the supercooled liquid fraction (SLF, Eq. 4.1) of 1, 0, and between 0 and 1 respectively. Ice-cloud tops dominate the distribution of cloud phase, 72% of MLC, 57% of 1st layer MLC, and 56% of SLC. Liquid-only cloud tops are rare (0.04%, 0.1%, and 0.26% respectively) while mixed-phase make up the rest of the distribution (28%, 42%, and 43%). The total number of profiles amounts to $6.7 \cdot 10^7$ MLCs, $1.9 \cdot 10^7$ 1st layer MLC, and 10^6 SLCs, during 04UTC on the 1st to 00UTC on the 3rd. Figure 6.10a shows the cloud top LW cooling for MLC, 1st layer MLC, and SLC sub-divided into ice, liquid, and mixed-phase cloud-tops. To examine the impact of temperature on this separation of cloud phase, Fig. 6.10b, shows the distribution of cloud top temperature for the different cloud top phases.

The radiative cooling is strongly modulated by the cloud top temperature (Fig. 6.10b). Clouds with ice-phase cloud tops tend to have a lower cloud top temperature and the SLCs with an ice-phase cloud top during these simulations are almost uniquely found within homogeneous freezing temperatures. This explains the low rate of LW radiative cooling for the ice-phase cloud tops in general (Fig. 6.10a) and the discrepancy in longwave radiative cooling rates between SLCs and MLCs. Lowest layer MLCs with icy cloud tops have the warmest cloud-top temperatures which is likely due to the presence of seeding, enforcing an ice-phase cloud top. These clouds still cool inefficiently with a high median cloud-top temperature (265 K) and we might see some impact from overlaying cloud layers. However, due to the difference in cloud-top temperature between these layers and the SLCs, it is difficult to reach a definitive conclusion.

We find that liquid cloud tops cool similarly to mixed-phase cloud tops (Fig. 6.10a), this can be understood from the similar cloud-top temperatures (Fig. 6.10b). For SLCs, this difference is marginal with medians at -1.4 K hour^{-1} and -1.5 K hour^{-1} for liquid and mixed-phase clouds. For MLCs and lowest layer MLCs, the difference is larger with a median of liquid cloud top cooling of -0.4 K hour^{-1} (for both) and mixed-phase cloud top cooling at -0.7 K hour^{-1} and -0.5 K hour^{-1} respectively. This may indicate that clouds with mixed-phase cloud tops are in general thicker as they exist at slightly lower cloud-top temperatures. For liquid cloud tops, due to the small sample size, the category for all MLCs is only slightly larger than the lowest layer indicating that most liquid layers are the lowest layer in an MLC system (as expected). A similar conclusion

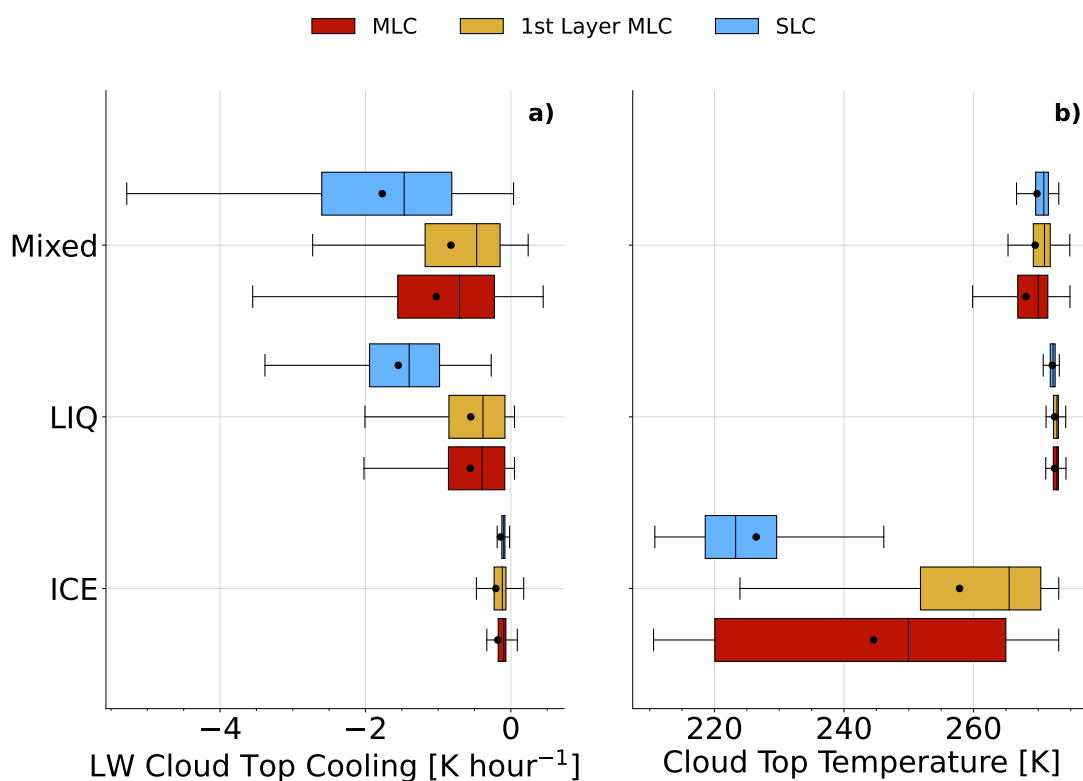


Figure 6.10: Cloud top a) longwave radiative cooling and b) temperature of the cloud tops identified as MLC, 1st layer MLC, and SLC over the entire domain (85°N - 90°N) during 04UTC 1st September to 00UTC 3rd September, filtered for cloud top phase; ice-only, liquid-only, and mixed-phase. Box plots show the median (black line) and the mean (black dots) for each cloud type indicated with the respective colour.

can be made for the mixed-phase MLCs where the 1st layer MLCs contribute 67% to the MLCs.

Through this analysis, a stronger signal of the suppression in radiative cooling can be seen for the 1st layer MLCs. The difference for mixed-phase cloud tops (and similarly for the few liquid cloud tops) amounts to 1 K hour⁻¹ (23.9 K day⁻¹).

The SW component is very small (mean values in the range of 0.05 K hour⁻¹), however, SLCs have a mean heating rate two times larger than the lowest MLCs and 1.6 times larger than all MLCs and is shown in Fig. B.4. The reduction in SW absorption in the MLCs is likely due to shielding from clouds above.

6.6 Summary & Discussion

Cloud radiative effects on cloud formation and persistence is an underrepresented topic, not just in the Arctic. In this chapter, we study the radiative impact on and of multilayer clouds. To study the cloud-radiation interaction, we employ the COOKIE method (Hunt, 1978; Stevens et al., 2012), incorporated into ICON (Voigt et al., 2023). This method allows for the cloud-radiation interaction to be selectively turned off within the atmosphere. Three simulations are performed, a reference and two sensitivity studies where the clouds are made invisible to radiation above and below 1 km respectively.

We investigate the radiative impact on the split of a double-layered cloud modelled during the 1st-2nd of September 2020. The split is not observed in the observations from the MOSAiC campaign. We find minimal impact from radiation. The clouds are found to be largely advected up to the ship location from the boundaries of the model domain. As the Arctic region is governed by advection and warm air intrusions (Pithan et al., 2018; Svensson et al., 2023) the advection is expected. The Lagrangian perspective, following the air parcels with the advection, might provide a better view of the processes that occur as you may follow the cloud from its initiation. The impact of Arctic air mass transformation and cloud formation has been thoroughly studied (e.g. Curry, 1983; Pithan et al., 2018; Dimitrelos et al., 2020; You et al., 2021; Silber and Shupe, 2022; Svensson et al., 2023) but the radiative impact of the clouds as they transform and move into the Arctic is a topic less represented in the literature.

Let us here define a radiatively inactive state, where the cloud-radiation interactions have been turned off, this includes the clouds above 1 km in the *Above Off* simulation and the clouds below 1 km in the *Below Off* simulation.

While studying the advection of the cloud layers to the ship location we find that liquid clouds in a radiatively inactive state persist during the ~ 8 hour advection, alluding to a persistence mechanism for stratocumulus clouds that does not pertain to longwave radiative cooling. The clouds are diminished but do not completely dissipate. We believe that the combination of large-scale advection of the clouds, consistently supplying a large amount of cloud mass through the boundaries together with a continuous (while low) supply of newly activated cloud droplets maintains the clouds. The saturation adjustment in the model, ensuring saturation, enables further droplet growth in supersaturated regions, while a lack of precipitation formation, possibly due to an unconstrained CCN parameterisation, helps the persistence. The role of a cloud-top moisture inversion is beyond the scope of this study but the implications would be beneficial to study further.

Clouds in a radiatively inactive state at the MOSAiC site show larger impacts from the absence of longwave radiative cooling. Shortwave absorption and heating have a negligible influence. Impacts on cloud ice and liquid are found to be opposite. In liquid, or liquid-dominated, layers, a lack of radiative cooling drives dissipation. Similarly to clouds that experience heavy absorption of shortwave heating, the clouds

will experience a lack of negatively buoyant parcels and the turbulence these initiate. A lack of turbulence will reduce the upward motion and limit new droplet formation. Full dissipation is only noted for thin upper layers while thicker liquid layers diminish but do not reach full dissipation within the 15 hour simulation period. Cloud ice experiences the opposite effect. In the simulation with upper clouds in a radiatively inactive state, a close-to-doubling of IWP can be seen. This is quite contrary to the view of ice clouds and their interaction with radiation. In general, a stronger cooling by LW radiation is seen with a larger ice mass (Turner et al., 2018; Sullivan et al., 2023), following a similar but weaker behaviour as liquid droplets. Thus, we would assume with a lack of cooling, the ice would sublimate, this is further shown by Young et al (2018) in a modelled Arctic stratocumulus case study. Disentangling the impacts of microphysics and radiation is challenging. We find large impacts across the domain with an overall increase in IWP, we hypothesise this may be due to a temporal effect, as in a change of dynamics with a lack of cloud-radiation interactions, as well as an impact of seeding, which promotes ice growth in lower layers.

For clouds in regions with active cloud-radiation interactions, the impact depends on whether we look at lower or upper cloud layers. Removing the radiation interaction in the lower layer does not impact the upper layers, this is quite expected as these low layers (at higher temperatures) emit longwave radiation on the same order of magnitude as the surface below. The cloud above would not see a large difference in incoming LW radiation between a low-level cloud and the surface. This lack of response is also seen in the shortwave.

The reduction in the longwave radiative cooling of lower layer multilayer clouds due to warming from the upper layers has been seen in observational studies in the Arctic (e.g. Shupe et al., 2013; Turner et al., 2018; Lonardi et al., 2022), (Arctic) idealised modelling studies (Luo et al., 2008; Chen et al., 2020), and in global satellite studies (Christensen et al., 2013; Adebiyi et al., 2020; Jian et al., 2022). Here, we find a local (at the MOSAiC site) longwave radiative cooling increase of 5.4 K day^{-1} (0.23 K hour^{-1}) of a lower liquid cloud layer when the upper ice cloud is made invisible to radiation. Further analysis of the full domain modelled reveals a strong reduction in longwave radiative cooling of lowest-layer MLC clouds compared to single-layer clouds. We find that we can categorise the cloud-top longwave radiative cooling by the cloud-top phase, due to the large difference in cloud-top temperature. Ice clouds tend to have low cloud-top temperatures and low rates of longwave cooling. 1st layer MLCs have a higher cloud top temperature but experience only a marginal increase in LW radiative cooling which indicates a reduction due to the presence of overlaying clouds.

A difference of 1 K hour^{-1} is found for liquid and mixed-phase 1st layer MLCs compared to SLCs. In a study by Christensen et al. (2013) on the free-tropospheric clouds overlaying stratocumulus (above 4 km and below 3 km respectively), they found a 4 K day^{-1} suppression during nighttime while a -2 K day^{-1} signal during the day. They

argue that during the day the upper cloud cools less efficiently due to the absorption of shortwave radiation. The impact on the lower cloud is then weakened compared to during the nighttime, when the lack of solar radiation enables the upper clouds to cool more efficiently, increasing the warming of the lower cloud. We see a similar impact on the rates of heating by shortwave absorption. Jian et al (2022) followed the work by Christensen et al. (2013) and reported a global mean 5 K day^{-1} (0.21 K hour^{-1}) reduction in longwave cloud-top cooling of the lowest cloud layers, irrespective of the time of the day. The authors do not discuss this discrepancy which may be due to the treatment of the data. In a further satellite study, Adebisi et al. (2020), show a 10 K day^{-1} suppression by mid-level Atlantic clouds. The doubling of LW suppression may be due to a lower abundance of ice clouds, this would further support the large LW suppression seen in this work. When we do not sample for the cloud phase, a weaker reduction in the longwave cloud-top cooling was found, amounting to 9.6 K day^{-1} . Acquiring vertically resolved satellite data over the Arctic would have been an invaluable tool for further validation of these heating rates. More modelling studies in other areas could help mitigate this uncertainty.

7 | LONG-TERM MODEL EVALUATION AT THE MOSAIC SITE

As seen in Chapter 5, the model performance, evaluated against observed quantities, differs substantially between the three days simulated within Chapter 5. To further investigate potential biases in the model and to systematically evaluate the performance of ICON in the Arctic, we set up a regional model with 32 consecutive simulations through August-September 2020. In this chapter, we evaluate the model’s suitability at the MOSAiC site in terms of atmospheric surface variables, vertical profiles as well as cloud occurrence.

7.1 Aerosol Constraints

Following the previous work in Chapter 5, we notice the importance of correctly describing the CCN and INP in the model. To this effect, we constrain the parameterisations to observations. We tune the cloud droplet activation scheme by Hande et al. (2016) by a factor of 0.01, following comparison between the MOSAiC 2019/2020 (Koontz et al., 2020) and MOCCHA 2018 (Duplessis et al., 2023) datasets in Fig. 4.5.

To improve on the INP parameterisation developed for Chapter 5 we use multiple INP datasets collected between August and September over numerous years and fit an Arctic late-summer INP parameterisation. Data from eight campaigns, including MOSAiC and MOCCHA, are presented in Fig. 7.1 together with the current immersion freezing parameterisation. The observational datasets were introduced and shown spatially in Chapter 4.2.2 (Fig. 4.6). An Arctic-appropriate parameterisation is developed, which captures a lower concentration of dust at cold temperatures and the abundance of oceanic INP species at warmer temperatures. At cold temperatures, $-36^{\circ}\text{C} < T < -20^{\circ}\text{C}$, an exponential function is fitted to the data, following the Hande et al. (2015) parameterisation;

$$INP = a \cdot \exp(-b \cdot (T - T_{min})^c) [\text{L}^{-1}] \quad (7.1)$$

with $a = 2.9$, $b = 0.0815$, and $c = 1.45$. T is the atmospheric temperature while $T_{min} = -36^\circ\text{C}$. To better represent the Arctic bio-organic aerosols, from the ocean, we fit a 2^{nd} order polynomial function at temperatures $-20^\circ\text{C} \leq T \leq -5.5^\circ\text{C}$. This fit is named "Arctic Fit" and is shown with a black dashed line in Fig. 7.1. To further investigate the need for representing the organics with a different function, a full fit of the data can be done using the exponential form in Eq. 7.1. The fit parameters are $a = 4.1$, $b = 0.0813$, and $c = 1.2$. This exponential-only fit (Exp. Fit) is shown in dark-red dash-dot in Fig. 7.1. For both these two implementations deposition nucleation and rain freeze are scaled down by a factor of 0.05.

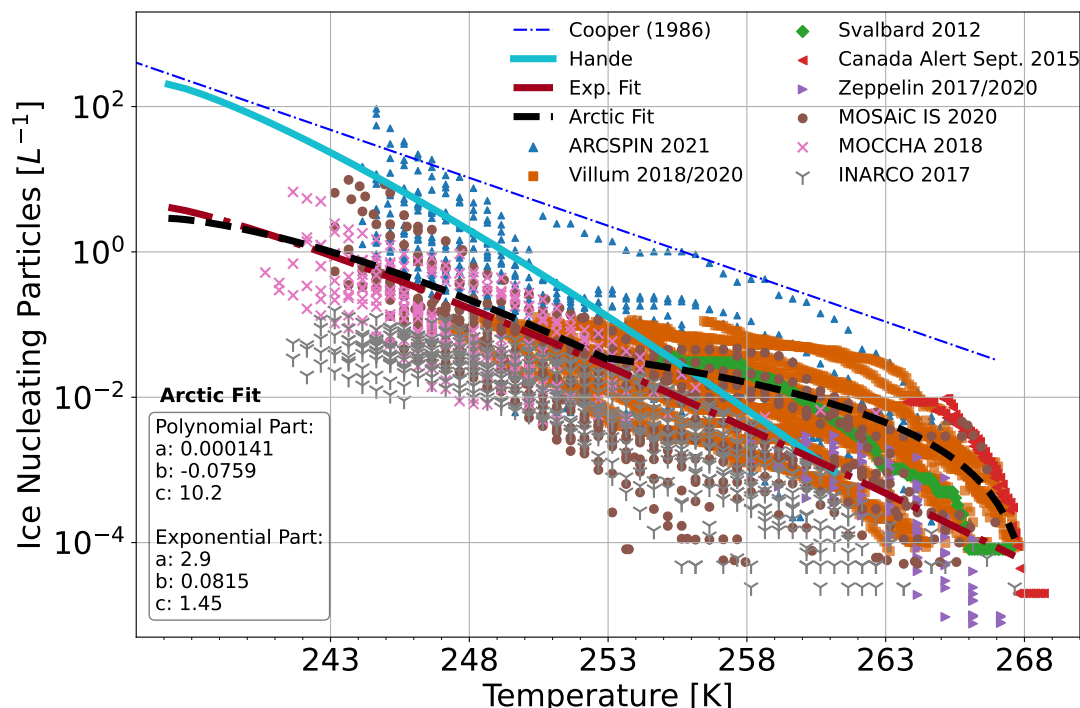


Figure 7.1: Ice nucleating particle data from eight campaigns (see Fig. 4.6) together with the current immersion freezing parameterisation by Hande et al. (2015) marked in cyan. A full exponential fit of the data (Exp. Fit) and the Arctic fit, including a low-temperature exponential fit and a high-temperature polynomial are shown in dark red and black respectively. The 1-moment immersion parameterisation by Cooper et al. (1986) is shown in blue for comparison.

Impact of INP Parameterisation

An investigation into the impacts of changing the parameterisation on the full domain (Fig. 4.1) is presented here. We use the simulation on the 31st of August 2020 at 18UTC, to explore the implications of changing the INP parameterisation. The domain is large enough to cover the entire temperature range relevant for ice nucleation. The model is initialised at 00UTC and after 18 hours of simulations, appreciable differences, if any, should be quantifiable. Of course, some discrepancies between this simulation and a full

evaluation of the 32 days simulated may exist but we will consider this day and time representative.

To remove the impact of ice falling from an upper layer, we select single-layer clouds only. A full evaluation across all temperatures shows the dominance of cold-temperature ice nucleation. The Hande et al. (2015) parameterisation gives a larger ice number concentration, N_{ice} . However, the differences are small with a mean N_{ice} of 1.03 L^{-1} for the Arctic fit and Exp. fit and 1.11 L^{-1} using the Hande et al. (2015) parameterisation, a 7.2% decrease in N_{ice} across all temperatures owing to the reduction of ice nuclei for immersion freezing, deposition nucleation, and rain freeze. To isolate the in-cloud effect for the addition of immersion nuclei we filter for single-layer clouds with cloud tops above 261 K, where the Hande et al. (2015) parameterisation is not active. The results, presented in Fig. 7.2, show small differences, with a 17% increase in the mean N_{ice} for the Arctic fit (0.028 L^{-1}) and 8% increase for Exp. Fit (0.026 L^{-1}). Median values remain higher for the Hande et al. (2015) implementation (mean 0.024 L^{-1}). Overall, the impact of changing INP parameterisation within this temperature range is, on the full domain, small. However, enabling INP activation at higher temperatures ($T > 261 \text{ K}$) allows for primary ice formation that can locally change the clouds. Thus, for the simulations performed within this chapter, we use the Arctic Fit parameterisation, to enable local, warm, mixed-phase cloud processes.

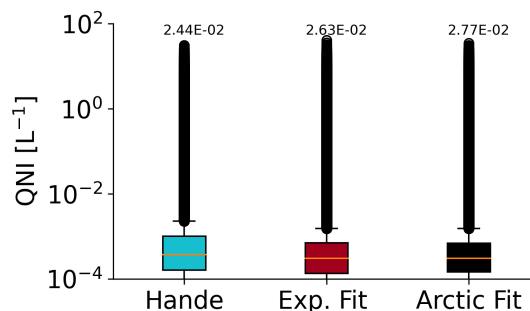


Figure 7.2: Ice number concentrations for the Hande et al. (2015) parameterisation, the Exponential fit, and the Arctic fit filtered for in-cloud ice concentrations of single-layer clouds with clouds tops above 261 K.

7.2 Long-term Comparison at the MOSAiC Site

The MOSAiC site is ideal for a side-by-side comparison of the model output. Here, we use meteograms from the model, to obtain a high temporal output frequency of one minute. In Fig. 7.3, the 32 simulations performed are shown next to the ShupeTurner microphysics retrieval (Shupe, 2023). Shown are the LWC in green and the frozen hydrometeors in blue. In the model, this combines ice, snow, and graupel, while in the observations this is classified as ice. Overall, the model represents the observed clouds remarkably well. It captures the persistent boundary layer clouds, however, the

cloud phase tends to be predominantly liquid in these low clouds. Most high clouds and events of frozen precipitation are also captured, with a tendency towards over-predicting high clouds and frequency of precipitation. Vertical, upward, motion in the lower cloud can be seen, showcasing a common problem in NWP models (Sandu et al., 2013), the very active cloud-top mixing. This may also be attributed to an insufficient subsidence rate that allows for larger vertical motions, excessive updrafts (less probable as the 2.5 km grid spacing is inadequate for resolving sufficient updrafts), weak temperature inversions, or a high entrainment rate. The clouds at MOSAiC have been shown to have a low entrainment rate (Neggers et al., 2024) and this has not been tuned for in the model.

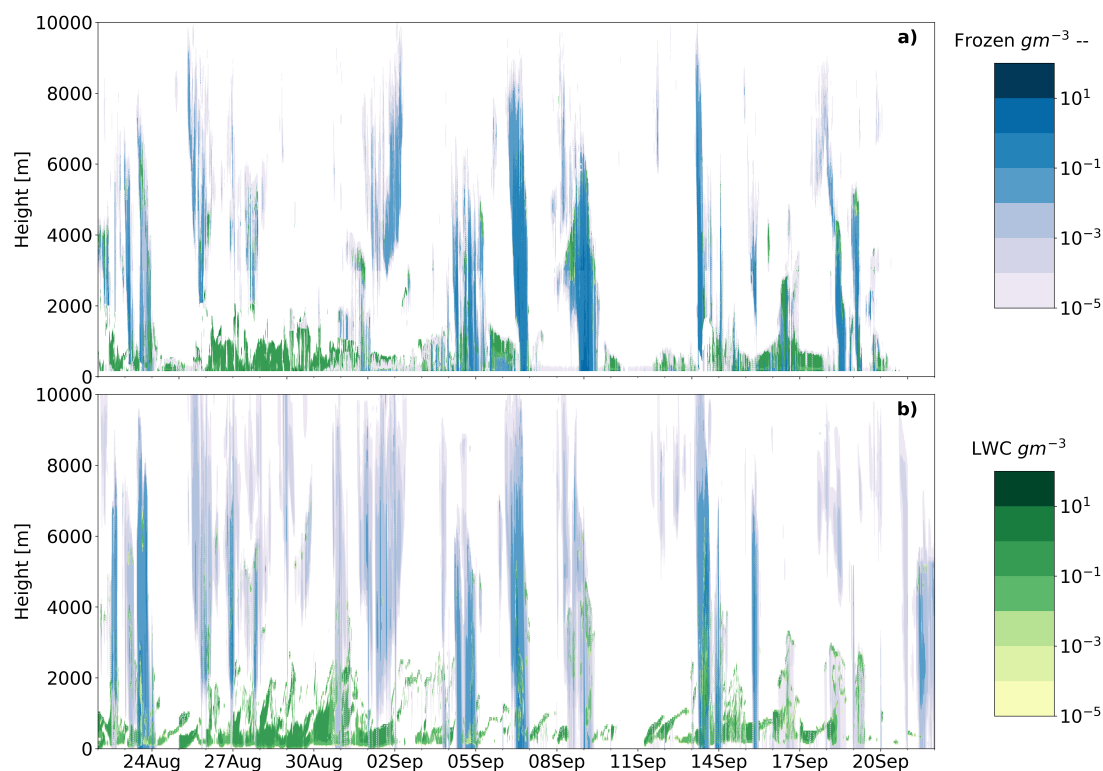


Figure 7.3: The long-term simulation performed at the MOSAiC site. Shown here is the ShupeTurner microphysics retrieval (Shupe, 2023) (a) together with the model output (b) between the 22nd of August and the 23rd of September. Liquid water content is shown in green. A frozen hydrometeor category is defined and is shown in blue. For the model, this includes ice, snow, and graupel while for the observations only ice is included. The model is initiated at 00UTC every day and runs for 24 hours.

Surface Variables

Looking further into the comparison between the model and the MOSAiC site, temperature, pressure, and wind from the so-called Met City (Cox et al., 2023) are shown in Fig. 7.4, where the lack of data indicates days where the instruments were not working. Furthermore, integrated water vapour (IWV) is additionally shown, as

the column integration of the specific moisture in the model and a multi-instrument retrieval product (Walbröl et al., 2024).

Quite large discrepancies can be seen in the 2 m temperature. Until the 10th of September the 2 m temperature is adequately captured with a maximum difference of 4 K while during the 10th-12th September window, a difference up to 6 K is recorded. This is during a relatively cloud-free period as seen in Fig. 7.3. This may be due to the sea ice parameterisation that is not adequately capturing the heat flux across the sea ice-atmosphere boundary. The freeze-up, when the sea ice freezes again and the surface temperature is no longer locked to the 273 K melting temperature, is accurately captured by the model around the 4th of September (Shupe et al., 2022). The subsequent days of colder temperatures and the mid-September storm, bringing warm air from the south (Shupe et al., 2022) also comes through in the model. A clear model bias can be observed in Fig. 7.4b, where the scatter plot shows the observed vs modelled values. The model is especially struggling to capture lower temperatures, likely in very stable conditions. The mean absolute error (MAE, see Chapter 4) for the entire period amounts to 1.16 K while the Spearman Correlation Coefficient (ρ) amounts to 0.93. These metrics show that the temporal evolution is well represented but with a bias, here a warm bias as seen in Fig. 7.4b.

Wind speeds are adequately well represented with no clear biases and a low MAE of 0.98 m s^{-1} . The temporal trend is also captured ($\rho=0.83$) to an acceptable level. The 2 m pressure and IWV are surprisingly well captured, showing that the surface pressure is governed by large-scale features which the model can more accurately reproduce. MAE for pressure is 0.6 hPa, a negligible error. Similarly, a Spearman Correlation Coefficient of 0.99 shows that the model is capturing the pressure fluctuations perfectly. The IWV follows with a correlation of 0.95 and MAE of 1.01 kg m^{-2} . The model is capturing the thermodynamics at the MOSAiC site remarkably well. Interestingly, the temperature has a larger bias, the impact of clouds on the surface temperature may be one aspect the model is misrepresenting.

Vertical Profiles

For the vertical aspect, we can compare the model data with radiosondes (Maturilli et al., 2022a). Figure 7.5 shows the observed and modelled vertical profiles of specific humidity (QV) and temperature.

Overall the distribution of moisture is well captured. The model tends towards a less moist lower atmosphere ($< 2 \text{ km}$), with a bias in the lowest levels. The mean shows a difference of 0.6 g kg^{-1} in the lowest height bin (0-250 m). At higher levels (between 2 and 10 km), the model is too moist. Interestingly, the observed trend is the opposite behaviour compared to the European Centre for Medium-Range Weather Forecasts (ECMWF) Integrated Forecasting System (IFS) model evaluation during the MOCCHA

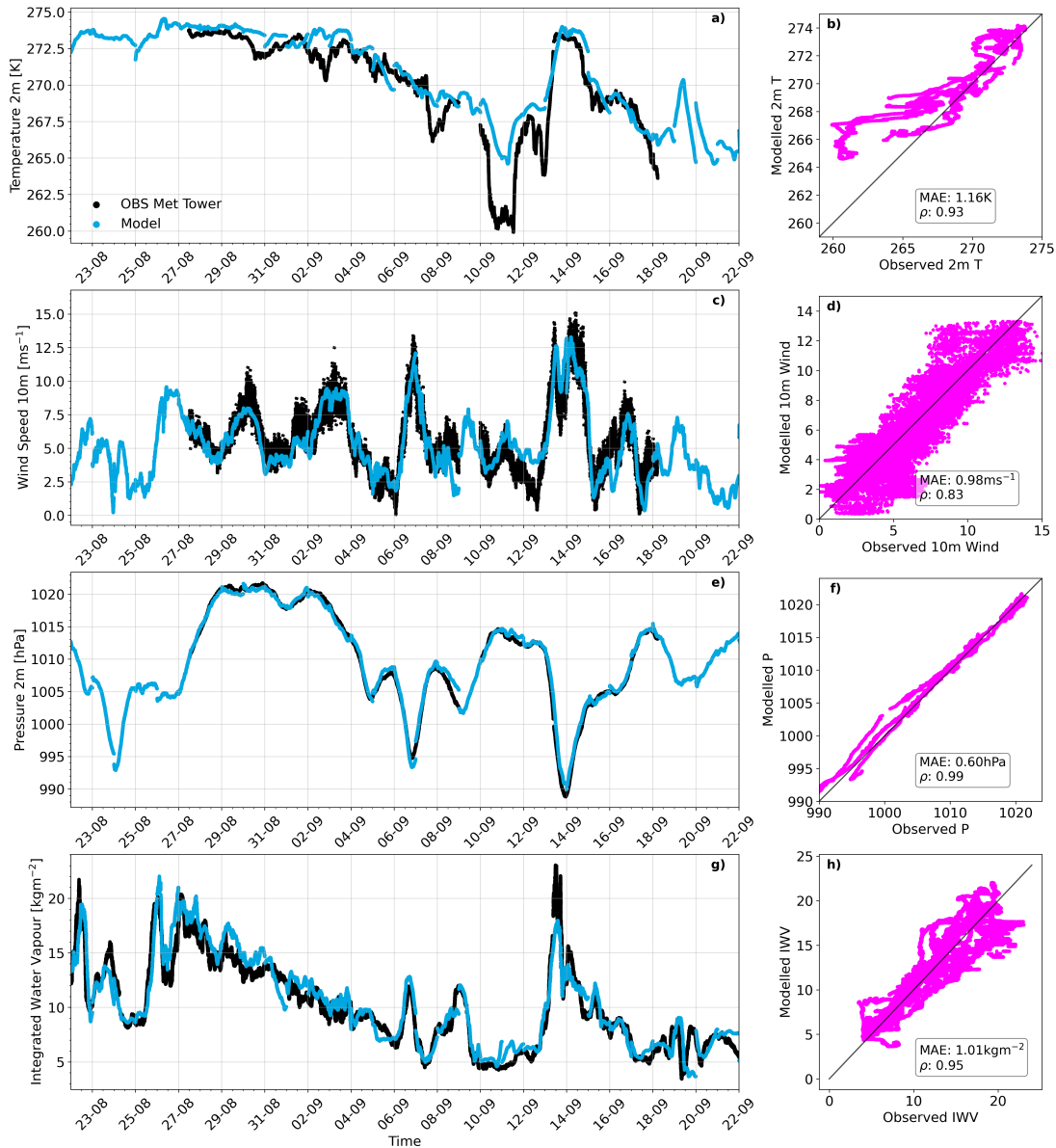


Figure 7.4: Time plots for surface variables at the MOSAiC site. Temporal evolution of the a) 2 m temperature, c) 10 m wind speed, e) 2 m pressure, and g) integrated water vapour (Walbröl et al., 2024). Observed vs modelled scatter plot of b) 2 m temperature, d) 10 m wind speed, f) 2 m pressure, and h) integrated water vapour (Walbröl et al., 2024), all showing the 1:1 line. Data in a)-f) are procured from Cox et al. (2023). Mean absolute error (MAE) and Spearman Correlation Coefficient (ρ) are shown in plots on the right.

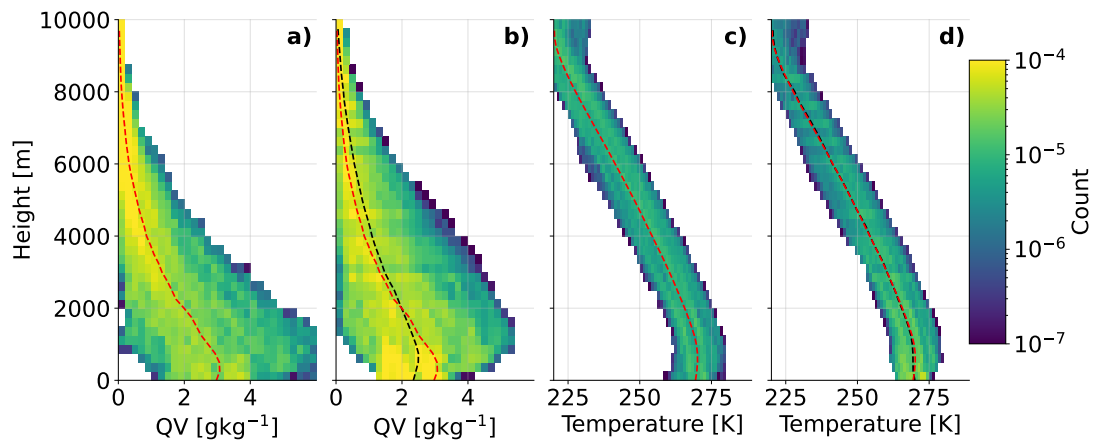


Figure 7.5: Specific moisture content with height from the a) radiosondes (Maturilli et al., 2022a) and b) the model data. Panel c) and d) show the observed temperature, also from the radiosonde, and model respectively. The mean is shown in each plot with a dashed line. The mean in the observations (red) is also shown on top of the model mean (black) in panels b and d for easier comparison. The model data contains profiles within two hours of each radiosonde.

campaign (Tjernström et al., 2021). A humidity inversion shows up in the mean between 250 m-750 m, while in the model it is less pronounced and a higher moisture content is found between 250 m-1000 m. Temperature profiles are better captured, where the model only fails to capture the lowest part of the atmosphere and the observed colder surface temperatures as previously discussed.

Cloud Representation

Moving into the cloud realm, column-integrated water paths of hydrometeors from the model and observations are compared in Fig. 7.6.

These box plots show the column integrated liquid water path (LWP) and the frozen water path (FWP) for the model and the two observational retrieval products Cloudnet (Engelmann et al., 2024) and ShupeTurner (Shupe, 2023) introduced in Chapter 4. We define a frozen water path, the combination of cloud ice, snow, and graupel (hail is negligible) column integrated water paths. This is a way for the model to account for what the retrievals include. The modelled LWP also contains integrated rainwater. The box plot shows the median in a line, while the interquartile range, the box itself, shows the distribution of the middle 50% of the data, between the 25th and 75th percentile. Thus, 25% of the data can be found within the upper and lower error bars. Maximum (and minimum) values are indicated by the head of the error bar and are calculated via $1.5 \cdot \text{inter-quartile range (IQR)}$. Values larger (or smaller) than this are named outliers and are not shown to simplify the interpretation. With the tunings performed (CCN and INP tunings, see above), the model produces less LWP and FWP than the observations. The model shows a larger spread in values for both LWP and FWP, indicating a more distributed cloud thickness than the observations portray. As we are

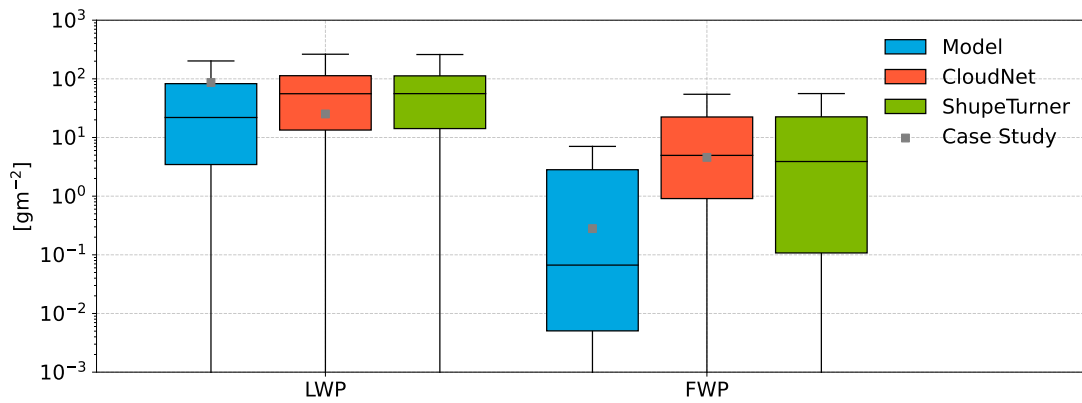


Figure 7.6: Box plots of liquid water path (LWP) including integrated rain and frozen water path (FWP, including cloud ice, snow, and graupel integrated water paths) for the model and the two observational retrieval products, Cloudnet (Engelmann et al., 2024) and ShupeTurner (Shupe, 2023) at the MOSAiC site. The case study markers show the *SIP* simulation and the mean observational values (Engelmann et al., 2023) from the case study in Chapter 5. The box plots show the 25th to the 75th quartile, defined as the inter-quartile range (IQR). The median is shown with a black line and the error bar shows the maximum values defined as $1.5 \cdot \text{IQR}$ (minimum values are defined similarly ($\cdot - 1$) but reach very low values here. Values larger (or smaller) than this are named outliers and are not shown to simplify the interpretation.

here looking at the full column integration, this may be due to the difference between the observational detection limit and the model, where the limit for hydrometeors is $10^{-20} \text{ kg kg}^{-1}$ allowing for thinner clouds in the column (that may not be quantified as a cloud layer by the algorithm). The modelled LWP median (15 g m^{-2}) is within the IQR of the observational products. The observations are similar to each other ($\sim 55 \text{ g m}^{-2}$ median), which we expect as the LWP is an observed quantity from the Microwave Radiometer. Overall we see a larger LWP than IWP, which may be expected during this time of the year for low clouds with temperatures seen in Fig. 7.5.

The FWP is greatly reduced in the model compared to observations, by more than an order of magnitude (model median; 0.04 g m^{-2} , 5 g m^{-2} and 4 g m^{-2} for ShupeTurner and Cloudnet respectively). It is unlikely the reduction in the immersion freezing routine is causing this as only small differences were seen (Ch. 7.1) across the model domain. The propensity for cold precipitation in the model was shown in Fig. 7.3 and may cause the FWP to diminish quicker. This is further discussed in Ch. 7.3.

The values for the case study presented in Chapter 5, are also shown in Fig. 7.6. Here, we only plot the values for the *SIP* simulation and the mean observed values from the Cloudnet retrieval in grey boxes. The observed values from the case study are representative in terms of IWP but are slightly lower than the median LWP of the monthly distribution. The modelled LWP extend to the 75th percentile and for FWP within the IQR of the simulations performed here.

7.3 Summary & Discussion

In this chapter, the performance of the ICON model is explored in 32 consecutive 24-hour simulations over the MOSAiC site during August-September 2020. A new immersion freezing parameterisation for the early-autumn Arctic is formulated and evaluated against observed cloud variables.

The new immersion freezing parameterisation is based on data from eight Arctic stations and campaigns during August-September. An exponential fit to the entire data set, extended to 268 K, and an Arctic early-autumn fit, where the warm temperature INPs are represented by a polynomial, are evaluated against the Hande et al. (2015) parameterisation. The improvements include representing the warm ($261 \text{ K} < T < 268 \text{ K}$), oceanic INPs better and reducing the large amount of dust present in the European parameterisation. A 17% increase in cloud ice number concentration at warm temperatures ($T > 261 \text{ K}$) is found for single-layer clouds. The differences seen within the domain are due to local processes but the addition of such low INP concentrations at high temperatures does not greatly impact the domain average. This was seen in Chapter 5 and can now be more regionally observed.

The model setup is evaluated at the MOSAiC site. Modelled atmospheric variables correlate temporally with the observed variables. Apart from a warm bias in surface temperatures, the model captures the local thermodynamics remarkably well. With the local data assimilation of the radiosondes, similarities are expected. However, as the model runs for 24 hours, deviations may be found after the initialisation. The temperature bias, the incapability of capturing cold surface temperatures, has been seen in other model evaluations (Tjernström et al., 2021). This study by Tjernström et al. (2021), on the biases in the ECMWF IFS model, shows a near-surface 1 K bias during the Arctic Ocean 2018 (MOCCHA) campaign (with assimilated radiosoundings), indicating that we are missing something in the model representation of the sea ice surface.

In regards to clouds, the model temporally captures the overall features of the observed clouds with a bias towards more frequent precipitation and a predominantly liquid boundary layer cloud. Conversely, the model underestimates both column-integrated LWP and frozen water paths ($\text{FWP} = \text{IWP} + \text{SWP} + \text{GWP}$). We evaluate the microphysics against the Cloudnet (Engelmann et al., 2024) and ShupeTurner (Shupe, 2023) retrievals. LWP in the model is underestimated by a factor of about 4 while IWP is underestimated by 2 orders of magnitude. An underestimated LWP is likely due to the formation of rain, in turn, due to the reduction in droplet activation that allows for cloud droplets to reach larger sizes. The lack of ice in the model follows the case study in Chapter 5 and previous studies on Arctic clouds (Morrison et al., 2009; Fridlind and Ackerman, 2017; Stevens et al., 2018). Due to the negligible differences using a different parameterisation, we believe this is not impacting the mass concentrations of ice to this degree. However,

we may be misrepresenting the ice due to other factors. The lack of vertical profiles may introduce a (too low) INP bias in the ground-based measurements limiting the primary ice nucleation in the model. The model also has a tendency for snow aggregation due to collisions, this would serve as a quick sink for frozen hydrometeors and act to diminish the clouds before they arrive at the ship location. We connect the distribution of LWP and FWP to the case study in Chapter 5. The observed values from the case study are representative in terms of IWP but are slightly lower than the median LWP of the monthly distribution. The most realistic set-up, with an observed INP concentration and active SIP, produces an LWP in the higher end of the simulated cases here. The modelled FWP is a well-representative case, somewhat above the median FWP of this long-term simulation. This might indicate that the lack of FWP in the simulations performed in this chapter may be due to too low primary ice nucleation rates, i.e. that the surface INP does not represent the in-cloud INP population, and/or that the clouds, in general, require efficient SIP present.

8 | REGIONAL LONG-TERM ARCTIC SIMULATIONS OF MULTILAYER CLOUDS

Multilayer clouds seem to be frequent in the Arctic region. However, this conclusion is drawn from the few, sparse campaigns that have made it to the high Arctic while satellite studies that only cover up to 82°N do not show an increase in MLCs towards the north (see Ch. 1). To fill in gaps in our knowledge of the MLC occurrence frequency in the Arctic, this chapter explores the occurrence frequency in the model world by simulating the Arctic sector, 71°N to 90°N (Fig. 4.1) for 32 days. This model setup was evaluated in Chapter 7 and in this chapter, the focus will be on the frequency of multilayer clouds. We further investigate the microphysical differences between single and multilayered clouds in the Arctic concerning integrated values, cloud height, temperature, in-cloud processes, and their radiative impact. The aim is to further deepen our understanding of how these clouds can be better represented in models, and to what degree they can be distinguished from single-layer clouds.

The occurrence of MLCs can be determined from the LWC, IWC, and relative humidity (RH) after making a few refinements to how we define a cloud layer. This algorithm is outlined in Chapter 4.1.2 and evaluated in Appendix C.1. The discussion on what makes a cloud a cloud, an observed limit due to instrumentation limitations, a modelled lower limit or when they start to interact with radiation is beyond the scope of this study (see Spänkuch et al. (2022)) and we will keep in mind the limitations a cloud mass threshold brings to the classification of MLCs. As we will also evaluate the radiative impact of these cloud layers, a cloud mass threshold of $10^{-9} \text{ kg kg}^{-1}$ is used. This is in line with the radiation solver's definition of when a cloud interacts with radiation (Rieger, 2019) and is more strict than some previous studies that use a mass threshold of $10^{-10} \text{ kg kg}^{-1}$. We combine this with an RH_i threshold of 100% to quantify the MLC occurrence frequency.

The main microphysical interaction between MLCs is the seeder-feeder effect, whereby frozen precipitation falls from an upper cloud into a lower layer. The seeding definition for the model data is defined in Chapter 4.1.2. Seeding has been shown to have great

impacts on the precipitation from lower layers and we further study the frequency of seeding and the microphysical impacts this has within this chapter.

To compare the model with radiosonde and radiosonde-driven variables (such as the MLC frequency from the observational algorithm by Vassel et al. (2019)), only profiles within two hours of the radiosonde launch are used, as introduced in Ch. 4.3.1.

8.1 Multilayer Clouds at MOSAiC

In this section, the multilayer cloud statistics and characteristics are evaluated between the model and observations. The methods of comparing these are defined in Chapter 4.3.1.

Occurrence Frequency

The MLC occurrence for the MOSAiC site is presented in Fig. 8.1. Figure 8.1a shows the model while Fig. 8.1b shows the observed distribution of clear sky, single-layer, and multilayer clouds using the algorithm by Vassel et al. (2019).

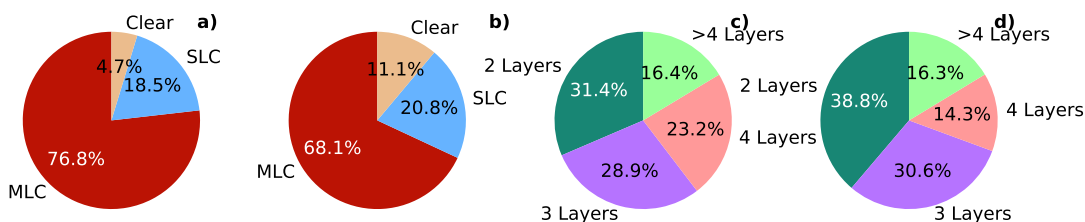


Figure 8.1: Pie chart showing the multilayer, single-layer, and clear sky distribution for the model at the MOSAiC site a) and observations b). The MLC layer distribution is shown for the model in c) and observations in d) and only profiles within two hours of the radiosonde launch are used.

The full set of model data over the MOSAiC site (including all time steps) is very similar to this subset of model data and is shown in Fig. C.2a. A bias towards a higher occurrence frequency of MLCs by the model can be seen with a modelled 76.8% versus an observed MLC occurrence of 68.1%. The difference may be derived from the underestimation of clear sky profiles which differs from the model (at 4.7% to 11.1% in the observations), while the single-layer statistics are very similar (18.5% vs 20.8%). Looking at the distribution of the number of cloud layers, in Fig. 8.1c-d, the model has higher four-layer statistics while two-layer clouds are underestimated by the model. Three-layer clouds and more than 4 layers are very similar to the observed values. To be noted, this does not indicate any temporal correlation.

The large difference in the frequency of occurrence of MLCs and SLCs gives 13411 modelled profiles of MLCs (these are within two hours of all the radiosondes) and only 3227 SLCs compared to the full dataset of 34852 MLCs and 8957 SLCs (these are shown in Fig. C.2a,e).

Cloud Properties

The column-integrated water paths for the model and observations for single and multilayer cloud profiles are shown in Fig. 8.2.

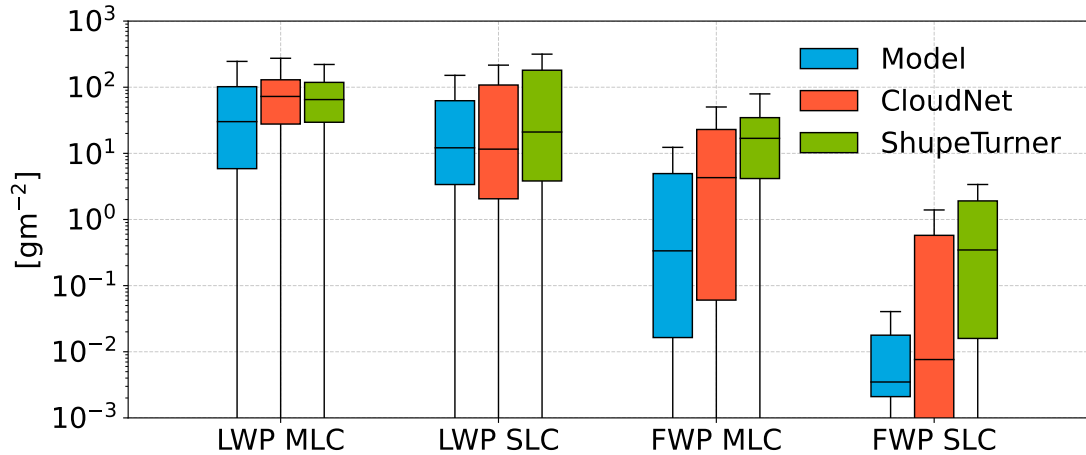


Figure 8.2: Box plots of liquid water path (LWP) including integrated rain and frozen water path (FWP, including cloud ice, snow and graupel integrated water paths) separated into multilayer clouds (MLC) and single-layer clouds (SLC) for the model and the two observational retrieval products, Cloudnet (Engelmann et al., 2024) and ShupeTurner (Shupe, 2023) at the MOSAiC site. The box plots of the observations are 2-hour means from the radiosonde launch while the model includes all profiles within those two hours.

The column-integrated water paths from the model are consistently underestimated (as for the full dataset in Fig. 7.6) but have medians within an order of magnitude from the observations. The observations agree well for LWP while large discrepancies between the retrieval algorithms can be seen for the integrated ice. This is most likely due to the temperature assumptions in the retrievals (see Chapter 4.2.1). Similar trends can still be noticed. Both the LWP and FWP for single-layer cloud profiles are lower than for multilayer cloud profiles. With microphysical interactions between multilayer clouds, such as the seeder-feeder interaction, we would expect multilayer clouds to contain more ice which may be why the MLC profiles have more than one order of magnitude more FWP than the single-layer cloud profiles. On the other hand, with a higher frequency of seeding, we would expect to see more glaciated clouds. This in turn should be visible in a lower LWP, this is not something we observe here. The modelled individual hydrometeor water paths are shown in Fig. 8.3. Here, the dominance of LWP compared to RWP and similarly for IWP and FWP is shown. An increase in precipitation hydrometeors (rain, snow, and graupel) can be easily seen for MLC profiles. The precipitation increase amounts to (about) an order of magnitude (factor of 8.2), governed by the large rainwater path (increase in frozen precipitation is a factor of 6), while the increase in IWP is 2 orders of magnitude. Snow and graupel concentrations are in general low with medians below 10^{-5} g m^{-2} .

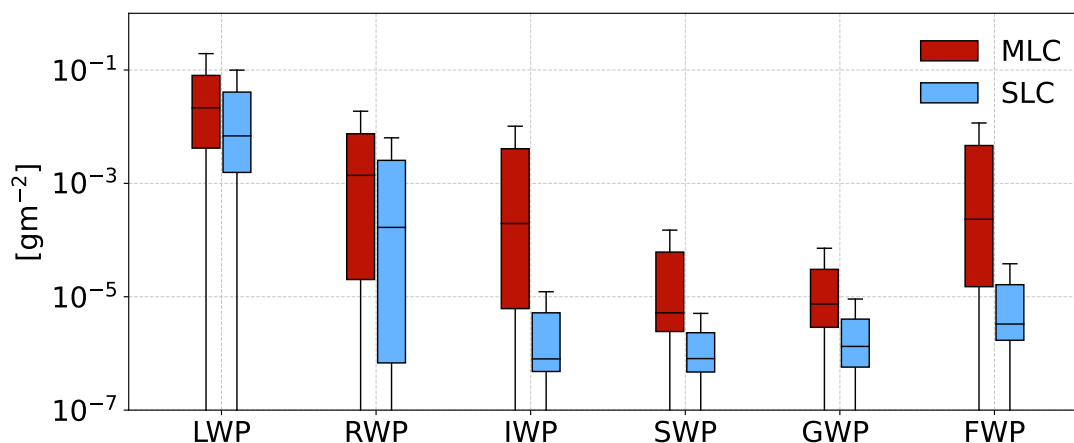


Figure 8.3: Modelled individual hydrometeors in box plots of liquid water path (LWP), rainwater path (RWP), ice water path (IWP), snow water path (SWP), and graupel water path (GWP) for MLCs and SLCs.

Cloud Characteristics

The cloud thickness of each MLC and SLC present in the model and observations are shown in Fig. 8.4a. The cloud top and base heights for MLCs and SLCs, identified as supersaturated layers in both the observational and model algorithms, during the 2-hour observational window, are then presented in Fig. 8.4b. The full set of model data is shown in Fig. C.4 and is very similar to this subset.

Cloud thickness for MLCs is slightly larger (model: 446 m, obs: 511 m) than for SLCs (model: 337 m, obs: 339 m). The trend can be seen in both the model and the observations. Modelled MLCs may exist as thin layers (less than 100 m thick) and a 12% occurrence of these is found. The modelled thickness of both SLCs and MLCs have a larger spread indicating thicker clouds present in the model, this is quite interesting as the model underestimates hydrometeor water paths in general. The large values found in thickness may belong to outliers in integrated water paths.

A similar trend in both the model and observations can be seen with higher cloud tops and bases for multilayer clouds than single-layer clouds in Fig. 8.4. The difference between MLC and SLC median cloud tops for the model (observations) is 2337 m (2055 m) while the cloud base difference is 2001 m (1861 m). Interestingly, the median cloud top and base are always higher in the observations than in the model. The single-layer clouds are thoroughly constrained to the lowest part of the troposphere. 75% of the modelled cloud tops and bases are within the first kilometre of the atmosphere. The observations also show low cloud bases but the median is around 1 km.

Cloud top height suppression, due to the presence of an overlaying cloud layer, can be seen in the 1st layer CT and CB in Fig. 8.4. The median cloud top height difference between SLC and 1st layer MLC, i.e. the suppression in cloud top height, is 141 m and 304 m in the model and observations while the CB values are 104 m and

516 m respectively. Discrepancies in this reduction in cloud height may be due to the skewness in modelled SLC cloud tops (and bases). In the observations, the SLCs are less constrained to the lowest kilometre and thus the median, and the suppression in height, are larger.

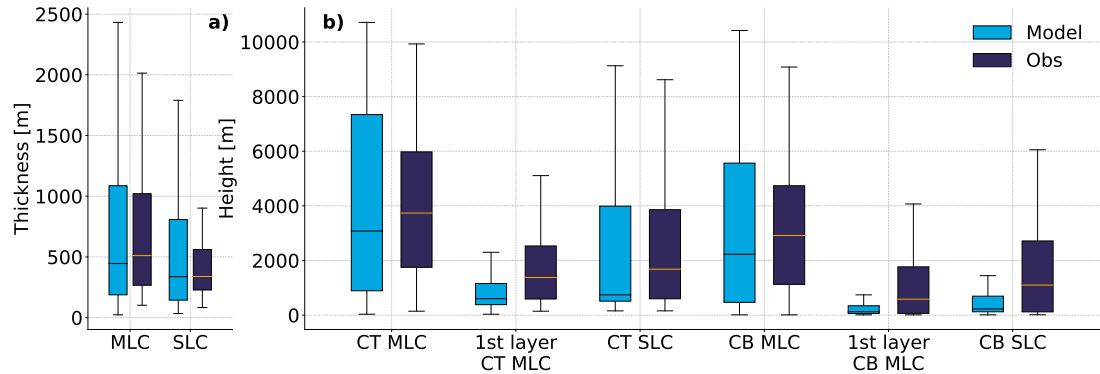


Figure 8.4: a) Cloud thickness for MLCs and SLCs for the model (light blue) and observations (dark blue). b) Cloud top (CT) and cloud base (CB) for the respective cloud systems. The cloud boundaries are determined in the observational MLC algorithm from the relative humidity measurement. The first layer (lowest cloud in the MLC system) cloud top and base from the MLC profiles are also extracted from the dataset.

Radiation

The relative radiative impact of MLCs and SLCs is investigated. We use the Met City data (Cox et al., 2023), collocate it in time to the radiosonde data and use a two-hour mean. Due to filtering for quality-controlled data, only 11 SLC radiation profiles remain, these all occur between the 6th and 19th of September. Thus, we add two Atmospheric Surface Flux Stations (ASFS), ASFS30 and ASFS50, that cover the entire time. The box plots in Fig. 8.5 show the net radiation (see Chapter 3) and indicate a small but significant difference between MLC and SLCs. The difference is expected as we see large differences in LWP, the major impact on radiation as liquid clouds tend to be optically thicker than ice clouds (Cesana et al., 2023). Interestingly, net radiation on the surface with overlaying single-layer clouds has negative medians, with maximum values reaching larger negative values than MLCs. The modelled SLC, and ASFS, have negative medians with maximum and IQR reaching positive net radiation. A negative net surface radiation indicates a cooling of the ground. The lack of positive values from the Met City data may be due to the timing of the SLC profiles which occur when the SW radiation is lower, reducing the heating in the column. MLCs have a median net positive radiation for the model and the ASFS while the Met City has a negative median. A full domain evaluation on the cloud radiative effect (CRE) of MLCs and SLCs is provided in Chapter 8.3.

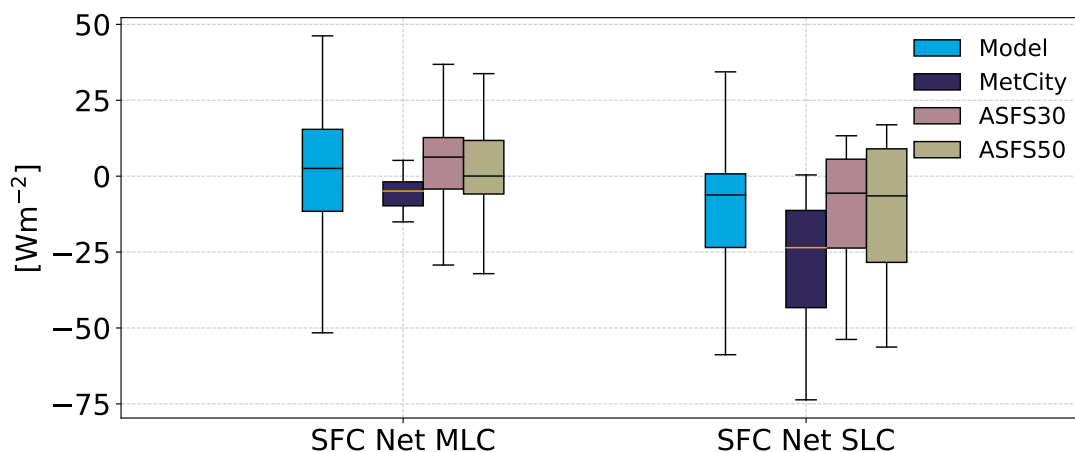


Figure 8.5: Surface net radiation for MLCs and SLCs.

Seeding

From the model multilayer algorithm, out of the 13411 vertical profiles, 44786 cloud layers are found within the 2-hour window of the radiosondes. We find that about half of these (48.2%), have been seeded. This implies that they have combined snow, graupel, and cloud ice mass above 10^{-9} kg kg $^{-1}$ (seeding mass threshold) falling into the cloud from a layer above. A large dependency of this threshold is observed and the seeding frequencies using different seeding mass thresholds are tabulated in Table 8.1. From the observational algorithm, we find that with $400 \mu\text{m}$ ice crystals, 46.4% of MLCs (have the potential to) seed the layer below. The respective (potential) seeding frequencies for ice crystals of sizes $200 \mu\text{m}$ and $100 \mu\text{m}$ are tabulated in Table 8.1. We do not currently possess an evaluation method that can single out which ice crystal size is more likely to occur and seed the lower layer, more work on this will be done in the future. In general, we can presume that a high seeding frequency is likely occurring in these Arctic multilayer clouds.

Model (10^{-9})	Model (10^{-8})	Model (10^{-7})	Model (10^{-6})	Obs ($400\mu\text{m}$)	Obs ($200\mu\text{m}$)	Obs ($100\mu\text{m}$)
48.2%	28%	18%	10%	46.4%	32.7%	18%

Table 8.1: Seeding occurrence for the model, with the seeding mass threshold indicated in brackets with units kg kg $^{-1}$, and observations, with the ice crystal size used for the sublimation calculations marked within the brackets.

8.2 Modelled Microphysical Differences between MLCs and SLC at the MOSAiC Site

To further distinguish differences between non-seeded and seeded clouds, in this section, we explore these clouds within the model world. We have used the 10^{-9} kg kg $^{-1}$

mass threshold for seeding and we use the 2-hour profiles surrounding the radiosonde launch as they have been shown to be representative of the full data set.

Cloud Characteristics

Figure 8.6 shows the cloud thickness, cloud top height and temperature for SLCs and seeded and non-seeded MLCs. Seeded clouds can be seen to be thinner than non-seeded clouds while having a warmer cloud top temperature. Median cloud thicknesses are 492 m, 398 m, and 337 m for non-seeded and seeded MLCs, and SLCs, shown in Fig. 8.6a.

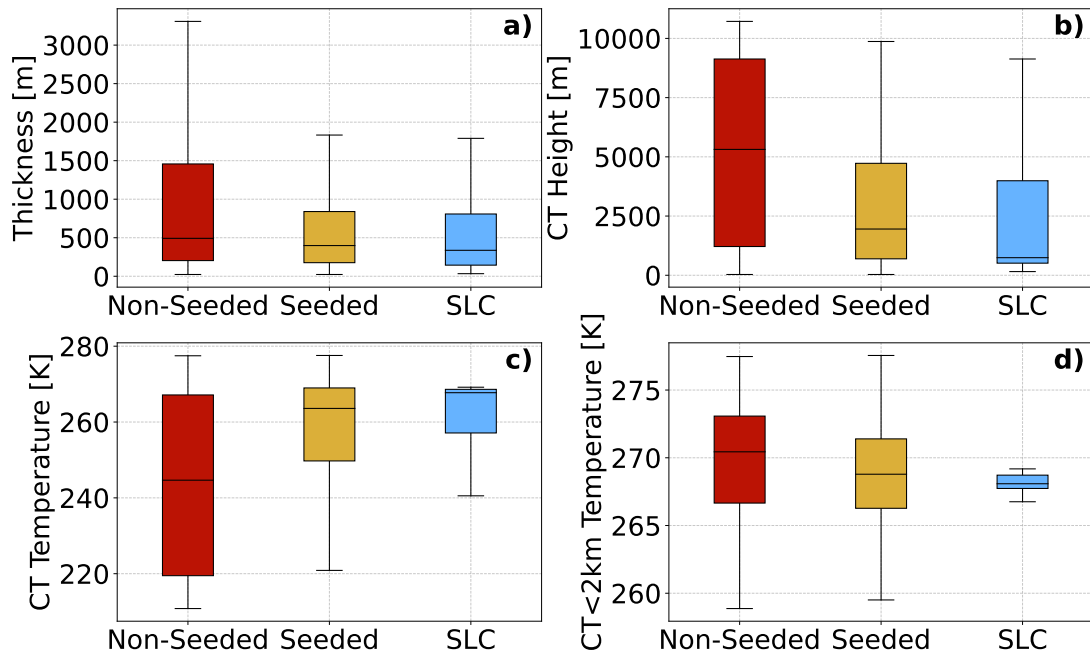


Figure 8.6: a) Cloud thickness, b) cloud top height, c) cloud top temperature, and d) cloud top temperature for clouds below 2 km for SLCs and non-seeded and seeded MLCs.

In Fig. 8.6c, with a median cloud-top temperature of 244K, almost 50% of the non-seeded MLCs exist in the homogeneous freezing ($T < -38^{\circ}\text{C}$) range and would likely be in the ice phase. Meanwhile, seeded clouds have a median of 264 K while SLCs have a very skewed distribution with a majority of the clouds existing in the temperature range just below freezing with a median of 267K. Cloud top height, in Fig. 8.6b, follows the same pattern, with non-seeded cloud top medians at 5313 m, while seeded clouds and SLCs have medians of 1951 m and 742 m respectively. The SLC cloud top heights are skewed towards low cloud tops indicating that the majority of SLCs appear as low clouds. Indeed, SLCs are rarely found as a cirrus cloud, only 20% of the SLC profiles have a cloud top above 7 km, while the occurrence below 2 km is 72%. Figure 8.6d, shows the cloud top temperature for clouds below 2 km. About 50% of seeded clouds exist below this threshold and about a third of non-seeded clouds. Non-seeded clouds can now be seen with a warmer cloud-top temperature than seeded clouds (and SLCs).

Integrated Water Path

The in-cloud integrated hydrometeors for SLCs for seeded and non-seeded clouds are shown in Fig. 8.7. Here, all water paths are integrated within the cloud boundaries, to gauge the difference between MLC and SLC and the impact of seeding. LWP are very similar between the three cloud types with a higher LWP for SLC (median at 11.9 g m^{-2}) than MLC (5.7 g m^{-2} for non-seeded and 7.2 g m^{-2} for seeded), but all with overlapping IQRs. Single-layer clouds have a higher rain content, by about an order of magnitude compared to non-seeded MLCs. Seeded MLCs have 3 times higher (lower) rain content than non-seeded MLCs (SLCs).

In the IWP, the seeded MLCs take precedence. Between SLC (median at 0.0004 g m^{-2}) and non-seeded MLCs (0.0015 g m^{-2}), a four-fold increase can be seen while the seeded MLCs reach 0.016 g m^{-2} , a 45-time (11) increase from SLC (non-seeded MLC). Snow and graupel show similar patterns but with overall smaller values with an approximately 2-fold increase in snow and graupel for seeded MLCs compared to both SLC (97% increase) and non-seeded MLC (123% increase). A similar plot is shown for a seeding mass threshold of $10^{-8} \text{ kg kg}^{-1}$ in Fig. C.5.

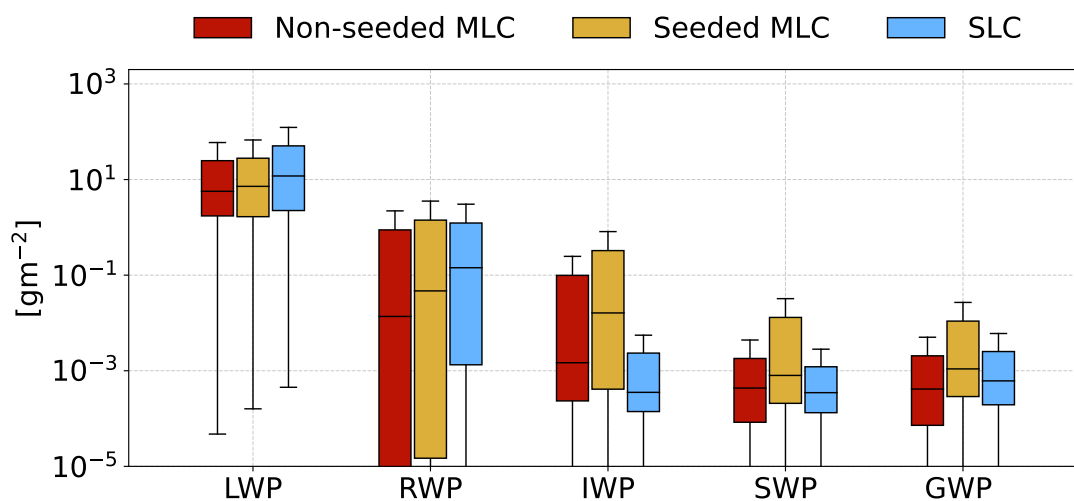


Figure 8.7: In-cloud integrated water paths for non-seeded and seeded MLCs and SLC.

Cloud Phase

The cloud-top supercooled liquid fractions (SLF) of seeded and non-seeded MLCs and SLCs are plotted vs temperature in Fig. 8.8.

The large difference in sample size makes a qualitative comparison difficult but the mean SLF (per 2 K temperature bin) can be evaluated. An SLF value of 1 indicates a fully liquid cloud top while 0 indicates a glaciated cloud. Numbers between indicate a mixed phase with ice-dominated ($\text{SLF} < 0.5$) or liquid-dominated ($\text{SLF} > 0.5$) mixed-phase cloud tops. All three cloud types tend to be predominantly in the ice phase

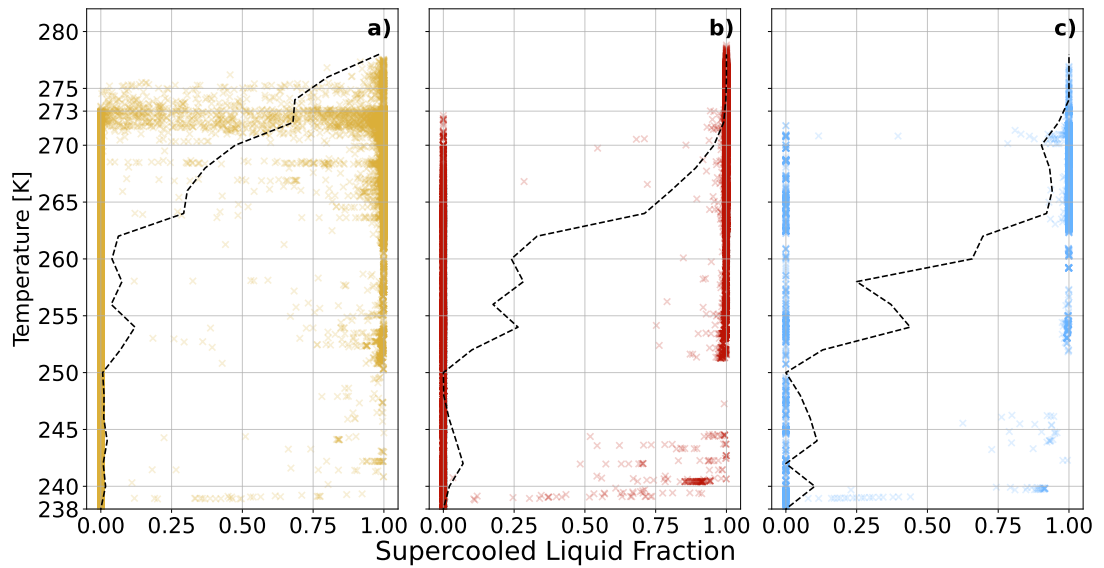


Figure 8.8: Supercooled liquid fraction (SLF) vs temperature for cloud tops at the MOSAiC site. a) Seeded MLCs, b) non-seeded MLCs, c) SLCs. The mean SLF in the dashed line is binned in 2 K bins.

below 250 K. The slope of the mean SLF can then be evaluated. In general, the SLCs (Fig. 8.8c) tend to have a higher SLF at colder temperatures, while MLCs stay mixed-phase at warmer temperatures. Non-seeded clouds (Fig. 8.8b) behave closer to SLCs with a constant bias towards lower SLF for each temperature bin. Seeded clouds (Fig. 8.8a) tend to be predominantly in the ice phase for a large range of temperatures (SLF below 0.5 until 270 K) and only become fully liquid above melting.

The ice phase dominates both seeded and non-seeded clouds with ice fractions of 71% and 62% respectively. Non-seeded MLCs have a higher fraction of liquid phase cloud tops (8%) than seeded (0.01%) while the mixed-phase fractions are similar (seeded: 29%, non-seeded: 30%). The single-layer cloud tops (8957 clouds) are on the other hand predominantly mixed-phase (65.2%) and have a higher ice-cloud fraction (34.0%) than liquid (0.8%). The SLC bases are similar to the MLC and predominantly ice.

Microphysical Process Rates

Here, we explore the process rates for multi and single-layer clouds. Microphysical process rates accumulated with time are shown as integrated values (in-cloud) in Fig. 8.9.

Fig. 8.9a, shows riming, aggregation, and vapour deposition where the seeded MLCs have a higher median than the others. Non-seeded clouds and SLCs are very similar with only small biases towards higher riming for SLCs, likely due to the higher rain and liquid water content within these clouds. The largest increase for seeded clouds can be seen in the aggregation with a 50-time increase in median rates, while vapour deposition increases by a factor of five. Riming increases by a factor of 12 and two for non-seeded and SLCs respectively. Figure 8.9b shows the cloud droplet activation and

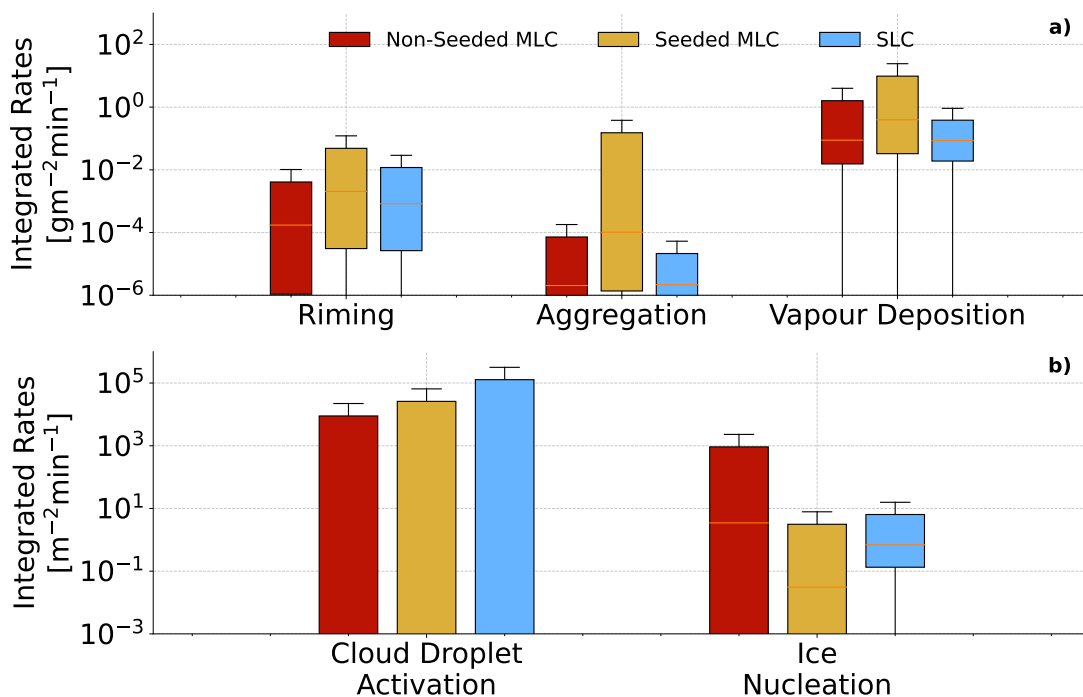


Figure 8.9: In-cloud integrated microphysical rates for SLCs, non-seeded and seeded MLCs. a) Shows riming, aggregation, and vapour deposition onto ice, snow, and graupel while b) shows nucleation rates of cloud droplets and heterogeneous ice nucleation.

ice nucleation rates. Median values for cloud droplet activation are very low but mean values for SLCs are more than double than for seeded and non-seeded clouds. This increase in activation for SLCs is due to the more positively skewed vertical velocity distribution, shown in Fig. C.6. For ice nucleation, Fig. 8.9b, non-seeded clouds have the highest median, double the rate of SLCs and five times larger than seeded MLCs.

8.3 Multilayer Clouds Across the Arctic

Here, we present the large-scale characteristics, impacts, and occurrences of multilayer clouds, with a focus on the open ocean and sea ice-covered regions. Due to a lack of satellite products above 82°N, this is the first vertically resolved cloud product in this region and while riddled with assumptions and biases is the closest to full Arctic coverage we can provide.

Occurrence Frequency

Figure 8.10 shows the statistics of multilayer clouds, single-layer, and clear sky over the entire region. MLC and SLC occurrence is 67% and 23%, respectively, using the $10^{-9} \text{ kg kg}^{-1}$ mass threshold.

While highly sensitive to the thresholds and model assumptions used, we may say with certainty that the Arctic has a high frequency of multilayer clouds during the

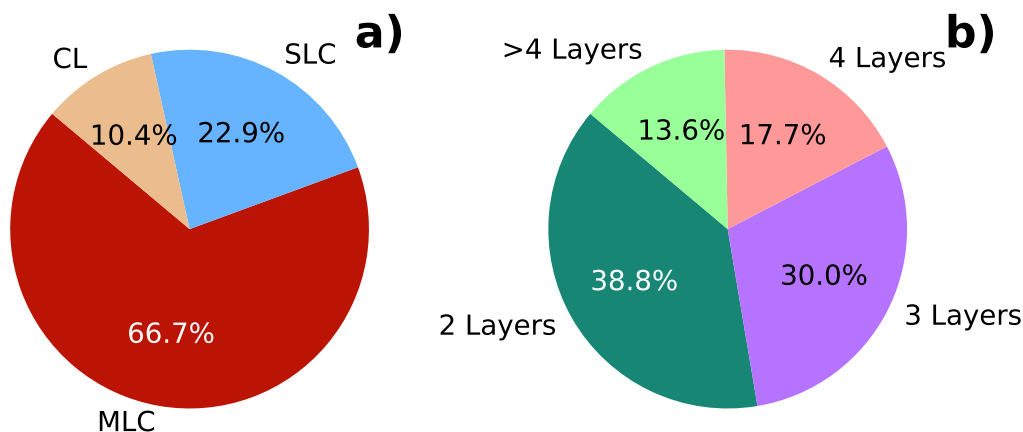


Figure 8.10: a) Full domain occurrence frequency of multilayer, single-layer, and clear sky. b) Distribution of the number of cloud layers for MLCs.

Autumn of 2020. Separating the MLC fraction, in Fig. 8.10b, into the number of layers in each profile we see a high frequency of two (38.8%) and three-layered structures (30%) with about half as many 4-layers (17%), surprisingly, a quite high value of 13.6% occurrence for systems with more than 4 layers can be seen.

The spatial distributions of multilayer and single-layer clouds during the 32 days simulated are presented in Fig. 8.11. Here, we notice the smooth distribution of MLCs over the Arctic region, with less frequent MLC occurrence ($\sim 50\%$) towards lower latitudes and the coastlines. The same plot with a colour bar covering 0-100% is shown in Fig. C.7. While reduced, the MLC occurrence is still substantial across the entire domain and shows no clear latitudinal dependency. The single-layer spatial occurrence in Fig. 8.11b is more evenly distributed, with a small increase in occurrence towards the coastlines and a decrease towards the high-Arctic. The opposite behaviour to the MLC occurrence.

Cloud Phase

The cloud phase is explored using the supercooled liquid fraction (SLF). In Fig. 8.12 the SLF (Chapter 3.2) is shown for a subset of the data of the full region. 10^6 random data points are taken from 20 random output files and are plotted against temperature. MLC (Fig. 8.12b) and SLC (Fig. 8.12d) (cloud) bases exist fully in the ice phase up to 273 K after which the SLF quickly goes up to 1, indicating a purely liquid state. This is expected for precipitating ice and mixed-phase clouds as the larger frozen hydrometeors would fall and grow through the cloud layer through vapour deposition, aggregation, and riming. In contrast, the cloud tops are significantly different. The implications include that MLCs cloud-tops (Fig. 8.12a) tend to stay more ice-dominated for a larger range of temperatures than SLCs (Fig. 8.12c). SLCs become liquid-dominated (SLF > 0.5) around 260 K, while MLCs remain ice-dominated until about 267 K. It is interesting to

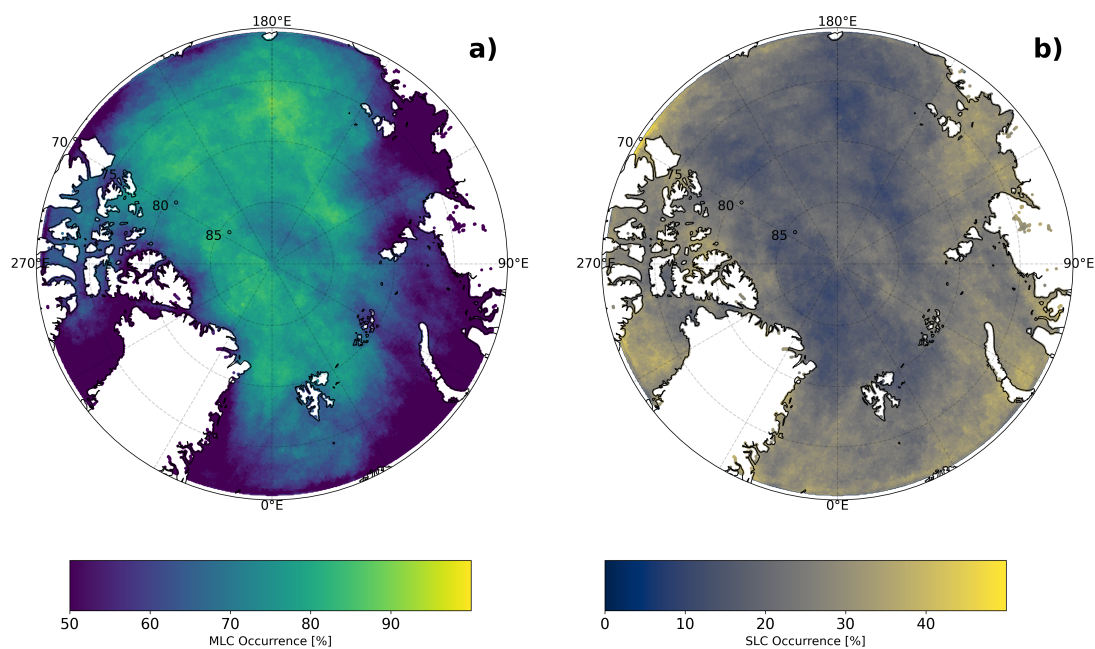


Figure 8.11: Spatial occurrence of MLC a) and SLC b) over the Arctic domain.

note that the MOSAiC site shows a similar pattern, indicating that the ship is somewhat representative of the Arctic region.

Radiative Impact

MLCs have been shown to exert a strong heating over lower Arctic latitudes (L'Ecuyer et al., 2019). Here, we explore their impact on the entire Arctic domain. We calculate the Cloud Radiative Effect (CRE, Chapter 3.3) for single and multilayer clouds. The use of CRE allows for the quantification of the radiative impact of clouds in comparison to a clear sky. This is plotted in Fig. 8.13. Similar patterns can be seen between the cloud types with a strong surface warming in the longwave and a weak cooling in the shortwave. The multilayer clouds, however, have a much stronger heating in the LW (medians at 63 W m^{-2} vs 50 W m^{-2}), while a slightly stronger cooling in the SW, leading to a median net positive CRE of 43 W m^{-2} vs the 22 W m^{-2} for single-layer clouds.

8.4 Summary & Discussion

In this chapter, the occurrence frequency of multilayer clouds and their microphysical and radiative differences compared to single-layer clouds are explored in 32 consecutive 24-hour simulations over the Arctic region.

Multilayer clouds are frequent across the Arctic sector during our simulation period. A 67% occurrence frequency is found across the region with a higher frequency of

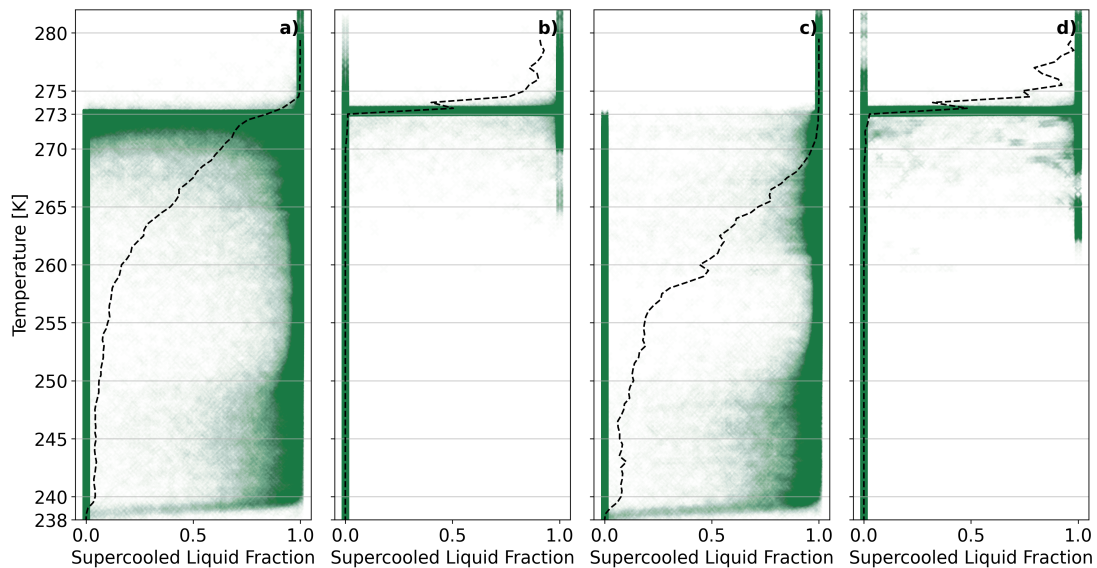


Figure 8.12: Supercooled liquid fraction (SLF) for the entire Arctic region for a) multilayer cloud tops, b) multilayer cloud bases, c) single layer cloud tops, and d) single layer cloud bases. The mean is shown in a black dashed line, binned in 2 K bins.

occurrence towards the higher latitudes. At the MOSAiC site, an observed MLC occurrence of 68% is found using the MLC detection algorithm by Vassel et al. (2019) while the model MLC algorithm identifies a 77% occurrence frequency. This shows a larger frequency of MLCs in the high-Arctic compared to the entire region. However, a concrete conclusion would require a longer temporal dataset. The lack of fog layers in the observational algorithm introduces a bias towards the model and the discrepancy may be due to fog or thin, high, layers that are not captured due to instrument limitations. The model is also too moist at higher altitudes (see Ch. 7, Fig. 7.5), which might enable cloud formation and more shallow layers. Overall, two layers are the most frequent ($\sim 35\%$) followed by three layers ($\sim 30\%$) for both the model and observations. Previous studies using the Vassel et al. (2019) algorithm have found a high-Arctic occurrence frequency in line with these values. During the MOCCHA campaign in 2018, Vüllers et al. (2021) found a 54% occurrence during August-September, while at lower latitudes 29% was found on Svalbard during a full-year analysis (Vassel et al., 2019). Both column-integrated LWP and FWP are higher for MLCs. This may add to the hypothesis that most of these cloud layers form independently of each other. Instead of splitting from a single-layer cloud as hypothesised by Herman and Goody (1976), clouds are piled on top of each other, adding mass to the column.

A discussion on the limitations of the model algorithm is warranted. The choice of mass threshold for determining the presence of a cloud layer is what governs the occurrence frequency. In the evaluation of the algorithm (Appendix C.1), the MLC frequency changes from 76% to 52%, when changing the mass threshold between $10^{-9} \text{ kg kg}^{-1}$ to $10^{-6} \text{ kg kg}^{-1}$. While the observed MLC occurrence (67%) fits between

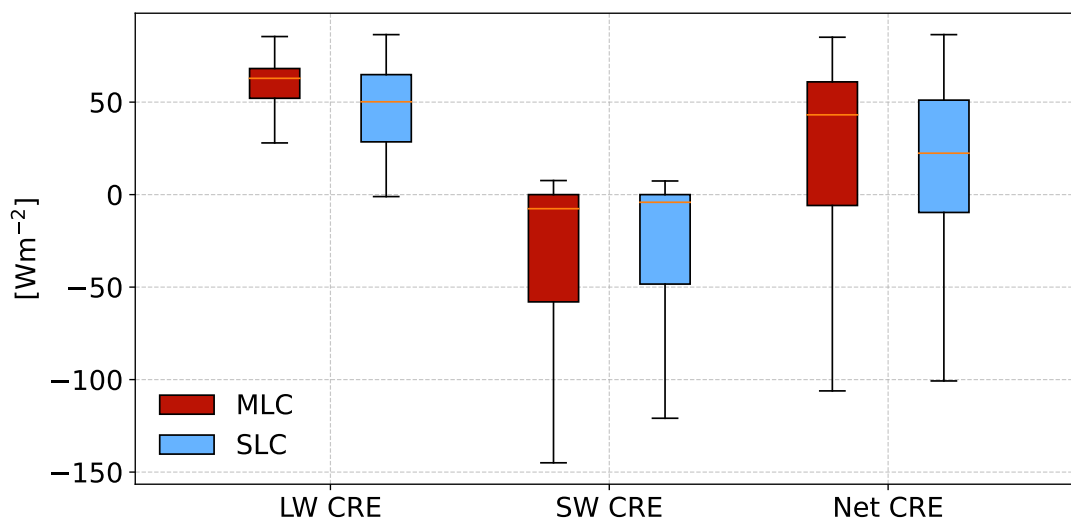


Figure 8.13: Cloud radiative effect over the Arctic region. The LW component, SW component, and net effect are shown for MLC and SLC, respectively.

occurrences using the mass thresholds of 10^{-9} kg kg $^{-1}$ and 10^{-8} kg kg $^{-1}$ (Fig. C.2), one may not conclude that this is more accurate than another threshold. How do we navigate this large discrepancy? This discussion becomes one of ground truth. The temporal changes during the ~ 2 hour ascent of the radiosonde may introduce errors as well as the neglect of fog layers. Furthermore, due to the presence of multiple layers, attenuation of the ground-based radar is possible, reducing the number of cloud layers identified in the observations. For these reasons, we may not with certainty say that the model is over-predicting the layers.

Trends captured by both observations and the model can thus be found more robust. MLCs have higher median cloud tops and bases than SLCs by approximately 2 km. The trend is captured by the model and the observations but the model consistently has lower median heights than observations. This is likely due to the observational MLC algorithm neglecting fog layers. Higher cloud tops and bases for MLCs are surprising as in general, a height suppression of the lowest MLC layer is found, with a 100 m height difference compared to modelled SLCs. In the observations, the suppression amounts to 300 m. Previous studies have noted a global average cloud top height suppression of 14-32 m (47-60 m) during daytime (nighttime) from satellite measurements (Christensen et al., 2013; Jian et al., 2022), more in line with the lower values of the model. Cloud thickness follows a similar trend with slightly thicker MLCs than SLCs, median values are, however, quite small (~ 350 m), indicating the prevalence of shallow layers. The thickness and height differences for MLCs and SLCs may be connected to the synoptic situation and the water vapour abundance. These characteristics are discussed in-depth further down with respect to seeded and non-seeded MLCs.

Radiatively, MLCs have a larger warming effect on the surface than SLCs. This is seen in surface fluxes, measured and modelled at the MOSAiC site as well as in the full domain cloud radiative effect. At the MOSAiC site, strong conclusions are hard to draw as large discrepancies between observational data sets are present. Surface net radiation is found to be slightly positive (warming) for MLCs while slightly negative for SLCs (cooling). These values are in line with previous studies in the Arctic sector, which show a small net positive radiative flux in September (Kay and L'Ecuyer, 2013) from Arctic clouds (irrespective of how many layers are present). This may indicate that the radiation budget in the Arctic is driven by the MLCs, due to their high occurrence frequency. In terms of large-scale Arctic impact, the net cloud radiative effect of MLCs, here, the warming due to the presence of clouds, is double the impact of SLCs with values of 43 W m^{-2} and 22 W m^{-2} respectively. The large difference stems from the discrepancy in LW CRE, with medians of 63 W m^{-2} and 50 W m^{-2} respectively. In a study using the CERES satellite, Barrientos et al. (2022) show similar values for the LW CRE with an Arctic mean of 51.3 W m^{-2} . From our study, we may conclude that MLCs drive the radiation budget in the high-Arctic similar to what has been seen from satellite studies at lower Arctic latitudes (L'Ecuyer et al., 2019).

Multilayer clouds may interact microphysically through the seeder-feeder mechanism. A high frequency of seeding is found, with a 48.2% occurrence in the model versus a 46.4% occurrence based on theoretical sublimation calculations on ice crystals with sizes of $400 \mu\text{m}$ using the Vassel et al. (2019) algorithm. A strong dependence on ice crystal size and seeding mass threshold is found, and it is difficult to draw a clear conclusion on the occurrence of seeding, except that it seems to be frequent for Arctic clouds. In comparison to other studies these values are large, Vassel et al. (2019) found a 23% occurrence at Svalbard using $400 \mu\text{m}$. In contrast, Proske et al. (2021) found a 31% occurrence of seeding from cirrus clouds over the Swiss Alps. This may indicate that the increase in multilayer clouds brings a following increase in seeding occurrence, which may be expected. Limitations to the seeding definition in the model pertain to the mass threshold and the exclusion of a cloud gap calculation. Including a limit to the seeding possibility for cloud gaps that exceed a certain distance, may further emphasise the findings here and reduce the occurrence of seeding. However, as clear distinctions can be made between seeded and non-seeded clouds, we conclude that the current algorithm is adequate for our purpose.

Further investigation into the differences between seeded and non-seeded MLCs and SLCs has led us to the conclusion that seeded clouds:

- Are thinner than non-seeded MLCs but thicker than SLCs
- Have higher IWP, SWP, and GWP
- Have a cloud-top dominated by the ice phase throughout the mixed-phase temperature range

- Appear at lower altitudes with warmer cloud-top temperatures than non-seeded MLCs but seeding lowers the cloud-top temperature
- Have lower INP and CCN activation
- Have higher rates of aggregation, riming, and vapour deposition

In general, most of the modelled clouds are thin. Seeded clouds are thinner than their non-seeded counterpart by almost 100 m, while SLCs are yet thinner than both. The difference in thickness is likely related to the seeding. This mechanism may act both as a strengthening mechanism and as a sink through increased precipitation. In-cloud IWP for seeded clouds is 45 times higher than SLCs while 11 times higher than non-seeded MLCs. Graupel and snow have low integrated values but are found to increase by a factor of 2. On the other hand, SLCs have higher LWP (approximately 2 times more) and higher integrated rain content. The difference in rain content is likely related to differences in LWP. The finding that non-seeded MLCs have a higher IWP than SLCs, as well as being thicker, may be an algorithm limitation. Clouds that are seeded by less than 10^{-9} kg kg⁻¹ will be classified as non-seeded while still affected by the seeding from above. For a low amount of seeding the cloud may only experience a strengthening and lack the exacerbated mechanisms that lead to a larger precipitation and cloud thinning. It may also be a temporal impact, clouds that have previously been seeded but are currently not would also be classified as non-seeded. A persistent source of new ice from above may be the driving factor in the maintenance of the seeded cloud layers as we do not see complete glaciation followed by cloud thinning in the statistics (LWP is still high and seeded clouds are thicker than SLCs).

In a recent observational study by D'Alessandro et al. (2023), in the Southern Ocean, multilayer clouds were found to have a higher probability to exist in the ice or mixed-phase state. Here we find similar features that multilayered clouds, generally, tend to have cloud tops that are more persistently ice-dominated at warmer temperatures than SLCs. This is both found at the MOSAiC site and across the Arctic domain. The SLCs, on the other hand, with a distribution dominated by mixed-phase cloud tops, show the picture we expect from the Arctic clouds, showcasing that the model accurately captures the mixed-phase cloud tops with falling ice as we commonly observe in the region. With a higher rate of cloud droplet activation, the mixed-phase state of SLCs is further strengthened. The lower cloud droplet activation rate for MLCs compared to SLCs is due to the decrease in in-cloud vertical velocity, potentially linked to the reduction of cloud-top cooling and the turbulence that is inhibited due to the overlaying clouds. The rate of ice nucleation is the largest for non-seeded clouds. A credible explanation is the colder cloud-top temperatures that enable larger rates of activation. Seeded clouds have about five times lower rates. This is potentially due to the reduction in supersaturation with respect to ice through larger rates of vapour deposition in seeded clouds, which limits the nucleation of new ice particles. The warmer

cloud-top temperature at lower altitudes may further limit the nucleation while the influx of ice particles maintains the dominant ice phase within the cloud.

Seeded clouds are more ice-dominated than non-seeded, which behave quite similarly to SLCs but with a smaller supercooled liquid fraction than SLCs for most temperature bins. The ice dominance for the seeded clouds can be traced back to very active in-cloud growth processes. Riming, aggregation, and vapour deposition onto frozen hydrometeors are highly active processes. The largest increases can be seen in the aggregation with a 50-time increase in median rates, while vapour deposition increases by a factor of five. SLCs and non-seeded clouds have similar rates apart from an increase in riming in the SLCs compared to non-seeded clouds. Riming rates increase with the availability of raindrops and cloud droplets and SLC has both a higher RWP and LWP than non-seeded clouds. The relatively smaller increases, for seeded MLCs, in rates of mixed-phase processes; riming and vapour deposition (through WBF), may be due to the predominance of ice-phase cloud tops.

Interestingly, the cloud-top temperature is warmer for seeded than non-seeded clouds. We find this is mostly due to the vertical placement of the cloud layers. Seeded clouds tend to have lower cloud tops with a median cloud-top height of 2 km. In contrast, the non-seeded cloud median is 5 km. Isolating clouds with cloud tops below 2 km reveals that MLCs have higher cloud-top temperatures than SLCs. This may be indicative of the impact of the longwave cooling suppression, where the lower cloud tops are not allowed to efficiently cool as seen in Chapter 6. Low-level seeded clouds tend to have a lower temperature than non-seeded ones, which may imply a reduction of the impact of the longwave cooling suppression. In the study by Jian et al. (2022), the interactions between longwave cooling and seeding were investigated from a satellite perspective. They found that in the presence of overlaying clouds, precipitation was suppressed. On the other hand, when seeding occurred, the precipitation was instead enhanced. The interaction between radiation and microphysics is a topic worth further investigation.

9 | CONCLUSIONS

Multilayer clouds remain an underrepresented topic in literature. In this thesis, we have explored MLCs through the modelling of case studies using the ICON model. These are evaluated in the high-Arctic during the MOSAiC campaign with the overarching aim of deepening our understanding of the MLCs and presenting improved methods for better representing them in the model. We provide a detailed microphysical perturbation study to investigate the response on a microphysical level. A radiation study explores the impact of radiation on the formation and persistence of MLCs and further provides a gauge of the radiative impact of overlaying clouds. We finish the thesis with a thorough model evaluation through a month of consecutive simulations over the whole Arctic. Biases in the modelled thermodynamics and cloud representation are identified. Furthermore, a final chapter explores the intricacies of multilayer clouds and compares them to their single-layer counterpart in an effort to isolate the characteristics of the MLCs. We finish with a brief overview of the full Arctic region occurrence and impacts of MLCs, to gauge a further need for the study of these clouds.

Chapter 5 provided a detailed modelling case study into what the limitations to modelling multilayer clouds in the Arctic are. Modelling of Arctic MLCs is challenging. Through our work, we found that the initialisation of the model governs the layering of the clouds. This implies that the high-resolution simulations do not improve on the initial state, which was provided by the global simulations. This points to a larger issue, to accurately simulate MLCs, the global representation of multilayer clouds must be improved. This is a challenging task which requires an improved model or better data assimilation. In the high-Arctic, far away from the closest permanent research station, this is a difficult problem.

In Chapter 5, we further investigated the possibility of improving the cloud representation with a finer grid spacing. For the interest here, of capturing the general cloud state, no improvements could be found. Sharper cloud boundaries occurred, mostly due to a decrease in vertical grid spacing with more vertical levels, but this did little to improve the cloud phase. On the contrary, the higher updrafts that were resolved on the finer grid enabled a large increase in cloud droplet activation. This resulted in a

notable increase in the cloud liquid, a quantity that is already over-estimated in the model. We may summarise:

RQ1.1 Can we accurately model MLCs in the high Arctic? What are the limitations imposed by the modelling strategy and setup, i.e. grid spacing and initial and boundary conditions?

Using the ICON model we can, to an acceptable level, model MLCs in the high-Arctic. We find that MLCs require accurate thermodynamic profiles at the location of evaluation for the correct representation of these clouds. The vertical layering of the clouds and their overall persistence is governed by the initialisation of the model. Horizontal grid spacing plays a small role in how well these clouds are represented, high-resolution simulations above 1.6 km do not improve much on the cloud representation, while an increase in vertical levels sharpens the cloud boundaries and allows for more shallow layers within the column.

Chapter 5 also supplied a detailed investigation into a better representation of Arctic aerosols by constraining the parameterisations towards observed quantities. Cloud droplet activation, primary ice and secondary ice processes parameterisations were explored with a focus on how to better simulate MLCs and Arctic clouds in general.

We find that constraining the cloud droplet activation is problematic due to the saturation adjustment which limits the possibilities of reducing cloud liquid within the clouds. Through this study, however, we can identify the drizzle suppression, as seen by previous studies (Stevens et al., 2018), due to the presence of high CCN concentrations when the CCN are not constrained to an Arctic fit. The constraint on the CCN concentration, on the other hand, increases the rain formation in the model to unreasonable levels. Further work should concentrate on better representing the cloud droplet size distribution in the Arctic, to limit the rain production.

The development of a case-specific INP parameterisation in Chapter 5, improves the cloud representation. It allows for ice nucleation at warmer temperatures ($-12^{\circ}\text{C} < T < -5^{\circ}\text{C}$), which is more suitable for clouds over sea ice and ocean due to the abundance of oceanic INPs that readily freeze at these temperatures. The measured INPs, however, are not sufficient to reproduce the observed cloud ice concentrations at the MOSAiC site. We hypothesise that the addition of such low concentrations of INPs only adds noise to the simulation and that the INPs that do activate are too few to survive in a liquid-dominated cloud. A large perturbation was required to capture the observed ice concentration; a factor of 10^6 applied to the new INP parameterisation. Considering the fact that many models seem to misrepresent IWP in Arctic clouds (Morrison et al., 2009; Fridlind and Ackerman, 2017; Stevens et al., 2018) our lack of ice is not surprising. Whether ground-based measurements of INPs are representative of an in-

cloud concentration is a larger discussion which we cannot further comment on here due to the lack of vertical profiles. To summarise:

RQ1.2 How do MLCs respond to microphysical perturbations?

We find that to a certain extent, MLCs respond similarly to single-layer clouds. A linear response in LWC with a decreased CCN is found with an increase in rain production with a lower CCN concentration and a reduction in LWP. With an increased INP concentration, higher mass concentrations of frozen hydrometeors are found with a propensity for snow formation due to in-cloud aggregation.

RQ1.2a Does constraining the microphysical parameterisations towards observations improve the representation of the clouds?

Constraining parameterisations to observations is not straightforward. The uncertainty in whether surface-based INP concentrations represent in-cloud INPs further complicates the validity of the constraint. The initialisation of the model puts certain bounds on the simulation of Arctic clouds and limits the impact of changes to the parameterisations. However, enabling processes at region-specific temperatures provides a basis for further perturbations such as an increase in INP or SIP that may better represent the clouds.

We introduce the concept of secondary ice production. We find SIP to be explosive, increasing the modelled ice number concentration by a factor of 10^5 . This increase is governed by the breakup upon ice-ice collision which is the only SIP that has an impact. Rime-splintering and droplet freezing and shattering only have negligible impacts. This rather extreme impact from the SIP gives an order of magnitude increase in mass concentration largely from falling snow. We further explore the more realistic implementation by Han et al. (2024), whereby the fragment generation is scaled by the diameter of the colliding particles. This has been shown to produce a more realistic SIP response (Han et al., 2024) but for these Arctic clouds, the impact is reduced to nothing. Explorations of how the primary ice formulation impacts the SIP show how important the initial representation of primary ice nucleation is. A low initial INP concentration, using the Arctic appropriate parameterisation, gives a more realistic impact from the breakup mechanism than a higher INP concentration. Interestingly, the enhancement from SIP is higher using a lower initial INP concentration. Our results follow some of the more recent model studies in the Arctic (Sotiropoulou et al., 2020; Schäfer et al., 2024; Sotiropoulou et al., 2024) but are quite contrary to the observational study by Pasquier et al. (2022) that showed the prevalence of droplet freezing and shattering. The limits of modelling SIP are a challenging topic, more modelling studies may shed light on the different situations and cloud systems that require SIP to be present but in

general, more laboratory and observational studies are required to further understand these processes.

RQ1.2b How important are secondary ice processes and how do they interact with the primary ice?

We find in this case study that SIP are likely present. Representing the primary ice production is of great importance. However, more work is required to better represent both the INP concentrations, that govern the primary ice production, and the SIP. Modelling SIP is a challenging topic that we by no means have solved. This case study may serve as a part of the puzzle, by showing the large influence of breakup upon ice-ice collision, governed by the large collisional rates within the model.

The seeder-feeder mechanism is an interesting feature of multilayer clouds. In the context of our case study, we find limited microphysical interactions between the modelled layers. Seeding from upper layers has seemingly only small impacts on the lower layer until an extreme perturbation in INPs is applied. This, on the other hand, drives an increase in snow falling from the lower layer by three orders of magnitude. Overall, it seems a high ice number concentration in the upper layer is required to impact the lower layer through seeding. This question will be further discussed on the topic of differences between MLCs and SLCs but we can summarise it for the case study:

RQ1.2c Do we simulate seeding between the layers? Which microphysical processes are involved and are we accurately representing them in the model?

We find that the seeder-feeder process is an elusive mechanism that we only capture when providing the model with a large number of ice crystals through an extreme INP perturbation. It seems to a large extent, simply the occurrence of seeding does not impact the lower layer.

Chapter 6 further explores this case study with a focus on the radiative interactions of the layers. A radiative isolation modelling approach is applied where the implications of making layers radiatively transparent are evaluated in regard to the formation of a double-layered system. In summary:

RQ2.1 How does the cloud-radiation interaction impact the evolution and persistence of the MLC system?

Using the COOKIE approach, the lower and upper layers, respectively, are rendered invisible to radiation in two sensitivity simulations. We find that the cloud-radiation interaction does not play a role in the formation of this double-layered cloud. The clouds advect northward from the model boundaries and while the lack of longwave cooling in a layer diminishes the cloud liquid, the clouds persist through an 8 hour advection to the ship location.

RQ2.2 Can we capture the suppression in longwave radiative cooling seen by observations?

Yes. The longwave suppression is evaluated both at the ship and throughout the domain. With an overlaying ice cloud, at the MOSAiC site, a suppression in the radiative longwave cooling is seen of 5.4 K day^{-1} for a liquid layer with an overlaying ice cloud. A full domain evaluation gives a large impact of 24 K day^{-1} suppression in longwave radiative cooling for clouds with a liquid or mixed-phase cloud top. The differences in local and regional longwave radiation suppression highlight the need for a statistical approach when evaluating radiative impacts.

In Chapter 7 we extend our evaluation of the ICON model over the MOSAiC site by simulating 32 consecutive days, through September 2020, across the Arctic region. An INP parameterisation, appropriate for a late-summer Arctic environment is developed using ground-based measurements over the Arctic region.

RQ3.1 How does the model compare with the MOSAiC data?

Observed atmospheric variables correlate temporally with the modelled variables and apart from a warm bias in surface temperatures, the model captures the local thermodynamics remarkably well throughout the simulations. On the other hand, the model underestimates LWP and IWP. Rain formation is likely the reason the LWP is not captured by the model, introduced by the CCN tunings performed. A lack of IWP is often seen in Arctic cloud modelling and points to a lack of understanding of both primary and secondary ice production. It is highly likely the inclusion of droplet freezing and shattering as well as the breakup upon ice-ice collision mechanism is needed to better capture the observed ice mass concentrations. A propensity for snow formation may also serve to deplete the cloud before the advected clouds arrive at the ship location.

RQ3.2 Does an improved representation of the Arctic INP population impact the clouds in the region?

An immersion freezing parameterisation is developed based on measured INP data across the region. We find a 17% increase in ice number concentration at single-layer cloud tops with warm temperatures when we better represent the warm, oceanic, INPs. While the impact is small across the domain, this again enables ice nucleation at warm ($-12^{\circ}\text{C} < T < -5^{\circ}\text{C}$) temperatures.

MLCs have been shown to be more frequently occurring in the Arctic region than the global mean. In Chapter 8, we provide further evidence for this using the evaluated model setup from Chapter 7. While riddled with assumptions, the MLC occurrence can be quantified from the definition of a mass threshold together with a clause for supersaturation. We choose the definition of a radiatively active cloud as a mass threshold and evaluate this against an observational algorithm (Vassel et al., 2019).

RQ4.1 What is the occurrence frequency of Arctic MLCs?

We find a 77% frequency of occurrence at the MOSAiC site versus an observed 68% during August-September 2020. Over the entire Arctic, the occurrence frequency is 67%, showing an increase in occurrence towards the higher latitudes. In general, we may say that the model has a propensity for multiple shallow

layers that are not evident in the observations but in conclusion, MLCs are very frequent in the high-Arctic in the early Autumn.

RQ4.2 Can we find microphysical differences between multilayer and single-layer clouds?

Multilayer and single-layer clouds have different characteristics. We find that MLCs occur more frequently at higher altitudes but seeding primarily occurs in the lower layers. SLCs are in general very low and mostly constrained to the boundary layer. The occurrence of seeding greatly impacts the MLCs compared to SLCs while non-seeded clouds behave similarly to SLCs, with some exceptions potentially brought on by algorithmic limitations. MLCs appear thicker than SLCs, brought on by a strengthening of the cloud ice. However, seeded MLCs are thinner than their non-seeded counterpart, likely due to the precipitation sinks caused by an increase in cloud ice, snow, and graupel. This increase is due to the seeding from above and exacerbated through an increase in riming, aggregation, and vapour deposition within the cloud. The seeding limits the ice nucleation, however, by reducing the supersaturation through the increase in vapour deposition.

Seeding from above lowers the cloud-top temperature and governs the cloud phase of the lower cloud. MLCs tend to have ice-dominated cloud tops in general, while SLCs are predominantly mixed-phase. Supercooled liquid fractions across the temperature range follow similarly with seeded clouds obtaining lower SLF values across the range. A reduction in vertical velocity, potentially due to the reduction in cloud-top longwave cooling, further limits the possibility of increasing the mixed-phase fraction for MLCs through cloud droplet activation.

RQ4.3 What is the impact of MLCs on the Arctic surface radiative balance?

Radiatively, MLCs have a larger warming effect on the surface than SLCs. This is seen in surface fluxes, measured and modelled at the MOSAiC site as well as in the full domain cloud radiative effect. From our study, we may conclude that MLCs drive the radiation budget in the high-Arctic due to their large occurrence frequency and have large impacts on surface heating.

Our work has covered microphysical and radiative interactions between multilayer clouds. Some of the conclusions made are sketched out in Fig. 9.1. We find that microphysically, the seeding has a great impact on the cloud morphology and thermodynamics.

Radiatively, overlaying clouds suppress the longwave radiative cooling of lower layers. We have not explicitly studied the microphysical and radiative interplay between MLCs though we can infer some conclusions from what we have seen within the separate studies. Disentangling microphysical responses when cloud-radiation interactions are removed is challenging. We found large impacts on both cloud liquid and ice followed by changes in precipitating hydrometeors with a lack of longwave radiative cooling. Cloud-top longwave radiative cooling maintains these clouds and without it, cloud liquid evaporates. Our opposite finding in integrated ice water path may point to processes regarding these clouds we do not fully understand. When upper layers do not interact with radiation, in general, a reduction in ice mass concentration is found. Here, the opposite is found and we may wonder if this has something to do with the presence of multiple layers. Does the sublimation of ice particles promote aggregation and riming which falls into lower layers, efficiently seeding them and increasing the IWP? We found that seeded, low-level, MLCs have a lower cloud-top temperature than non-seeded clouds. MLCs are, in general, thicker than SLCs which further points to a strengthening mechanism of the clouds that opposes the reduction in longwave radiative cooling and the precipitation enhancement from the seeding. Thus, the lack of longwave cooling may not be a trigger for cloud ice reductions. These findings must be further investigated in future work.

As a final conclusion, our work has brought to light the intrinsic differences between single and multilayer clouds. While some responses seem universal for SLCs and MLCs, their impact and characteristics differ substantially. The large frequency of MLCs reveals the importance of resolving the cloud layers to fully capture the radiation budget in the Arctic. Properly modelling the frequency and impacts of seeding is further vital to accurately simulate the clouds and their surface precipitation. Through this exploration into the most accurate ways of representing these multilayer clouds, we lay the foundation for further studies into how these layers form, evolve and impact the Arctic climate system.

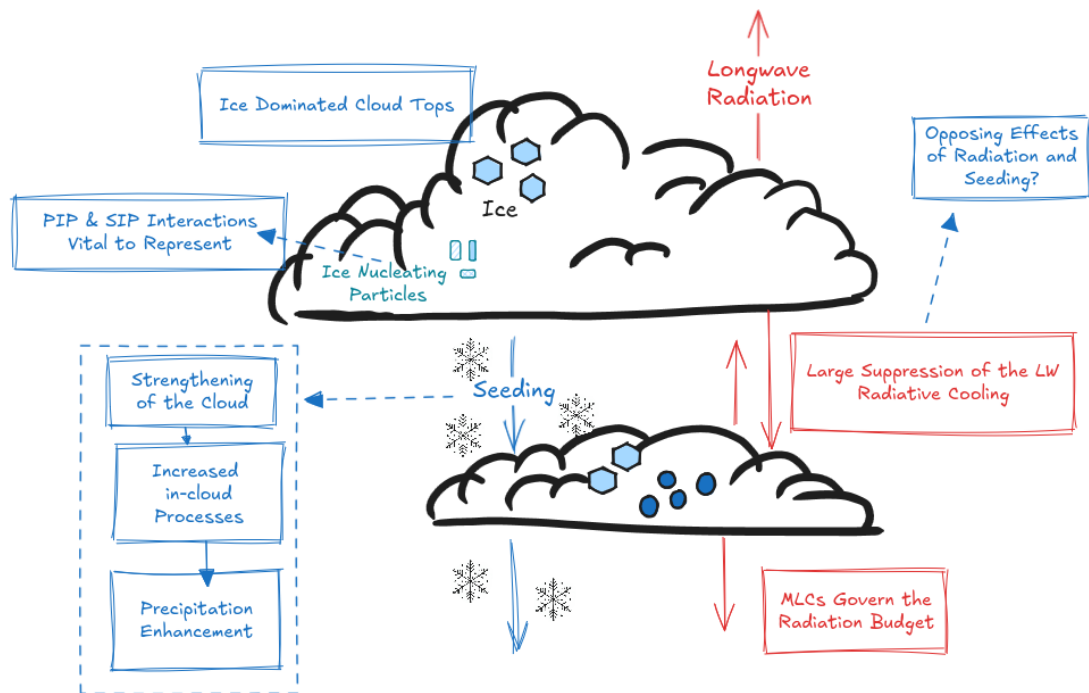


Figure 9.1: Some of the answers to the questions posed in Fig. 1.1. Through our work, we have realised the importance of correctly representing the primary ice production (PIP) in the model through improvements that better capture the local aerosol distribution. SIP are likely present, but we lack parameterisations that realistically capture the observed ice concentrations. We find that MLCs are commonly found with ice-dominated cloud tops, likely influenced by the large frequency of seeding, increasing the cloud ice concentration. The introduction of more cloud ice initiates more in-cloud processes such as riming, aggregation, and vapour deposition which leads to an increase in frozen hydrometeors falling from the lower layer. In terms of radiation, a large suppression of cloud-top longwave radiative cooling is found for clouds that have mixed-phase (or liquid) cloudtops. We find traces of opposing effects from seeding and radiation, which will be a future topic of research. MLCs dominate the cloud occurrence in the Arctic and hence, govern the radiation budget at the surface. MLC profiles have twice as large an impact on surface heating than SLCs. The conclusions presented here highlight the importance of accurately capturing these clouds in model representations of the Arctic.

10 | OUTLOOK

The six questions posed as knowledge gaps in Chapter 2 within multilayer clouds and the general modelling of Arctic clouds have been partially answered through the research questions answered in the previous chapter. However, we are still left with many gaps in our understanding of these clouds and how to best model them in the Arctic. Some possible pathways and solutions to the outstanding questions are presented here.

a) Microphysically, do multilayer clouds differ from single-layer clouds?

From our study, MLCs differ from SLCs. This is mostly seen from a statistical view, and less so in our case study. The differences in microphysical process rates indicate small-scale mechanisms that differ depending on whether a clear sky or other cloudy layers are above the cloud. The seeding plays a large role in this and more studies and evaluations on how well we capture frozen precipitation are needed. The Video In-Situ Snowfall Sensor (VISS) (Maahn et al., 2024), which quantifies the surface precipitation and the degree of riming that has occurred, was active during the first half of the MOSAiC campaign. It will not give any indications on the between-cloud precipitation but future work evaluating ICON's aggregation and riming mechanisms would be a useful start in disentangling primary ice production and precipitation formation. Collocating data with in-situ measurements by aircraft would be further beneficial. Unfortunately, due to the pandemic, the planned aircraft campaign during MOSAiC was moved. A collocation between in-situ ice number concentrations and surface measurements could prove vital to further understanding the discrepancy in modelled cloud ice. Furthermore, idealised high-resolution modelling may give insights into these processes on a smaller scale than we can capture with an NWP model, where turbulence and entrainment may be better described.

b) What is the preferred formation mechanism of MLCs?

The identification of different formation mechanisms has eluded us through this modelling study. If it is pure chance or model constraints we cannot say. The clouds we have investigated are mostly initialised at the model boundaries which are then

brought up to the ship location. This limits our possibilities of understanding upstream formation mechanisms further than the advection. Future work applying a Lagrangian modelling approach may provide a better understanding of these formation mechanisms. By following an air mass as it is advected towards the pole, one may identify in-cloud processes that change, by being less constrained by the initialisation of the domain.

Additionally, an interesting feature of Arctic clouds is the moisture inversion coinciding with the cloud top temperature inversion. We hypothesise that it plays a role in the persistence of MLCs, but to what degree is impossible to further comment on. We propose a modelling study, where sensitivity studies are performed on the relative importance of the role of the cloud-top moisture in regards to MLC formation and persistence.

- c) How do MLCs interact with radiation and what is the impact on other clouds and the surface in the high Arctic?

Cloud-radiation interaction is a difficult and underrepresented topic in general. Few studies exist on the impact of radiation on cloud formation and persistence. The COOKIE approach we employed here may be further used to identify these impacts. Using temperature thresholds for lower clouds may remove the sharp gradient in heating rates for example and allow for easier evaluation across the domain. Our results point to something interesting, on the one hand, we see a large radiative suppression of longwave cooling. On the other hand, the clouds do not diminish fully with the lack of longwave cooling. Thus, we may wonder what the mechanisms are for the cloud to survive. If we take our results as a ground truth, the longwave suppression diminishes the clouds but they do not fully dissipate, granted they are thick enough. The dissipation theories for MLCs thus become more intriguing. Furthermore, the seeding, as seen here, does not force the dissipation of the clouds. Rather a strengthening in general is simulated, with a propensity for cloud ice. Does the seeding limit the impacts of the lack of cloud-top radiative cooling? This interplay between seeding and radiation suppression should be further studied, perhaps in an idealised version of COOKIE where we may control the full environment.

Further modelling studies, over the Southern Ocean specifically, as MLCs have been found to have an appreciable occurrence, could elucidate differences or similarities between these polar regions. The Southern Ocean, at markedly lower latitudes than the Arctic, has been found to have a large radiative bias (Cesana et al., 2022). Perhaps similarly to the Arctic, the radiative signal is governed by MLCs. Coarse models would struggle to represent shallow layers which could be crucial to reproduce the SW reflection in the Southern Ocean.

- d) Are MLCs more common in the Arctic region than globally?

It seems from our investigation into MLCs from observations and modelling that MLCs are abundant in the Arctic region. However, the model may have a bias towards multiple shallow layers and this would require a large-scale evaluation to further distinguish if this is an Arctic-specific occurrence or a model characteristic in general. We propose more studies perform an MLC evaluation such that potential systematic bias may be identified. The Python code for the MLC identification will be published to further enable an identical evaluation. Furthermore, a holistic approach to this may be needed. A combined satellite, model, in-situ, and remote sensing comparisons into the abundance of MLCs. Only while inspecting the same data from different perspectives could we compare and evaluate the benefits of using each method. Quantifying MLCs is a difficult task when the instrument and model resolutions differ substantially and developing evaluation methods that take this into account would be highly beneficial. Future work could involve analyses similar to our work across the globe.

Furthermore, a detailed investigation into surface dependency would be interesting. Our analysis did not isolate any occurrence differences between open ocean and sea ice and we hypothesise that the impact on the lower cloud structure is large. How this translates into larger differences in the multilayer cloud system would be further interesting to study. With an additional source of moisture beneath the lowest cloud, these clouds, while experiencing a suppressed cloud-top longwave radiative cooling, may tap into another survival mechanism to maintain the cloud mass. Further studies into how INP recycling in the sub-cloud layer interacts with this could be an interesting case study.

e) What model biases, if any, can we highlight in the high-Arctic?

In our study, no large biases were found, apart from a warm bias in the surface temperature. A full-year evaluation of the ICON model should be performed to better evaluate and identify potential seasonal biases that are not captured by the model. Our study points to the lack of proper sea ice parameterisation, as the biases arrive with the freeze-up and variability in surface temperatures. Improvements in the representation of snow on top of sea ice have been shown to have an important impact on other models (Arduini et al., 2022) and could further benefit the representation of Arctic clouds in ICON.

- f) How do we better represent Arctic clouds in the model, with a focus on the general misrepresentation of cloud ice?

Improvements in the primary ice nucleation schemes have a small but important impact on the simulations. SIP mechanisms, apart from rime-splintering, seem to be a necessary component for the Arctic cloud system and improvements or potentially Arctic-appropriate developments are required to better represent these clouds. We suggest tuning the cloud droplet size distribution to smaller sizes. This in turn would reduce the rain formation and the impact of droplet freezing. The breakup upon ice-ice collision parameterisations may also need tuning. As we find no impact with diameter-aware parameterisations, this may point to small particle sizes in general, which may be expected with shallow clouds, as the time for growth is shorter than for deep convective clouds. Different pre-factors may be required instead of a diameter scaling. Further case studies on SIP with Arctic clouds, in general, would be beneficial as thus far still very few exist.

Additionally, in regards to the potential misrepresentation of primary ice in the model, through our work, we find that even region-specific parameterisations are not sufficient to capture observed ice concentrations. This may be due to missing SIP formulation but we believe representing the primary ice is of utmost importance. A first potential solution would be to update the immersion freezing parameterisation in the global model. By finding a way to better represent INPs in different regions the modelled ice may be closer to observations. A climatology of INPs may be an option, though difficult to procure. A modelling approach, using an aerosol dynamics model, with the major INP sources included and evaluated at existing sites for INP measurements could be another option.

This lack of ice in the model indicates that we may still be missing other aspects of primary ice formation. INP recycling and time-dependent activation, are two implementations that may improve the representation of primary ice even better. We propose, following the study by Fu et al. (2019) to make sensitivity tests on INP parameterisations, SIP, and INP recycling, and also include time-dependent INP activation. The longevity of Arctic clouds is still quite mysterious and only the combination of different approaches may illuminate the science behind it.

Appendices

A | APPENDIX TO CHAPTER 5

A.1 High resolution simulations

Clouds are sensitive to the resolution on which the simulation is done. Better representation can in general be expected when the grid spacing is decreased. Two simulations are performed on smaller grid spacing, which are initialised by the pr_{1L-1} simulation. For the 400 m simulation (Fig. A.1f), with a finer horizontal as well as vertical grid spacing (see Sect. 4.1), contours are similar to the pr_{1L-1} simulation, Fig. A.1c. The finest grid spacing simulation at 100 m changes the clouds marginally more than the 400 m setup and is shown for the 3rd in Fig. A.1g. For the 100 m simulation, the explicit turbulence parameterisation is switched on and the vertical grid spacing is increased. Most impacts seem to be due to the higher vertical resolution, rendering the cloud boundaries sharper. Some collisions are initiated giving a larger contribution of snow falling into the lower layer. This is, however, not enough to have any appreciable impact on the lower layer.

The time-averaged (06 UTC-12 UTC, Fig. A.2b) maximum liquid water content in the lower layer barely increases between the simulations. In terms of droplet number concentrations larger impacts are seen with a 4-time (15-time) increase from the pr_{1L-1} simulation for the 400 m (100 m) simulation respectively (Fig. A.2a). Meanwhile, the cloud thickness decreases. This shows the impact of finer horizontal grid spacing on the CCN activation. With a smaller grid spacing an increase in vertical velocity is found which increases the CCN activation. An increase in cloud ice by a factor of 4 can be seen for the 100 m simulation (Fig. A.2d), but this is deemed to be not enough impact to justify the large computational cost of performing microphysical sensitivity tests at such high resolution.

On the 1st (Fig. A.3b,c), the high-resolution simulations impose sharper cloud boundaries, similar to the 3rd, and the upper cloud obtains more individual features due to the increased vertical resolution. The time-averaged (10 UTC-12 UTC) vertical profiles are shown in Fig. A.4. An impact on cloud liquid is noted with a 3-time increase

in droplet number concentration for the 100 m simulation compared to the pr_{1L-1} simulation meanwhile the liquid water content only increases by a factor of 1.1. Cloud ice mass content in the upper layer increases by a factor of 2 while the ice number concentration increases by 5. The lower layer does not see an increase in cloud ice with a smaller horizontal grid spacing.

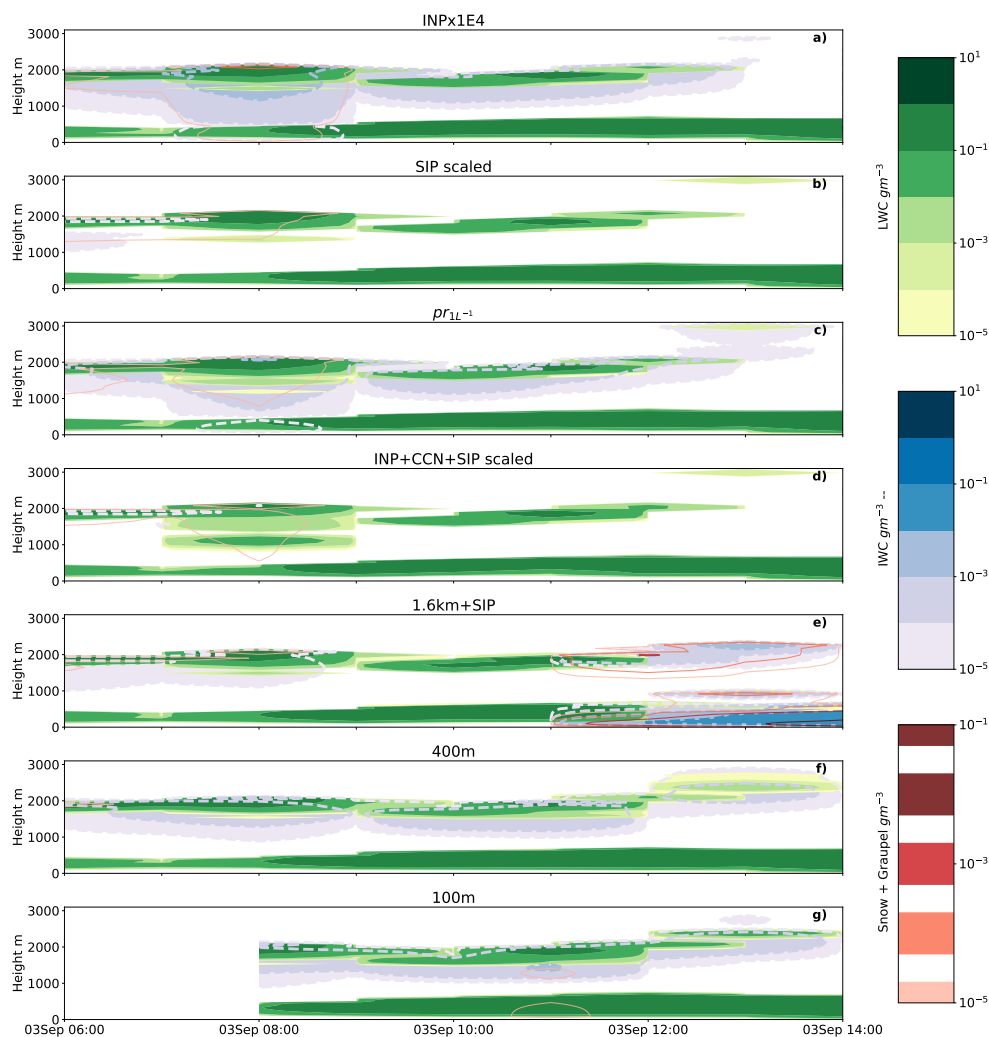


Figure A.1: Time height plot of hydrometeors from the 3rd of September with liquid water mass content (green) and cloud ice water mass content (filled contours in blue and dashed outlines). (a) Polynomial scaling of $1E4$, (b) SIP simulation with a scaled breakup upon ice-ice collision parameterisation, (c) the prescribed INP to 1 per L at warm temperatures, (d) new immersion freezing parameterisation with a CCN scaling by 0.1 and SIP included whereby the breakup upon ice-ice collisions is scaled down, (e) 1.6km+SIP, original primary ice production with added SIP, (f) 400 m simulation initialised using pr_{1L-1} , and (g) 100 m simulation initialised using the 400 m simulation. Due to a 2 h delay between nests, the 100 m nest is only initialised at 08 UTC. Additional model parameters are the snow and graupel mass contents in red (solid line).

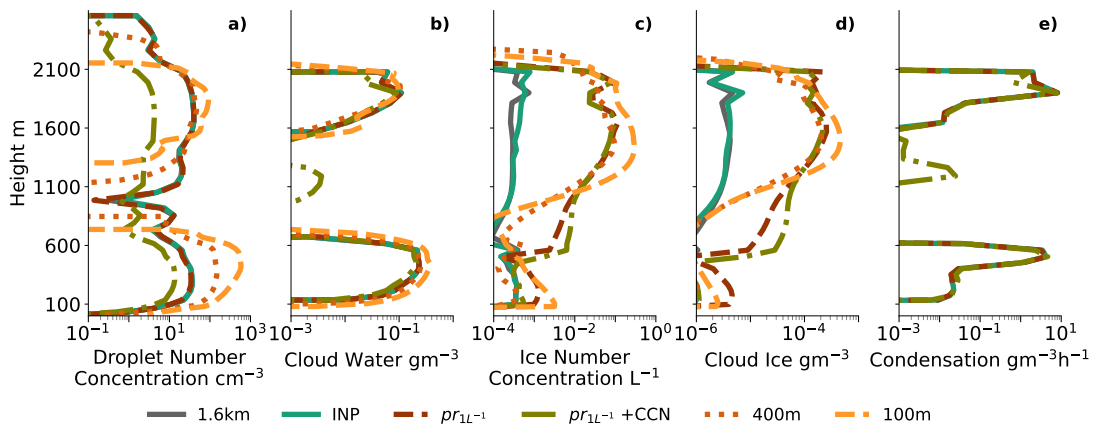


Figure A.2: (a) Cloud droplet number concentrations, (b) cloud water mass content, (c) cloud ice number concentration, (d) cloud ice mass concentration and, first and second saturation adjustments, effectively the cloud droplet condensation routine, called to adjust the excess or deficit of vapour. Panel (d) only shows the first four simulations as listed in the legend. All were calculated for the 3rd of September as a temporal and spatial mean between 06 UTC-12 UTC.

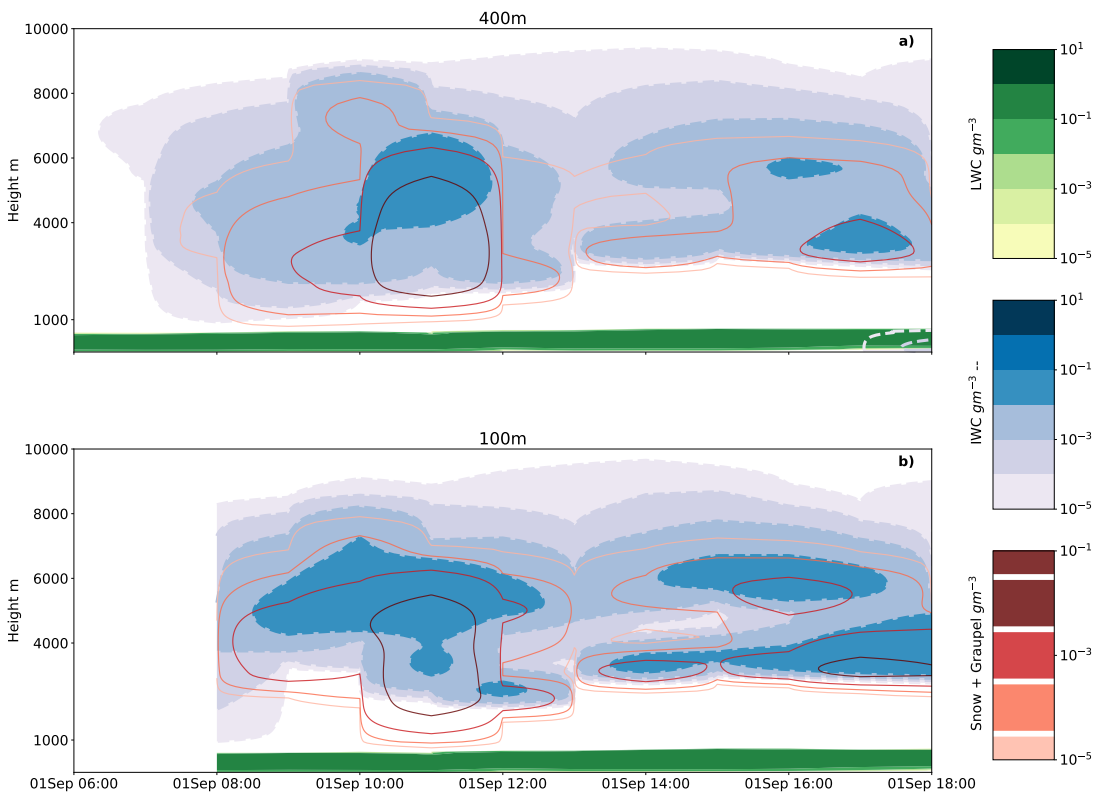


Figure A.3: Time height plot of hydrometeors from the 1st of September with liquid water mass content (green) and cloud ice water mass content (filled contours in blue and dashed outlines). (a) 400 m simulation, initialised from the output of $pr_{1L^{-1}}$ and, (b) 100 m initialised using the 400 m simulation. Due to a 2 h spin-up between nests, the 400 m (100 m) nest is only initialised at 06 UTC (08 UTC). Additional model parameters are the snow and graupel mass contents in red (solid line).

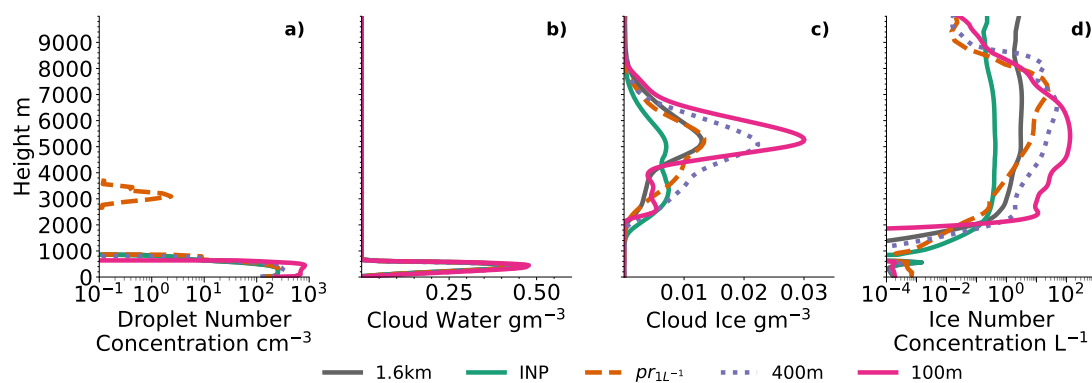


Figure A.4: (a) Cloud droplet number concentrations, (b) cloud water mass content, (c) cloud ice mass content, and (d) cloud ice number concentration. All were calculated for the 1st of September as a temporal and spatial mean between 10 UTC-12 UTC.

A.2 Additional Figures

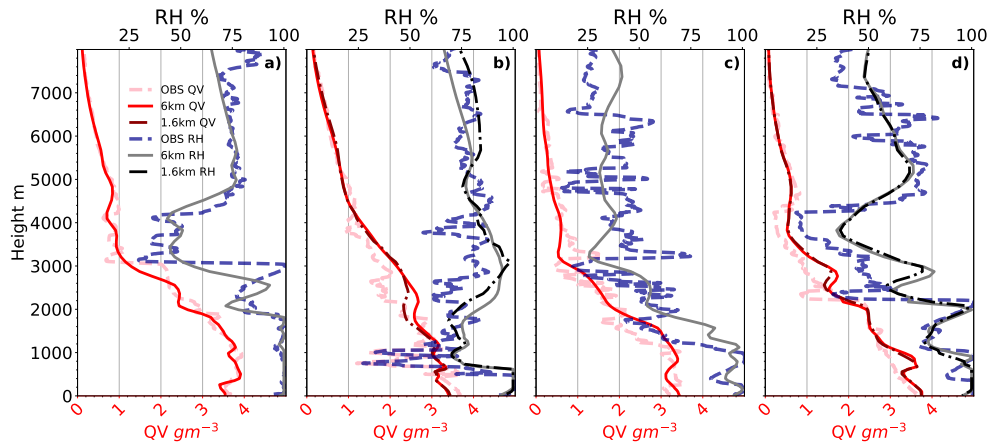


Figure A.5: Vertical profiles of moisture content (QV) in red and relative humidity with respect to liquid water (RH) in grey. (a) 1st at initialisation time 00UTC, (b) 1st at 12UTC, (c) 3rd at initialisation time 00UTC, and (d) 3rd at 12UTC. The observational data (in dashed lines) are from the radiosondes (Maturilli et al., 2022b) and the model data are the 6 km grid spacing simulation and at 12UTC for both days the 1.6 km simulation is additionally shown (initialisation at 04UTC). The figure is reprinted from Wallentin et al. (2024) under the licence.

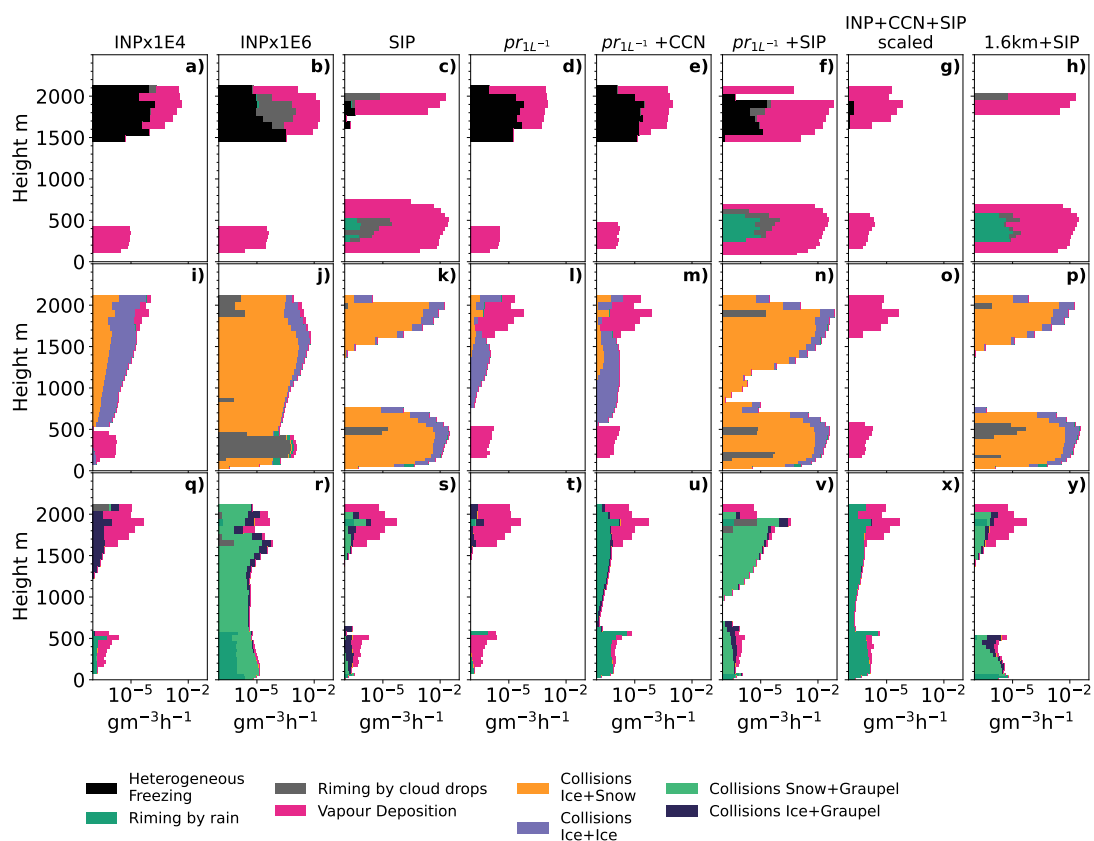


Figure A.6: Microphysical process rates accumulated during the simulation and here taken as a mean between 06-12UTC on the 3rd of September. a-f) Show processes contributing to ice mass growth, g-l) for snow and m-r) for graupel. Colours correspond to the various process rates defined in the legend. The figure is reprinted from Wallentin et al. (2024) under the licence.

B | APPENDIX TO CHAPTER 6

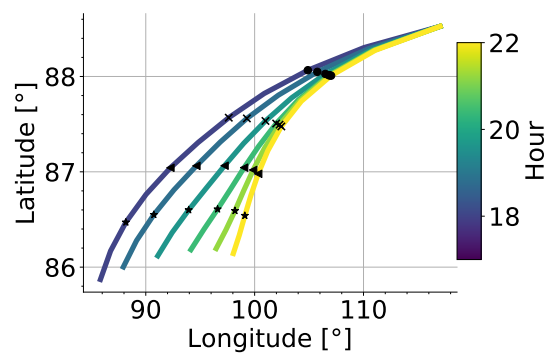


Figure B.1: Mean (vertical) back trajectories from the daily average ship position for 10 hours starting at every hour between 17UTC and 22UTC. Two (four, six, and eight) hours are marked with a dot (cross, triangle, star).

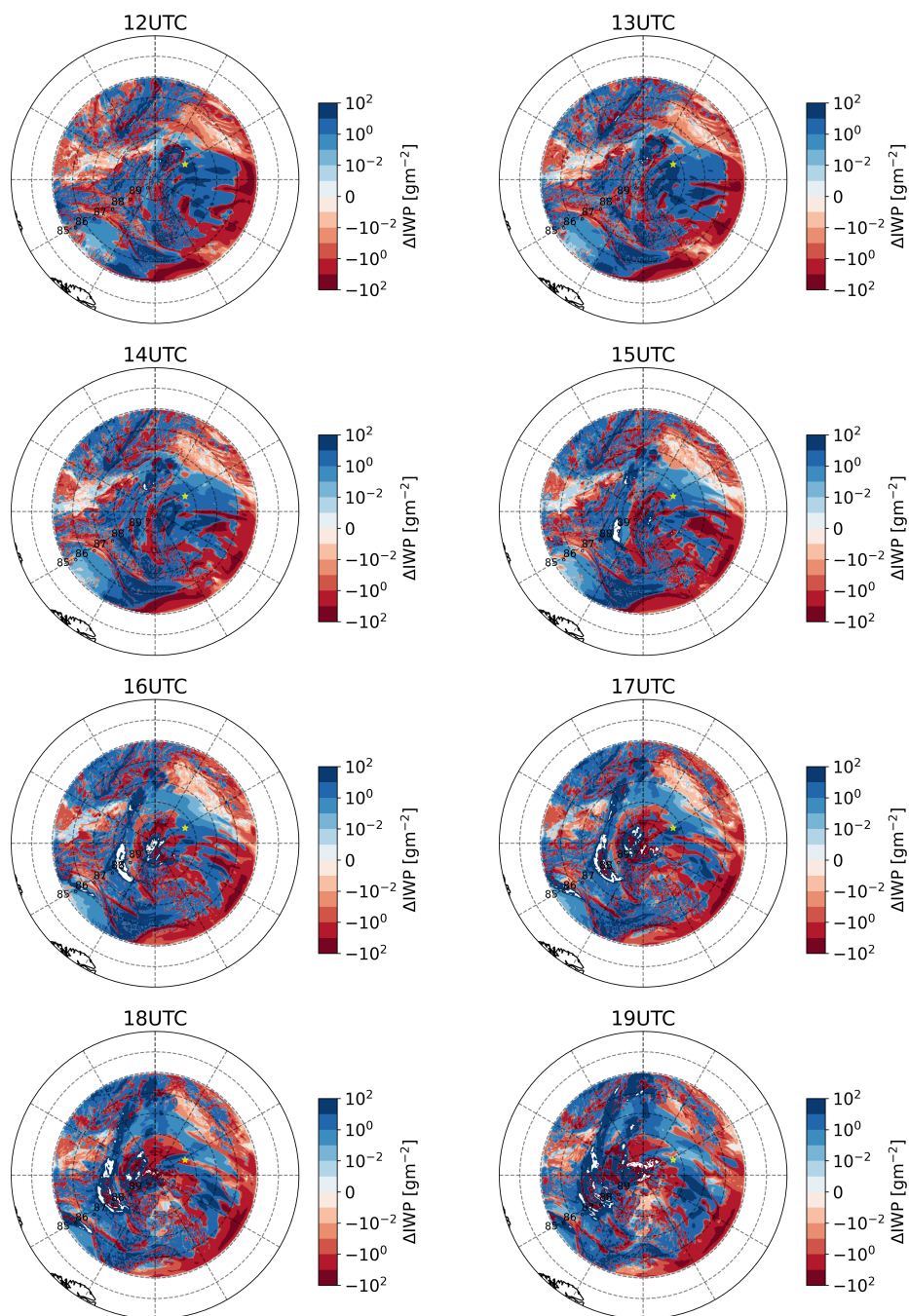


Figure B.2: Difference between *Above Off* and reference column-integrated ice water content (IWP) across the domain during the 1st of September 2020 for the hour indicated in each title. The ship location is marked with a yellow star at 88.3°N , 117°E .

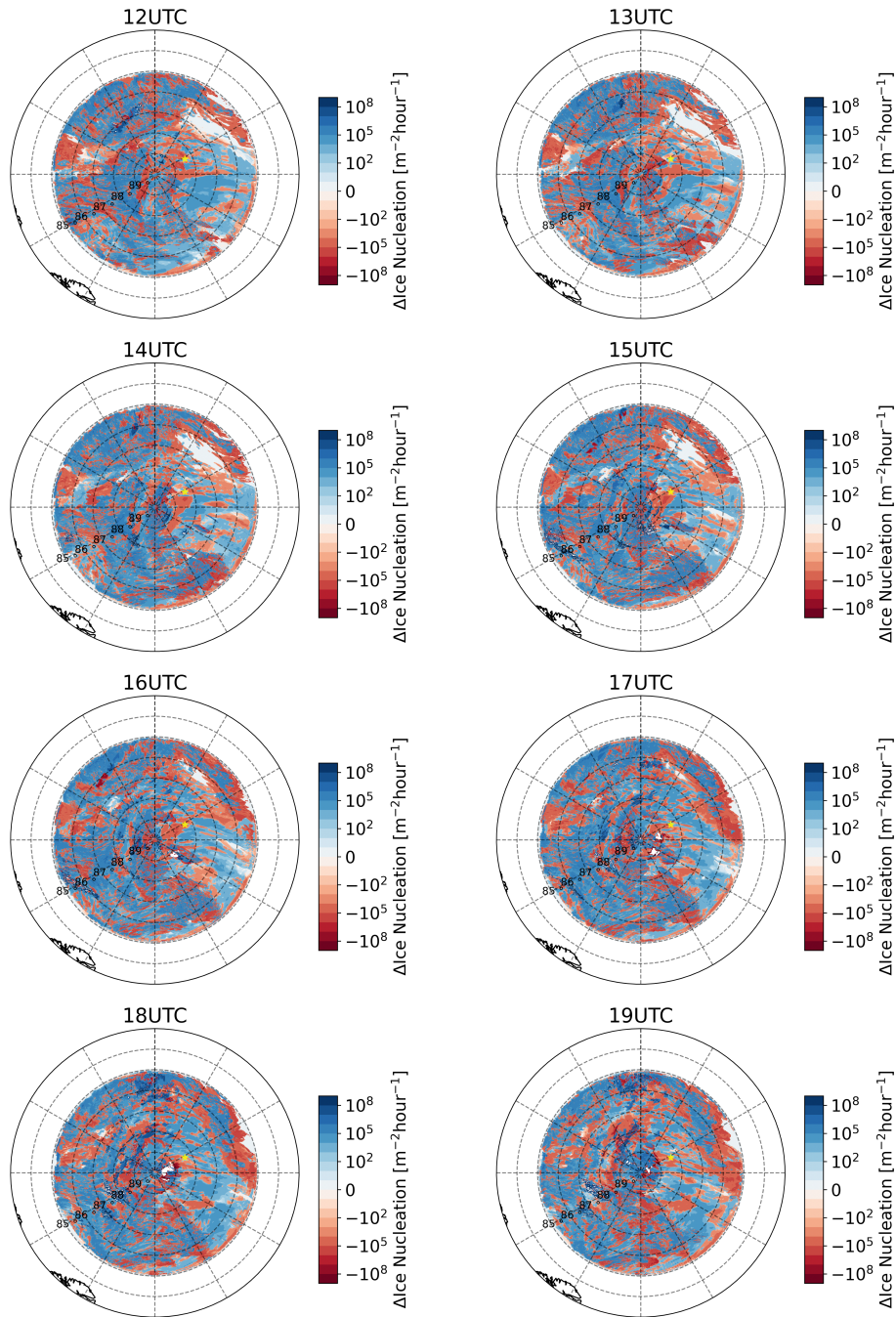


Figure B.3: Difference between *Above Off* and reference column-integrated homogeneous and heterogeneous ice nucleation rates across the domain during the 1st of September 2020 for the ice formation within the hour indicated in each title. The ship location is marked with a yellow star at 88.3°N , 117°E .

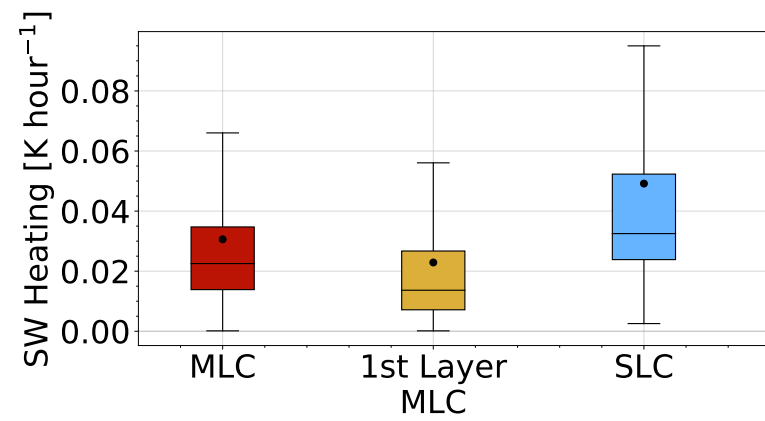


Figure B.4: Shortwave cloud radiative heating for MLCs, first layer MLC, and SLCs. Medians are marked with a line while means are marked with dots.

C | APPENDIX TO CHAPTER 8

C.1 MLC Algorithm Evaluation

Evaluating the Relative Humidity Threshold

Figure C.1, shows the evaluation of fluctuations in relative humidity over ice (RH_i) for the profiles at the MOSAiC site using a mass threshold of $10^{-9} \text{ kgkg}^{-1}$. Fluctuations in RH_i from the calculation using the Tetens formula (Eq. 3.10), may be due to temperature changes between the time steps, rendering clouds that were previously supersaturated in a sub-saturated environment.

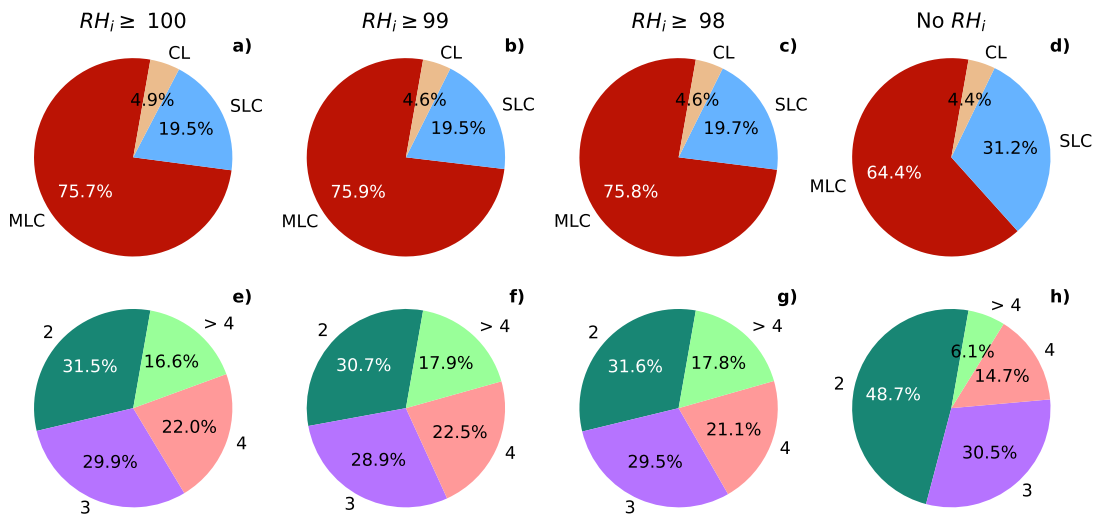


Figure C.1: Cloud statistics of profiles at the MOSAiC site between 22nd of August and 22nd of September for clear (CL) sky, single-layer clouds (SLC) and multilayer clouds (MLC), using the model MLC algorithm with a) a 100% relative humidity over ice (RH_i) requirement, b) 99% RH_i threshold, and c) 98% RH_i threshold. d) shows the statistics without a relative humidity threshold included (only mass threshold).

When including an RH_i threshold (Fig. C.1a) the MLC occurrence increases (64.4% to 75.7%). The SLC occurrence decreases while the clear sky statistics remain approximately the same. This shows the presence of sub-saturated layers within clouds initially identified

as SLC such as precipitating ice clouds. The double-layer cloud frequency reduces in favour of four or more layers as can be seen in the second row of Fig. C.1. The statistics for the three-layered structures remain very similar. The fluctuations in RH may be evident in single cases but with a statistical approach, Fig. C.1a-c, only small variations between RH_i thresholds can be observed. We thus settled on using the more intuitive threshold of 100% relative humidity over ice.

Evaluating the Mass Threshold

Figure C.2 shows the differences introduced from variations in the cloud mass threshold, keeping the RH_i threshold to 100%, also evaluated at the MOSAiC site.

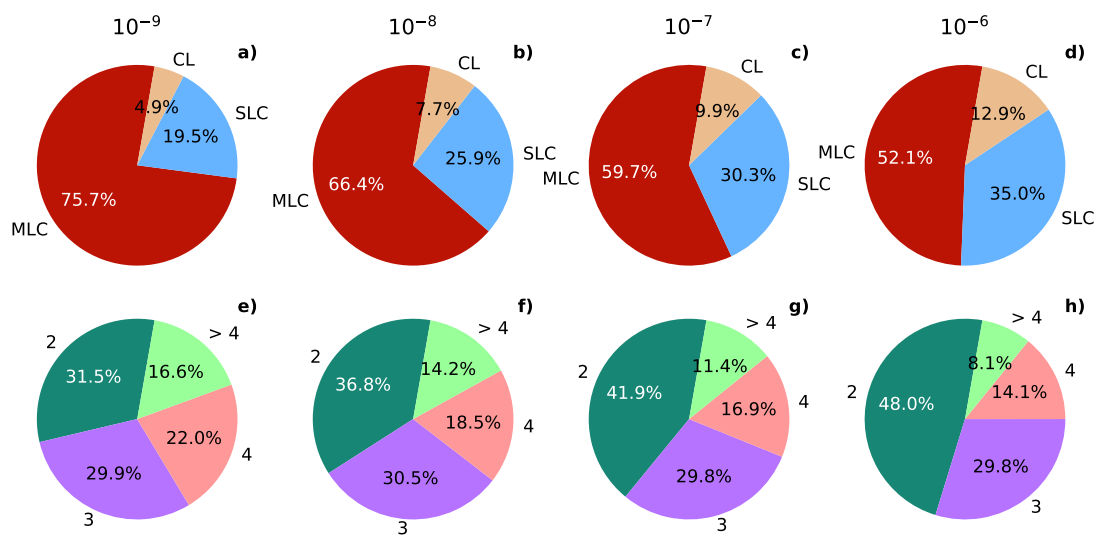


Figure C.2: Statistics for a)-d) cloudy profiles at the MOSAiC site between the 22nd of August and the 22nd of September for clear (CL) sky, single-layer clouds (SLC) and multilayer clouds (MLC). Shown here are the differences in layer statistics using the algorithm with a threshold of 100% RH over liquid water and ice while varying the LWC+IWC threshold between 10^{-9} and 10^{-6} kg kg^{-1} . e)-h) show the respective distribution of the number of layers in the MLC profiles.

A low cloud mass threshold (10^{-9} kg kg^{-1}) gives more cloud layers compared to larger mass thresholds. The MLC occurrence for each mass threshold amounts to 75.7%, 66.4%, 59.7%, 52.1% going from a mass threshold of 10^{-9} kg kg^{-1} , 10^{-8} kg kg^{-1} , 10^{-7} kg kg^{-1} , to 10^{-6} kg kg^{-1} . With a larger number of MLCs, either single-layer clouds or clear sky fraction has to decrease. We notice that the clear sky fraction changes less (4.9% to 12.9%) than the single-layer fraction (19.5% to 35.0%). This indicates that more profiles change from multilayer to single-layer with the exclusion of more shallow layers below the mass threshold rather than multiple thin layers (full vertical profiles) being filtered. In the second row in Fig. C.2, the distribution of the number of cloud layers for the MLC profiles is shown. This shows the increase in 2-layer profiles with a higher mass threshold, going from left to right in the plot. Again, the statistics for 3-layers remain constant while 4-layers and above 4-layers are reduced in favour of the 2-layers. This

may indicate that 2 and 3-layered structures are relatively robust while cloud systems with four or more layers contain shallower clouds.

C.2 Additional Figures

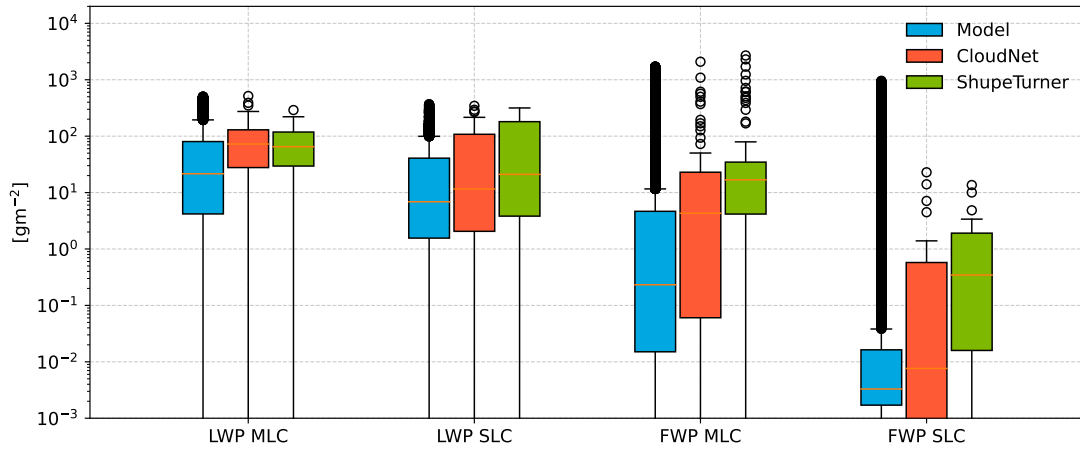


Figure C.3: Boxplots of liquid water path (LWP) and frozen water path (FWP, including cloud ice, snow and graupel integrated water paths) separated into multilayer clouds (MLC) and single layer clouds (SL) for the model and the two observational retrieval products, CloudNet (Engelmann et al., 2024) and ShupeTurner (Shupe, 2023) at the MOSAiC site. The boxplots from the model include all profiles during the 32 days.

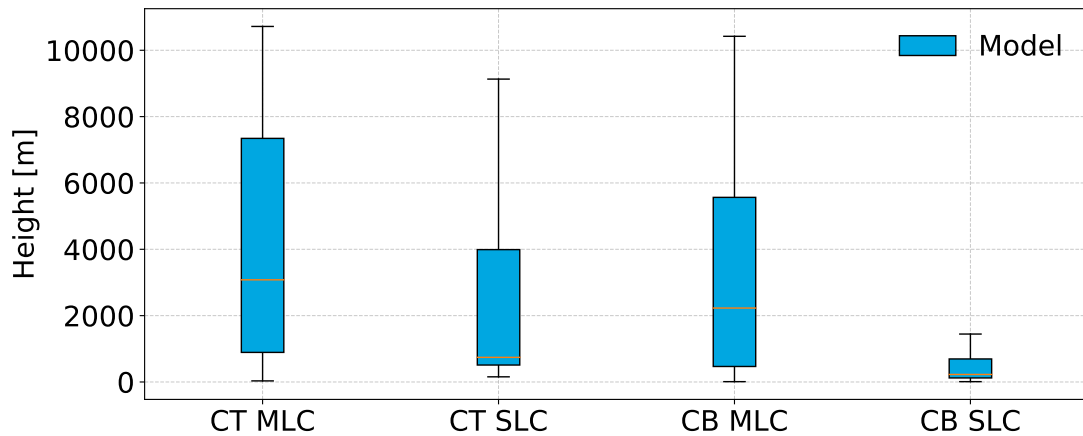


Figure C.4: Cloud top (CT) and cloud base (CB) for multi and single-layer clouds for all the model profiles.

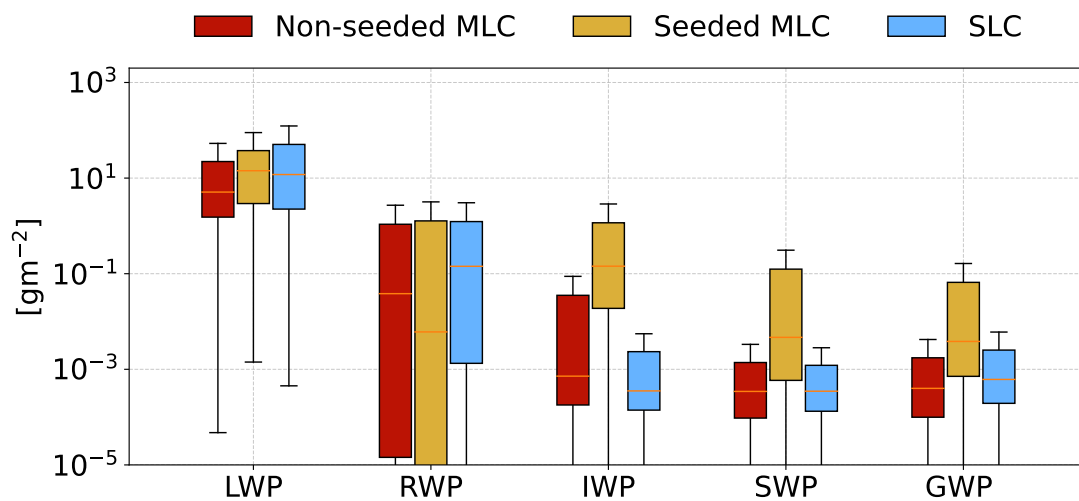


Figure C.5: In-cloud integrated water paths for non-seeded and seeded MLCs and SLCs for a higher seeding mass threshold of 10^{-8} kg kg^{-1} .

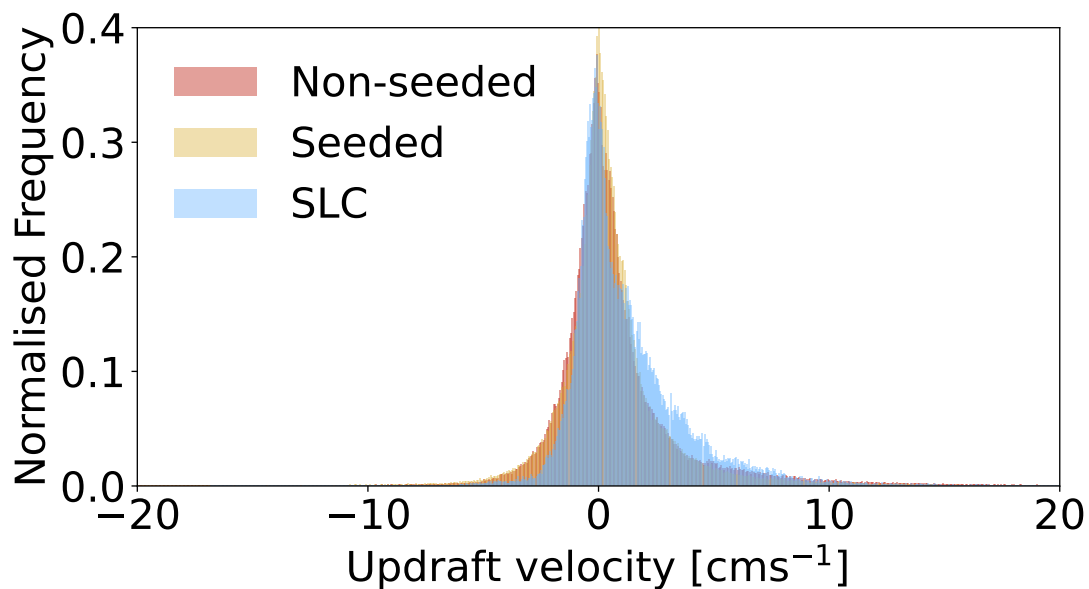


Figure C.6: In-cloud vertical velocity distribution for SLCs and seeded and non-seeded MLCs. Positive values indicate an upward direction.

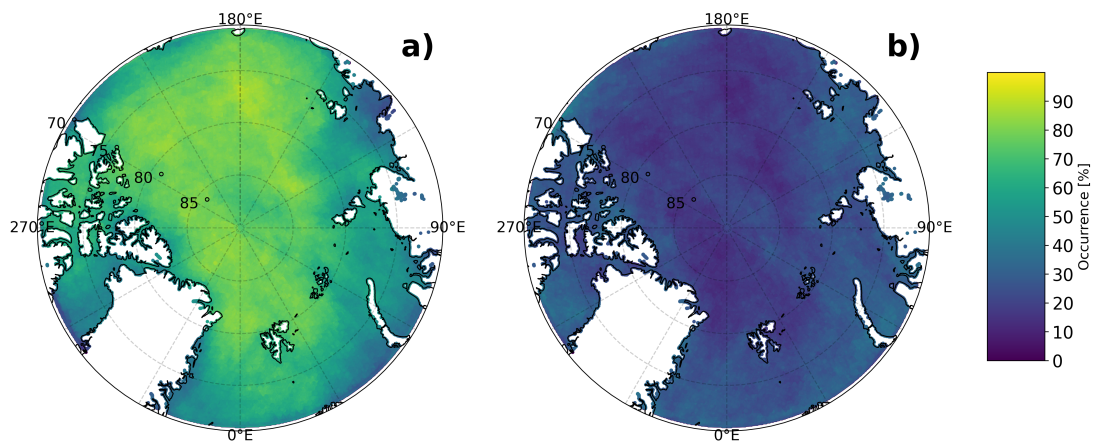


Figure C.7: Spatial occurrence of MLCs a) and SLCs b) over the Arctic domain with a colour bar covering 0-100% for both plots.

ACKNOWLEDGEMENTS

I would like to first express my deepest gratitude to my supervisor, Corinna. You gave me the freedom to pursue my ideas allowing me to grow into a researcher while supporting me through all these stages. Thank you for the independence, for trusting me to do the work the way I wanted. I think I will carry this with me throughout my science career. Thank you for granting and encouraging me to travel and attend all the conferences I could possibly have time for. I believe my PhD journey would be quite different without these experiences, so thank you for supporting me through that. I would like to further thank my second supervisor, Luisa. You helped me through my PhD from afar with so much enthusiasm, our meetings always left me very motivated to continue my work. And thank you for taking so much personal time to be my second supervisor. I am thankful for the unwaivering trust from the both of you, giving me guidance and motivation to get through this PhD.

Secondly, I would like to give thanks the project support and infrastructure that made my project possible. I would like to thank the Bundesministerium für Bildung und Forschung (BMBF) for funding the project for my PhD. I acknowledge the supercomputer HoreKa funded by the Ministry of Science, Research and the Arts Baden-Württemberg and by the Federal Ministry of Education and Research for providing computing and storage resources used in this project. I would further thank all those who contributed to the MOSAiC campaign. A special thanks is extended to Matt Shupe and Jessie Creamean for in-depth discussions and expert advice on everything regarding the Arctic. I believe my PhD experience was thoroughly improved by my cooperation with the AC3 project. I would like to extend my gratitude in taking me in and supporting me as though I was part of the project. Thanks to the friends I found within the project that I'm sure I'll get to follow through our careers.

I would like to thank my colleagues in the Cloud Physics group, a special thanks to Christian who always has an answer to all my ICON questions. Thank you also to those who "volunteered" to read parts of my thesis, Deepak, Behrooz, Fatemeh, Florian, and Annika. A further thanks is extended to the Dynamics group who made sure I got

invited to lunch during those first months during COVID when I was feeling quite alone. Thank you, especially, Marlon for just always being there.

As much as I am proud to complete my PhD, these last three years would have felt incomplete without all the work I have done on the side. My deepest gratitude to Katharina who helped me use my rants for something useful. The PhD council we created together will remain one of my proudest achievements.

To Lea and Beth. My pillars of support. I never thought I would find friends just as good as you are. Thank you for fuelling my rants Lea and thank you Beth for always keeping us contained. IMKTRO has not only given me dear friends and colleagues but also a partner and for that I will be forever grateful. Your belief in me, Athul, surpass my own in every aspect and through all the rants and science discussions you've been my greatest supporter. I can never thank you enough for that.

Finally, I thank my mum and my sister for always supporting my dream of research. Uttrycket borde kanske gå: "Sikta mot stjärnorna och landa i molnen", eller vad tycks?

BIBLIOGRAPHY

- Abdul-Razzak, H. and Ghan, S. J.: A parameterization of aerosol activation 2. Multiple aerosol types, *Journal of Geophysical Research Atmospheres*, 105, 6837–6844, doi: 10.1029/1999JD901161, 2000.
- Adebiyi, A. A., Zuidema, P., Chang, I., Burton, S. P., and Cairns, B.: Mid-level clouds are frequent above the southeast Atlantic stratocumulus clouds, *Atmospheric Chemistry and Physics*, 20, 11 025–11 043, doi: 10.5194/acp-20-11025-2020, 2020.
- Albrecht, B. A.: Aerosols, Cloud Microphysics, and Fractional Cloudiness, *Science*, 245, 1227–1230, doi: 10.1126/science.245.4923.1227, 1989.
- AMS Glossary: URL <https://www.ametsoc.org/index.cfm/ams/publications/glossary-of-meteorology/>, [Accessed 22.02.2024].
- Arakawa, A. and Lamb, V.: Computational Design of the Basic Dynamical Processes of the UCLA General Circulation Model, in: *General Circulation Models of the Atmosphere*, edited by CHANG, J., vol. 17 of *Methods in Computational Physics: Advances in Research and Applications*, pp. 173–265, Elsevier, doi: <https://doi.org/10.1016/B978-0-12-460817-7.50009-4>, 1977.
- Arduini, G., Keeley, S., Day, J. J., Sandu, I., Zampieri, L., and Balsamo, G.: On the Importance of Representing Snow Over Sea-Ice for Simulating the Arctic Boundary Layer, *Journal of Advances in Modeling Earth Systems*, 14, doi: 10.1029/2021MS002777, 2022.
- Arfin, T., Pillai, A. M., Mathew, N., Tirpude, A., Bang, R., and Mondal, P.: An overview of atmospheric aerosol and their effects on human health, *Environmental Science and Pollution Research*, 30, 125 347–125 369, doi: 10.1007/s11356-023-29652-w, 2023.
- Ávila, E. E., Castellano, N. E., Saunders, C. P., Bürgesser, R. E., and Aguirre Varela, G. G.: Initial stages of the riming process on ice crystals, *Geophysical Research Letters*, 36, doi: 10.1029/2009GL037723, 2009.

- Barrientos-Velasco, C., Deneke, H., Hünnerbein, A., Griesche, H. J., Seifert, P., and MacKe, A.: Radiative closure and cloud effects on the radiation budget based on satellite and shipborne observations during the Arctic summer research cruise, PS106, *Atmospheric Chemistry and Physics*, 22, 9313–9348, doi: 10.5194/acp-22-9313-2022, 2022.
- Barry, K.: ARCTic Study of Permafrost Ice Nucleation (ARCSPIN) Cumulative Ice Nucleating Particles (INP) Data Alaska, 2021, doi: doi:10.18739/A2833N072, 2023.
- Barthlott, C., Zarboon, A., Matsunobu, T., and Keil, C.: Importance of aerosols and shape of the cloud droplet size distribution for convective clouds and precipitation, *Atmospheric Chemistry and Physics*, 22, 2153–2172, doi: 10.5194/acp-22-2153-2022, 2022.
- Bechtold, P., Köhler, M., Jung, T., Doblas-Reyes, F., Leutbecher, M., Rodwell, M. J., Vitart, F., and Balsamo, G.: Advances in simulating atmospheric variability with the ECMWF model: From synoptic to decadal time-scales, *Quarterly Journal of the Royal Meteorological Society*, 134, 1337–1351, doi: <https://doi.org/10.1002/qj.289>, 2008.
- Beck, I., Quéléver, L., Laurila, T., Jokinen, T., Baccarini, A., Angot, H., and Schmale, J.: Pollution mask for the continuous corrected particle number concentration data in 1 min resolution, measured in the Swiss aerosol container during MOSAiC 2019/2020, doi: 10.1594/PANGAEA.941335, 2022.
- Bergeron, T.: Über die dreidimensional verknüpfende Wetteranalyse, I kommisjon hos Cammermeyers boghandel, 1928.
- Bergeron, T.: The problem of artificial control of rainfall on the globe 1: II. The coastal orographic maxima of precipitation in autumn and winter, *Tellus*, 1, 15–32, 1949.
- Bergner, N., Heutte, B., Angot, H., Dada, L., Beck, I., Quéléver, L., Jokinen, T., Laurila, T., and Schmale, J.: Cloud Condensation Nuclei (CCN) concentrations measured in the Swiss container during MOSAiC 2019/2020, doi: 10.1594/PANGAEA.961131, 2023.
- Bigg, E.: The Supercooling of Water, *Proceedings of the Physical Society. Section B*, 66, 688–694, 1953a.
- Bigg, E. K.: The formation of atmospheric ice crystals by the freezing of droplets, *Quarterly Journal of the Royal Meteorological Society*, 79, 510–519, doi: 10.1002/qj.49707934207, 1953b.
- Bjerknes, V.: Das Problem der Wettervorhersage, betrachtet vom Standpunkte der Mechanik und der Physik, *Meteorol. Z*, 21, 1–7, 1904.

-
- Boucher, O., Randall, D., Artaxo, P., Bretherton, C., Feingold, G., Forster, P., Kerminen, V.-m., Kondo, Y., Liao, H., Lohmann, U., Rasch, P., Satheesh, S., Sherwood, S., Stevens, B., Zhang, X., Qin, D., Plattner, G.-k., Tignor, M., Allen, S., Boschung, J., Nauels, A., Xia, Y., Bex, V., Midgley, P., Boucher, O., and Randall, D.: Clouds and Aerosols. In: *Climate Change 2013: The Physical Science Basis. Contribution of Working Group I to the Fifth Assessment Report of the Intergovernmental Panel on Climate Change* [Stocker, T.F., D. Qin, G.-K. Plattner, M. Tignor, S.K. Allen, J. Boschung, A. Nauels, Y. Xia, V. Bex and P.M. Midgley (eds.)], Cambridge University Press, 2013.
- Bulatovic, I., Igel, A. L., Leck, C., Heintzenberg, J., Riipinen, I., and Ekman, A. M.: The importance of Aitken mode aerosol particles for cloud sustenance in the summer-time high Arctic-A simulation study supported by observational data, *Atmospheric Chemistry and Physics*, 21, 3871–3897, doi: 10.5194/acp-21-3871-2021, 2021.
- Bulatovic, I., Savre, J., Tjernström, M., Leck, C., and Ekman, A. M. L.: Large-eddy simulation of a two-layer boundary-layer cloud system from the Arctic Ocean 2018 expedition, *Atmospheric Chemistry and Physics*, 23, 7033–7055, doi: 10.5194/acp-2022-809, 2023.
- Burrows, S. M., McCluskey, C. S., Cornwell, G., Steinke, I., Zhang, K., Zhao, B., Zawadowicz, M., Raman, A., Kulkarni, G., China, S., Zelenyuk, A., and DeMott, P. J.: Ice-Nucleating Particles That Impact Clouds and Climate: Observational and Modeling Research Needs, doi: 10.1029/2021RG000745, 2022.
- Cesana, G. V., Khadir, T., Chepfer, H., and Chiriaco, M.: Southern Ocean Solar Reflection Biases in CMIP6 Models Linked to Cloud Phase and Vertical Structure Representations, *Geophysical Research Letters*, 49, doi: 10.1029/2022GL099777, 2022.
- Cesana, G. V., Ackerman, A. S., de Guelis, T. V., and Henderson, D. S.: Cloud-Radiation Interactions and Cloud-Climate Feedbacks From an Active-Sensor Satellite Perspective, in: *Clouds and Their Climatic Impacts*, chap. 4, pp. 87–102, American Geophysical Union (AGU), doi: <https://doi.org/10.1002/9781119700357.ch4>, 2023.
- Chen, C. and Cotton, W. R.: The Physics of the Marine Stratocumulus-Capped Mixed Layer, *Journal of the Atmospheric Sciences*, 44, 2951, 1987.
- Chen, Y. S., Harrington, J. Y., Verlinde, J., Zhang, F., and Oue, M.: Dynamical Response of an Arctic Mixed-Phase Cloud to Ice Precipitation and Downwelling Longwave Radiation From an Upper-Level Cloud, *Journal of Geophysical Research: Atmospheres*, 125, doi: 10.1029/2019JD031089, 2020.
- Christensen, M. W., Carrió, G. G., Stephens, G. L., and Cotton, W. R.: Radiative impacts of free-tropospheric clouds on the properties of marine stratocumulus, *Journal of the Atmospheric Sciences*, 70, 3102–3118, doi: 10.1175/JAS-D-12-0287.1, 2013.
-

- Clapeyron, E.: Mémoire sur la puissance motrice de la chaleur [Memoir on the motive power of heat], *Journal de l'école royale polytechnique*, 14, 153–190, URL <https://gallica.bnf.fr/ark:/12148/bpt6k4336791/f157.item>, 1834.
- Clausius, R.: Ueber die bewegende Kraft der Wärme und die Gesetze, welche sich daraus für die Wärmelehre selbst ableiten lassen, *Annalen der Physik*, 155, 500–524, doi: 10.1002/andp.18501550403, 1850.
- Cooper, W. A.: Ice Initiation in Natural Clouds, *Meteorological Monographs*, 21, 29 – 32, doi: 10.1175/0065-9401-21.43.29, 1986.
- Cox, C., Gallagher, M., Shupe, M., Persson, O., Blomquist, B., Grachev, A., Riihimaki, L., Kutchenreiter, M., Morris, V., Solomon, A., Brooks, I., Costa, D., Gottas, D., Hutchings, J., Osborn, J., Morris, S., Preusser, A., and Uttal, T.: Met City meteorological and surface flux measurements (Level 3 Final), Multidisciplinary Drifting Observatory for the Study of Arctic Climate (MOSAiC), central Arctic, October 2019 - September 2020. Arctic Data Center., doi: 10.18739/A2PV6B83F, 2023.
- Creamean, J.: Ice nucleating particle data from summer 2017 in the Arctic, doi: 10.1594/PANGAEA.903695, supplement to: Creamean, Jessie; Cross, Jessica; Pickart, Robert; McRaven, Leah; Lin, P; Pacini, A; Hanlon, R; Schmale, David G; Cenicerros, J; Aydell, T; Colombi, N; Bolger, E; DeMott, P J (2019): Ice nucleating particles carried from below a phytoplankton bloom to the Arctic atmosphere. *Geophysical Research Letters*, 46(14), 8572-8581, <https://doi.org/10.1029/2019GL083039>, 2019.
- Creamean, J., Hill, T., Demott, P., Barry, K., and Hume, C.: Arctic Ice Nucleation Sampling during MOSAiC (INPMOSAIC2) Field Campaign Report, Tech. rep., 2021a.
- Creamean, J. M., De Boer, G., Telg, H., Mei, F., Dexheimer, D., Shupe, M. D., Solomon, A., and McComiskey, A.: Assessing the vertical structure of Arctic aerosols using balloon-borne measurements, *Atmospheric Chemistry and Physics*, 21, 1737–1757, doi: 10.5194/acp-21-1737-2021, 2021b.
- Creamean, J. M., Barry, K., Hill, T. C., Hume, C., DeMott, P. J., Shupe, M. D., Dahlke, S., Willmes, S., Schmale, J., Beck, I., Hoppe, C. J., Fong, A., Chamberlain, E., Bowman, J., Scharien, R., and Persson, O.: Annual cycle observations of aerosols capable of ice formation in central Arctic clouds, *Nature Communications*, 13, doi: 10.1038/s41467-022-31182-x, 2022.
- Curry, J.: On the Formation of Continental Polar Air, *Journal of the Atmospheric Sciences*, 40, 2278–2292, 1983.

-
- Dada, L., Angot, H., Beck, I., Baccarini, A., Quéléver, L. L., Boyer, M., Laurila, T., Brasseur, Z., Jozef, G., de Boer, G., Shupe, M. D., Henning, S., Bucci, S., Dütsch, M., Stohl, A., Petäjä, T., Daellenbach, K. R., Jokinen, T., and Schmale, J.: A central arctic extreme aerosol event triggered by a warm air-mass intrusion, *Nature Communications*, 13, doi: 10.1038/s41467-022-32872-2, 2022.
- Dedekind, Z., Lauber, A., Ferrachat, S., and Lohmann, U.: Sensitivity of precipitation formation to secondary ice production in winter orographic mixed-phase clouds, *Atmospheric Chemistry and Physics*, 21, 15 115–15 134, doi: 10.5194/acp-21-15115-2021, 2021.
- Dedekind, Z., Proske, U., Ferrachat, S., Lohmann, U., and Neubauer, D.: Simulating the seeder–feeder impacts on cloud ice and precipitation over the Alps, *Atmospheric Chemistry and Physics*, 24, 5389–5404, doi: 10.5194/acp-24-5389-2024, 2024.
- DeMott, P. J., Hill, T. C., McCluskey, C. S., Prather, K. A., Collins, D. B., Sullivan, R. C., Ruppel, M. J., Mason, R. H., Irish, V. E., Lee, T., Hwang, C. Y., Rhee, T. S., Snider, J. R., McMeeking, G. R., Dhaniyala, S., Lewis, E. R., Wentzell, J. J., Abbatt, J., Lee, C., Sultana, C. M., Ault, A. P., Axson, J. L., Martinez, M. D., Venero, I., Santos-Figueroa, G., Stokes, M. D., Deane, G. B., Mayol-Bracero, O. L., Grassian, V. H., Bertram, T. H., Bertram, A. K., Moffett, B. F., and Franc, G. D.: Sea spray aerosol as a unique source of ice nucleating particles, *Proceedings of the National Academy of Sciences of the United States of America*, 113, 5797–5803, doi: 10.1073/pnas.1514034112, 2016.
- Dietel, B., Sourdeval, O., and Hoose, C.: Characterisation of low-base and mid-base clouds and their thermodynamic phase over the Southern Ocean and Arctic marine regions, *Atmospheric Chemistry and Physics*, 24, 7359–7383, doi: 10.5194/acp-24-7359-2024, 2024.
- Dimitrelos, A., Ekman, A. M., Caballero, R., and Savre, J.: A Sensitivity Study of Arctic Air-Mass Transformation Using Large Eddy Simulation, *Journal of Geophysical Research: Atmospheres*, 125, doi: 10.1029/2019JD031738, 2020.
- Duplessis, P., Chang, R. Y.-W., Wheeler, M., Leaitch, R., Svenningsson, B., Karlsson, L., and Zieger, P.: Cloud condensation nuclei (CCN) concentration during the Arctic Ocean 2018 expedition. Dataset version 1. Bolin Centre Database., URL <https://doi.org/10.17043/oden-ao-2018-ccnc-1>, 2023.
- DWD Intro Course: URL https://download.dwd.de/pub/DWD/Forschung_und_Entwicklung/ICON_Training_2018/Talks/ICONTraining2018_PhysOver_Klocke.pdf.
- D’Alessandro, J. J., McFarquhar, G. M., Stith, J. L., Diao, M., DeMott, P. J., McCluskey, C. S., Hill, T. C., Roberts, G. C., and Sanchez, K. J.: An Evaluation of Phase, Aerosol-

- Cloud Interactions and Microphysical Properties of Single- and Multi-Layer Clouds Over the Southern Ocean Using in Situ Observations From SOCRATES, *Journal of Geophysical Research: Atmospheres*, 128, doi: 10.1029/2023JD038610, 2023.
- Eastman, R. and Warren, S. G.: Interannual variations of arctic cloud types in relation to sea ice, *Journal of Climate*, 23, 4216–4232, doi: 10.1175/2010JCLI3492.1, 2010.
- Edwards, J. M. and Slingo, A.: Studies with a flexible new radiation code. I: Choosing a configuration for a large-scale model, *Quarterly Journal of the Royal Meteorological Society*, 122, 689–719, doi: 10.1002/qj.49712253107, 1996.
- Egerer, U., Ehrlich, A., Gottschalk, M., Griesche, H., Neggers, R. A., Siebert, H., and Wendisch, M.: Case study of a humidity layer above Arctic stratocumulus and potential turbulent coupling with the cloud top, *Atmospheric Chemistry and Physics*, 21, 6347–6364, doi: 10.5194/acp-21-6347-2021, 2021.
- Engelmann, R., Althausen, D., Baars, H., Griesche, H., Hofer, J., Radenz, M., and Seifert, P.: Custom collection of categorize, classification, droplet effective radius, ice effective radius, ice water content, and 2 other products from RV Polarstern between 1 and 3 Sep 2020, URL <https://cloudnet.fmi.fi/collection/d342273f-413b-46a0-95ea-985f863f9b79>, 2023.
- Engelmann, R., Althausen, D., Baars, H., Griesche, H., Hofer, J., Radenz, M., and Seifert, P.: Custom collection of categorize, ice water content, and liquid water content data from RV Polarstern between 22 Aug and 22 Sep 2020, URL <https://doi.org/10.60656/5e4497c883504316>, 2024.
- Fan, J., Ghan, S., Ovchinnikov, M., Liu, X., Rasch, P. J., and Korolev, A.: Representation of Arctic mixed-phase clouds and the Wegener-Bergeron-Findeisen process in climate models: Perspectives from a cloud-resolving study, *Journal of Geophysical Research Atmospheres*, 116, doi: 10.1029/2010JD015375, 2011.
- Findeisen, W.: Kolloid-meteorologische Vorgänge bei Niederschlagsbildung, *Meteorol. Z*, 55, 121–133, 1938.
- Freitas, G. P., Conen, F., Adachi, K., Yttri, K. E., Krejci, R., and Zieger, P.: Concentration of bioaerosols and ice nucleating particles at Zeppelin Observatory, Svalbard, 2017-2020. Dataset version 1., doi: doi:10.17043/zeppelin-freitas-2023-bioaerosols-1, 2023.
- Fridlind, A. M. and Ackerman, A. S.: Simulations of Arctic Mixed-Phase Boundary Layer Clouds: Advances in Understanding and Outstanding Questions, in: *Mixed-Phase Clouds: Observations and Modeling*, pp. 153–183, Elsevier, doi: 10.1016/B978-0-12-810549-8.00007-6, 2017.

-
- Frisch, A. S.: On cloud radar and microwave radiometer measurements of stratus cloud liquid water profiles, *Journal of Geophysical Research Atmospheres*, 103, 23 195–23 197, doi: 10.1029/98JD01827, 1998.
- Fu, Q.: An Accurate Parameterization of the Solar Radiative Properties of Cirrus Clouds for Climate Models, *Journal of Climate*, 1996.
- Fu, S., Deng, X., Shupe, M. D., and Xue, H.: A modelling study of the continuous ice formation in an autumnal Arctic mixed-phase cloud case, *Atmospheric Research*, 228, 77–85, doi: 10.1016/j.atmosres.2019.05.021, 2019.
- Gassmann, A. and Herzog, H. J.: Towards a consistent numerical compressible non-hydrostatic model using generalized Hamiltonian tools, *Quarterly Journal of the Royal Meteorological Society*, 134, 1597–1613, doi: 10.1002/qj.297, 2008.
- Georgakaki, P., Sotiropoulou, G., Vignon, , Billault-Roux, A. C., Berne, A., and Nenes, A.: Secondary ice production processes in wintertime alpine mixed-phase clouds, *Atmospheric Chemistry and Physics*, 22, 1965–1988, doi: 10.5194/acp-22-1965-2022, 2022.
- Griesche, H. J., Ohneiser, K., Seifert, P., Radenz, M., Engelmann, R., and Ansmann, A.: Contrasting ice formation in Arctic clouds: Surface-coupled vs. surface-decoupled clouds, *Atmospheric Chemistry and Physics*, 21, 10 357–10 374, doi: 10.5194/acp-21-10357-2021, 2021.
- Griesche, H. J., Seifert, P., Engelmann, R., Radenz, M., Hofer, J., Althausen, D., Walbröl, A., Barrientos-Velasco, C., Baars, H., Dahlke, S., Tukiainen, S., and Macke, A.: Cloud micro- and macrophysical properties from ground-based remote sensing during the MOSAiC drift experiment, *Scientific Data*, 11, doi: 10.1038/s41597-024-03325-w, 2024.
- Guichard, F. and Couvreux, F.: A short review of numerical cloud-resolving models, *Tellus, Series A: Dynamic Meteorology and Oceanography*, 69, 1–36, doi: 10.1080/16000870.2017.1373578, 2017.
- Hallet, J. and Mossop S.C: Production of secondary ice particles during the riming process, *Nature*, 249, 26–28, 1974.
- Han, C., Hoose, C., and Dürlich, V.: Secondary ice production in simulated deep convective clouds: A sensitivity study, *Journal of the Atmospheric Sciences*, doi: 10.1175/JAS-D-23-0156.1, 2024.
- Hande, L. B., Engler, C., Hoose, C., and Tegen, I.: Seasonal variability of Saharan desert dust and ice nucleating particles over Europe, *Atmospheric Chemistry and Physics*, 15, 4389–4397, doi: 10.5194/acp-15-4389-2015, 2015.

- Hande, L. B., Engler, C., Hoose, C., and Tegen, I.: Parameterizing cloud condensation nuclei concentrations during HOPE, *Atmospheric Chemistry and Physics*, 16, 12 059–12 079, doi: 10.5194/acp-16-12059-2016, 2016.
- Harrington, J. Y., Reisin, T., Cotton, W. R., and Kreidenweis, S. M.: Cloud resolving simulations of Arctic stratus Part II: Transition-season clouds, *Atmospheric Research*, 51, 45–75, 1999.
- Harrop, B. E. and Hartmann, D. L.: The role of cloud radiative heating within the atmosphere on the high cloud amount and top-of-atmosphere cloud radiative effect, *Journal of Advances in Modeling Earth Systems*, 8, 1391–1410, doi: 10.1002/2016MS000670, 2016.
- Haslehner, K., Gasparini, B., and Voigt, A.: Radiative Heating of High-Level Clouds and Its Impacts on Climate, *Journal of Geophysical Research: Atmospheres*, 129, doi: 10.1029/2024JD040850, 2024.
- Herman, G. and Goody, R.: Formation and Persistence of Summertime Arctic Stratus Clouds, *Journal of Atmospheric Sciences*, 33, 1537 – 1553, doi: [https://doi.org/10.1175/1520-0469\(1976\)033<1537:FAPOSA>2.0.CO;2](https://doi.org/10.1175/1520-0469(1976)033<1537:FAPOSA>2.0.CO;2), 1976.
- Hobbs, P. V. and Rangno, A. L.: Microstructures of low and middle-level clouds over the Beaufort Sea, *Quarterly Journal of the Royal Meteorological Society*, 124, 2035–2071, doi: 10.1002/qj.49712455012, 1998.
- Hogan, R. J. and Bozzo, A.: A Flexible and Efficient Radiation Scheme for the ECMWF Model, *Journal of Advances in Modeling Earth Systems*, 10, 1990–2008, doi: <https://doi.org/10.1029/2018MS001364>, 2018.
- Hogan, R. J. and Illingworth, A. J.: Deriving cloud overlap statistics from radar, *Quarterly Journal of the Royal Meteorological Society*, 126, 2903–2909, doi: 10.1002/qj.49712656914, 2000.
- Hogan, R. J., Mittermaier, M. P., and Illingworth, A. J.: The Retrieval of Ice Water Content from Radar Reflectivity Factor and Temperature and Its Use in Evaluating a Mesoscale Model, *Journal of Applied Meteorology and Climatology*, 45, 301 – 317, doi: <https://doi.org/10.1175/JAM2340.1>, 2006.
- Hoose, C. and Möhler, O.: Heterogeneous ice nucleation on atmospheric aerosols: A review of results from laboratory experiments, *Atmospheric Chemistry and Physics*, 12, 9817–9854, doi: 10.5194/acp-12-9817-2012, 2012.
- Hunt, B. G.: On the general circulation of the atmosphere without clouds, *Quarterly Journal of the Royal Meteorological Society*, 104, 91–102, doi: 10.1002/qj.49710443907, 1978.

- Ickes, L., Welts, A., Hoose, C., and Lohmann, U.: Classical Nucleation Theory of homogeneous freezing of water: Thermodynamic and kinetic parameters, doi: 10.1039/c4cp04184d, 2015.
- Illingworth, A. J., Hogan, R. J., O'Connor, E., Bouniol, D., Brooks, M. E., Delanoé, J., Donovan, D. P., Eastment, J. D., Gaussiat, N., Goddard, J. W. F., Haeffelin, M., Baltink, H. K., Krasnov, O. A., Pelon, J., Piriou, J.-M., Protat, A., Russchenberg, H. W. J., Seifert, A., Tompkins, A. M., van Zadelhoff, G.-J., Vinit, F., Willén, U., Wilson, D. R., and Wrench, C. L.: Cloudnet, Bulletin of the American Meteorological Society, 88, 883–898, doi: 10.1175/BAMS-88-6-883, 2007.
- Intrieri, J. M., Fairall, C. W., Shupe, M. D., Persson, P. O. G., Andreas, E. L., Guest, P. S., and Moritz, R. E.: An annual cycle of Arctic surface cloud forcing at SHEBA, 107, 1–14, doi: 10.1029/2000JC000439, 2002a.
- Intrieri, J. M., Shupe, M. D., Uttal, T., and McCarty, B. J.: An annual cycle of Arctic cloud characteristics observed by radar and lidar at SHEBA, Journal of Geophysical Research: Oceans, 107, doi: 10.1029/2000jc000423, 2002b.
- Jakobsson, J. K., Waman, D. B., Phillips, V. T., and Bjerring Kristensen, T.: Time dependence of heterogeneous ice nucleation by ambient aerosols: laboratory observations and a formulation for models, Atmospheric Chemistry and Physics, 22, 6717–6748, doi: 10.5194/acp-22-6717-2022, 2022.
- Jeffery, C. A. and Austin, P. H.: Homogeneous nucleation of supercooled water: Results from a new equation of state, Journal of Geophysical Research: Atmospheres, 102, 25 269–25 279, doi: <https://doi.org/10.1029/97JD02243>, 1997.
- Jian, B., Li, J., Zhang, L., Wang, Y., Zhang, W., and Li, Y.: Competition Between Radiative and Seeding Effects of Overlying Clouds on Underlying Marine Stratocumulus, Geophysical Research Letters, 49, doi: 10.1029/2022GL100729, 2022.
- Jiang, Z., Ding, M., Zhong, L., Li, Y., and Hu, X.: Seasonal variations of Arctic cloud in recent 14 years using CALIPSO-GOCCP, Atmospheric Research, 309, doi: 10.1016/j.atmosres.2024.107598, 2024.
- Kärcher, B. and Lohmann, U.: A parameterization of cirrus cloud formation: Homogeneous freezing of supercooled aerosols, Journal of Geophysical Research Atmospheres, 107, doi: 10.1029/2001jd000470, 2002.
- Kärcher, B., Hendricks, J., and Lohmann, U.: Physically based parameterization of cirrus cloud formation for use in global atmospheric models, Journal of Geophysical Research Atmospheres, 111, doi: 10.1029/2005JD006219, 2006.

- Kay, J. E. and L'Ecuyer, T.: Observational constraints on Arctic Ocean clouds and radiative fluxes during the early 21st century, *Journal of Geophysical Research Atmospheres*, 118, 7219–7236, doi: 10.1002/jgrd.50489, 2013.
- Keshtgar, B.: Cloud-Radiative Impact on the Dynamics of Extratropical Cyclones and Implications for Predictability, Ph.D. thesis, Karlsruher Institut für Technologie (KIT), doi: 10.5445/IR/1000173433, 2024.
- Klein, S. A., McCoy, R. B., Morrison, H., Ackerman, A. S., Avramov, A., Boer, G. d., Chen, M., Cole, J. N. S., Del Genio, A. D., Falk, M., Foster, M. J., Fridlind, A., Golaz, J.-C., Hashino, T., Harrington, J. Y., Hoose, C., Khairoutdinov, M. F., Larson, V. E., Liu, X., Luo, Y., McFarquhar, G. M., Menon, S., Neggers, R. A. J., Park, S., Poellot, M. R., Schmidt, J. M., Sednev, I., Shipway, B. J., Shupe, M. D., Spangenberg, D. A., Sud, Y. C., Turner, D. D., Veron, D. E., Salzen, K. v., Walker, G. K., Wang, Z., Wolf, A. B., Xie, S., Xu, K.-M., Yang, F., and Zhang, G.: Intercomparison of model simulations of mixed-phase clouds observed during the ARM Mixed-Phase Arctic Cloud Experiment. I: single-layer cloud, *Quarterly Journal of the Royal Meteorological Society*, 135, 979–1002, doi: <https://doi.org/10.1002/qj.416>, 2009.
- Kleinheins, J., Kiselev, A., Keinert, A., Kind, M., and Leisner, T.: Thermal Imaging of Freezing Drizzle Droplets: Pressure Release Events as a Source of Secondary Ice Particles, *Journal of the Atmospheric Sciences*, 78, 1703–1713, doi: 10.1175/JAS-D-20, 2021.
- Kneifel, S. and Moisseev, D.: Long-term statistics of riming in nonconvective clouds derived from ground-based doppler cloud radar observations, *Journal of the Atmospheric Sciences*, 77, 3495–3508, doi: 10.1175/JAS-D-20-0007.1, 2020.
- Knight, C. A.: Ice growth from the Vapor at - 5°C, *Journal of the Atmospheric Sciences*, 69, 2031–2041, doi: 10.1175/JAS-D-11-0287.1, 2012.
- Knust, R.: Polar Research and Supply Vessel POLARSTERN Operated by the Alfred-Wegener-Institute, *Journal of large-scale research facilities JLSRF*, 3, A119, doi: 10.17815/jlsrf-3-163, 2017.
- Köhler, H.: The nucleus in and the growth of hygroscopic droplets, *Trans. Faraday Soc.*, 32, 1152–1161, doi: 10.1039/TF9363201152, 1936.
- Kokhanovsky, A. and Tomasi, C.: *Physics and chemistry of the arctic atmosphere*, Springer, 2020.
- Komurcu, M., Storelvmo, T., Tan, I., Lohmann, U., Yun, Y., Penner, J. E., Wang, Y., Liu, X., and Takemura, T.: Intercomparison of the cloud water phase among global climate models, *Journal of Geophysical Research*, 119, 3372–3400, doi: 10.1002/2013JD021119, 2014.

-
- Koontz, A., Uin, J., Andrews, E., Enekwizu, O., Hayes, C., and Salwen, C.: Cloud Condensation Nuclei Particle Counter (AOSCCN2COLA), doi: 10.5439/1323892, accessed November 8, 2023., 2020.
- Korolev, A.: Limitations of the Wegener-Bergeron-Findeisen mechanism in the evolution of mixed-phase clouds, *Journal of the Atmospheric Sciences*, 64, 3372–3375, doi: 10.1175/JAS4035.1, 2007.
- Korolev, A. and Leisner, T.: Review of experimental studies of secondary ice production, *Atmospheric Chemistry and Physics*, 20, 11 767–11 797, doi: 10.5194/acp-20-11767-2020, 2020.
- Korolev, A., McFarquhar, G., Field, P. R., Franklin, C., Lawson, P., Wang, Z., Williams, E., Abel, S. J., Axisa, D., Borrmann, S., Crosier, J., Fugal, J., Krämer, M., Lohmann, U., Schlenczek, O., Schnaiter, M., and Wendisch, M.: Mixed-Phase Clouds: Progress and Challenges, *Meteorological Monographs*, 58, 1–5, doi: 10.1175/amsmonographs-d-17-0001.1, 2017.
- Ladino Moreno, L. A., Stetzer, O., and Lohmann, U.: Contact freezing: A review of experimental studies, doi: 10.5194/acp-13-9745-2013, 2013.
- Lamb, D. and Verlinde, J.: Physics and chemistry of clouds, doi: 10.1017/CBO9780511976377, 2011.
- Lauber, A., Kiselev, A., Pander, T., Handmann, P., and Leisner, T.: Secondary Ice Formation during Freezing of Levitated Droplets, doi: 10.1175/JAS-D-18.
- L’Ecuyer, T. S., Hang, Y., Matus, A. V., and Wang, Z.: Reassessing the Effect of Cloud Type on Earth’s Energy Balance in the Age of Active Spaceborne Observations. Part I, *American Meteorological Society*, 32, 6197–6217, doi: 10.2307/26831705, 2019.
- Li, J., Yi, Y., Minnis, P., Huang, J., Yan, H., Ma, Y., Wang, W., and Kirk Ayers, J.: Radiative effect differences between multi-layered and single-layer clouds derived from CERES, CALIPSO, and CloudSat data, *Journal of Quantitative Spectroscopy and Radiative Transfer*, 112, 361–375, doi: 10.1016/J.JQSRT.2010.10.006, 2011.
- Li, J., Huang, J., Stamnes, K., Wang, T., Lv, Q., and Jin, H.: A global survey of cloud overlap based on CALIPSO and CloudSat measurements, *Atmospheric Chemistry and Physics*, 15, 519–536, doi: 10.5194/acp-15-519-2015, 2015.
- Lilly, D. K.: On the numerical simulation of buoyant convection, *Tellus*, 14, 148–172, doi: 10.1111/j.2153-3490.1962.tb00128.x, 1962.
- Lilly, D. K.: Models of cloud-topped mixed layers under a strong inversion, *Quarterly Journal of the Royal Meteorological Society*, 94, 292–309, doi: 10.1002/qj.49709440106, 1968.

- Liou, K.-N.: An Introduction to Atmospheric Radiation, Academic Press, New York, 1st edn., 1980.
- Liu, Y., Key, J. R., Ackerman, S. A., Mace, G. G., and Zhang, Q.: Arctic cloud macrophysical characteristics from CloudSat and CALIPSO, *Remote Sensing of Environment*, 124, 159–173, doi: 10.1016/j.rse.2012.05.006, 2012.
- Lonardi, M., Pilz, C., Akansu, E. F., Dahlke, S., Egerer, U., Ehrlich, A., Griesche, H., Heymsfield, A. J., Kirbus, B., Schmitt, C. G., Shupe, M. D., Siebert, H., Wehner, B., and Wendisch, M.: Tethered balloon-borne profile measurements of atmospheric properties in the cloudy atmospheric boundary layer over the Arctic sea ice during MOSAiC: Overview and first results, *Elementa*, 10, doi: 10.1525/elementa.2021.000120, 2022.
- López-García, V., Neely, R. R., Dahlke, S., and Brooks, I. M.: Low-level jets over the Arctic Ocean during MOSAiC, *Elementa*, 10, 4993–5007, doi: 10.1525/elementa.2022.00063, 2022.
- Luo, Y., Xu, K. M., Morrison, H., McFarquhar, G. M., Wang, Z., and Zhang, G.: Multi-layer arctic mixed-phase clouds simulated by a cloud-resolving model: Comparison with ARM observations and sensitivity experiments, *Journal of Geophysical Research Atmospheres*, 113, doi: 10.1029/2007JD009563, 2008.
- Maahn, M., Moisseev, D., Steinke, I., Maherndl, N., and Shupe, M. D.: Introducing the Video In Situ Snowfall Sensor (VISSS), *Atmospheric Measurement Techniques*, 17, 899–919, doi: 10.5194/amt-17-899-2024, 2024.
- Marchant, B., Platnick, S., Meyer, K., and Wind, G.: Evaluation of the MODIS Collection 6 multilayer cloud detection algorithm through comparisons with CloudSat Cloud Profiling Radar and CALIPSO CALIOP products, *Atmospheric Measurement Techniques*, 13, 3263–3275, doi: 10.5194/amt-13-3263-2020, 2020.
- Mason, B. J. and Maybank, J.: The fragmentation and electrification of freezing water drops, *Quarterly Journal of the Royal Meteorological Society*, 86, 176–185, doi: 10.1002/qj.49708636806, 1960.
- Matrosov, S. Y.: Retrievals of vertical profiles of ice cloud microphysics from radar and IR measurements using tuned regressions between reflectivity and cloud parameters, Tech. rep., 1999.
- Maturilli, M., Sommer, M., Holdridge, D. J., Dahlke, S., Graeser, J., Sommerfeld, A., Jaiser, R., Deckelmann, H., and Schulz, A.: MOSAiC radiosonde data (level 3), doi: 10.1594/PANGAEA.943870, 2022a.
- Maturilli, M., Sommer, M., Holdridge, D. J., Dahlke, S., and Schulz, A.: Radiosonde measurements in 2020-09 during MOSAiC Legs PS122/5 (level 3 data), doi: 10.

-
- 1594/PANGAEA.944834, in: Maturilli, Marion; Sommer, Michael; Holdridge, Donna J.; Dahlke, Sandro; Graeser, Jürgen; Sommerfeld, Anja; Jaiser, Ralf; Deckelmann, Holger; Schulz, Alexander (2022): MOSAiC radiosonde data (level 3). PANGAEA, <https://doi.org/10.1594/PANGAEA.943870>, 2022b.
- Matus, A. V. and L'Ecuyer, T. S.: The role of cloud phase in Earth's radiation budget, *Journal of Geophysical Research*, 122, 2559–2578, doi: 10.1002/2016JD025951, 2017.
- Mauritsen, T., Sedlar, J., Tjernström, M., Leck, C., Martin, M., Shupe, M., Sjogren, S., Sierau, B., Persson, P. O., Brooks, I. M., and Swietlicki, E.: An Arctic CCN-limited cloud-aerosol regime, *Atmospheric Chemistry and Physics*, 11, 165–173, doi: 10.5194/acp-11-165-2011, 2011.
- McInnes, K. L. and Curry, J. A.: Modelling the Mean and Turbulent Structure of the Summertime Arctic Cloudy Boundary Layer, *Boundary-layer meteorology*, 73, 125–143, 1995.
- Medeiros, B., Clement, A. C., Benedict, J. J., and Zhang, B.: Investigating the impact of cloud-radiative feedbacks on tropical precipitation extremes, *npj Climate and Atmospheric Science*, 4, doi: 10.1038/s41612-021-00174-x, 2021.
- Mellado, J. P.: Cloud-Top Entrainment in Stratocumulus Clouds, *Annual Review of Fluid Mechanics*, 49, 145–169, doi: 10.1146/annurev-fluid-010816-060231, 2017.
- Mellor, G. L. and Yamada, T.: Development of a turbulence closure model for geophysical fluid problems, *Reviews of Geophysics*, 20, 851–875, doi: <https://doi.org/10.1029/RG020i004p00851>, 1982.
- Mironov, D., Ritter, B., Schulz, J. P., Buchhold, M., Lange, M., and Machulskaya, E.: Parameterisation of sea and lake ice in numerical weather prediction models of the German Weather Service, *Tellus, Series A: Dynamic Meteorology and Oceanography*, 64, doi: 10.3402/tellusa.v64i0.17330, 2012.
- Monteith, J. and Unsworth, M.: *Principles of Environmental Physics*, Elsevier Science, 2007.
- Morrison, H., Curry, J. A., and Khvorostyanov, V. I.: A New Double-Moment Microphysics Parameterization for Application in Cloud and Climate Models. Part I: Description, *Tech. rep.*, 2005a.
- Morrison, H., Shupe, M. D., Pinto, J. O., and Curry, J. A.: Possible roles of ice nucleation mode and ice nuclei depletion in the extended lifetime of Arctic mixed-phase clouds, *Geophysical Research Letters*, 32, 1–5, doi: 10.1029/2005GL023614, 2005b.
- Morrison, H., Pinto, J. O., Curry, J. A., and McFarquhar, G. M.: Sensitivity of modeled arctic mixed-phase stratocumulus to cloud condensation and ice nuclei over regionally

- varying surface conditions, *Journal of Geophysical Research Atmospheres*, 113, doi: 10.1029/2007JD008729, 2008.
- Morrison, H., McCoy, R. B., Klein, S. A., Xie, S., Luo, Y., Avramov, A., Chen, M., Cole, J. N., Falk, M., Foster, M. J., del Genio, A. D., Harrington, J. Y., Hoose, C., Khairoutdinov, M. F., Larson, V. E., Liu, X., McFarquhar, G. M., Poellot, M. R., von Salzen, K., Shipway, B. J., Shupe, M. D., Sud, Y. C., Turner, D. D., Veron, D. E., Walker, G. K., Wang, Z., Wolf, A. B., Xu, K. M., Yang, F., and Zhang, G.: Intercomparison of model simulations of mixed-phase clouds observed during the ARM Mixed-Phase Arctic Cloud Experiment. II: Multilayer cloud, *Quarterly Journal of the Royal Meteorological Society*, 135, 1003–1019, doi: 10.1002/qj.415, 2009.
- Morrison, H., Zuidema, P., Ackerman, A. S., Avramov, A., De Boer, G., Fan, J., Fridlind, A. M., Hashino, T., Harrington, J. Y., Luo, Y., Ovchinnikov, M., and Shipway, B.: Intercomparison of cloud model simulations of Arctic mixed-phase boundary layer clouds observed during SHEBA/FIRE-ACE, *Journal of Advances in Modeling Earth Systems*, 3, doi: 10.1029/2011MS000066, 2011.
- Morrison, H., De Boer, G., Feingold, G., Harrington, J., Shupe, M. D., and Sulia, K.: Resilience of persistent Arctic mixed-phase clouds, doi: 10.1038/ngeo1332, 2012.
- Mossop, S. C.: The Freezing of Supercooled Water, *Proceedings of the Physical Society. Section B*, 68, 193–208, doi: 10.1088/0370-1301/68/4/301, 1954.
- Mossop, S. C.: Production of secondary ice particles during the growth of graupel by riming, *Quarterly Journal of the Royal Meteorological Society*, 102, 45–57, doi: 10.1002/qj.49710243104, 1976.
- Murray, F. W.: On the Computation of Saturation Vapor Pressure, *Journal of Applied Meteorology and Climatology*, 6, 203 – 204, doi: 10.1175/1520-0450(1967)006<0203:OTCOSV>2.0.CO;2, 1967.
- Neggers, R., Chylik, J., and Schnierstein, N.: The entrainment efficiency of persistent Arctic mixed-phase clouds as inferred from daily large-eddy simulations during the MOSAiC drift, *ESS Open Archive*, doi: 10.22541/essoar.172710718.86866606/v1, 2024.
- Niemand, M., Möhler, O., Vogel, B., Vogel, H., Hoose, C., Connolly, P., Klein, H., Bingemer, H., Demott, P., Skrotzki, J., and Leisner, T.: A particle-surface-area-based parameterization of immersion freezing on desert dust particles, *Journal of the Atmospheric Sciences*, 69, 3077–3092, doi: 10.1175/JAS-D-11-0249.1, 2012.
- Nieuwstadt, F. T. M. and Duynkerke, P. G.: *ATMOSPHERIC RESK4-RCH Turbulence in the atmospheric boundary layer*, Tech. rep., 1996.

-
- Nomokonova, T., Ebell, K., Löhnert, U., Maturilli, M., Ritter, C., and O'Connor, E.: Statistics on clouds and their relation to thermodynamic conditions at Ny-Ålesund using ground-based sensor synergy, *Atmospheric Chemistry and Physics*, 19, 4105–4126, doi: 10.5194/acp-19-4105-2019, 2019.
- Oreopoulos, L., Cho, N., and Lee, D.: New insights about cloud vertical structure from CloudSat and CALIPSO observations, *Journal of Geophysical Research: Atmospheres*, 122, 9280–9300, doi: 10.1002/2017JD026629, 2017.
- Overland, J., Dunlea, E., Box, J. E., Corell, R., Forsius, M., Kattsov, V., Olsen, M. S., Pawlak, J., Reiersen, L.-O., and Wang, M.: The urgency of Arctic change, *Polar Science*, 21, 6–13, doi: <https://doi.org/10.1016/j.polar.2018.11.008>, 2019.
- Palo, T., Vihma, T., Jaagus, J., and Jakobson, E.: Observations of temperature inversions over central Arctic sea ice in summer, *Quarterly Journal of the Royal Meteorological Society*, 143, 2741–2754, doi: 10.1002/qj.3123, 2017.
- Pasquier, J. T., Henneberger, J., Ramelli, F., Lauber, A., David, R. O., Wieder, J., Carlsen, T., Gierens, R., Maturilli, M., and Lohmann, U.: Conditions favorable for secondary ice production in Arctic mixed-phase clouds, *Atmospheric Chemistry and Physics*, 22, 15 579–15 601, doi: 10.5194/acp-22-15579-2022, 2022.
- Petty, G. W.: *A First Course in Atmospheric Radiation*, Sundog Publishing, second edn., URL <https://api.semanticscholar.org/CorpusID:129376785>, 2004.
- Pincus, R., Barker, H. W., and Morcrette, J. J.: A fast, flexible, approximate technique for computing radiative transfer in inhomogeneous cloud fields, *Journal of Geophysical Research: Atmospheres*, 108, doi: 10.1029/2002jd003322, 2003.
- Pithan, F., Svensson, G., Caballero, R., Chechin, D., Cronin, T. W., Ekman, A. M., Neggers, R., Shupe, M. D., Solomon, A., Tjernström, M., and Wendisch, M.: Role of air-mass transformations in exchange between the Arctic and mid-latitudes, doi: 10.1038/s41561-018-0234-1, 2018.
- Porter, G. C., Adams, M. P., Brooks, I. M., Ickes, L., Karlsson, L., Leck, C., Salter, M. E., Schmale, J., Siegel, K., Sikora, S. N., Tarn, M. D., Vüllers, J., Wernli, H., Zieger, P., Zinke, J., and Murray, B. J.: Highly Active Ice-Nucleating Particles at the Summer North Pole, *Journal of Geophysical Research: Atmospheres*, 127, doi: 10.1029/2021JD036059, 2022.
- Prill, F., Reinert, D., Rieger, D., Zängl, G., Rieger, D., and Prill, F.: *ICON Tutorial*, Tech. rep., doi: 10.5676/DWDpub/nwv/icontutorial2020, 2020.
- Proske, U., Bessenbacher, V., Dedekind, Z., Lohmann, U., and Neubauer, D.: How frequent is natural cloud seeding from ice cloud layers (-35°C) over Switzerland?,

- Atmospheric Chemistry and Physics, 21, 5195–5216, doi: 10.5194/acp-21-5195-2021, 2021.
- Pruppacher, H. R. and Klett, J. D.: *Microphysics of Clouds and Precipitation*, Springer Dordrecht, 2 edn., doi: <https://doi.org/10.1007/978-0-306-48100-0>, 1979.
- Pu, Z. and Kalnay, E.: Numerical Weather Prediction Basics: Models, Numerical Methods, and Data Assimilation, in: *Handbook of Hydrometeorological Ensemble Forecasting*, pp. 1–31, Springer Berlin Heidelberg, doi: 10.1007/978-3-642-40457-3{_}11-1, 2018.
- Raif, E. N., Barr, S. L., Tarn, M. D., McQuaid, J. B., Daily, M. I., Abel, S. J., Barrett, P. A., Bower, K. N., Field, P. R., Carslaw, K. S., and Murray, B. J.: High ice-nucleating particle concentrations associated with Arctic haze in springtime cold-air outbreaks, *EGUsphere* [preprint], doi: 10.5194/egusphere-2024-1502, 2024.
- Ramanathan, V.: The Role of Earth Radiation Budget Studies in Climate and General Circulation Research, *Journal of Geophysical Research*, 92, 4075–4095, 1987.
- Rantanen, M., Karpechko, A. Y., Lipponen, A., Nordling, K., Hyvärinen, O., Ruosteenoja, K., Vihma, T., and Laaksonen, A.: The Arctic has warmed nearly four times faster than the globe since 1979, *Communications Earth and Environment*, 3, doi: 10.1038/s43247-022-00498-3, 2022.
- Raschendorfer, M.: The new turbulence parameterization of LM, 2001.
- Rieger, D.: *ecRad in ICON Implementation Overview Issue 004 Reports on ICON*, doi: 10.5676/DWD, 2019.
- Roe, G. H.: Orographic precipitation, *Annual Review of Earth and Planetary Sciences*, 33, 645–671, doi: 10.1146/annurev.earth.33.092203.122541, 2005.
- Roudsari, G., Lbadaoui-Darvas, M., Welti, A., Nenes, A., and Laaksonen, A.: The molecular scale mechanism of deposition ice nucleation on silver iodide, *Environmental Science: Atmospheres*, 4, 243–251, doi: 10.1039/d3ea00140g, 2023.
- Sandu, I., Beljaars, A., Bechtold, P., Mauritsen, T., and Balsamo, G.: Why is it so difficult to represent stably stratified conditions in numerical weather prediction (NWP) models?, *Journal of Advances in Modeling Earth Systems*, 5, 117–133, doi: 10.1002/jame.20013, 2013.
- Sato, M. and Hattanji, T.: A laboratory experiment on salt weathering by humidity change: salt damage induced by deliquescence and hydration, *Progress in Earth and Planetary Science*, 5, doi: 10.1186/s40645-018-0241-2, 2018.

-
- Schäfer, B., David, R. O., Georgakaki, P., Pasquier, J. T., Sotiropoulou, G., and Storelmo, T.: Simulations of primary and secondary ice production during an Arctic mixed-phase cloud case from the Ny-Ålesund Aerosol Cloud Experiment (NASCENT) campaign, *Atmospheric Chemistry and Physics*, 24, 7179–7202, doi: 10.5194/acp-24-7179-2024, 2024.
- Schäfer, S. A. and Voigt, A.: Radiation Weakens Idealized Midlatitude Cyclones, *Geophysical Research Letters*, 45, 2833–2841, doi: 10.1002/2017GL076726, 2018.
- Schmale, J., Zieger, P., and Ekman, A. M.: Aerosols in current and future Arctic climate, *Nature Climate Change*, 11, 95–105, doi: 10.1038/s41558-020-00969-5, 2021.
- Seidel, J. S., Kiselev, A. A., Keinert, A., Stratmann, F., Leisner, T., and Hartmann, S.: Secondary ice production - No evidence of efficient rime-splintering mechanism, *Atmospheric Chemistry and Physics*, 24, 5247–5263, doi: 10.5194/acp-24-5247-2024, 2024.
- Seifert, A. and Beheng, K. D.: A two-moment cloud microphysics parameterization for mixed-phase clouds. Part 1: Model description, *Meteorology and Atmospheric Physics*, 92, 45–66, doi: 10.1007/s00703-005-0112-4, 2006.
- Serreze, M. C. and Barry, R. G.: Processes and impacts of Arctic amplification: A research synthesis, *Global and Planetary Change*, 77, 85–96, doi: 10.1016/j.gloplacha.2011.03.004, 2011.
- Shupe, M.: ShupeTurner cloud microphysics retrieval MOSAiC 2019-2020, doi: 10.5439/1871015, 2023.
- Shupe, M. D. and Intrieri, J. M.: Cloud Radiative Forcing of the Arctic Surface: The Influence of Cloud Properties, Surface Albedo, and Solar Zenith Angle, *Journal of Climate*, 2003.
- Shupe, M. D., Uttal, T., and Matrosov, S. Y.: Arctic Cloud Microphysics Retrievals from Surface-Based Remote Sensors at SHEBA, *Journal of Applied Meteorology*, 44, 1544 – 1562, doi: <https://doi.org/10.1175/JAM2297.1>, 2005.
- Shupe, M. D., Persson, P. O., Brooks, I. M., Tjernström, M., Sedlar, J., Mauritsen, T., Sjogren, S., and Leck, C.: Cloud and boundary layer interactions over the Arctic sea ice in late summer, *Atmospheric Chemistry and Physics*, 13, 9379–9400, doi: 10.5194/acp-13-9379-2013, 2013.
- Shupe, M. D., Turner, D. D., Zwink, A., Thieman, M. M., Mlawer, E. J., and Shippert, T.: Deriving arctic cloud microphysics at Barrow, Alaska: Algorithms, results, and radiative closure, *Journal of Applied Meteorology and Climatology*, 54, 1675–1689, doi: 10.1175/JAMC-D-15-0054.1, 2015.

Shupe, M. D., Rex, M., Blomquist, B., G. Persson, P. O., Schmale, J., Uttal, T., Althausen, D., Angot, H., Archer, S., Bariteau, L., Beck, I., Bilberry, J., Bucci, S., Buck, C., Boyer, M., Brasseur, Z., Brooks, I. M., Calmer, R., Cassano, J., Castro, V., Chu, D., Costa, D., Cox, C. J., Creamean, J., Crewell, S., Dahlke, S., Damm, E., de Boer, G., Deckelmann, H., Dethloff, K., Dütsch, M., Ebell, K., Ehrlich, A., Ellis, J., Engelmann, R., Fong, A. A., Frey, M. M., Gallagher, M. R., Ganzeveld, L., Gradinger, R., Graeser, J., Greenamyre, V., Griesche, H., Griffiths, S., Hamilton, J., Heinemann, G., Helmig, D., Herber, A., Heuzé, C., Hofer, J., Houchens, T., Howard, D., Inoue, J., Jacobi, H. W., Jaiser, R., Jokinen, T., Jourdan, O., Jozef, G., King, W., Kirchgassner, A., Klingebiel, M., Krassovski, M., Krumpfen, T., Lampert, A., Landing, W., Laurila, T., Lawrence, D., Lonardi, M., Loose, B., Lüpkes, C., Maahn, M., Macke, A., Maslowski, W., Marsay, C., Maturilli, M., Mech, M., Morris, S., Moser, M., Nicolaus, M., Ortega, P., Osborn, J., Pätzold, F., Perovich, D. K., Petäjä, T., Pils, C., Pirazzini, R., Posman, K., Powers, H., Pratt, K. A., Preußner, A., Quéléver, L., Radenz, M., Rabe, B., Rinke, A., Sachs, T., Schulz, A., Siebert, H., Silva, T., Solomon, A., Sommerfeld, A., Spreen, G., Stephens, M., Stohl, A., Svensson, G., Uin, J., Viegas, J., Voigt, C., von der Gathen, P., Wehner, B., Welker, J. M., Wendisch, M., Werner, M., Xie, Z. Q., and Yue, F.: Overview of the MOSAiC expedition-Atmosphere, doi: 10.1525/elementa.2021.00060, 2022.

Siebesma, A. P., Bony, S., Jakob, C., and Stevens, B.: *Clouds and Climate: Climate Science's Greatest Challenge*, Cambridge University Press, Cambridge, doi: DOI: 10.1017/9781107447738, 2020.

Silber, I. and Shupe, M. D.: Insights on sources and formation mechanisms of liquid-bearing clouds over MOSAiC examined from a Lagrangian framework, *Elementa*, 10, doi: 10.1525/elementa.2021.000071, 2022.

Smagorinsky, J.: General circulation experiments with the primitive equations: I. The basic experiment, *Monthly weather review*, 91, 99–164, 1963.

Solomon, A., Feingold, G., and Shupe, M. D.: The role of ice nuclei recycling in the maintenance of cloud ice in Arctic mixed-phase stratocumulus, *Atmospheric Chemistry and Physics*, 15, 10631–10643, doi: 10.5194/acp-15-10631-2015, 2015.

Solomon, A., De Boer, G., Creamean, J. M., McComiskey, A., Shupe, M. D., Maahn, M., and Cox, C.: The relative impact of cloud condensation nuclei and ice nucleating particle concentrations on phase partitioning in Arctic mixed-phase stratocumulus clouds, *Atmospheric Chemistry and Physics*, 18, 17047–17059, doi: 10.5194/acp-18-17047-2018, 2018.

Sotiropoulou, G., Sedlar, J., Tjernström, M., Shupe, M. D., Brooks, I. M., and Persson, P. O.: The thermodynamic structure of summer Arctic stratocumulus and the dynamic

-
- coupling to the surface, *Atmospheric Chemistry and Physics*, 14, 12 573–12 592, doi: 10.5194/acp-14-12573-2014, 2014.
- Sotiropoulou, G., Sullivan, S., Savre, J., Lloyd, G., Lachlan-Cope, T., Ekman, A. M., and Nenes, A.: The impact of secondary ice production on Arctic stratocumulus, *Atmospheric Chemistry and Physics*, 20, 1301–1316, doi: 10.5194/acp-20-1301-2020, 2020.
- Sotiropoulou, G., Vignon, E., Young, G., Morrison, H., O’Shea, S. J., Lachlan-Cope, T., Berne, A., and Nenes, A.: Secondary ice production in summer clouds over the Antarctic coast: An underappreciated process in atmospheric models, *Atmospheric Chemistry and Physics*, 21, 755–771, doi: 10.5194/acp-21-755-2021, 2021.
- Sotiropoulou, G., Lewinschal, A., Georgakaki, P., Phillips, V. T. J., Patade, S., Ekman, A. M. L., and Nenes, A.: Sensitivity of Arctic Clouds to Ice Microphysical Processes in the NorESM2 Climate Model, *American Meteorological Society*, 37, doi: 10.1175/JCLI-D-22-0458.s1, 2024.
- Spänkuch, D., Hellmuth, O., and Görndorf, U.: What Is a Cloud?: Toward a More Precise Definition, *Bulletin of the American Meteorological Society*, 103, E1894–E1929, doi: 10.1175/BAMS-D-21-0032.1, 2022.
- Sprenger, M. and Wernli, H.: The LAGRANTO Lagrangian analysis tool - Version 2.0, *Geoscientific Model Development*, 8, 2569–2586, doi: 10.5194/gmd-8-2569-2015, 2015.
- Sterzinger, L. J. and Igel, A. L.: Above-cloud concentrations of cloud condensation nuclei help to sustain some Arctic low-level clouds, *Atmospheric Chemistry and Physics*, 24, 3529–3540, doi: 10.5194/acp-24-3529-2024, 2024.
- Sterzinger, L. J., Sedlar, J., Guy, H., Neely, R. R., and Igel, A. L.: Do Arctic mixed-phase clouds sometimes dissipate due to insufficient aerosol? Evidence from comparisons between observations and idealized simulations, *Atmospheric Chemistry and Physics*, 22, 8973–8988, doi: 10.5194/acp-22-8973-2022, 2022.
- Stevens, B., Bony, S., and Webb, M.: Clouds On-Off Klimate Intercomparison Experiment (COOKIE), Tech. rep., 2012.
- Stevens, R. G., Loewe, K., Dearden, C., Dimitrellos, A., Possner, A., Eirund, G. K., Raatikainen, T., Hill, A. A., Shipway, B. J., Wilkinson, J., Romakkaniemi, S., Tonttila, J., Laaksonen, A., Korhonen, H., Connolly, P., Lohmann, U., Hoose, C., Ekman, A. M., Carslaw, K. S., and Field, P. R.: A model intercomparison of CCN-limited tenuous clouds in the high Arctic, *Atmospheric Chemistry and Physics*, 18, 11 041–11 071, doi: 10.5194/acp-18-11041-2018, 2018.

- Subrahmanyam, K. V. and Kumar, K. K.: CloudSat observations of multi layered clouds across the globe, *Climate Dynamics*, 49, 327–341, doi: 10.1007/s00382-016-3345-7, 2017.
- Sullivan, S., Keshtgar, B., Albern, N., Bala, E., Braun, C., Choudhary, A., Hörner, J., Lentink, H., Papavasileiou, G., and Voigt, A.: How does cloud-radiative heating over the North Atlantic change with grid spacing, convective parameterization, and microphysics scheme in ICON version 2.1.00?, *Geoscientific Model Development*, 16, 3535–3551, doi: 10.5194/gmd-16-3535-2023, 2023.
- Sullivan, S. C., Barthlott, C., Crosier, J., Zhukov, I., Nenes, A., and Hoose, C.: The effect of secondary ice production parameterization on the simulation of a cold frontal rainband, *Atmospheric Chemistry and Physics*, 18, 16 461–16 480, doi: 10.5194/acp-18-16461-2018, 2018.
- Svensson, G., Murto, S., Shupe, M. D., Pithan, F., Magnusson, L., Day, J. J., Doyle, J. D., Renfrew, I. A., Spengler, T., and Vihma, T.: Warm air intrusions reaching the MOSAiC expedition in April 2020- The YOPP targeted observing period (TOP), *Elementa*, 11, doi: 10.1525/elementa.2023.00016, 2023.
- Sze, K. C. H., Wex, H., Hartmann, M., Skov, H., Massling, A., and Stratmann, F.: Sample and droplet volume information of Ice Nucleating Particles (INP) including original files, from Villum Research Station (VRS) in Northern Greenland, doi: 10.1594/PANGAEA.953839, 2023.
- Takahashi, T., Nagao, Y., and Kushiyama, Y.: Possible High Ice Particle Production during Graupel-Graupel Collisions, *American Meteorological Society*, 52, 4523–4527, 1995.
- Taylor, P. C. and Monroe, E.: Isolating the Surface Type Influence on Arctic Low-Clouds, *Journal of Geophysical Research: Atmospheres*, 128, doi: 10.1029/2022JD038098, 2023.
- Tetens, O.: Über einige meteorologische Begriffe, *Z. Geophys*, 6, 297–309, 1930.
- Tiedtke, M.: A Comprehensive Mass Flux Scheme for Cumulus Parameterization in Large-Scale Models, *Monthly Weather Review*, 117, 1779 – 1800, doi: [https://doi.org/10.1175/1520-0493\(1989\)117<1779:ACMFSF>2.0.CO;2](https://doi.org/10.1175/1520-0493(1989)117<1779:ACMFSF>2.0.CO;2), 1989.
- Tjernström, M., Svensson, G., Magnusson, L., Brooks, I. M., Prytherch, J., Vüllers, J., and Young, G.: Central Arctic weather forecasting: Confronting the ECMWF IFS with observations from the Arctic Ocean 2018 expedition, *Quarterly Journal of the Royal Meteorological Society*, 147, 1278–1299, doi: 10.1002/qj.3971, 2021.

-
- Tompkins, A. M. and Di Giuseppe, F.: An interpretation of cloud overlap statistics, *Journal of the Atmospheric Sciences*, 72, 2877–2889, doi: 10.1175/JAS-D-14-0278.1, 2015.
- Tsay, S.-C. and Jayaweera, K.: American Meteorological Society Physical Characteristics of Arctic Stratus Clouds, Tech. Rep. 4, 1984.
- Turner, D. D., Shupe, M. D., and Zwink, A. B.: Characteristic atmospheric radiative heating rate profiles in arctic clouds as observed at Barrow, Alaska, *Journal of Applied Meteorology and Climatology*, 57, 953–968, doi: 10.1175/JAMC-D-17-0252.1, 2018.
- Twomey, S.: Pollution and Planetary Albedo, *Atmospheric Environment*, 8, 1251–1256, 1974.
- Twomey, S.: The Influence of Pollution on the Shortwave Albedo of Clouds, *Journal of Atmospheric Sciences*, 34, 1149–1152, 1977.
- Udisti, R., Bazzano, A., Becagli, S., Bolzacchini, E., Caiazza, L., Cappelletti, D., Ferrero, L., Frosini, D., Giardi, F., Grotti, M., Lupi, A., Malandrino, M., Mazzola, M., Moroni, B., Severi, M., Traversi, R., Viola, A., and Vitale, V.: Sulfate source apportionment in the Ny-Ålesund (Svalbard Islands) Arctic aerosol, *Rendiconti Lincei*, 27, 85–94, doi: 10.1007/s12210-016-0517-7, 2016.
- Vaisala Radiosonde RS41 Measurement Performance: URL <https://www.vaisala.com/sites/default/files/documents/White%20paper%20RS41%20Performance%20B211356EN-A.pdf>, [Accessed 2024-09-05].
- Vali, G.: Quantitative Evaluation of Experimental Results on the Heterogeneous Freezing Nucleation of Supercooled Liquids, *Journal of the Atmospheric Sciences*, 28, 402–409, 1971.
- Van Der Dussen, J. J., De Roode, S. R., and Siebesma, A. P.: Factors controlling rapid stratocumulus cloud thinning, *Journal of the Atmospheric Sciences*, 71, 655–664, doi: 10.1175/JAS-D-13-0114.1, 2014.
- Vardiman, L.: The Generation of Secondary Ice Particles in Clouds by Crystal-Crystal Collision, *Journal of the Atmospheric Sciences*, 35, 2168–2180, 1978.
- Vassel, M., Ickes, L., Maturilli, M., and Hoose, C.: Classification of Arctic multilayer clouds using radiosonde and radar data in Svalbard, *Atmospheric Chemistry and Physics*, 19, 5111–5126, doi: 10.5194/acp-19-5111-2019, 2019.
- Voigt, A., Albern, N., Ceppi, P., Grise, K., Li, Y., and Medeiros, B.: Clouds, radiation, and atmospheric circulation in the present-day climate and under climate change, doi: 10.1002/wcc.694, 2021.

- Voigt, A., Keshtgar, B., and Butz, K.: Tug-Of-War on Idealized Midlatitude Cyclones Between Radiative Heating From Low-Level and High-Level Clouds, *Geophysical Research Letters*, 50, doi: 10.1029/2023GL103188, 2023.
- Vüllers, J., Achtert, P., Brooks, I. M., Tjernström, M., Prytherch, J., Burzik, A., and Neely III, R.: Meteorological and cloud conditions during the Arctic Ocean 2018 expedition, *Atmospheric Chemistry and Physics*, 21, 289–314, doi: 10.5194/acp-21-289-2021, 2021.
- Walbröl, A., Griesche, H. J., Mech, M., Crewell, S., and Ebell, K.: Combining low and high frequency microwave radiometer measurements from the MOSAiC expedition for enhanced water vapour products, *EGUsphere[preprint]*, doi: 10.5194/egusphere-2024-1301, 2024.
- Walbröl, A., Engelmann, R., Griesche, H., Radenz, M., Hofer, J., Althausen, D., Ebell, K., Mech, M., and Crewell, S.: Improved integrated water vapour derived from the combination of the microwave radiometers HATPRO and MiRAC-P aboard the Polarstern during the MOSAiC expedition, doi: 10.1594/PANGAEA.968778, 2024.
- Wallentin, G., Oertel, A., Ickes, L., Achtert, P., Tesche, M., and Hoose, C.: Arctic Multilayer Clouds Require Accurate Thermodynamic Profiles and Efficient Primary and Secondary Ice Processes for a Realistic Structure and Composition, *EGUsphere[submitted]*, doi: 10.5194/egusphere-2024-2988, 2024.
- Wang, P. K. and Ji, W.: Collision Efficiencies of Ice Crystals at Low-Intermediate Reynolds Numbers Colliding with Supercooled Cloud Droplets: A Numerical Study, *Journal of the Atmospheric Sciences*, 57, 1001–1009, 2000.
- Wang, T., Fetzer, E. J., Wong, S., Kahn, B. H., and Yue, Q.: Validation of MODIS cloud mask and multilayer flag using CloudSat-CALIPSO cloud profiles and a cross-reference of their cloud classifications, *Journal of Geophysical Research: Atmospheres*, 121, doi: 10.1002/2016JD025239, 2016.
- Wedi, N. and Malardel, S.: Non-hydrostatic modelling at ECMWF, doi: 10.21957/rzojr98e, 2010.
- Wegener, A.: *Thermodynamik der Atmosphäre*, Leipzig, Germany; Barth, 1911.
- Wernli, H. and Davies, H. C.: A Lagrangian-based analysis of extratropical cyclones. I: The method and some applications, *Quarterly Journal of the Royal Meteorological Society*, 123, 467–489, doi: <https://doi.org/10.1002/qj.49712353811>, 1997.
- Wex, H., Huang, L., Sheesley, R., Bossi, R., and Traversi, R.: Annual concentrations of ice nucleating particles at different Arctic stations, doi: 10.1594/PANGAEA.899701, supplement to: Wex, Heike; Huang, Lin; Zhang, W; Hung, Hayley; Traversi, Rita;

- Becagli, Silvia; Sheesley, Rebecca; Moffett, James; Barrett, T E; Bossi, Rossana; Skov, Henrik; Hünerbein, Anja; Lubitz, Jasmin; Löffler, M; Linke, O; Hartmann, Markus; Herenz, Paul; Stratmann, Frank (2019): Annual variability of ice-nucleating particle concentrations at different Arctic locations. *Atmospheric Chemistry and Physics*, 19(7), 5293-5311, <https://doi.org/10.5194/acp-19-5293-2019>, 2019.
- Wind, G., Platnick, S., King, M. D., Hubanks, P. A., Pavolonis, M. J., Heidinger, A. K., Yang, P., and Baum, B. A.: American Meteorological Society Multilayer Cloud Detection with the MODIS Near-Infrared Water Vapor Absorption Band, Source: *Journal of Applied Meteorology and Climatology*, 49, 2315–2333, doi: 10.2307/26173983, 2010.
- Wood, R.: Stratus and Stratocumulus, *Encyclopedia of Atmospheric Sciences*, 2, 196–200, 2015.
- You, C., Tjernström, M., and Devasthale, A.: Warm-Air Advection Over Melting Sea-Ice: A Lagrangian Case Study, *Boundary-Layer Meteorology*, 179, 99–116, doi: 10.1007/s10546-020-00590-1, 2021.
- Young, G., Connolly, P. J., Dearden, C., and Choullarton, T. W.: Relating large-scale subsidence to convection development in Arctic mixed-phase marine stratocumulus, *Atmospheric Chemistry and Physics*, 18, 1475–1494, doi: 10.5194/acp-18-1475-2018, 2018.
- Zängl, G., Reinert, D., Rípodas, P., and Baldauf, M.: The ICON (ICOsahedral Non-hydrostatic) modelling framework of DWD and MPI-M: Description of the non-hydrostatic dynamical core, *Quarterly Journal of the Royal Meteorological Society*, 141, 563–579, doi: 10.1002/qj.2378, 2015.
- Zhao, X. and Liu, X.: Primary and secondary ice production: Interactions and their relative importance, *Atmospheric Chemistry and Physics*, 22, 2585–2600, doi: 10.5194/acp-22-2585-2022, 2022.
- Zhao, X., Liu, X., Phillips, V. T., and Patade, S.: Impacts of secondary ice production on Arctic mixed-phase clouds based on ARM observations and CAM6 single-column model simulations, *Atmospheric Chemistry and Physics*, 21, 5685–5703, doi: 10.5194/acp-21-5685-2021, 2021.
- Zieger, P., Heslin-Rees, D., Karlsson, L., Koike, M., Modini, R., and Krejci, R.: Black carbon scavenging by low-level Arctic clouds, *Nature Communications*, 14, doi: 10.1038/s41467-023-41221-w, 2023.